Ole Henrik Waagaard

Inverse scattering and experimental characterization of optical grating filters

Doctoral thesis
for the degree of doktor ingeniør

Trondheim, February 2006

Norwegian University of
Science and Technology
Fakultet for informasjonsteknologi, matematikk og elektroteknikk
Institutt for Elektronikk og Telekommunikasjon

NTNU
Innovation and Creativity

NTNU
Norwegian University of Science and Technology

Doctoral thesis
for the degree of doktor ingeniør

Fakultet for informasjonsteknologi, matematikk og elektroteknikk
Institutt for Elektronikk og Telekommunikasjon

ISBN ISBN 82-471-7818-4 (printed ver.)
ISBN ISBN 82-471-7817-6 (electronic ver.)
ISSN 1503-8181

Doctoral Theses at NTNU, 2006:37

Printed by Tapir Uttrykk

Abstract

This thesis mainly studies inverse scattering applied to the field of fiber Bragg gratings. I focus on the layer-peeling inverse scattering algorithm, and use this algorithm to design gratings and reconstruct their spatial profile from measured complex reflection spectra.

Using a discrete grating model, we find necessary and sufficient conditions for the reflection response to be realizable as a grating of finite length. With the help of these conditions, a general method for designing gratings with a given finite length is proposed. The proposed method is demonstrated to give designs with better side lobe suppression and less ripple than designs based on windowing.

Fiber Bragg gratings is known to be birefringent with slightly polarization-dependent background index and polarization-dependent effective index contrast. The birefringence may lead to coupling between polarization modes. Scattering will now involve two forward-propagating and two backward-propagating modes, and the response from the grating is characterized by a frequency-dependent reflection Jones matrix. A polarization-resolved layer-peeling algorithm is developed to reconstruct the polarization-dependent background index and polarization-dependent effective index contrast from the reflection Jones matrix. Realizability criteria for birefringent gratings of a finite length is obtained.

In some cases, more than two waveguide modes interact. There may be interaction between bounded modes within a fiber supporting several modes, or between the core mode and cladding modes in a "single mode" fiber. To handle inverse scattering in such cases, we have developed a layer-peeling algorithm that takes into account any number of interacting modes, where the interaction may be both codirectional and contradirectional. The modes may have equal or different propagation constants. We will show that this method can also be used for discrete multimode structures and 3D structures.

The complex reflectivity spectrum of gratings is measured with optical frequency domain reflectometry. The response from a Michelson interferometer, where the grating constitutes one of the reflectors, is recorded while sweeping the laser. The measured spectrum is fed into the layer-peeling algorithm for calculation of the spatial profile of the grating. The method gives satisfactory results for gratings up to 98-99 %. In order to spatially characterize stronger gratings, the grating is thermally chirped so that the reflectivity is reduced and the spectral information is spread over a wider bandwidth. In this way, the spatial profile of a grating with -66 dB minimum transmission is successfully reconstructed.

A method for measuring the reflection Jones matrix of gratings has been de-

veloped. The source polarization is continuously modulated through four states of polarization that can be represented by four linearly independent Stokes vectors. This polarization modulation is achieved by placing a Mach-Zehnder-type interferometer in between the laser and the Michelson interferometer containing the grating. The polarization modulation interferometer has three paths with different delay and retardation. It spreads different components of the grating impulse response Jones matrix into separable bands in the optical time domain. The impulse response is reconstructed from these bands, and is fed into the polarization-resolved layer-peeling algorithm to calculate the polarization-dependent index modulation and birefringence. This measurement setup is used to characterize the polarization dependence of index modulation resulting from different uv-polarization used to fabricate the gratings.

Acknowledgments

I wish to thank my supervisor Johannes Skaar at Department of Electronics and Telecommunication at NTNU for his support and guidance during this work. All the papers in the first part of this thesis have been written in collaboration with him. He has never rejected any of my suggestions for solutions to a problem without thorough investigation. This collaboration has therefore been very fruitful, and the results could not have been produced by neither of us alone. I would also like to thank Helge Engan at the same department for supervising me my first 1 1/2 years as a doctoral student.

All the work of this thesis has been carried out while I have been an employee at Optoplan AS. I am therefore very grateful for the support of many of my colleges there. Especially, I would like to thank Erlend Rønnekleiv and Jon Thomas Kringlebotn for their support and collaboration, and for reading and commenting on much of the material in this thesis. The work on spatial characterization was initiated by them, and they have made many suggestions to how the measurement setup can be improved. I would also especially thank Morten Eriksrud for giving me the opportunity to work on my doctoral thesis while being an employee at Optoplan. I also thank Erik Magnus Bruvik, for making the FBG and fiber laser samples used for spatial characterization, Sigurd Løvseth and Kyrre Aksnes for interesting discussions and their help with fiber lasers, Dag Thingbø, Stig Forbord and Mads Hoaas for their help with electronics, and Hilde Nakstad for planning my activities at Optoplan so that the thesis work could be carried out.

Finally, I would like to thank my fiancèe Marianne Solberg for her encouragements during all these years.

This work has been financed by Norwegian Research Council (2000-2001) and Optoplan AS (2001-2006).

Contents

Chapter 1

Introduction

1.1 Background

A fiber Bragg grating (FBG) is a type of optical filter that is formed by periodic or quasi-periodic perturbation of the refractive index in the core of an optical fiber. In each period of the perturbation, a small amount of the incident light is scattered or reflected. When the scattering from all periods adds up in phase, the amount of reflected light is at maximum. The wavelength of light for which this condition occurs, is called the Bragg wavelength. Both pitch and amplitude of the perturbation may vary along the grating, leading to complex gratings with independent control of reflectivity and group delay.

The formation of permanent gratings by photosensitivity was first observed by Hill *et. al.* in 1978 [1]. During experiments where light from an argon laser was launched into a germanium-doped silica fiber, they observed that as a function of time, the transmissivity of the fiber dropped and the amount of reflected light increased. They recognized that this effect was caused by permanent perturbation of the refractive index. A small portion of the light was reflected from each of the end faces, resulting in a standing wave pattern. This pattern caused a periodic change in the refractive index along the fiber. The fiber was photosensitive in the sense that light formed permanent changes in the refractive index. This type of grating is commonly known as a "Hill"-grating.

The photosensitivity of fibers generated limited interest until Meltz *et. al.* [2] developed a holographic writing technique for gratings based on single-photon absorption at 244 nm. They inscribed the grating by illuminating the fiber from the side by an interference pattern formed by two uv-beams. While the "Hill"-gratings had a grating period given by the wavelength of the uv-light, this method gave the opportunity to shift the Bragg wavelength to a range used for optical communication.

Since then, there has been significant attention to exploit this technology in telecommunications and wavelength division multiplexing (WDM). There has been some attempts to use FBGs as WDM-filters, but this technology appears not to be competitive with thin-film technology. However, the technology has found some niches, especially for stabilization of the emitted power and reduction of the band-

width of multimode semiconductor lasers, gain flattening of fiber amplifiers, and dispersion compensation.

Another important application of fiber Bragg grating technology is sensing [3]. The reflected wavelength from the FBG depends on physical properties such as strain and temperature. By interrogating the FBG with broadband light, the shift in the peak reflectivity wavelength can be used as a measure for the physical property. This type of sensors is passive, and has its advantage over traditional electrical sensors in terms of immunity to electromagnetic radiation, robustness in hash environments, and long distance between sensor and interrogation unit. Applications of this technology include structural monitoring and measurements of physical parameters such as temperature and pressure in hash environments, e.g. in an oil well. The FBG may also be used with interferometric sensors. In this case, the FBG is not used for sensing directly, but as reflectors in Fabry-Perot interferometers. By using sensors with FBGs at different wavelengths, WDM of several sensors on the same fiber is possible.

In many of the applications mentioned above need good control of the grating properties. In order to do this, design tools and characterization methods are required. In this thesis both these two requirements are investigated in detail.

1.2 Thesis outline

This thesis consists of two parts. Each part has its own introduction chapter.

The first part deals with different aspects of inverse scattering applied to the field of fiber Bragg gratings. In chapter 3, realizability criteria for a finite length grating are developed, which are used as a basis for a new design algorithm. In chapter 4, the layer-peeling inverse scattering algorithm is extended to the case of birefringent reflective gratings, while in chapter 5 the algorithm is extended to any number of interacting modes.

The second part deals with spatial characterization of fiber Bragg gratings using optical frequency domain reflectometry (OFDR). Chapter 7 demonstrates that OFDR in combination with the layer-peeling algorithm can be used to extract the spatial profile of relatively strong gratings. In chapter 8, thermal chirping is used to extend the method to gratings with very large grating strength. In chapter 9, a method for polarization-resolved spatial characterization is developed.

Finally, the thesis is summarized in chapter 10, and some lines for future work are drawn.

Part I

Inverse scattering theory of optical grating filters

Chapter 2

Inverse scattering

Inverse scattering is the science of extracting structural information about an object from the scattered wave fields from the object. Inverse scattering has been a important tool in applied physics the last century, since much of our knowledge about the physical world comes from scattering experiments. Inverse scattering has therefore applications in numerous fields of physics. An overview of many problems in direct and inverse scattering is collected in a series of books edited by R. Pike and P. Sabatier [4, 5].

This part of the thesis focuses on electromagnetic wave inverse scattering, more specifically on scattering of light in optical fibers. It should be pointed out the close relation with other fields of physics such as acoustic wave inverse scattering and quantum mechanical potential inverse scattering. For simplicity, consider scattering of scalar fields along a line (one-dimensional scattering). Quantum mechanical potential scattering is governed by the Schrödinger equation,

$$\left(\frac{\partial^2}{\partial x^2} + k^2 - V(x)\right)\psi(x,k) = 0, \tag{2.1}$$

where $\psi(x,k)$ is the field, k is the wavenumber and $V(x)$ is the scattering potential.

Electromagnetical and acoustical waves are scattered by perturbations of the wave velocity (or the impedance) of the medium. The local wave velocity in the medium can be written $c(x) = c_0/(\bar{n} + \Delta n(x))$, where in the case of electromagnetic scattering, c_0 is the velocity of light, $\bar{n}$ is the refractive index and $\Delta n(x)$ is the perturbation of the index. The local wavenumber is given by $k(x) = \omega/c(x) = (\bar{n} + \Delta n(x))\omega/c_0 = k(1 + \Delta n(x)/\bar{n})$, where k is the wavenumber of the unperturbed waveguide. When $\Delta n(x) \ll \bar{n}$, $k(x)^2 \approx k^2 + 2k^2\Delta n(x)/\bar{n}$. Inserting $k(x)$ into the Helmholtz equation gives

$$\left(\frac{\partial^2}{\partial x^2} + k(x)^2\right)\psi(x,k) \approx \left(\frac{\partial^2}{\partial x^2} + k^2 + 2k^2\Delta n(x)/\bar{n}\right)\psi(x,k) = 0. \tag{2.2}$$

With $V(x) = -2k^2\Delta n(x)/\bar{n}$, we find that there is a close relationship between quantum mechanical potential scattering, electromagnetic and acoustic wave scattering. Inverse scattering methods developed for Schrödinger equation can therefore often be applied for electromagnetic and acoustic scattering.

In one dimension, the field $\psi(x,k)$ is a superposition of a forward(left)-propagating field component $u(x,k)$ and a backward(right)-propagating field component $v(x,k)$, and the scattering potential provides coupling between $u(x,k)$ and $v(x,k)$. By writing $\psi(x,k) = u(x,k)+v(x,k)$, (2.1) can be expressed as first order coupling equations [6], where the potential $V(x)$ give rise to a coupling function $q(x)$ between $u(x,k)$ and $v(x,k)$.

Reconstruction of the structural information is obtained from a measurement of $v(x,k)$ at a fixed position $x = x_0$ to the left of the coupling structure upon excitation of a known field $u(x_0,k)$. When the coupling is weak, one can assume that $u(x,k)$ is unperturbed by the coupling structure. It this case the coupling function $q(x)$ can be found from the Fourier transform of $v(x_0,k)/u(x_0,k)$. This approximation is called the first Born approximation or the "weak scattering" approximation. It is also a single scattering approximation, since multiple scattering events are neglected.

With stronger coupling between the forward-propagating and backward-propagating fields, the coupling function can no longer be found without considering multiple scattering events, and the first Born approximation does no longer give an accurate solution for the coupling function $q(x)$. In this case an inverse scattering algorithm that takes into acount multiple scattering must be used. One such algorithm is the Gel'fand-Levitan-Machenko (GLM) method [7]. This was the first method that gave a complete solution to one-dimensional inverse scattering problems. This method is based on a set of coupled integral equations that gives the relation between two kernel functions $A_1(x,y)$ and $A_2(x,y)$ and the reflection response [8]. From these two integral equations the kernel functions are found. Once the GLM equations are solved for the kernel functions $A_1(x,y)$ and $A_2(x,y)$, the coupling function can be found from $q(x) = -2A_2^*(x,x)$.

The GLM equations are complicated to solve numerically, and with a coupling structure of N layers of length Δx, the computation complexity becomes $O(N^3)$. Neither do the GLM equations have clear physical interpretations. An alternative method is the layer-peeling algorithm [9, 10] (may also be called layer-stripping or dynamic deconvolution). This method is based on causality of the scattering medium and has therefore a simple physical interpretation: Given a stack of N layers, the leading edge of the impulse response is caused by a reflection from the first layer only. Once the reflectivity of the first layer is found, an impulse response of the structure consisting of layer 2 to N can be found using the inverse transfer matrix of layer 1. This matrix can be found from the reflectivity of the first layer using losslessness and reciprocity conditions. The leading edge of this new impulse response provides the reflectivity of second layer, and so on. The following chapters deal with the layer-peeling algorithm for design and reconstruction of fiber Bragg gratings supporting one or multiple propagation modes. The layer-peeling algorithm is called a differential inverse scattering algorithm, since the solution is a direct consequence of the first-order coupled-wave equations, and since the structure is evaluated layer by layer. In the GLM method, the structure is evaluated as a whole to find the kernel functions from the integral equations. The GLM method is therefore called an integral inverse scattering algorithm.

The layer-peeling algorithm can be evaluated both in the frequency-domain and

in the time-domain. In the time-domain, the impulse response is not calculated explicitly. Instead, the forward-propagating field $u_j(t)$ and the backward-propagating field $v_j(t)$ within layer j is evaluated. These fields are found from $u_{j-1}(t)$ and $v_{j-1}(t)$ using the transfer matrix of layer $j-1$, with the initiation $u_0(t) = \delta(t)$ and $v_0(t) = h(t)$, where $\delta(t)$ is the dirac delta-function and $h(t)$ is the impulse response. From a layer to the next, the reference time is also shifted so that the first sample $u_j(t)$ is always $u_j(0)$. Then the leading edge of the impulse response after removing the first j layers equals $v_j(0)/u_j(0)$. From this fraction, $q(j\Delta x)$ can be found. Alternatively, frequency-domain implementation can be used. In this case, the solution can be found by a recursive equation that calculates the reflection spectrum $R_j(\omega)$ for structure after removing the first j layers. This equation is called the Schur formula, since it is the same as the equation used by Schur for testing the boundedness of an analytic function outside the unit circle of the complex plane [9]. The computation complexity becomes $O(N^2)$ for both implementations, and is therefore much more efficient than the GLM method.

In the nineties, the transverse holographic technique [2, 11, 12] made it possible to write grating with an almost arbitrary, complex reflection response. Inverse scattering techniques for designing gratings were first introduced by Song and Shin [13]. Their method which was based on the GLM method, was restricted to the case when the reflection spectrum can be written as a rational function. Later, numerical implementations of the GLM method without the above mentioned constrains on the reflection spectrum was proposed [8, 14, 15].

In 1999, the use of layer-peeling for the design of gratings where introduced by Feced *et. al.* [16]. A similar algorithm was proposed by Poladian [17]. These algorithms were compared and simplified by Skaar *et. al.* in [18]. However, it is an interesting historical note that a polarization-resolved layer-peeling algorithm used for spatial characterization was presented by Sandel *et.al.* [19] almost a year before Feced.

Any reflection function can certainly not be admissible, that is any reflection function cannot be the response of a physical structure. For instance, the reflection spectrum must be strictly less than one. When the inverse scattering algorithm is used for reconstructing the spatial profile from a measurement of a real grating, noise may lead to that this criteria is not fulfilled, and the inverse scattering will become unstable. Additional limitations are imposed on the reflection response when the grating has a limited length. For instance, it is well known from filter theory that an ideal bandpass-filter cannot be realized with a finite length filter. In [16], it was used a window on the impulse response to obtain a realizable (admissible) spectrum. However, this method has its shortcomings since this results in a finite duration impulse response, while the impulse response of a physical grating must have infinite duration. In chapter 3, we formulate a set of realizability criteria for an FBG of finite length. These realizability criteria are used to approximate the reflection spectrum by one that is realizable for a given length. Once this reflection spectrum is found, the layer-peeling algorithm can be used to compute the required index modulation of the grating to obtain the reflection spectrum. In contrast to other techniques, before applying the inverse scattering algorithm, we know that

the obtained reflection spectrum has a physical representation. It is also shown that the method can improve the result from reconstruction of measured, noisy reflection responses.

In chapter 4, a layer-peeling algorithm is developed for design and reconstruction of birefringent Bragg gratings. Both the index modulation and the background index of an FBG may be polarization dependent. Scattering in this case involves two forward-propagating and two backward-propagating polarization modes, and the scattering and the transfer matrices become 4×4. The inverse scattering algorithm is developed much in the same way as in the polarization-independent case, however the coupling can no longer be fully described by a single coupling function. Each layer is divided into a retardation section, a reflector section and a time-delay section. The retardation section describes the phase delay and the retardation between the polarization modes from one layer to the next. The reflector section describe coupling between forward- and backward-propagating fields. Any reflection phase is attributed to the retardation section. A time-delay section delays the fields from one layer to the next. Losslessness and reciprocity can be used to factorize the local reflection response into retardation and reflection. In similar manner as in chapter 3, realizability criteria for birefringent gratings with a given finite length are obtained.

In chapter 5, the layer-peeling algorithm is extended even further to include any finite number of propagation modes. In contrast to other algorithms in the literature and the algorithm in chapter 4, different modes may have different propagation constants. This complicates inverse scattering, since the impulse response from a discrete structure no longer has its points equidistant in time, and since the matrix describing time-delay from one layer to the next no longer commutes with the matrix describing the phase-delay. Models for scattering in both discrete and continuous coupling structures are presented. It is described how this algorithm can be used to reconstruct gratings with coupling between multiple modes. We also show that the proposed algorithm can be used for two- or three-dimensional inverse scattering.

Chapter 3

Design and Characterization of Finite Length Fiber Gratings*

A rigorous analysis of the response of fiber Bragg gratings of finite length is presented. For the discrete grating model, we find necessary and sufficient conditions for the response to be realizable as a grating of finite length. These conditions are used to develop a general method for designing gratings with a prescribed length. The design process is divided into two parts: First, we find a realizable reflection spectrum which approximates the target spectrum. Once the spectrum is found, one can determine the associated grating profile by straightforward layer-peeling inverse-scattering or transfer matrix factorization methods. As an example, a dispersionless bandpass filter is designed and compared to the results when the layer-peeling algorithm is applied directly to a windowed impulse response. We also discuss potential applications to grating characterization including regularization and finding the absolute reflection spectrum from a measured, normalized version.

3.1 Introduction

During the recent decades, several methods for the synthesis of advanced fiber Bragg gratings or corrugated waveguide gratings have been proposed. Grating synthesis is a critical tool, both for design and also for characterization of already fabricated devices. The simplest and most straightforward approach is the Fourier transform method, which is based on the first order Born approximation and therefore only valid in the limit of weak gratings [20]. This relation provides valuable intuition and relative accurate results for gratings with top reflectivity less than about 10-50%. Although the Fourier transform technique can be made more accurate by nonlinear renormalization [21, 22, 23], it remains an approximate technique and leads to large errors for strong gratings.

*This chapter is published as J. Skaar and O. H. Waagaard, "Design and characterization of finite length fiber gratings", *IEEE Journal of Quantum Electronics*, vol. 39, no. 10, pp. 1238-1245, 2003. I have mainly contributed to section 3.4.2 of this chapter.

Based on the classical Gel'fand-Levitan-Marchenko (GLM) inverse scattering theory, Song and Shin found exact solutions to the synthesis problem when the reflection coefficient is expressed as a rational function of complex frequency ω [13]. The main problem with the exact GLM method is that grating reflection spectra are generally not rational functions and the approximation of a target spectrum by rational functions is unpractical and often leads to oscillations and inaccuracies in the realized spectrum. To overcome this problem, one can instead solve the GLM integral equations numerically by iterative methods [8, 14, 15, 24, 25]. Peral *et al.* demonstrated this approach through several grating designs [15]. The weaknesses of the iterative, numerical solutions to the GLM equations are low efficiency and inaccuracies due to finite discretization steps and a finite number of iterations.

A simpler, more direct approach to the synthesis problem is the layer-peeling methods [9, 10, 16, 17, 26], first applied in the field of grating synthesis by Feced *et al.* [16]. The layer-peeling method is based on causality and the fact that the leading edge of the reflection impulse response corresponds directly to the coupling coefficient of the first grating layer. Thus one can identify the first layer from the desired response, and remove its effect by propagating the fields to the next layer. For computer implementation, one discretizes the grating model itself [16] or one keeps the grating model continuous and discretizes while evaluating the impulse response and propagating the fields [17]. The former approach is the most efficient and usually the most stable [26].

While the exact inverse scattering methods, such as the layer-peeling, are extremely useful for reconstructing any grating structure from the associated reflection spectrum, they cannot always be applied directly for design since the target spectrum is not necessarily realizable. A common way to make the target spectrum realizable is to specify a spectrum which corresponds to an impulse response of finite duration. This is achieved with conventional methods for design of finite impulse response (FIR) filters using windows [27]. However, since the impulse response of any fiber grating has infinite duration, this procedure is strictly not applicable, and leads to an unwanted tail in the realized impulse response. For relatively short and strong gratings this tail can be significant and gives a deviation from the target spectrum. A solution to this problem could be numerical optimization of the design [28]. However, the degrees of freedom can be large even for relatively short gratings, and thus the time consumed may be large.

The purpose of this work is to find conditions for the reflection spectrum to be realizable. These conditions can be used to develop a general method for approximation of a target spectrum by one that is realizable. Once the realizable spectrum is found, we will apply the layer-peeling algorithm or a similar transfer matrix factorization algorithm to determine the grating structure. In Section 2 we summarize the grating model, discretize, and describe the layer-peeling algorithm. Section 3 gives necessary and sufficient conditions for realizability, leading to a general design algorithm. This algorithm will be tested on a practical design example in Section 4. In addition we will discuss two other applications of the theory: stabilizing the reconstruction process, and finding the absolute reflection spectrum from a normalized spectrum.

3.2 Fiber grating model and grating reconstruction

A fiber Bragg grating can be characterized by its quasi-sinusoidal effective index as a function of position x:

$$n - n_{\text{eff}} = \Delta n_{\text{ac}}(x) \cos\left(\frac{2\pi}{\Lambda}x + \theta(x)\right) + \Delta n_{\text{dc}}(x). \tag{3.1}$$

In (3.1), n_{eff} is the modal effective index, Λ is a reference (design) period, $\Delta n_{\text{ac}}(x)$ and $\Delta n_{\text{dc}}(x)$ are the "ac" and "dc" index perturbations, respectively, and $\theta(x)$ is the grating phase once the $2\pi x/\Lambda$ dependence has been removed. From coupled-mode theory, it follows that the forward and backward propagating modes are mutually coupled by [6, 29, 30]

$$\frac{\mathrm{d}u(x;\delta)}{\mathrm{d}x} = +i\delta u + q(x)v \tag{3.2a}$$

$$\frac{\mathrm{d}v(x;\delta)}{\mathrm{d}x} = -i\delta v + q^*(x)u. \tag{3.2b}$$

The slowly varying envelopes u and v are related to the forward (e_u) and backward (e_v) field amplitudes by

$$e_u(x) = u(x) \exp\left(+i\frac{\pi}{\Lambda}x\right) \exp\left(+i\frac{2\pi}{\lambda_B}\int_0^x \Delta n_{\text{dc}}(x')\mathrm{d}x'\right) \tag{3.3a}$$

$$e_v(x) = v(x) \exp\left(-i\frac{\pi}{\Lambda}x\right) \exp\left(-i\frac{2\pi}{\lambda_B}\int_0^x \Delta n_{\text{dc}}(x')\mathrm{d}x'\right). \tag{3.3b}$$

The detuning parameter is $\delta = \beta - \pi/\Lambda$, where β is the propagation constant of the mode. The coupling coefficient $q(x)$ is related to the index profile as

$$q(x) = i\frac{\pi \Delta n_{\text{ac}}(x)}{\lambda_B} \exp\left[i\left(\theta(x) - \frac{4\pi}{\lambda_B}\int_0^x \Delta n_{\text{dc}}(x')\mathrm{d}x'\right)\right], \tag{3.4}$$

where $\lambda_B = 2n_{\text{eff}}\Lambda$ is the design Bragg wavelength. The modulus of the coupling coefficient determines the grating amplitude, and the phase corresponds to the grating phase envelope. Note that the phase term due to the "dc" index perturbation has the same effect as the geometrical phase θ; as a result the two phase contributions cannot be separately identified from the grating response. Throughout this paper, we will characterize the grating by the following parameters; the modal effective index n_{eff}, the design Bragg wavelength $\lambda_B = 2n_{\text{eff}}\Lambda$, and the slowly varying coupling coefficient or coupling function $q(x)$. Once these three parameters are given, we find the index modulation amplitude $n_{\text{ac}}(x)$ from the modulus of (3.4) and the combination of geometrical phase and dc index variation from the phase of (3.4).

The reflection spectrum of a fiber grating with a certain n_{eff}, λ_B, and $q(x)$ is conveniently computed using the transfer matrix method. The grating is divided into N sections or layers of length $\Delta x = L/N$, where L is the total length. If N

is sufficiently large, the grating can be treated as uniform in each section. For a uniform grating of length Δx, the coupled-mode equations are easy to be solved analytically, yielding the transfer relation

$$\begin{bmatrix} u(x+\Delta x) \\ v(x+\Delta x) \end{bmatrix} = \begin{bmatrix} \cosh(\gamma\Delta x) + i\frac{\delta}{\gamma}\sinh(\gamma\Delta x) & \frac{q}{\gamma}\sinh(\gamma\Delta x) \\ \frac{q^*}{\gamma}\sinh(\gamma\Delta x) & \cosh(\gamma\Delta x) - i\frac{\delta}{\gamma}\sinh(\gamma\Delta x) \end{bmatrix} \begin{bmatrix} u(x) \\ v(x) \end{bmatrix}, \tag{3.5}$$

where $\gamma^2 = |q|^2 - \delta^2$. Hence, we can connect the fields at the two ends of the grating through

$$\begin{bmatrix} u(L) \\ v(L) \end{bmatrix} = \mathbf{T} \begin{bmatrix} u(0) \\ v(0) \end{bmatrix}, \tag{3.6}$$

where $\mathbf{T} = \mathbf{T}_N \cdot \mathbf{T}_{N-1} \cdots \mathbf{T}_1$ is the overall transfer matrix. The matrix $\mathbf{T}_j$ is the transfer matrix written in (3.5) with $q = q_j \equiv q(j\Delta x)$ the coupling coefficient of the jth section. The overall matrix $\mathbf{T}$ is a 2×2 matrix:

$$\mathbf{T} = \begin{bmatrix} T_{11} & T_{12} \\ T_{21} & T_{22} \end{bmatrix}. \tag{3.7}$$

Once $\mathbf{T}$ is found, the reflection coefficient from the left and the transmission coefficient are calculated by the relations

$$r(\delta) = -T_{21}/T_{22} \tag{3.8a}$$

$$t(\delta) = 1/T_{22}, \tag{3.8b}$$

obtained by substitution of the appropriate boundary conditions into (3.6).

While this transfer matrix model is convenient for the analysis of gratings, the synthesis is facilitated by discretizing the grating into a stack of complex reflectors. Feced *et al.* showed that the transfer matrix in (3.5) can be approximated by a cascade $\mathbf{T}_{\Delta x}\mathbf{T}_\rho$ of a discrete reflector and a pure propagation section [16]. By letting $|q| \to \infty$ holding the total coupling $|q|\Delta x$ constant, we obtain the reflector matrix

$$\mathbf{T}_\rho = (1 - |\rho|^2)^{-1/2} \begin{bmatrix} 1 & -\rho^* \\ -\rho & 1 \end{bmatrix}, \tag{3.9}$$

where ρ is given by

$$\rho = -\tanh(|q|\Delta x)q^*/|q|. \tag{3.10}$$

Similarly, by letting $q \to 0$ we get the propagation matrix

$$\mathbf{T}_{\Delta x} = \begin{bmatrix} \exp(i\delta\Delta x) & 0 \\ 0 & \exp(-i\delta\Delta x) \end{bmatrix}. \tag{3.11}$$

It is convenient to use the convention that the grating is represented as a stack of $N+1$ complex reflectors $\rho_j = -\tanh(|q_j|\Delta x)q_j^*/|q_j|$ for $j = 0, 1, \ldots, N$, separated by N propagation sections Δx, see Fig. 3.1.

The reflection impulse response $h(k)$ of the discrete grating is clearly also discrete, i.e., the reflection spectrum is given by

$$r(\delta) = \sum_{k=0}^{\infty} h(k)\exp(i\delta \cdot k2\Delta x), \tag{3.12}$$

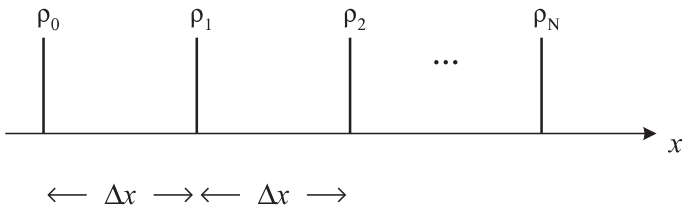

Figure 3.1: The discrete grating model.

since the time between two pulses corresponds to propagation over a length $2\Delta x$. It follows that $r(\delta)$ is periodic with the spectral period $\delta_w = \pi/\Delta x$.

The reconstruction problem of fiber gratings can now be stated as follows: Given a realizable reflection spectrum $r(\delta)$ in the interval $-\delta_w/2 \leq \delta < \delta_w/2$, find the reflectors ρ_j for $j = 0, ..., N$. The samples of the coupling function are then found from $q(j\Delta x) = -\arctan(|\rho_j|)/\Delta x \cdot \rho_j^*/|\rho_j|$. The bandwidth δ_w is usually given, which dictates the spatial resolution Δx. If a higher resolution is desired, one can pad the reflection spectrum with zeros on each side, giving a larger δ_w.

The layer-peeling algorithm is based on the simple fact that the first point of the impulse response must be independent of the ρ_j's for $j \geq 1$ due to causality. Hence we find $\rho_0 = h(0)$. Then, since ρ_0 already is known, we can propagate the fields using $\mathbf{T}_{\Delta x}\mathbf{T}_\rho$, yielding the fields at the next layer. More precisely, in the time domain we get the following algorithm:

1. Initialize the forward- and backward-propagating time domain fields at layer $j = 0$:

$$\begin{aligned}\mathbf{u} &= \begin{bmatrix} u(0) & u(1) & \dots & u(N) \end{bmatrix} = \begin{bmatrix} 1 & 0 & \dots & 0 \end{bmatrix} \\ \mathbf{v} &= \begin{bmatrix} v(0) & v(1) & \dots & v(N) \end{bmatrix} = \begin{bmatrix} h(0) & h(1) & \dots & h(N) \end{bmatrix}\end{aligned}$$

2. Compute the local reflection coefficient $\rho_j = v(0)/u(0)$.

3. Propagate $\mathbf{u}$ and $\mathbf{v}$ using the transfer relations

$$\begin{bmatrix} \mathbf{u} \\ \mathbf{v} \end{bmatrix} \leftarrow (1 - |\rho_j|^2)^{-1/2} \begin{bmatrix} \mathbf{u} - \rho_j^* \mathbf{v} \\ -\rho_j \mathbf{u} + \mathbf{v} \end{bmatrix}$$

4. Left shift $\mathbf{v}$ (delay $\mathbf{u}$ with respect to $\mathbf{v}$ by one time unit):

$$\mathbf{v} \leftarrow \begin{bmatrix} v(1) & \dots & v(N) & 0 \end{bmatrix}$$

5. If $j < N$, increase j and goto step 2.

If one is not concerned about the fields themselves, the factor $(1 - |\rho_j|^2)^{-1/2}$ in step 3 can be omitted since it is common for both the forward and backward propagating fields. Note that only the first $N + 1$ points of the impulse response are needed to reconstruct the grating. While the layer-peeling algorithm is exact and extremely efficient for reconstruction of gratings, an important task remains for design, namely to find a realizable spectrum to apply as input to the inversion.

3.3 Realizable spectra

The goal in this section is to find relations that the reflection spectrum must satisfy in order to be realizable for a discretized grating with a prescribed length. These relations will form the basis for the design algorithm. It will become clear that we can make use of conventional filter design algorithms to find a realizable spectrum which is close to the target spectrum.

Since the grating model is discrete, it is convenient to reformulate the transfer matrix model using z-transform techniques [27, 31, 32, 33, 34, 35, 36], defining the unit delay $z^{-1} = \exp(i2\delta\Delta x)$. A very useful analysis is provided by Dowling *et al.* for the similar problem with multistage etalons and resonators [31]. While the results in [31] provides valuable guidance in our case as well, we cannot use them directly for the following reasons: First, the conditions developed in [31] are not sufficient for realizability, which means that the synthesis algorithm may diverge for some input parameters (the reflectors may become larger than 1). Second, the method in [31] is only suitable for designing the transmission (or reflection) magnitude and do not consider the phase response in reflection. In addition, the model used in [31] is not directly applicable in our case since it deals with real reflectors.

In order to study the class of filter responses that fiber gratings can provide, we consider the discrete grating model in more detail. By successively multiplying together the transfer matrices (3.9) and (3.11), we show in Appendix 3.A that the transfer matrix of the total structure can be expressed in the form of

$$\mathbf{M}_N = \begin{bmatrix} A_*(z) & B_*(z) \\ B(z) & A(z) \end{bmatrix}. \tag{3.14}$$

In (3.14), $B(z)$ and $A(z)$ are symmetrically defined Nth order polynomials with complex coefficients

$$A(z) = z^{N/2} \sum_{k=0}^{N} a(k) z^{-k} \tag{3.15a}$$

$$B(z) = z^{N/2} \sum_{k=0}^{N} b(k) z^{-k} \tag{3.15b}$$

which satisfy

$$\det(\mathbf{M}_N) = A(z)A_*(z) - B(z)B_*(z) = 1. \tag{3.16}$$

The asteriks in the subscript stands for the para-Hermitian conjugate operation, $A_*(z) = A^*(1/z^*)$, which has the effect of reversing and complex conjugating the coefficients, i.e., $A_*(z) = z^{N/2} \sum_{k=0}^{N} a^*(N-k) z^{-k}$. Similarly, we can prove that $A(z)$ is a minimum phase function, i.e. all zeros α_j of $A(z)$ is located inside the unit circle of the complex z-plane,

$$|\alpha_j| < 1 \quad \text{for } j = 1, 2, \ldots, N. \tag{3.17}$$

This condition ensures that the reflection transfer function $r(z) = -B(z)/A(z)$ is causal and stable. Finally, we find that the zeroth coefficient of the A polynomial

is real and positive

$$a(0) > 0. \tag{3.18}$$

Conditions (3.14)-(3.18) are actually necessary *and sufficient* for the transfer matrix $\mathbf{M}_N$ to be realizable as a stack of $N+1$ reflectors separated by N propagation sections. In Appendix 3.A we give a rigorous proof based on transfer matrix factorization. The factorization procedure is actually very similar to the layer-peeling; however, it enables exploring the conditions for realizability in more detail. While the layer-peeling uses the impulse response $h(k)$ as the starting point, the factorization procedure starts from a pair of polynomials $A(z)$ and $B(z)$, or equivalently, coefficient vectors $a(k)$ and $b(k)$.

As evident from (3.8), the complex reflection spectrum is given by the ratio of the (2,1) and (2,2) entries of the transfer matrix. All realizable reflection spectra can be expressed as rational functions $r(z) = -B(z)/A(z)$, where the polynomials A and B satisfy (3.15)-(3.18). The converse is also true; all rational functions $-B(z)/A(z)$, where A and B satisfy (3.15)-(3.18), are realizable as discretized gratings with $N+1$ coupling points.

Note that this is not the same as expressing the reflection spectrum as a rational function of frequency ω in the continuous model, which is the requirement in the exact GLM method. In the continuous model, a finite length grating has a reflection spectrum that can be expressed as a ratio between two Fourier integrals of finite support, as realized by taking the limit $N \to \infty$ in (3.15) and using $z^{-1} = \exp(i2\delta L/N)$.

At the unit circle $|z| = 1$ the condition (3.16) becomes $|A|^2 - |B|^2 = 1$, which means that the power reflection $|B/A|^2$ and transmission $1/|A|^2$ add to 1. Moreover, the minimum phase condition (3.17) means that $\log|A|$ and $\arg(A)$ form a discrete Hilbert transform pair. In other words, for real frequencies the key conditions for realizability are:

- A and B are the discrete-time Fourier transform of $N+1$ point sequences;
- $|A|^2 - |B|^2 = 1$;
- $\arg A = \mathcal{H}\{\log|A|\}$, where $\mathcal{H}$ denotes the discrete Hilbert transform.

The condition (3.18) can easily be fulfilled without altering the reflection spectrum by multiplying A and B by a suitable common phase factor.

Similar conditions have been used previously for the design of optical lattice-form filters with a prescribed power reflection or transmission [31, 33, 35]. However, when the phase response in reflection is to be considered as well, it is not trivial to use the conditions for design, since the reflection phase depends on both functions A and B. In order to find a realizable *complex* reflection spectrum that is close to a specified target spectrum, we propose the following algorithm:

1. Specify a target reflection spectrum $r(\delta)$ and an associated bandwidth δ_w. The target spectrum must satisfy $|r(\delta)| < 1$ for all δ. One should use a large number of spectral points, at least larger than $N+1$.

2. Compute $|A|$ using $1/|A|^2 = 1 - |r|^2$. This relation ensures that (3.16) is fulfilled.

3. Set $A = |A|e^{i\varphi}$, where $\varphi = \mathcal{H}\{\log|A|\}$. Since the phase and logarithmic amplitude form a Hilbert transform pair, the minimum phase condition is satisfied.

4. Set $B = -rA$ and find a $(N+1)$th-order FIR filter implementing the transfer function B. This is the critical point which involves approximation. When using the algorithm for grating design, it is appropriate to use conventional methods from digital filter design such as window methods or least-square fits. For reconstruction or when the target spectrum is already almost realizable, one can use a straightforward inverse Fourier transform. Denote the filter coefficients by $b(k)$, $k = 0, \ldots, N$.

5. Compute $|A|$ using $|A|^2 = 1 + |B|^2$, where B is the spectrum of the designed filter in the previous point.

6. Set r equal to $|B|/|A| \cdot r/|r|$ and repeat steps 3-5. This iteration step can be omitted, but it leads usually to better correspondence between the target group delay and the designed group delay since the change in $|A|$ in the previous step involves a change in its phase through the minimum phase relationship.

7. Set $A = |A|e^{i\varphi}$, where $\varphi = \mathcal{H}\{\log|A|\}$, and find the $(N+1)$th order FIR filter implementing A by an inverse (discrete time) Fourier transform of A. Denote the filter coefficients by $a(k)$, $k = 0, \ldots, N$. Adjust globally the phase of the vector of coefficients $a(k)$ and $b(k)$ such that $a(0)$ is real.

8. Reconstruct the grating having $r(z) = -B(z)/A(z)$ using one of two equivalent approaches: Transfer matrix factorization, or layer-peeling. In the latter case, one must first compute the $N+1$ first points of the reflection impulse response; that is, the first $N+1$ coefficients of the ratio $-B(z)/A(z)$.

3.4 Applications

3.4.1 Grating design

We will now test the algorithm by designing a dispersionless top-hat filter and compare with the results from layer-peeling with windowed impulse response as in [16, 17, 26]. We specify a 3 cm long, nondispersive bandpass filter with 99% reflectivity. The bandwidth should be 50 GHz or 0.4 nm centered about the wavelength 1550 nm. In step 4 of the design algorithm, we compute the coefficients of the FIR filter $B(z)$ by a simple windowing method using a Hanning (raised cosine) function. While this is a very efficient approach there exist more accurate methods since $B(z)$ should be a nonlinear-phase filter, corresponding to an unsymmetrical coefficient vector $b(k)$. We performed one iteration (step 6). The resulting design (FBG1) is depicted in Fig. 3.2 and compared to the grating resulting from a

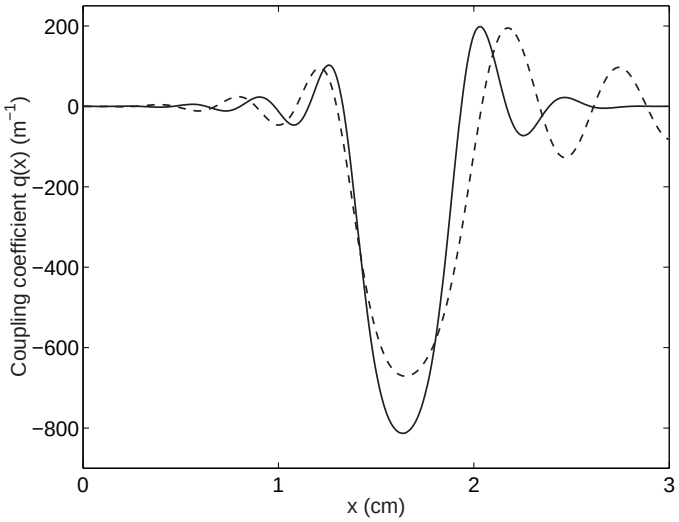

Figure 3.2: Coupling coefficient functions of the 3 cm long gratings with bandpass filter response. The solid curve shows the grating designed with the present algorithm (FBG1) and the dashed curve shows the grating designed with FIR windowing (FBG2).

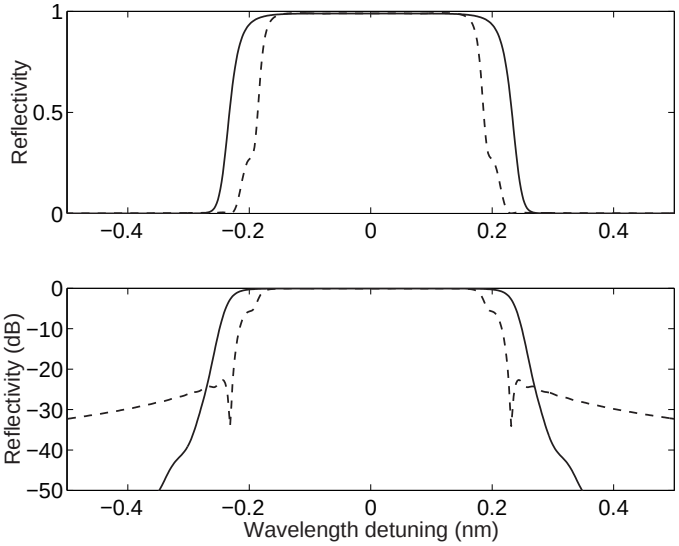

Figure 3.3: Reflection spectrum of the grating designed with the present algorithm (solid curve) and with FIR windowing (dashed curve).

straightforward windowing of the target impulse response (FBG2). We observe that while FBG2 has a discontinuity at the right end, the coupling function of FBG1 approaches zero smoothly. The spectra of the two gratings are computed using the "continuous" transfer-matrix model (3.5) and plotted in Figs. 3.3-3.4. It is apparent that the response of FBG1 is smoother than the response of FBG2. This can be understood from the associated impulse responses in Fig. 3.5. The first 6 cm of the target impulse response, corresponding to propagation back and forth the grating

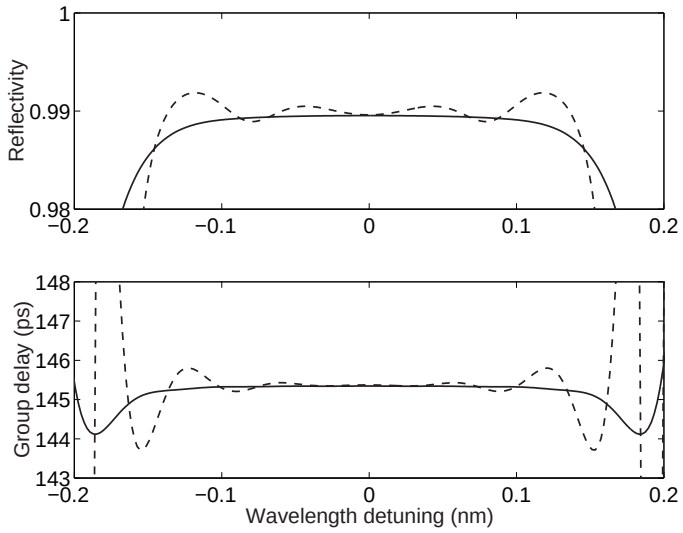

Figure 3.4: In-band details of the grating: Reflectivity and group delay spectrum of the grating designed with the present algorithm (solid curve) and with FIR windowing (dashed curve).

length, is perfectly generated by the grating FBG2; however in addition there is an unwanted tail giving rise to oscillations in the realized spectrum. For the grating FBG1, there is certainly also a tail, since any fiber grating has infinite impulse response. However it is made decaying much faster at the expense on the first part of the impulse response, which in this case was slightly asymmetric. An important property with the present design method is that one has full control with the entire impulse response or reflection spectrum. Once the grating response has been forced to satisfy (3.14)-(3.18), we are guaranteed that the response will be realized exactly.

3.4.2 Grating characterization and reconstruction

When reconstructing a fiber grating from its reflection spectrum, one can in principle apply the layer-peeling algorithm directly to the data. However, there are still reasons to consider the realizability conditions. First of all, any measurements include noise, which may make the data unphysical. When reconstructing the coupling function, such noise is roughly amplified by a factor of $1/T_{\min}$, where $T_{\min}$ is the minimum power transmission of the grating [37]. By forcing the measured response to satisfy (3.14)-(3.18) we may make the reconstruction process more stable. This can be achieved with the algorithm in Section 3.3. To demonstrate this kind of regularization, we first compute the reflection spectrum of a strong, uniform grating with $q(x) = 500$ m^{-1} and $L = 1$ cm. The 5000 spectrum samples are uniformly distributed in a 10 nm bandwidth. To simulate a real measurement, the spectrum samples are added independently, Gaussian noise with standard deviation 10^{-5}, and applied as input to the algorithm. We imagine that the grating length is known in advance to be less than 1.5 cm so that the length which is specified in the algorithm is 1.5 cm. In this case, we omitted the iteration step 6 although the accuracy seems

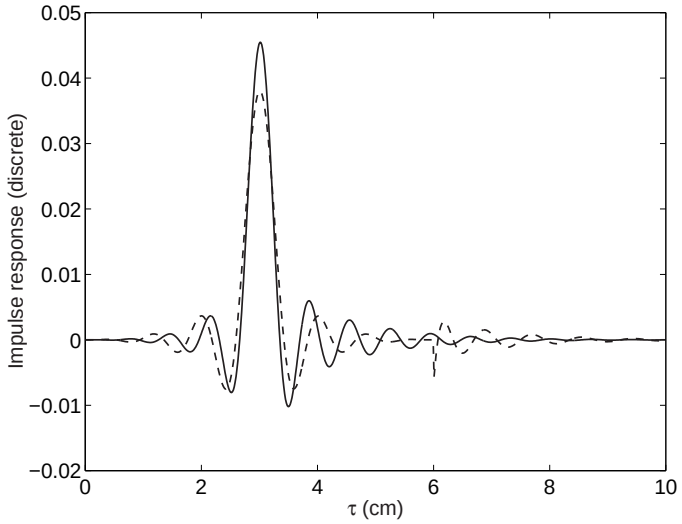

Figure 3.5: Impulse responses of the gratings FBG1 and FBG2. The solid curve shows the response of FBG1 and the dashed curve shows the response of FBG2. Note that the time variable τ is normalized so that $\tau = 2L$ corresponds to the round trip time $2Ln_{\text{eff}}/c$.

to increase with the number of iterations. The reconstructed coupling function is plotted in Fig. 3.6, and compared to the results when using the layer-peeling directly and when diminishing the spectrum before applying the layer-peeling [37]. The spectrum was dimished with a factor $1 - 0.00234$, which turned out to be the optimal regularization parameter in this case. We observe that the two regularization approaches give accurate and comparable results in this case, as opposed to the plain layer-peeling. Note that the layer-peeling process was performed over a 2 cm length for the three methods, but $q(x)$ for the method based on realizability is exactly zero for $x > 1.5$ cm.

It turns out that the methods comply with noise in different ways. In this example, there are essentially two different types of noise; in addition to the pseudo-random generated noise, there is "noise" associated with the finite bandwidth in the calculations. While the latter dominates in the case of applying layer-peeling on the diminished spectrum, the present algorithm is in this case most sensitive to the former noise source. Another difference between the two regularization methods is that the present approach requires no knowledge of a regularization parameter other than an upper bound on the grating length. To use the dimishing approach, one must determine the optimal regularization parameter by performing layer-peeling several times in order to minimize the unphysical tail for $x > L$ [37].

There are also other reasons to consider the realizability conditions in grating characterization. For example, in some cases, one is only able to measure the reflection spectrum up to a multiplicative constant since the transmission may be not accessible. As we will show below, this constant is uniquely given by (3.14)-(3.16). In other words, one can determine the absolute reflection spectrum from a normalized version of it, provided the grating has finite length. This can be proved as

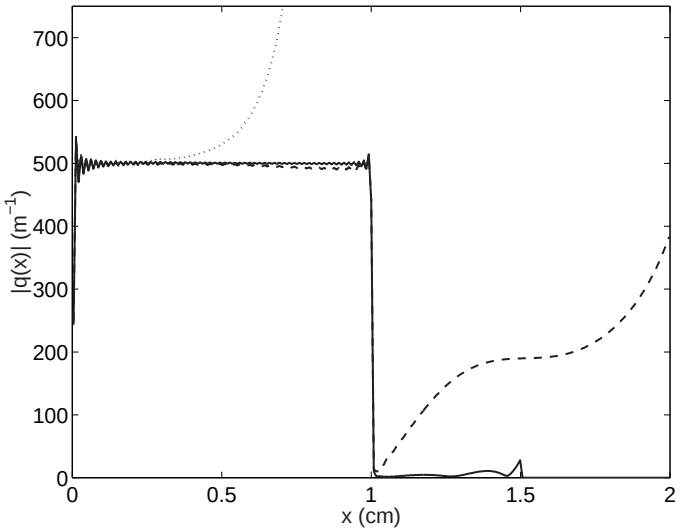

Figure 3.6: Reconstructed coupling function $q(x)$ using the present algorithm (solid curve), layer-peeling with spectrum dimishing $r \to (1 - 0.00234)r$ (dashed curve), plain layer-peeling (dotted curve).

follows: Let r be the "true" reflection spectrum of the grating under study. Associated with the grating are also the polynomials $A(z)$ and $B(z)$, which satisfy (3.16). The reflection response is given by $r(z) = -B(z)/A(z)$, yielding

$$A(z)A_*(z) = \frac{1}{1 - r(z)r_*(z)}. \tag{3.19}$$

Define another reflection spectrum as $\tilde{r}(z) = r(z)/C$, where $C > 0$. We want to find out whether the response $\tilde{r}$ can be associated with a grating of finite length. If this is the case, we can determine its inverse transmission polynomial $\tilde{A}(z)$ in the same way as (3.19):

$$\tilde{A}(z)\tilde{A}_*(z) = \frac{1}{1 - r(z)r_*(z)/C^2}. \tag{3.20}$$

By substituting (3.19) into (3.20) we obtain

$$\tilde{A}(z)\tilde{A}_*(z) = \frac{C^2 A(z)A_*(z)}{1 + (C^2 - 1)A(z)A_*(z)}. \tag{3.21}$$

Since $A(z)$ is a polynomial, the ratio in (3.21) contains generally both zeros and poles. For a finite length grating, (3.15a) tells us that $\tilde{A}\tilde{A}_*$ should be a polynomial. Thus, since the numerator and denominator cannot be zero simultaneously, C must be 1. Note however that if C is sufficiently large, we also get a valid solution to (3.21), corresponding to a weak grating with $\tilde{A}\tilde{A}_* \approx 1$. For weak gratings, the transformation $q(x) \leftrightarrow r(\delta)$ is linear, and thus the scaling of $r(\delta)$ cannot be determined. We conclude that the reflection spectrum can be uniquely determined by a normalized version, provided the grating is known to be sufficiently strong. In other words, in measurement situations where the transmission cannot be measured

and the input power to the grating is not known, the reflection spectrum can still be uniquely determined by the reflected power from the grating.

To find the constant, one can perform layer-peeling on the spectrum $r = C\tilde{r}$, where $\tilde{r}$ now is a normalized version, choosing C so as to minimize the "tail" of the coupling function for $x > L$. Alternatively, one can use the relation (3.19) for real frequencies

$$|A| = \frac{1}{\sqrt{1 - C^2|\tilde{r}|^2}}, \tag{3.22}$$

together with the fact that A is a minimum phase function. The phase $\arg(A)$ is computed by a Hilbert transform of $\log|A|$, yielding A and the polynomial coefficients $a(k)$. The constant can be found as the value of C in (3.22) that minimizes the "tail" $\sum_{k=N+1}^{\infty}|a(k)|^2$, which ideally should be zero. In Fig 3.7 we plot the energy of the tails for different values of C for a uniform grating with $|q|L = 1$. The top reflectivity is 58%. As we can see, the correct solution $C = 1$ gives a clear minimum in both tail energies, but the tails also get small when C is small since the response $C\tilde{r}$ then corresponds to a weak grating. The minima would be more (less) visible if the grating was stronger (weaker).

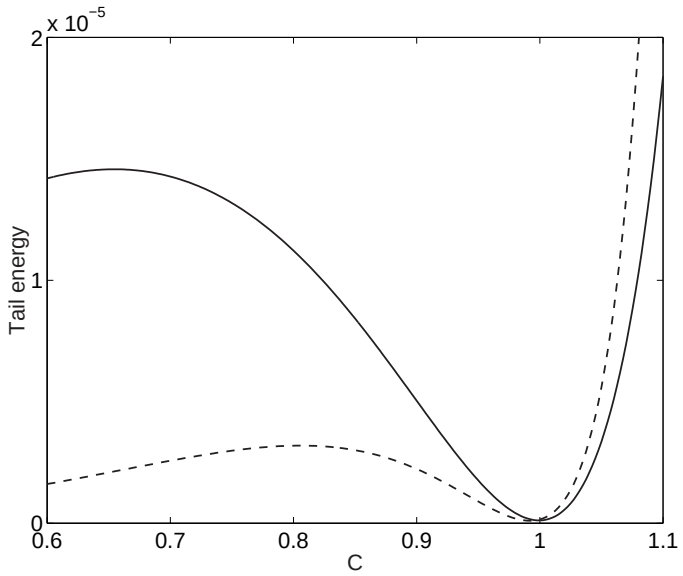

Figure 3.7: Tails $\sum_{j=N+1}^{\infty}|\rho_j|^2$ (solid curve) and $\sum_{k=N+1}^{\infty}|a(k)|^2$ (dashed curve) as a function of C for a uniform grating with $|q|L = 1$. The latter curve is multiplied by 10 to enable comparison. The correct value of C is 1.

3.5 Conclusion

In this paper we have proved necessary and sufficient conditions for a reflection spectrum to be realizable as the response of a grating with a prescribed length. Within the discrete grating model, all reflection spectra can be expressed as rational function of z with some constraints on the coefficients. Based on these conditions, a

general design algorithm has been developed and applied for designing a relatively short grating with dispersionless bandpass filter response.

We also outline possible applications in grating characterization; regularization of the reconstruction process and determining the reflection spectrum from a measured, normalized version. Since the performance of these methods is dependent on the nature of the noise, the usefulness in practical situations can only be verified using real measurements.

Appendices

3.A Proof of realizability conditions

Here, we will show that the response of a $N+1$ point lossless, discretized grating is realizable if and only if it can be written on the form

$$\mathbf{M}_N = \begin{bmatrix} A_*(z) & B_*(z) \\ B(z) & A(z) \end{bmatrix}. \tag{3.23}$$

In (3.23), $B(z)$ and $A(z)$ are symmetrically defined Nth order polynomials with complex coefficients

$$A(z) = z^{N/2} \sum_{k=0}^{N} a(k) z^{-k} \tag{3.24a}$$

$$B(z) = z^{N/2} \sum_{k=0}^{N} b(k) z^{-k} \tag{3.24b}$$

which satisfy

$$\det(\mathbf{M}_N) = A(z)A_*(z) - B(z)B_*(z) = 1. \tag{3.25}$$

The polynomial $A(z)$ is a minimum phase function, that is, its N zeros α_j are located inside the unit circle of the complex plane:

$$|\alpha_j| < 1, \quad j = 1, \ldots, N, \tag{3.26}$$

and $a(0)$ is a real, positive number

$$a(0) > 0. \tag{3.27}$$

3.A.1 Necessity: Transfer matrix multiplication

The necessity of (3.23)-(3.27) follows by induction. The entire grating has the response

$$\mathbf{M}_N = \mathbf{T}_N \mathbf{T}_{N-1} \cdots \mathbf{T}_1 \mathbf{T}_0, \tag{3.28}$$

where the transfer matrices $\mathbf{T}_j$ are given by

$$\mathbf{T}_j = (1 - |\rho_j|^2)^{-1/2} \begin{bmatrix} 1 & -\rho_j^* \\ -\rho_j & 1 \end{bmatrix} \begin{bmatrix} z^{-1/2} & 0 \\ 0 & z^{1/2} \end{bmatrix}, \tag{3.29}$$

for $1 \leq j \leq N$, and

$$\mathbf{T}_0 = (1 - |\rho_0|^2)^{-1/2} \begin{bmatrix} 1 & -\rho_0^* \\ -\rho_0 & 1 \end{bmatrix}. \tag{3.30}$$

The local reflection coefficients ρ_j are allowed to be in the range $|\rho_j| < 1$.

For $N = 0$, it is immediately found that $\mathbf{M}_N = \mathbf{T}_0$ satisfies (3.23)-(3.27). Assuming that $\mathbf{M}_N$ satisfies (3.23)-(3.27), we must now prove that $\mathbf{M}_{N+1}$ can also be written in the form (3.23), where the new polynomials satisfy (3.24)-(3.27). Thus, we consider $\mathbf{M}_{N+1} = \mathbf{T}_{N+1}\mathbf{M}_N$:

$$\mathbf{M}_{N+1} = (1 - |\rho_{N+1}|^2)^{-1/2} \begin{bmatrix} z^{-1/2}A_* - \rho_{N+1}^* z^{1/2}B & -\rho_{N+1}^* z^{1/2}A + z^{-1/2}B_* \\ -\rho_{N+1}z^{-1/2}A_* + z^{1/2}B & z^{1/2}A - \rho_{N+1}z^{-1/2}B_* \end{bmatrix}. \tag{3.31}$$

It is apparent that the new matrix $\mathbf{M}_{N+1}$ can be written in the form (3.23) and $\det(\mathbf{M}_{N+1}) = \det(\mathbf{T}_{N+1})\det(\mathbf{M}_N) = 1$. Moreover, we find that the first coefficient of the polynomial in the (2,2)-entry of (3.31) continues to be a positive number. It remains to prove that the zeros of the (2,2)-entry of (3.31) are located inside the unit circle. Define the new complex variable $w = z^{-1}$ and the function $\hat{r}(w) = B_*/A$. From (3.25), it follows that $|\hat{r}(w)| < 1$ on the unit circle $|w| = 1$. Since $\hat{r}(w)$ is analytic for $|w| < 1$, the maximum principle of complex analysis [38] states that $|\hat{r}(w)| < 1$ for $|w| \leq 1$. Hence the (2,2)-entry of (3.31) cannot be zero for $|w| \leq 1$ or equivalently for $|z| \geq 1$.

3.A.2 Sufficiency: Transfer matrix factorization

To prove that (3.23)-(3.27) are sufficient for realizability, we will show by induction that the total transfer matrix (3.23) can be factorized into N "unit cell" matrices as in (3.28).

For $N = 0$, the factorization is trivial and it is clear that any matrix $\mathbf{M}_0$ given by (3.23)-(3.27) can be expressed in the form (3.30). To proceed, we assume $N \geq 1$. Defining $\mathbf{M}_{N-1} \equiv \mathbf{T}_N^{-1}\mathbf{M}_N$, we obtain

$$\mathbf{M}_{N-1} = (1 - |\rho_N|^2)^{-1/2} \begin{bmatrix} z^{1/2}A_* + z^{1/2}\rho_N^* B & z^{1/2}\rho_N^* A + z^{1/2}B_* \\ z^{-1/2}\rho_N A_* + z^{-1/2}B & z^{-1/2}A + z^{-1/2}\rho_N B_* \end{bmatrix}. \tag{3.32}$$

By substituting (3.24) into (3.32), it is straightforward to show that $\mathbf{M}_{N-1}$ can be written on the form (3.23), where the entries have been reduced to $(N-1)$th-order polynomials, provided that we choose

$$\rho_N = -\frac{b(N)}{a(0)} = -\frac{a(N)}{b(0)^*}, \tag{3.33}$$

and provided $|\rho_N| < 1$. It is easy to show that the two equalities in (3.33) are consistent by substituting (3.24) into (3.25); considering the highest power of z, we obtain $a(0)a(N)^* - b(0)b(N)^* = 0$. Before we can show that the conditions (3.25)-(3.27) are valid for the reduced system, we must prove that $|\rho_N| = |b(N)|/a(0) < 1$. Define the function $\hat{r}(z) = B_*(z)/A(z)$. Since $A(z)$ is a minimum phase function with all zeros inside the unit circle of the z-plane, it is clear that the ratio $B_*(z)/A(z)$

represents a causal and stable transfer function. Hence, $\hat{r}$ can be written as the power series

$$\hat{r}(z) \equiv \frac{\sum_{k=0}^{N} b^*(N-k)z^{-k}}{\sum_{k=0}^{N} a(k)z^{-k}} = \sum_{k=0}^{\infty} \hat{h}(k)z^{-k}. \tag{3.34}$$

Letting $z \to \infty$, we find $\hat{h}(0) = -\rho_N^*$ and consequently

$$|\rho_N|^2 = |\hat{h}(0)|^2 \leq \sum_{k=0}^{\infty} |\hat{h}(k)|^2 = \frac{1}{2\pi} \int_{-\pi}^{\pi} |\hat{r}(e^{i\theta})|^2 d\theta, \tag{3.35}$$

where we have used the Parseval's relation. The amplitude $|\hat{r}(z)|$ is less than 1 on the unit circle according to (3.25), and we can therefore conclude that $|\rho_N| < 1$.

Returning to the reduced transfer matrix in (3.32), we can now realize that the first coefficient of the reduced $A(z)$-polynomial remains positive. From the definition of $\mathbf{M}_{N-1}$, it also follows that $\det \mathbf{M}_{N-1} = \det \mathbf{T}_N^{-1} = 1$. Finally, it is easy to prove that there are no zeros of the reduced $A(z)$-polynomial outside the unit circle using the maximum principle on the function $\hat{r}$. Since all conditions (3.23)-(3.27) remain valid for the reduced system, we can continue the process until we have reached the zeroth layer.

The transfer matrix factorization algorithm outlined here is actually equivalent to the layer-peeling algorithm applied to the reflection response from the right. As evident from (3.8), the reflection response from the left is given by the ratio $r = -B/A$, and similarly the reflection coefficient from the other side is $\hat{r} = B_*/A$. While the layer-peeling algorithm applied to the spectrum from the left is based on the relation $\rho_0 = h(0) = b(0)/a(0)$, its reverse counterpart must be based on $-\rho_N^* = \hat{h}(0) = b^*(N)/a(0)$. This demonstrates the fact that the transfer matrix factorization and the layer-peeling methods are closely related.

Chapter 4

Synthesis of birefringent reflective gratings*

The layer-peeling method for reconstruction of fiber and waveguide gratings is extended to the case of birefringent reflective gratings with polarization-dependent background index and polarization-dependent effective index contrast. Using a discrete grating model, we characterize the set of possible reflection and transmission Jones matrices and show that for a given wavelength, the total structure can be represented by a discrete reflector sandwiched between two retardation sections. In reflection the discrete reflector acts as a partial polarizer. A method for designing birefringent gratings is developed and tested numerically.

4.1 Introduction

Fiber Bragg gratings and waveguide gratings have important applications in the optical communication and sensor industry. Fiber gratings are usually assumed to be polarization independent, i.e., the reflection and transmission spectra are treated as scalar functions. Such gratings can be analyzed by using the 2×2 transfer matrix method [39, 40] and designed or characterized by using scalar layer-peeling methods [16, 40, 26]. However, the fabrication of uv-induced fiber gratings introduces a weak birefringence [41, 42, 43] including a polarization-dependent index contrast [44], which for some applications can be significant. Larger polarization dependence may be present in gratings written in anisotropic fibers [45] or in fiber grating sensors with transverse loads [46, 47, 48, 49]. Another important class of birefringent filters is etched gratings in waveguides (grating-assisted waveguides). Such structures can exhibit a significant difference in the background index of refraction for the two orthogonal polarizations, and also an effective index contrast that is strongly dependent on polarization [50, 44]. These two birefringence parameters can in principle be controlled separately under the fabrication process.

*This chapter is published as O.H. Waagaard, J. Skaar, "Synthesis of birefringent reflective gratings" in *Journal of Optical Society of America A*, vol. 21, pp. 1207-1220. An errata has been submitted for publication and will appear in the same journal.

Coupling within birefringent devices involves two forward-propagating and two backward-propagating optical modes, and the reflection and transmission responses of birefringent devices must in general be described by using full Jones matrix analysis [51, 52, 19]. In this paper we will generalize the layer-peeling and design algorithm in [40] such that it takes an arbitrary polarization dependence into account. This can be useful for reconstructing the grating profile from a measured reflection Jones matrix and for characterizing the set of possible responses from a birefringent grating. It may also prove useful for designing gratings with a desired reflection Jones matrix as a function of wavelength. This new type of birefringent grating may provide filter responses that are not possible in polarization-independent grating structures.

The organization of this paper is as follows. In Section 4.2 we state the grating model and present the coupled-mode equations for the grating. We further discretize the grating such that it is represented as a stack of discrete reflectors sandwiched between retardation sections. The reflector and retardation sections are represented by using 4×4 transfer matrices, where each 2×2 block is Jones matrices. In Section 4.3 the full polarization-dependent layer-peeling algorithm is presented. Section 4.4 contains an analysis of the set of possible (realizable) grating responses. It is shown that for a given wavelength, the response of any birefringent grating can be represented as a discrete reflector sandwiched between two retardation sections. The realizability conditions are also used to develop a design algorithm for approximating a desired Jones reflection matrix by one that is realizable. In Section 4.5, the layer-peeling algorithm and also the design algorithm are tested on practically useful examples.

4.2 Grating model

We will describe lossless and reciprocal gratings with polarization-dependent index modulation, as well as an arbitrary birefringence that is slowly varying with respect to the wavelength scale. We restrict ourselves to the situation where the propagation direction is along one of the principal axes of the permittivity tensor. Examples of such structures include birefringent fiber Bragg gratings or other corrugated waveguide structures that are asymmetric or made of anisotropic materials. The effective refractive index as function of position x along the grating can be expressed as a 2×2 matrix:

$$\begin{aligned}\boldsymbol{n}(x) =& \boldsymbol{U}_{\mathrm{dc}}(x) \begin{bmatrix} \bar{n} + \Delta n_{\mathrm{dc}}^{(s)}(x) & 0 \\ 0 & \bar{n} + \Delta n_{\mathrm{dc}}^{(f)}(x) \end{bmatrix} \boldsymbol{U}_{\mathrm{dc}}^{\dagger}(x) \\ &+ \boldsymbol{U}_{\mathrm{ac}}(x) \begin{bmatrix} n_{\mathrm{ac}}^{(1)}(x) \cos[2\pi x/\Lambda + \phi^{(1)}(x)] & 0 \\ 0 & n_{\mathrm{ac}}^{(2)}(x) \cos[2\pi x/\Lambda + \phi^{(2)}(x)] \end{bmatrix} \boldsymbol{U}_{\mathrm{ac}}^{\dagger}(x). \end{aligned} \tag{4.1}$$

In (4.1), the unitary matrices $\boldsymbol{U}_{\mathrm{ac}}(x)$ and $\boldsymbol{U}_{\mathrm{dc}}(x)$ relate the orientation of the coordinate axes to the orientation of the ac index and dc index eigenaxes, respectively. At this point we let both ac and dc index eigenaxes be general elliptic. The dc index

term therefore combines both linear and circular birefringence. Later it will become clear that the eigenmodes of the ac index term are real for reciprocal gratings. The grating amplitudes of the two polarizations are denoted $n_{\mathrm{ac}}^{(1)}(x)$ and $n_{\mathrm{ac}}^{(2)}(x)$, and the change in the dc indices with respect to a common modal index $\bar{n}$ are $\Delta n_{\mathrm{dc}}^{(s)}(x)$ and $\Delta n_{\mathrm{dc}}^{(f)}(x)$, where the superscripts indicate the slow and the fast eigenmode, respectively. The parameter Λ is a defined design period or the mean grating period, and $\phi^{(1)}(x)$ and $\phi^{(2)}(x)$ are the x-dependent phases once the dependence $2\pi x/\Lambda$ has been removed. All x-dependent parameters on the right-hand side of (4.1) are slowly varying with respect to Λ. Note that the index modulation does not necessarily have to be quasi-sinusoidal; any quasi-periodic index modulation can be described by letting the two terms in (4.1) correspond to the zeroth and first-order Fourier coefficients. Higher-order terms can be neglected as long as we are interested only in wavelengths near the first-order Bragg resonance.

It is convenient to represent the four optical modes as a column vector $\mathbf{E}(x)$ with four elements. The first two elements are the complex amplitudes of the two forward-propagating and orthogonal polarization modes, and the last two elements are the backward propagating modes. The first and third elements refer to the same polarization but opposite propagation direction, and similarly with the second and the fourth elements. Throughout this paper, we will assume that these polarization modes are expressed in a linear basis, i.e. they are defined in a fixed, real coordinate system. The time dependence $\exp(-i\omega t)$ and the spatial dependence $\exp(\pm i\pi x/\Lambda)$ have been removed from the fields. The vacuum wavenumber is denoted $\beta = \omega/c$, where ω is the angular frequency and c is the velocity of light in vacuum. The interaction among the four optical modes is described by coupled-mode theory[53] as follows:

$$\frac{\mathrm{d}\mathbf{E}}{\mathrm{d}x} = i\mathbf{C}\mathbf{E}, \tag{4.2}$$

where $\mathbf{C}$ has three contributions

$$\mathbf{C} = \mathbf{D} + \mathbf{C}_{\boldsymbol{\psi}} + \mathbf{C}_{\boldsymbol{q}}. \tag{4.3}$$

Here the three contributions can be expressed as 2×2 matrices with 2×2 block matrices as elements:

$$\mathbf{D} = \delta \begin{bmatrix} \boldsymbol{I} & \mathbf{0} \\ \mathbf{0} & -\boldsymbol{I} \end{bmatrix}, \quad \boldsymbol{I} = \begin{bmatrix} 1 & 0 \\ 0 & 1 \end{bmatrix}, \tag{4.4a}$$

$$\mathbf{C}_{\boldsymbol{q}} = \begin{bmatrix} \mathbf{0} & \boldsymbol{q} \\ -\boldsymbol{q}^{\dagger} & \mathbf{0} \end{bmatrix}, \quad \boldsymbol{q} = \boldsymbol{U}_{\mathrm{ac}} \begin{bmatrix} \frac{\pi n_{ac}^{(1)}}{2\bar{n}\Lambda} \mathrm{e}^{i\phi^{(1)}} & 0 \\ 0 & \frac{\pi n_{ac}^{(2)}}{2\bar{n}\Lambda} \mathrm{e}^{i\phi^{(2)}} \end{bmatrix} \boldsymbol{U}_{\mathrm{ac}}^{\dagger} \tag{4.4b}$$

$$\mathbf{C}_{\boldsymbol{\psi}} = \begin{bmatrix} \boldsymbol{\psi} & \mathbf{0} \\ \mathbf{0} & -\boldsymbol{\psi}^{\mathrm{T}} \end{bmatrix}, \quad \boldsymbol{\psi} = \boldsymbol{U}_{\mathrm{dc}} \begin{bmatrix} \beta\Delta n_{\mathrm{dc}}^{(s)} & 0 \\ 0 & \beta\Delta n_{\mathrm{dc}}^{(f)} \end{bmatrix} \boldsymbol{U}_{\mathrm{dc}}^{\dagger}. \tag{4.4c}$$

The first part, $\mathbf{D}$, describes the common frequency dependence; $\delta = \bar{n}\beta - \pi/\Lambda$ is the wavenumber detuning with respect to the design Bragg wavenumber. The second part, $\mathbf{C}_{\boldsymbol{q}}$, describe the coupling between counter-propagating modes that are due to the presence of the grating. The last part, $\mathbf{C}_{\boldsymbol{\psi}}$, accounts for the deviation in the

propagation constants from $\bar{n}\beta$ for the two dc index eigenmodes. It includes two contributions so it can also be written on the form:

$$\boldsymbol{\psi} = \boldsymbol{P}_{\rm dc} \begin{bmatrix} \beta\Delta n_{\rm dc}^{({\rm lin},s)} & 0 \\ 0 & \beta\Delta n_{\rm dc}^{({\rm lin},f)} \end{bmatrix} \boldsymbol{P}_{\rm dc}^{\rm T} + \begin{bmatrix} 0 & i\alpha \\ -i\alpha & 0 \end{bmatrix}. \tag{4.5}$$

Here the first term represents the linear birefringence ($\boldsymbol{P}_{\rm dc}$ is a real rotation matrix and $\Delta n_{\rm dc}^{({\rm lin},s)} - \Delta n_{\rm dc}^{({\rm lin},f)}$ is the birefringence), and the second term describes the circular birefringence (optical activity with α as the rotation in rad/m).

The coupled-mode equations (4.2)-(4.4) can in principle be derived directly from Maxwells equations. However, each part in the coupling matrix $\mathbf{C}$ can be verified separately from the scalar counterpart by transforming it to the basis where the associated interaction matrix is diagonal such that there is no coupling between the polarization modes. The form of $\mathbf{C}_{\boldsymbol{\psi}}$ can be realized from decomposition (4.5) by considering the two terms separately.

As in the scalar, polarization-independent case, it is convenient to discretize the grating into $N+1$ layers, each of thickness $\Delta x = L/(N+1)$, where L is the total grating length. We assume that N is so large that the amplitude, phase, and dc-index functions in (4.1), and also $\boldsymbol{U}_{\rm ac}$ and $\boldsymbol{U}_{\rm dc}$, can be treated as constants in each layer. Since $\mathbf{C}$ is constant in each layer we can solve (4.2) exactly to find the relation between the fields at layers j and $j+1$:

$$\mathbf{E}(x_j + \Delta x) = \exp\left(i\mathbf{C}\Delta x\right)\mathbf{E}(x_j), \quad x_j = j\Delta x. \tag{4.6}$$

This transfer matrix relation can be used to propagate the fields through the piecewice uniform grating. With the help of the connection between the transfer matrix and the scattering matrix (Appendix 4.A), we can find the reflection and transmission response from the total transfer matrix (direct scattering). Note that the exponential of a matrix is easily computed from its diagonal form.

To facilitate inverse scattering, it is convenient to push the discretization even further. For infinitesimal Δx, the transfer matrix $\exp(i\mathbf{C}\Delta x)$ can be written $\exp(i\mathbf{D}\Delta x)\exp(i\mathbf{C}_{\boldsymbol{q}}\Delta x)\exp(i\mathbf{C}_{\boldsymbol{\psi}}\Delta x)$, as realized by expanding the exponentials to first order in Δx. Thus we can approximate each layer by a cascade of three sections: a retardation section, a discrete reflector, and a time-delay section. The transfer matrix of the jth layer becomes

$$\mathbf{T}_j \equiv \exp(i\mathbf{C}\Delta x) = \mathbf{T}_z \mathbf{T}_{\boldsymbol{\rho}_j} \mathbf{T}_{\boldsymbol{\Phi}_j}, \tag{4.7}$$

where

$$\mathbf{T}_z \equiv \exp(i\mathbf{D}\Delta x) = \begin{bmatrix} z^{-1/2}\boldsymbol{I} & \mathbf{0} \\ \mathbf{0} & z^{1/2}\boldsymbol{I} \end{bmatrix},\ z^{-1} = \exp(i2\delta\Delta x), \tag{4.8a}$$

$$\mathbf{T}_{\boldsymbol{\rho}_j} \equiv \exp(i\mathbf{C}_{\boldsymbol{q}}\Delta x) = \begin{bmatrix} \boldsymbol{t}_j^{-1} & -\boldsymbol{t}_j^{-1}\boldsymbol{\rho}_j^\dagger \\ -\boldsymbol{t}_j^{-1}\boldsymbol{\rho}_j & \boldsymbol{t}_j^{-1} \end{bmatrix},\ \begin{array}{l} \boldsymbol{\rho}_j = i\boldsymbol{q}^\dagger(\boldsymbol{q}^\dagger\boldsymbol{q})^{-1/2}\tanh[(\boldsymbol{q}^\dagger\boldsymbol{q})^{1/2}\Delta x], \\ \boldsymbol{t}_j = \cosh[(\boldsymbol{q}^\dagger\boldsymbol{q})^{1/2}\Delta x]^{-1} = (\boldsymbol{I} - \boldsymbol{\rho}_j^\dagger\boldsymbol{\rho}_j)^{1/2} \end{array} \tag{4.8b}$$

$$\mathbf{T}_{\boldsymbol{\Phi}_j} \equiv \exp(i\mathbf{C}_{\boldsymbol{\psi}}\Delta x) = \begin{bmatrix} \boldsymbol{\Phi}_j & \mathbf{0} \\ \mathbf{0} & \boldsymbol{\Phi}_j^* \end{bmatrix},\ \boldsymbol{\Phi}_j = \boldsymbol{U}_{\rm dc} \begin{bmatrix} \exp(i\beta\Delta n_{\rm dc}^{(s)}\Delta x) & 0 \\ 0 & \exp(i\beta\Delta n_{\rm dc}^{(f)}\Delta x) \end{bmatrix} \boldsymbol{U}_{\rm dc}^\dagger. \tag{4.8c}$$

Here, z^{-1} represents the dual-pass time delay through a layer. The form of the matrices in (4.8) may, for example, be verified by evaluating the power-series expansion of the matrix exponentials.

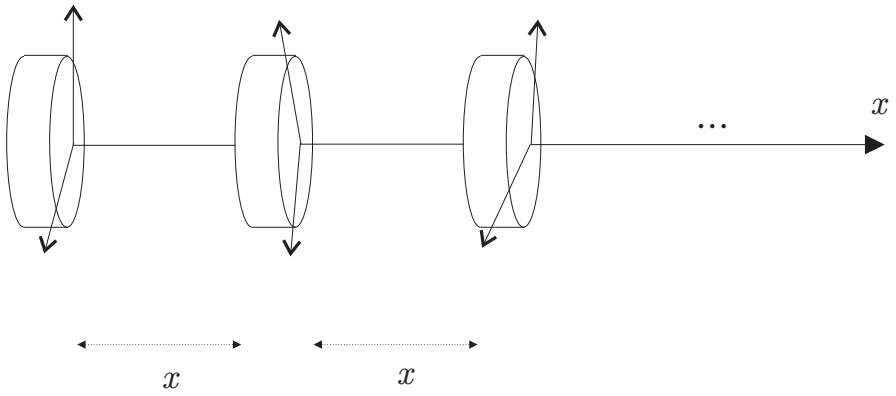

Figure 4.1: Discrete model of the birefringent grating. The cylinders indicate the retardation or phase-delay sections $\boldsymbol{\Phi}_j$, and the arrows represent the eigenvalues of the discrete reflectors ($\rho_j^{(1)}$ and $\rho_j^{(2)}$).

The matrix $\boldsymbol{\Phi}_j$ is a retardation (Jones) matrix describing the phase delay in each layer when the common time-delay due to $z^{-1/2}$ has been removed. Let $\delta_w \equiv \bar{n}\Delta\beta$ be the range of the wavenumber detuning that corresponds to one period of the reflection (or transmission) spectrum of a discretized grating without the retardation sections. Since the impulse response is discrete with a (normalized) time $2\Delta x$ between neighboring points, the sampling theorem implies that $\delta_w \Delta x = \pi$. This means that the variation of the phases of the eigenvalues of $\boldsymbol{\Phi}_j$ are

$$\Delta\beta\Delta n_{\mathrm{dc}}^{(s,f)}\Delta x = \frac{\pi\Delta n_{\mathrm{dc}}^{(s,f)}}{\bar{n}}. \tag{4.9}$$

The ratio $\Delta n_{\mathrm{dc}}^{(s,f)}/\bar{n}$ is usually less than 10^{-3}, so the variation of this phase term is less than about 3 mrad. We therefore choose to treat $\boldsymbol{\Phi}_j$ as a frequency-independent matrix;

$$\boldsymbol{\Phi}_j = \boldsymbol{U}_{\mathrm{dc}} \begin{bmatrix} \mathrm{e}^{i\varphi^{(s)}} & 0 \\ 0 & \mathrm{e}^{i\varphi^{(f)}} \end{bmatrix} \boldsymbol{U}_{\mathrm{dc}}^{\dagger}, \tag{4.10}$$

where $\varphi^{(s)} = \beta_B \Delta n_{\mathrm{dc}}^{(s)} \Delta x$, $\varphi^{(f)} = \beta_B \Delta n_{\mathrm{dc}}^{(f)} \Delta x$, and $\beta_B = \pi/(\Lambda\bar{n})$ is the vacuum Bragg or design wavenumber.

Until now, we have allowed that the ac-index modulation to have elliptic eigenaxes. However, each section must obey reciprocity. Using (4.38) in Appendix 4.A we find that scattering matrix of the discrete reflector is given by

$$\mathbf{S}_{\boldsymbol{\rho}_j} = \begin{bmatrix} \boldsymbol{\rho}_j & \boldsymbol{t}_j \\ \boldsymbol{t}_j & -\boldsymbol{\rho}_j^{\dagger} \end{bmatrix}. \tag{4.11}$$

From (4.39) in Appendix 4.B it follows that $\boldsymbol{\rho}_j$ is symmetric. This means that ac index modulation eigenaxes have to be linear; i.e. $\boldsymbol{U}_{\mathrm{ac}}$ can be replaced by a real unitary matrix $\boldsymbol{P}_{\mathrm{ac}}$ (see Appendix 4.D.1).

The effect of a varying geometrical grating phase cannot be distinguished from the effect of a varying dc-index [40]. For fiber gratings, the two geometrical grating phases are equal, $\phi^{(1)} = \phi^{(2)}$, so that any difference in the reflection phase for the two polarizations must be assigned to the dc-indices. The geometrical phases $\phi^{(1)} = \phi^{(2)}$ may be assumed to be constant through the grating, which means that the phase variation must be implemented by a varying dc index. Alternatively, we may set $\Delta n_{\mathrm{dc}}^{(s)} = -\Delta n_{\mathrm{dc}}^{(f)}$ so that any balanced phase variation is implemented by varying geometrical phases. In this work we choose to attribute the reflection phase of each layer to the phase-delay section on the left-hand side of the reflector, so that $\boldsymbol{q}(x)$ and $\boldsymbol{\rho}_j$ are real (and symmetric).

To summarize our discrete model, each layer consists of three lossless and reciprocal sections with transfer matrices $\mathbf{T}_z$, $\mathbf{T}_{\boldsymbol{\rho}_j}$, and $\mathbf{T}_{\boldsymbol{\Phi}_j}$. We have used the convention that the discrete reflector is sandwiched between the phase-delay and time-delay sections. Only $\mathbf{T}_z$ is dependent on detuning. The transfer matrix of layer j is given by

$$\mathbf{T}_j = \mathbf{T}_z \mathbf{T}_{\boldsymbol{\rho}_j} \mathbf{T}_{\boldsymbol{\Phi}_j} = \begin{bmatrix} z^{-1/2}\boldsymbol{t}_j^{-1}\boldsymbol{\Phi}_j & -z^{-1/2}\boldsymbol{t}_j^{-1}\boldsymbol{\rho}_j\boldsymbol{\Phi}_j^* \\ -z^{1/2}\boldsymbol{t}_j^{-1}\boldsymbol{\rho}_j\boldsymbol{\Phi}_j & z^{1/2}\boldsymbol{t}_j^{-1}\boldsymbol{\Phi}_j^* \end{bmatrix}. \tag{4.12}$$

Note that $\mathbf{T}_j$ is of the form of (4.44) for real frequencies. The transfer matrix can be converted back into a scattering matrix:

$$\mathbf{S}_j = \begin{bmatrix} \boldsymbol{\Phi}_j^{\mathrm{T}}\boldsymbol{\rho}_j\boldsymbol{\Phi}_j & z^{-1/2}\boldsymbol{\Phi}_j^{\mathrm{T}}\boldsymbol{t}_j \\ z^{-1/2}\boldsymbol{t}_j\boldsymbol{\Phi}_j & -z^{-1}\boldsymbol{\rho}_j \end{bmatrix}. \tag{4.13}$$

The combined transfer matrix describing a grating with $N+1$ layers is given by

$$\mathbf{M}_N = \mathbf{T}_N \mathbf{T}_{N-1} \cdots \mathbf{T}_1 \mathbf{T}_0. \tag{4.14}$$

Equations (4.12) and (4.14) can be used to compute the reflection and transmission response of the discretized grating, similarly to the method based on the continuous model (4.6).

The discrete grating model can also be justified from a another perspective: Similarly to the scalar case [16, 40] we can approximate the response of a layer by a coupling point in cascade with a pure propagation section. If the thickness of the coupling point is zero, the response of the jth layer is described by frequency-independent Jones reflection and transmission matrices. With the help of singular value decomposition and the reciprocity and lossless conditions (see Appendix 4.B, it is possible to prove that the coupling point can be described by a discrete reflector with a real and symmetric Jones matrix sandwiched between two retardation sections. Since the cascade of two retardation sections is a new retardation section, we can leave out the retardation section on the right-hand side of all reflectors but the last; moreover, the retardation section on the right-hand side of the grating has no effect on the reflection spectrum from the left, so it can be ignored. Thus each layer can be modeled as a retardation section, a discrete reflector, and a pure propagation section.

4.3 Layer-peeling reconstruction algorithm

In the polarization-independent case, the layer-peeling algorithm has been successfully applied to the reconstruction of gratings [16, 26, 40]. The layer-peeling algorithm is based on the simple fact that the leading edge of the impulse response is independent of the later part of the grating as a result of causality. Hence, one can identify the first layer of the grating, and remove its effect by using the associated transfer matrix. A similar algorithm is described in [19] which also considers the polarization dependence. The algorithm in [19] has the weakness that it diverges if one or several of the local reflection coefficients $\boldsymbol{\rho}_j$ turns out to be (near-)singular. While the algorithm in [19] is based on a continuous grating model, we will generalize the time-domain version of the discrete layer-peeling algorithm such that it is applicable to an arbitrary birefringent grating.

The reflection response of a birefringent grating must be described as a 2×2 Jones matrix $\boldsymbol{R}$. From reciprocity relation (4.39b) we find that $\boldsymbol{S}_{11} = \boldsymbol{R}$ is symmetric. This matrix can be viewed as the operator that takes the input field vector (from the left) to the reflected field vector. Its two columns can be interpreted as the responses for orthonormal input vectors $\begin{bmatrix}1 & 0\end{bmatrix}^{\mathrm{T}}$ and $\begin{bmatrix}0 & 1\end{bmatrix}^{\mathrm{T}}$, respectively. Similarly, we can define the forward ($\boldsymbol{u}$) and backward ($\boldsymbol{v}$) propagating fields and the impulse response $\boldsymbol{h}$ as 2×2 field matrices, where the two columns are the fields for input field vectors $\begin{bmatrix}1 & 0\end{bmatrix}^{\mathrm{T}}$ and $\begin{bmatrix}0 & 1\end{bmatrix}^{\mathrm{T}}$, respectively.

A stack of discrete reflectors that is interrogated by an impulse will give a nonzero response only for a time-delays that is a multiple of the dual-pass delay of a layer. Thus, the grating impulse response and the optical fields within the grating structure are discrete in time with a sampling period equal to $2\Delta x$ (normalized). If the discrete impulse response is denoted $\boldsymbol{h}(k)$, the reflection spectrum is a Fourier series of the form

$$\boldsymbol{R}(\delta) = \sum_{k=0}^{\infty} \boldsymbol{h}(k)\exp(i2k\delta\Delta x) = \sum_{k=0}^{\infty} \boldsymbol{h}(k)z^{-k}. \tag{4.15}$$

It follows that the reflection spectrum is periodic with a spectral period $\delta_w = \pi/\Delta x$.

The transfer matrix in (4.12) can be written

$$\mathbf{T}_j = z^{-1/2}\begin{bmatrix}\boldsymbol{t}_j^{-1}\boldsymbol{\Phi}_j & \mathbf{0}\\ \mathbf{0} & z\boldsymbol{t}_j^{-1}\boldsymbol{\Phi}_j^*\end{bmatrix}\begin{bmatrix}\boldsymbol{I} & -\boldsymbol{\Phi}_j^{\dagger}\boldsymbol{\rho}_j\boldsymbol{\Phi}_j^*\\ -\boldsymbol{\Phi}_j^{\mathrm{T}}\boldsymbol{\rho}_j\boldsymbol{\Phi}_j & \boldsymbol{I}\end{bmatrix}. \tag{4.16}$$

In the time domain, $z^{-1/2}$ in (4.16) represents a time delay equal to the single-pass delay of a layer. In the layer-peeling algorithm, the grating will be evaluated layer by layer, and the time reference may be chosen differently for each layer. We may therefore omit the delay represented by the common factor $z^{-1/2}$ in (4.16). This means that the reference time follows the leading edge of the impulse. The remaining factor z in (4.16) represents a negative (anti-causal) dual-pass delay. Thus, at time-step k the fields within layer $j+1$ relate to the fields within layer j as follows:

$$\begin{bmatrix}\boldsymbol{u}_{j+1}(k)\\ \boldsymbol{v}_{j+1}(k-1)\end{bmatrix} = \begin{bmatrix}\boldsymbol{t}_j^{-1}\boldsymbol{\Phi}_j & \mathbf{0}\\ \mathbf{0} & \boldsymbol{t}_j^{-1}\boldsymbol{\Phi}_j^*\end{bmatrix}\begin{bmatrix}\boldsymbol{I} & -\boldsymbol{\Phi}_j^{\dagger}\boldsymbol{\rho}_j\boldsymbol{\Phi}_j^*\\ -\boldsymbol{\Phi}_j^{\mathrm{T}}\boldsymbol{\rho}_j\boldsymbol{\Phi}_j & \boldsymbol{I}\end{bmatrix}\begin{bmatrix}\boldsymbol{u}_j(k)\\ \boldsymbol{v}_j(k)\end{bmatrix}. \tag{4.17}$$

The forward-propagating field matrix into the first layer is initialized as an impulse, i.e. $\boldsymbol{u}_0(0) = \boldsymbol{I}$ and $\boldsymbol{u}_0(k) = \boldsymbol{0}$, $k = 1, 2, \ldots, N$, while the backward-propagating field matrix out of the first layer is initiated as the $N+1$ first points of the impulse response, i.e. $\boldsymbol{v}_0(k) = \boldsymbol{h}(k)$, $k = 0, 1, \ldots, N$. In scattering matrix formulation, (4.17) can be written

$$\begin{bmatrix} \boldsymbol{v}_j(k) \\ \boldsymbol{u}_{j+1}(k) \end{bmatrix} = \begin{bmatrix} \boldsymbol{\Phi}_j^{\mathrm{T}} \boldsymbol{\rho}_j \boldsymbol{\Phi}_j & \boldsymbol{\Phi}_j^{\mathrm{T}} \boldsymbol{t}_j \\ \boldsymbol{t}_j \boldsymbol{\Phi}_j & -\boldsymbol{\rho}_j \end{bmatrix} \begin{bmatrix} \boldsymbol{u}_j(k) \\ \boldsymbol{v}_{j+1}(k-1) \end{bmatrix}. \tag{4.18}$$

Assuming that the grating is dark for times $k < 0$, we have $\boldsymbol{v}_{j+1}(-1) = 0$. Thus,

$$\boldsymbol{v}_j(0) = \boldsymbol{\Phi}_j^{\mathrm{T}} \boldsymbol{\rho}_j \boldsymbol{\Phi}_j \boldsymbol{u}_j(0). \tag{4.19}$$

Note that $\boldsymbol{u}_j(0)$ is always invertible since all preceding transmission matrices $\boldsymbol{t}_m$, $m = 0, \ldots, j-1$ are nonsingular when the norm of the reflection matrices $\boldsymbol{\rho}_m$ are less than 1. Thus we can find the product $\boldsymbol{\Phi}_j^{\mathrm{T}} \boldsymbol{\rho}_j \boldsymbol{\Phi}_j$ from $\boldsymbol{\Upsilon} \equiv \boldsymbol{v}_j(0) \boldsymbol{u}_j^{-1}(0)$. For $j = 0$, we have $\boldsymbol{u}_0(0) = \boldsymbol{I}$ and $\boldsymbol{v}_0(0) = \boldsymbol{h}(0)$, which gives $\boldsymbol{\Phi}_0^{\mathrm{T}} \boldsymbol{\rho}_0 \boldsymbol{\Phi}_0 = \boldsymbol{h}(0)$.

We must now find a real symmetric $\boldsymbol{\rho}_j$ and a unitary $\boldsymbol{\Phi}_j$ such that $\boldsymbol{\Phi}_j^{\mathrm{T}} \boldsymbol{\rho}_j \boldsymbol{\Phi}_j = \boldsymbol{\Upsilon}$. The properties of $\boldsymbol{\rho}_j$ and $\boldsymbol{\Phi}_j$ give that $\boldsymbol{\Upsilon}$ is symmetric, which agrees with reciprocity. The matrix $\boldsymbol{\rho}_j$ can be written $\boldsymbol{\rho}_j = \boldsymbol{P}_{\boldsymbol{\rho}} \boldsymbol{\Lambda} \boldsymbol{P}_{\boldsymbol{\rho}}^{\mathrm{T}}$, where $\boldsymbol{P}_{\boldsymbol{\rho}}$ is a rotation matrix (real and special unitary matrix), and $\boldsymbol{\Lambda}$ is real and diagonal. In Appendix 4.D.3 it is shown that a 2×2 unitary matrix $\boldsymbol{\Phi}_j$ can be factorized into a rotation matrix $\boldsymbol{P}_{\boldsymbol{\Phi}}$ and a symmetrical unitary $\boldsymbol{Q}_{\boldsymbol{\Phi}}$, so that $\boldsymbol{\Phi}_j = \boldsymbol{P}_{\boldsymbol{\Phi}} \boldsymbol{Q}_{\boldsymbol{\Phi}}$. Physically, $\boldsymbol{P}_{\boldsymbol{\Phi}}$ and $\boldsymbol{Q}_{\boldsymbol{\Phi}}$ represent circular and linear birefringence, respectively. This gives

$$\boldsymbol{\Upsilon} = \boldsymbol{\Phi}_j^{\mathrm{T}} \boldsymbol{\rho}_j \boldsymbol{\Phi}_j = \boldsymbol{Q}_{\boldsymbol{\Phi}} \boldsymbol{P}_{\boldsymbol{\Phi}}^{\mathrm{T}} \boldsymbol{P}_{\boldsymbol{\rho}} \boldsymbol{\Lambda} \boldsymbol{P}_{\boldsymbol{\rho}}^{\mathrm{T}} \boldsymbol{P}_{\boldsymbol{\Phi}} \boldsymbol{Q}_{\boldsymbol{\Phi}} = \boldsymbol{Q}_{\boldsymbol{\Phi}} \boldsymbol{P} \boldsymbol{\Lambda} \boldsymbol{P}^{\mathrm{T}} \boldsymbol{Q}_{\boldsymbol{\Phi}}, \tag{4.20}$$

where $\boldsymbol{P} = \boldsymbol{P}_{\boldsymbol{\Phi}}^{\mathrm{T}} \boldsymbol{P}_{\boldsymbol{\rho}}$ is another rotation matrix. This equation shows that it is not possible from a reflection measurement to distinguish circular birefringence from the orientation of the polarization eigenaxes of the reflector. We therefore associate circular birefringence with the orientation of the eigenaxes of the reflector. Thus, in the presence of circular birefringence, the reference coordinate axes rotates from one layer to the next at an angle that is equal to the amount of circular birefringence. In this rotating coordinate system, $\boldsymbol{\Phi}_j = \boldsymbol{Q}_{\boldsymbol{\Phi}}$ and $\boldsymbol{\rho}_j = \boldsymbol{P} \boldsymbol{\Lambda} \boldsymbol{P}^{\mathrm{T}}$, yielding $\boldsymbol{\Upsilon} = \boldsymbol{\Phi}_j \boldsymbol{\rho}_j \boldsymbol{\Phi}_j = \boldsymbol{\Phi}_j \boldsymbol{P} \boldsymbol{\Lambda} \boldsymbol{P}^{\mathrm{T}} \boldsymbol{\Phi}_j$.

The method in Appendix 4.D.2 is used to decompose the complex symmetric matrix $\boldsymbol{\Upsilon}$ into a unitary $\boldsymbol{U}$ and a diagonal nonnegative $\boldsymbol{\Lambda}$ so that $\boldsymbol{\Upsilon} = \boldsymbol{U}^{\mathrm{T}} \boldsymbol{\Lambda} \boldsymbol{U}$.

In the nontrivial case when the singular values are distinct, the order of the singular values must be established. This can be done using some smoothness criteria on the coupling function. Once the order is established, the decomposition is unique up to a diagonal matrix $\boldsymbol{J}$ with elements ± 1, i.e. $\boldsymbol{\Upsilon} = (\boldsymbol{J}\boldsymbol{U})^{\mathrm{T}} \boldsymbol{\Lambda} \boldsymbol{J} \boldsymbol{U} = \boldsymbol{U}^{\mathrm{T}} \boldsymbol{\Lambda} \boldsymbol{U}$. Setting $\boldsymbol{J}\boldsymbol{U} = \boldsymbol{P}^{\mathrm{T}} \boldsymbol{\Phi}_j$ for some choice of $\boldsymbol{J}$, we can find $\boldsymbol{\Phi}_j$ and $\boldsymbol{P}$ by using the factorization method described in Appendix 4.D.3. By introducing a spectral decomposition of $\boldsymbol{\Phi}_j$ (Appendix 4.D.1) we can easy realize that the different choices for $\boldsymbol{J}$ can be interpreted as different signs for the eigenvalues of the phase-delay matrix $\boldsymbol{\Phi}_j$. As in the scalar, polarization-independent case, it is most natural to choose $\boldsymbol{J}$ so that the phase-delay of each layer is minimum.

Once $\boldsymbol{\Phi}_j$ and $\boldsymbol{\rho}_j$ are found, the optical fields in the next layer $j+1$ can be found using (4.17). When these fields have been calculated, $\boldsymbol{\Phi}_{j+1}$ and $\boldsymbol{\rho}_{j+1}$ can be found by the same procedure.

From the discussion above, we conclude that the local profile of any birefringent grating can be found by the polarization resolved layer-peeling algorithm, which is here presented in pseudocode:

Initialize $\boldsymbol{u}(0) = \boldsymbol{I}$ and $\boldsymbol{u}(k) = \boldsymbol{0}$, $k = 1, 2, \ldots, N$.
Initialize $\boldsymbol{v}(k) = \boldsymbol{h}(k)$, $k = 0, 1, \ldots, N$.
FOR $j = 0$ TO N,
Calculate $\boldsymbol{\Upsilon} \equiv \boldsymbol{v}(0)\boldsymbol{u}^{-1}(0)$.
Decompose $\boldsymbol{\Upsilon}$ into a unitary matrix $\boldsymbol{U}$ and a diagonal and
nonnegative matrix $\boldsymbol{\Lambda}$ so that $\boldsymbol{\Upsilon} = \boldsymbol{U}^{\mathrm{T}}\boldsymbol{\Lambda}\boldsymbol{U}$ (Appendix 4.D.2).
Find a rotation matrix $\boldsymbol{P}^{\mathrm{T}}$ and a symmetric, unitary matrix $\boldsymbol{\Phi}_j$,
so that $\boldsymbol{U} = \boldsymbol{P}^{\mathrm{T}}\boldsymbol{\Phi}_j$ (Appendix 4.D.3),
Calculate an eigenvalue matrix $\boldsymbol{\Lambda}'$
and an eigenvector matrix $\boldsymbol{P}'$ of $\boldsymbol{\Phi}_j$ (Appendix 4.D.1)
Find a diagonal matrix $\boldsymbol{J}$ with coefficients ± 1 so that $\boldsymbol{J}\boldsymbol{\Lambda}'$ produces
phase-delays in the range 0 to π.
Recalculate $\boldsymbol{\Phi}_j \leftarrow \boldsymbol{P}'\boldsymbol{J}\boldsymbol{\Lambda}'\boldsymbol{P}'^{\mathrm{T}}$ and $\boldsymbol{P} \leftarrow \boldsymbol{P}'\boldsymbol{J}\boldsymbol{P}'^{\mathrm{T}}\boldsymbol{P}\boldsymbol{J}$.
Calculate $\boldsymbol{\rho}_j = \boldsymbol{P}\boldsymbol{\Lambda}\boldsymbol{P}^{\mathrm{T}}$.
Calculate $\boldsymbol{K} = \boldsymbol{P}(\boldsymbol{I} - \boldsymbol{\Lambda}^2)^{-1/2}\boldsymbol{P}^{\mathrm{T}}\boldsymbol{\Phi}_j$.
Propagates the field matrices to the next layer using (4.18),
and moves the reference plane to layer $j+1$:
FOR $k = 0$ TO $N - j - 1$,
$\boldsymbol{u}(k) = \boldsymbol{K}(\boldsymbol{u}(k) - \boldsymbol{\Upsilon}^*\boldsymbol{v}(k))$
$\boldsymbol{v}(k) = \boldsymbol{K}^*(\boldsymbol{v}(k+1) - \boldsymbol{\Upsilon}\boldsymbol{u}(k+1))$
END
END

The spatial index j of $\boldsymbol{u}$ and $\boldsymbol{v}$ is omitted since the algorithm operates only on one layer at the time, and $\boldsymbol{u}$ and $\boldsymbol{v}$ do not need to be saved.

4.4 Spectrum properties and realizability

In this section, we will give the necessary and sufficient conditions that the response must satisfy in order to be realizable as a birefringent grating. These conditions will be used as a foundation for characterizing the possible reflection and transmission responses, and for developing a design method based on digital finite-impulse-response (FIR) filter design tools.

Any discrete, birefringent grating is described by the transfer matrix product (4.14), where each layer is described by (4.12). To facilitate the analysis of the total response, we omit the trivial time delay matrix at the right-hand end of the grating (the very first matrix in the total transfer matrix product) and instead insert an extra retardation matrix at the right-hand end. Obviously, this modification will

not influence the reflection spectrum from the left or the layer-peeling algorithm as described in Section 4.3. The response of the entire structure is then described by the transfer matrix product $\mathbf{M}_N = \mathbf{T}_N\mathbf{T}_{N-1}\cdots\mathbf{T}_1\mathbf{T}_0$, where $\mathbf{T}_j$ is still given by (4.12) for $0 \le j \le N-1$, but $\mathbf{T}_N$ is

$$\mathbf{T}_N = \begin{bmatrix} \boldsymbol{\Phi} & \mathbf{0} \\ \mathbf{0} & \boldsymbol{\Phi}^* \end{bmatrix} \begin{bmatrix} \boldsymbol{t}_N^{-1} & -\boldsymbol{t}_N^{-1}\boldsymbol{\rho}_N \\ -\boldsymbol{t}_N^{-1}\boldsymbol{\rho}_N & \boldsymbol{t}_N^{-1} \end{bmatrix} \begin{bmatrix} \boldsymbol{\Phi}_N & \mathbf{0} \\ \mathbf{0} & \boldsymbol{\Phi}_N^* \end{bmatrix} = \begin{bmatrix} \boldsymbol{\Phi}\boldsymbol{t}_N^{-1}\boldsymbol{\Phi}_N & -\boldsymbol{\Phi}\boldsymbol{t}_N^{-1}\boldsymbol{\rho}_N\boldsymbol{\Phi}_N^* \\ -\boldsymbol{\Phi}^*\boldsymbol{t}_N^{-1}\boldsymbol{\rho}_N\boldsymbol{\Phi}_N & \boldsymbol{\Phi}^*\boldsymbol{t}_N^{-1}\boldsymbol{\Phi}_N^* \end{bmatrix}. \tag{4.21}$$

In Appendix 4.C we show that the total transfer matrix can be written on the form

$$\mathbf{M}_N = \begin{bmatrix} \boldsymbol{A}_*(z) & \boldsymbol{B}_*(z) \\ \boldsymbol{B}(z) & \boldsymbol{A}(z) \end{bmatrix}. \tag{4.22}$$

In (4.22), $\boldsymbol{B}(z)$ and $\boldsymbol{A}(z)$ are symmetrically defined Nth order polynomials with matrix coefficients,

$$\boldsymbol{A}(z) = z^{N/2}\sum_{k=0}^{N} \boldsymbol{a}(k)z^{-k} \tag{4.23a}$$

$$\boldsymbol{B}(z) = z^{N/2}\sum_{k=0}^{N} \boldsymbol{b}(k)z^{-k} \tag{4.23b}$$

which satisfy

$$\boldsymbol{A}\boldsymbol{A}_*^{\mathrm{T}} - \boldsymbol{B}\boldsymbol{B}_*^{\mathrm{T}} = \boldsymbol{I} \tag{4.24a}$$

$$\boldsymbol{A}\boldsymbol{B}^{\mathrm{T}} - \boldsymbol{B}\boldsymbol{A}^{\mathrm{T}} = \mathbf{0} \tag{4.24b}$$

$$\boldsymbol{A}^{\mathrm{T}}\boldsymbol{B}_* - \boldsymbol{B}_*^{\mathrm{T}}\boldsymbol{A} = \mathbf{0}. \tag{4.24c}$$

The asterisk in the subscript stands for the para-Hermitian conjugate operation, $\boldsymbol{A}_*(z) = \boldsymbol{A}^*(1/z^*)$, which has the effect of reversing and complex conjugating the matrix coefficients, i.e., $\boldsymbol{A}_*(z) = z^{N/2}\sum_{k=0}^{N}\boldsymbol{a}^*(N-k)z^{-k}$. The transmission response from the right, $\boldsymbol{S}_{12} = \boldsymbol{A}^{-1}(z)$, must be causal and stable for all $|z| > 1$. Thus, the matrix $\boldsymbol{A}(z)$ is nonsingular on and outside the unit circle, that is, the $2N$ zeros α_j of $\det \boldsymbol{A}(z)$ are located inside the unit circle of the complex plane:

$$|\alpha_j| < 1, \quad j = 1, \ldots, 2N. \tag{4.25}$$

At the unit circle $|z| = 1$ we recognize conditions (4.22)-(4.25) as the lossless, reciprocity and stability conditions of the filter response (see Appendix 4.B. In Appendix 4.C we prove that (4.22)-(4.25) are not only necessary but also *sufficient* for a response to be realizable for a birefringent grating with $N+1$ layers. In other words, by forcing a response to satisfy (4.22)-(4.25), we know that there exists a grating with that specific response, and the structure can be found by using the layer-peeling algorithm (Section 4.3 or the equivalent transfer matrix factorization (Appendix 4.C.2.

Since the realizability conditions (4.22)-(4.25) are exactly the ones that the response must satisfy, we can use them to analyze in detail what kind of reflection and

transmission responses a birefringent grating can provide. Note that the reflection spectrum from the left is $\boldsymbol{R} = -\boldsymbol{A}^{-1}\boldsymbol{B}$ and the transmission spectrum from the left to the right is $\boldsymbol{T} = \boldsymbol{A}^{-1\mathrm{T}}$ (See (4.38) and (4.40a).

For real frequencies, i.e., on the unit circle $|z| = 1$, the para-Hermitian conjugate operation is the same as the complex conjugate. According to the discussion in Appendix 4.B, the realizability conditions mean that we can decompose $\boldsymbol{A}$ and $\boldsymbol{B}$ by using the singular value decompositions

$$\boldsymbol{A} = \boldsymbol{\Phi}_r^* \boldsymbol{t}^{-1} \boldsymbol{\Phi}_l^* \tag{4.26a}$$

$$\boldsymbol{B} = -\boldsymbol{\Phi}_r^* \boldsymbol{t}^{-1} \boldsymbol{\rho} \boldsymbol{\Phi}_l, \tag{4.26b}$$

where $\boldsymbol{\Phi}_l = \boldsymbol{\Phi}_l(\omega)$ and $\boldsymbol{\Phi}_r = \boldsymbol{\Phi}_r(\omega)$ are unitary matrices, $\boldsymbol{\rho} = \boldsymbol{\rho}(\omega)$ is a diagonal, real non-negative matrix satisfying $\|\boldsymbol{\rho}\| < 1$, and $\boldsymbol{t} = (\boldsymbol{I} - \boldsymbol{\rho}^2)^{1/2}$. In general, note that all matrices in (4.26) are dependent on frequency.

The physical meaning of (4.26) becomes clearer if we consider the reflection spectrum from the left and the transmission spectrum from the left to the right:

$$\boldsymbol{R} = -\boldsymbol{A}^{-1}\boldsymbol{B} = \boldsymbol{\Phi}_l^{\mathrm{T}} \boldsymbol{\rho} \boldsymbol{\Phi}_l \tag{4.27a}$$

$$\boldsymbol{T} = \boldsymbol{A}^{-1\mathrm{T}} = \boldsymbol{\Phi}_r \boldsymbol{t} \boldsymbol{\Phi}_l, \tag{4.27b}$$

Since $\boldsymbol{\rho}$ is real and symmetric and satisfies $\|\boldsymbol{\rho}\| < 1$, and $\boldsymbol{\Phi}_l$ and $\boldsymbol{\Phi}_r$ are unitary for all real frequencies, the physical interpretation of (4.26) and (4.27) is as follows: *For a given, real frequency, the response of the entire grating is the same as for a discrete reflector sandwiched between two retardation sections.* In reflection or transmission, the discrete reflector acts as a partial polarizer. This result is analogous to the Jones equivalence theorems [51]. The parameters of the three elements are certainly dependent on frequency. Note that $\boldsymbol{A}$, $\boldsymbol{B}$, $\boldsymbol{R}$ and $\boldsymbol{T}$ are not necessarily are normal matrices, i.e, in general the eigenvectors of the reflection and transmission Jones matrices do not have to be orthogonal.

We will now see how the realizability conditions can be used for the design of birefringent gratings. The goal is to find a response that is realizable and close to the target spectrum. This can be approximately achieved by a FIR windowing procedure on the impulse response, similarly to the common practice in fiber grating design. However, since the impulse response has infinite duration, we will instead generalize the design approach presented in [40] which consider the realizability conditions in a rigorous way.

1. First we specify a target reflection spectrum (Jones matrix) $\boldsymbol{R}$ and an associated bandwidth. The matrix $\boldsymbol{R}$ must be symmetric and satisfy $\|\boldsymbol{R}\| < 1$ for all frequencies. These properties are guaranteed satisfied if the reflection matrix is specified in the form (4.27a) for some frequency dependent matrices $\boldsymbol{\Phi}_l$ (unitary) and $\boldsymbol{\rho}$ (diagonal with nonnegative elements less than 1).

2. The next step is to compute $\boldsymbol{A}$ and $\boldsymbol{B}$ from $\boldsymbol{R}$ by identifying the matrices in the decompositions (4.26). The matrix $\boldsymbol{R}$ is symmetric, and using singular value decomposition (Appendix 4.D.2) we can find $\boldsymbol{\Phi}_l$, $\boldsymbol{\rho}$ and $\boldsymbol{t} = (\boldsymbol{I} - \boldsymbol{\rho}^2)^{1/2}$.

The matrix $\boldsymbol{\Phi}_r$ cannot be determined from $\boldsymbol{R}$, so $\boldsymbol{\Phi}_r$ can be chosen arbitrarily when only $\boldsymbol{R}$ is relevant for the design. If the transmission response is relevant as well, $\boldsymbol{\Phi}_r$ can in principle be chosen to tailor $\boldsymbol{T} = \boldsymbol{\Phi}_r \boldsymbol{t} \boldsymbol{\Phi}_l$. For simplicity, however, we will choose $\boldsymbol{\Phi}_r = \boldsymbol{\Phi}_l^\dagger \boldsymbol{D}^*$ with $\boldsymbol{D}$ diagonal and unitary, such that $\boldsymbol{A}$ is normal:

$$\boldsymbol{A} = \boldsymbol{\Phi}_l^{\mathrm{T}} \boldsymbol{t}^{-1} \boldsymbol{D} \boldsymbol{\Phi}_l^*. \tag{4.28}$$

The unknown unitary matrix $\boldsymbol{D}$ has two nonzero components comprising two independent phase functions. First, according to (4.25) we must choose $\det \boldsymbol{A} = \det(\boldsymbol{t}^{-1}\boldsymbol{D})$ minimum phase. Thus, $\det \boldsymbol{D}$ is determined from $\det \boldsymbol{t}^{-1}$ by using the Hilbert transform $\mathcal{H}\{\cdot\}$:

$$\arg(\det \boldsymbol{D}) = \mathcal{H}\{\ln(\det \boldsymbol{t}^{-1})\}. \tag{4.29}$$

The second unknown phase function can in principle be chosen arbitrary; however choosing this phase function such that $\boldsymbol{A}$ is causal might improve the result from the approximation in step 3. The phase function that makes $\boldsymbol{A}$ causal could be found by some iterative approach. We will choose $\boldsymbol{D}$ so that both eigenvalues (that is, the two elements of $\boldsymbol{t}^{-1}\boldsymbol{D}$) are minimum phase.

Once $\boldsymbol{A}$ is found, $\boldsymbol{B}$ can be calculated by using (4.26b), or

$$\boldsymbol{B} = -\boldsymbol{A}\boldsymbol{R}. \tag{4.30}$$

Note that with this choice of $\boldsymbol{\Phi}_r$, it follows from (4.27a) and (4.28) that $\boldsymbol{B}$ is symmetric.

3. Now we must approximate the three transfer functions in $\boldsymbol{B}$ with Nth order FIR filters (polynomials as a function of z). This is the critical point in the design. Depending on the properties of $\boldsymbol{B}$ it may be appropriate to use conventional methods from FIR filter design such as window methods or least square fits, or simply an inverse Fourier transform. The resulting $\boldsymbol{B}$ matrix is still symmetric, and returning to the frequency domain we can express it in the form

$$\boldsymbol{B} = -\boldsymbol{\Phi}_l^{\mathrm{T}} \boldsymbol{t}^{-1} \boldsymbol{\rho} \boldsymbol{\Phi}_l. \tag{4.31}$$

The unitary matrix $\boldsymbol{\Phi}_l$ and the real diagonal $\boldsymbol{t}^{-1}\boldsymbol{\rho}$ in the singular value decomposition (4.31) can be found using the method in Appendix 4.D.2. Noting that (4.31) also can be written $\boldsymbol{B} = -\boldsymbol{\Phi}_l^{\mathrm{T}} \sqrt{\boldsymbol{D}} \boldsymbol{t}^{-1} \boldsymbol{\rho} \sqrt{\boldsymbol{D}^*} \boldsymbol{\Phi}_l$ for some diagonal unitary $\boldsymbol{D}$, we calculate $\boldsymbol{A}$ as

$$\boldsymbol{A} = \boldsymbol{\Phi}_l^{\mathrm{T}} \boldsymbol{t}^{-1} \boldsymbol{D} \boldsymbol{\Phi}_l^*. \tag{4.32}$$

The function $\det \boldsymbol{A}$ must satisfy the minimum-phase condition; i.e., $\det(\boldsymbol{t}^{-1}\boldsymbol{D})$ must be minimum phase. The remaining parameter (or function of frequency) in $\boldsymbol{D}$ must be chosen such that $\boldsymbol{A}$ becomes a polynomial. This could be achieved by an iterative approach; however, for our case we let both eigenvalues of $\boldsymbol{A}$ be minimum phase. At least, this is a valid choice for the decoupled example in Section 4.5.2.

4. Finally, we reconstruct the grating having the reflection response $\boldsymbol{R} = -\boldsymbol{A}^{-1}\boldsymbol{B}$ by using the layer-peeling method.

4.5 Numerical examples

4.5.1 Reconstruction

As a first example, we want to verify the reconstruction algorithm presented in Section 4.3. When a fiber grating is written in a birefringent fiber, both the coupling coefficient profile ($\boldsymbol{\rho}_j$) and the phase delay ($\boldsymbol{\Phi}_j$) may be polarization dependent. We simulate a grating in a fiber with intrinsic birefringence $B_{\mathrm{i}} = \Delta n^{(s)}_{\mathrm{dc,i}} - \Delta n^{(f)}_{\mathrm{dc,i}} = 1 \cdot 10^{-5}$. The grating has a length of 30 mm and is assumed to be Gaussian apodized with a maximum index-modulation amplitude $n_{\mathrm{ac,max}} = 12 \cdot 10^{-5}$. The apodization of the index modulation is achieved by dithering [54]. We assume a relative difference in polarization-dependent index modulation between the axis of the fiber oriented parallel and orthogonal to the uv-laser beam equal to 8% [43, 44]. The uv-laser beam will also induce birefringence in addition to the intrinsic birefringence of the fiber. If the uv-induced index change in fiber is proportional to the energy density of the exposed uv-light, the dc index change should be independent of the apodization. We therefore assume that the uv-induced birefringence also is constant and equal to the difference in index modulation at maximum modulation amplitude. This gives a uv-induced birefringence equal to $B_{\mathrm{uv}} = 0.08 n_{\mathrm{ac,max}} = 0.96 \cdot 10^{-5}$, and thus almost equal to the intrinsic birefringence of the fiber. The uv-induced birefringence axes are generally not oriented in the same direction as the intrinsic birefringence axes. If one is not careful during production, the grating may by twisted, which results in a varying effective birefringence as a result of the varying angle between the intrinsic birefringence axis and the uv-induced birefringence axis. Assuming that the fiber is twisted one turn during production, the effective birefringence B_{eff} varies along the grating and is at maximum $1.96 \cdot 10^{-5}$ and at minimum $0.04 \cdot 10^{-5}$.

The grating response was calculated by successive calculation of the polynomial coefficients of $\boldsymbol{A}$ and $\boldsymbol{B}$ by using (4.55) in Appendix 4.C.1. The simulated reflection response $\boldsymbol{R}$ from this fiber grating is shown in Fig. 4.2. The R_{12}-component is at maximum 20 %, which indicates that the response from this grating will be strongly polarization-dependent, and that the reflection spectrum do have frequency-dependent eigenaxes. The figure also shows the inner product between the eigenvectors of $\boldsymbol{R}$ as function of frequency. This value is between 0 and 1, where 0 represents orthogonal eigenvectors and 1 represents parallel eigenvectors. The eigenvectors are almost orthogonal within the main band, whereas the inner product even exceeds 0.5 at the band edge, which means that the eigenvectors are closer to being parallel than orthogonal. This illustrates that a birefringent grating response does not in general have orthogonal eigenvectors, i.e. the eigenvector matrices are not always unitary. Eigenvector matrices that are not unitary cannot be associated with birefringence only. This is the reason why we discuss the response by using singular value decomposition and not eigenvalue decomposition. As discussed in Section 4.4, the singular value decomposition shows that any grating response for a given optical frequency can be described by a discrete reflector sandwiched between two retardation sections.

The figure also shows the square of singular value responses of $\boldsymbol{R}$; $\rho^{(1)2}$ and

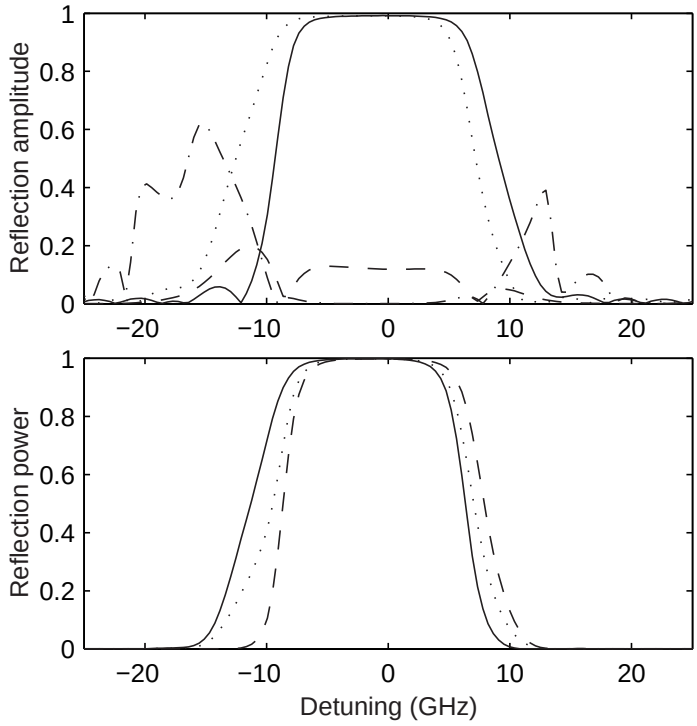

Figure 4.2: Top: Reflection response amplitude $|R_{11}|$ (solid curve), $|R_{12}| = |R_{21}|$ (dashed curve) and $|R_{22}|$ (dotted curve) for grating example 1. Inner product between the eigenvectors of $\boldsymbol{R}$ (dashed-dotted curve). Bottom: Singular values squared of $\boldsymbol{R}$; $\rho^{(1)2}$ (solid curve), $\rho^{(2)2}$ (dashed curve) and $(\rho^{(1)2} + \rho^{(2)2})/2$ (dotted curve).

$\rho^{(2)2}$. A direct measurement of the reflected power from this grating with varying input polarization can be any mixture of these two responses. At the band-edges, the difference in reflected power can vary by up to 60 % depending on input polarization. Variations in reflected power as a function of input polarization is also observed in fiber gratings with intrinsic birefringence but without uv-induced birefringence and polarization-dependent index modulation. However, the singular value $\rho^{(2)2}$ should in that case be a shifted version of $\rho^{(1)2}$, and the eigenvectors should be orthogonal and frequency independent. The asymmetry of the spectrum is due to the varying effective birefringence within the grating. The mean $(\rho^{(1)2} + \rho^{(2)2})/2$ is also shown. This is the expected response when the grating is interrogated with depolarized light.

Fig. 4.3 shows the reconstructed profile with the use of the layer-peeling algorithm described in Section 4.3. The reconstructed index modulation amplitude n_{ac} has a Gaussian profile with a maximum amplitude $12 \cdot 10^{-5}$ in one of the eigenaxes, and $12.96 \cdot 10^{-5}$ in the other. Also shown is the index-modulation amplitude reconstructed from the R_{11}-component using the scalar layer-peeling algorithm[26]. The scalar layer-peeling clearly gives an incorrect reconstruction of the index modulation amplitude. The rotation angle θ_q, which specifies the orientation of the index modulation eigenaxes, varies linearly from 0 to 2π along the fiber length. This agrees with the one turn twist that was assumed to be present during production. The recon-

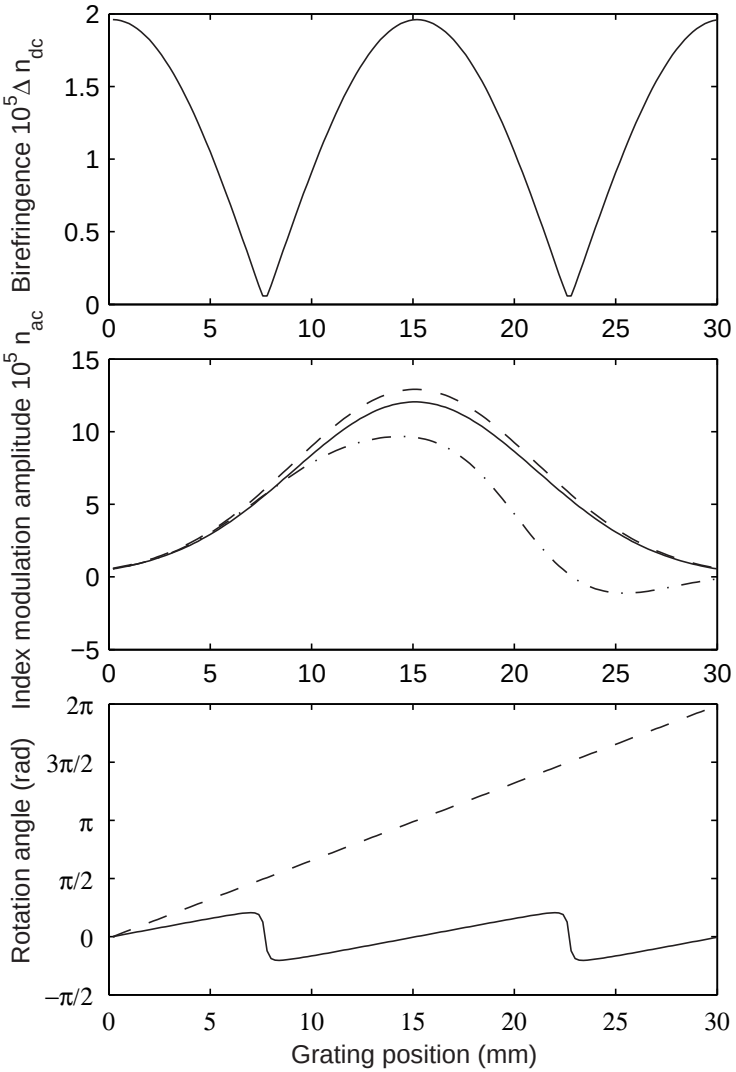

Figure 4.3: Reconstructed spatial profile of grating example 1. Top: Birefringence (the difference in eigenvalue phases of $\mathbf{\Phi}$). Middle: Index modulation amplitudes (from the eigenvalues of $\boldsymbol{q}$) (solid and dashed curves) and the index modulation amplitude calculated with scalar layer-peeling (dashed-dotted curve). Bottom: Rotation angle θ_Φ of $\mathbf{\Phi}$-eigenvectors (solid curve) and θ_q of $\boldsymbol{q}$-eigenvectors (dashed curve).

structed birefringence is periodic with values between $1.96 \cdot 10^{-5}$ and $0.04 \cdot 10^{-5}$, as expected. The rotation angle θ_Φ, which specifies the orientation of the birefringence eigenaxes, varies with grating position. If $\Delta n_{\mathrm{dc,i}} \gg \Delta n_{\mathrm{dc,uv}}$, θ_Φ should be almost constant, whereas if $\Delta n_{\mathrm{dc,i}} \ll \Delta n_{\mathrm{dc,uv}}$, θ_Φ should follow the orientation of the index modulation axes, θ_q. In this case, the intrinsic and the uv-induced birefringence is almost equal, which means that θ_Φ is somewhere between these two regimes. The orientation of the eigenaxes changes rapidly with an angle of $\pi/2$ when the effective birefringence approaches zero, because the fast and the slow birefringence axes have been interchanged. The intrinsic and the uv-induced linear birefringence will in general combine into an effective birefringence that is elliptic. In the layer-peeling algorithm, we associate the circular part of the effective birefringence with the rotation angle of the index modulation. The initial and the reconstructed profile are therefore not directly comparable, since they are not defined in the same coordinate system. The reconstructed index modulation amplitudes are independent of appearance of circular birefringence, and the relative error is in the range of 10^{-13}. We conclude that the reconstruction algorithm described in Section 4.3 can be used to reconstruct the spatial profile of a birefringent grating.

4.5.2 Design

As a second example, we use the design algorithm described in Section 4.4 to design a birefringent fiber grating. We want to design a nondispersive grating that acts as an unpolarized reflector in two 150 GHz wide frequency bands (i.e. $\boldsymbol{R}$ is a scalar times the identity matrix), while it flips the reflected polarization in a 50 GHz wide interleaved band (i.e. only the $R_{12} = R_{21}$-components are different from zero). Fig. 4.4 shows the designed reflection response realized in a 40 mm long grating with maximum reflection amplitude equal to 99 %. The grating has a flat-top response and constant group delay in all grating bands.

Fig. 4.5 shows the spatial profile of the designed grating. Here, the phase delays was not chosen to be in the range 0 to π; the $\boldsymbol{J}$ matrix was instead chosen such that the rotation angles in the bottom plot were constant. The orientation of the eigenaxes of the phase-delays and the index modulation are equal and constant for almost all grating positions. Thus, there is no coupling between the two eigenaxes of the index modulation. Any birefringent grating that is decoupled can be made by using a polarization controller (PC), a polarization beam splitter (PBS) and a polarization-independent grating in each of the two output arms of the PBS as shown in Fig. 4.6. A birefringent grating is decoupled if the reflection spectrum has orthogonal eigenvectors and can be written $\boldsymbol{R} = \boldsymbol{P}\boldsymbol{\rho}\boldsymbol{P}^{\mathrm{T}}$, where $\boldsymbol{P}$ is a frequency-independent rotation matrix, and $\boldsymbol{\rho}$ is a diagonal matrix. Then the polarization controller can produce a rotation of the polarization into the PBS as given by the Jones matrix $\boldsymbol{P}$. The profile of the two gratings can be synthesized from the two diagonal elements of $\boldsymbol{\rho}$.

The grating has rapid quasi-periodic variations in coupling coefficient amplitudes, which is typical for multi-band gratings. For every layer where one of coupling coefficient amplitudes approaches zero, an extra phase delay of $\pi/2$ is added. When

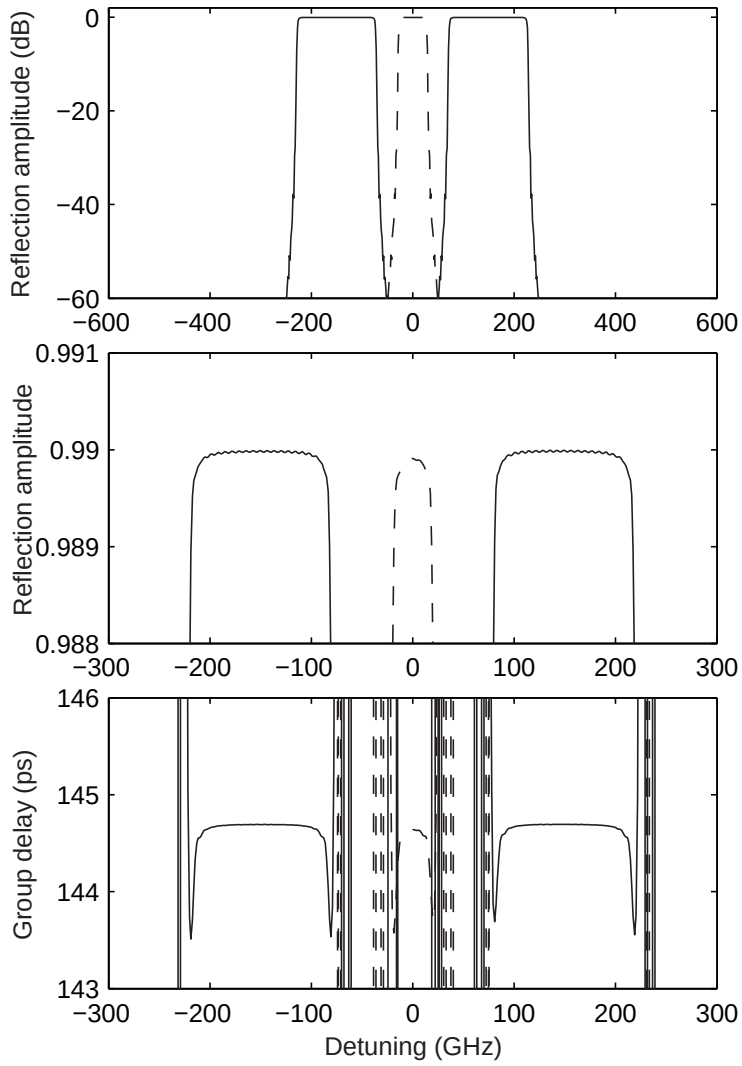

Figure 4.4: Reflection response $R_{11} = R_{22}$ (solid curve) and $R_{12} = R_{21}$ (dashed curve) for grating example 2. Top: Reflection response. Middle: In-band details of reflection response. Bottom: Group delay response.

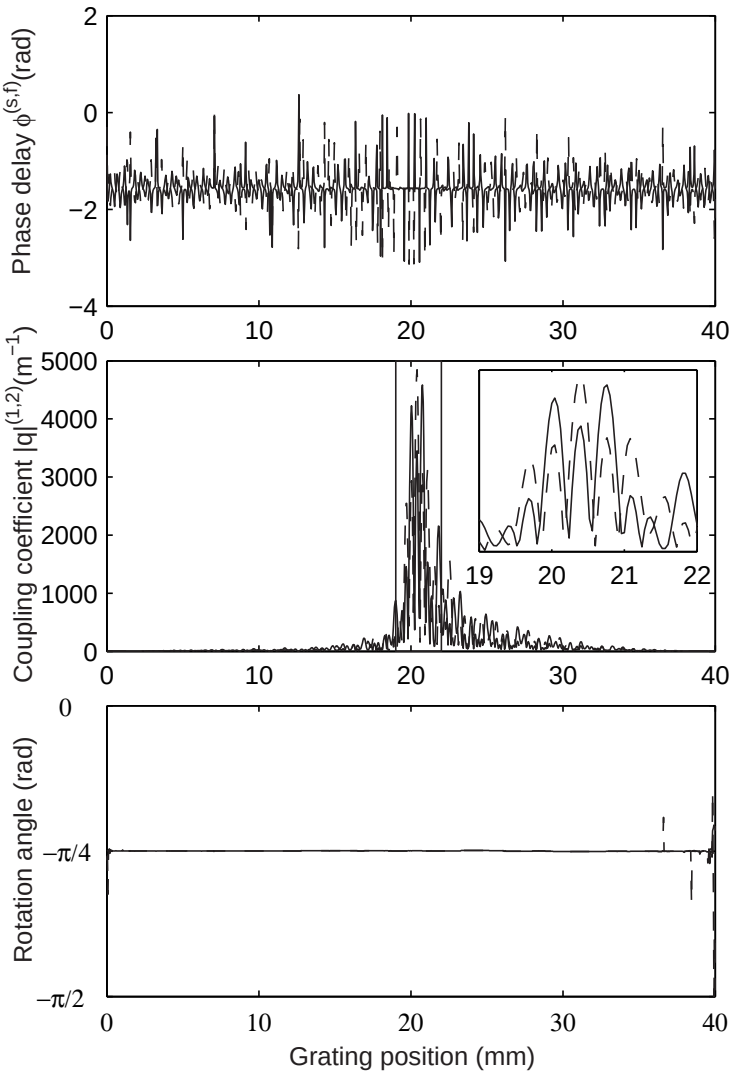

Figure 4.5: Spatial profile of grating example 2. Top: Phase-delays (phase of eigenvalues of $\mathbf{\Phi}$). Middle: Coupling coefficient amplitudes (eigenvalues of $\boldsymbol{q}$). Bottom: Rotation angle of $\mathbf{\Phi}$-eigenvectors (solid curve) and $\boldsymbol{q}$-eigenvectors (dashed curve).

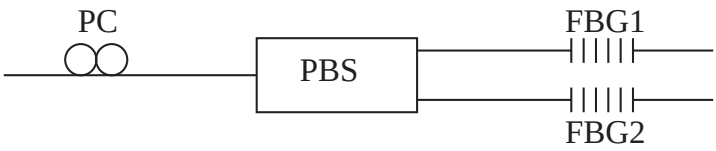

Figure 4.6: An alternative realization of a decoupled grating.

the grating is implemented as in Fig. 4.6, the $\pi/2$-phase delays correspond to π phase-shifts in the associated coupling coefficient that are due to the propagation back and forth through the phase-delay section.

The zeros of the coupling-coefficient amplitudes are not always overlapping, which gives a relative difference in index-modulation amplitude that is almost 100 %. Thus, the grating cannot be realized in a fiber grating, where the difference in index-modulation amplitude is less than 10% [43]. However, differences in index-modulation amplitude up to almost 100 % are observed in grating-assisted waveguides [50], so this grating may be produced in such a waveguide. Alternatively, one can use an iterative approach similar to the method developed for polarization-independent gratings [55], which searches for a realization with difference in index modulation limited to $\sim$10% at the expense of the spectral properties of the grating.

4.6 Conclusion

The discrete layer-peeling algorithm for reconstruction and design of fiber Bragg gratings has been generalized to the full polarization-dependent case of birefringent gratings. Any polarization-dependent index contrast and any linear birefringence in the dc index can be identified from the reflection Jones matrix. Circular birefringence that is reciprocal (optical activity) is equivalent to a reciprocal rotation of the polarization along the fiber, and thus cannot be determined from the reflection matrix. The reconstruction algorithm can be used for polarization-sensitive characterization of fabricated gratings.

The possible (realizable) responses of birefringent gratings have been analyzed in detail. It turns out that for each wavelength, the grating can be represented as a discrete reflector sandwiched between two retardation sections. The realizability conditions have been used as a starting point for designing birefringent gratings. The designed gratings can possibly be implemented by using birefringent fiber gratings in the case with small index-contrast differences, or etched, grating-assisted waveguide structures in the more general case.

Appendices

4.A The relation between scattering matrix and transfer matrix formalism

The coupling between optical modes in a linear device with two ports is described by either scattering matrix formalism or transfer matrix formalism. The scattering matrix formalism is more intuitive and describes the reflection from and transmission through the device. However, with transfer matrix formalism, a linear device consisting of several sub-devices can be described by multiplication of the transfer matrices of the sub-devices. Here, we will discuss the relation between the scattering matrix and the transfer matrix of a two-port device.

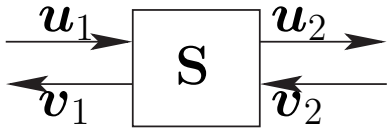

Figure 4.7: Scattering matrix formulation for a linear optical device.

Figure 4.7 shows a two-port linear device described by a scattering matrix $\mathbf{S}$. The optical field matrices $\boldsymbol{u}_1$ and $\boldsymbol{u}_2$ are the optical fields propagating to the right on each side of the device, and the optical field matrices $\boldsymbol{v}_1$ and $\boldsymbol{v}_2$ are the optical fields propagating to the left. Recall that the optical field matrices represent a multiple of optical modes, or more precisely, the columns of a field matrix form a complete, orthogonal set of field vectors. In a special case the optical modes are two orthogonal polarization modes. Then the optical field matrices are 2×2 Jones matrices, and the scattering matrix is 4×4.

The relation between the reflected optical fields $\boldsymbol{v}_1$ and $\boldsymbol{u}_2$ and the incident optical fields $\boldsymbol{u}_1$ and $\boldsymbol{v}_2$ is described by the scattering matrix $\mathbf{S}$,

$$\begin{bmatrix} \boldsymbol{v}_1 \\ \boldsymbol{u}_2 \end{bmatrix} = \mathbf{S} \begin{bmatrix} \boldsymbol{u}_1 \\ \boldsymbol{v}_2 \end{bmatrix} = \begin{bmatrix} \boldsymbol{S}_{11} & \boldsymbol{S}_{12} \\ \boldsymbol{S}_{21} & \boldsymbol{S}_{22} \end{bmatrix} \begin{bmatrix} \boldsymbol{u}_1 \\ \boldsymbol{v}_2 \end{bmatrix}, \tag{4.33}$$

where the block matrices $\boldsymbol{S}_{11}$ and $\boldsymbol{S}_{22}$ describe the reflection from the left and right side of the device, respectively, and $\boldsymbol{S}_{21}$ and $\boldsymbol{S}_{12}$ describe the transmission through the device from the left and right, respectively. These block matrices have the same dimension as the optical field matrices.

The transfer matrix $\mathbf{T}$ relates the optical fields on the left side with the optical fields on the right side of the device,

$$\begin{bmatrix} \boldsymbol{u}_2 \\ \boldsymbol{v}_2 \end{bmatrix} = \mathbf{T} \begin{bmatrix} \boldsymbol{u}_1 \\ \boldsymbol{v}_1 \end{bmatrix} = \begin{bmatrix} \boldsymbol{T}_{11} & \boldsymbol{T}_{12} \\ \boldsymbol{T}_{21} & \boldsymbol{T}_{22} \end{bmatrix} \begin{bmatrix} \boldsymbol{u}_1 \\ \boldsymbol{v}_1 \end{bmatrix}. \tag{4.34}$$

The components of the transfer matrix relates to the components of the scattering

matrix as follows. With $\boldsymbol{u}_1 = 0$,

$$\boldsymbol{v}_1 = \boldsymbol{S}_{12}\boldsymbol{v}_2 \tag{4.35a}$$
$$\boldsymbol{u}_2 = \boldsymbol{S}_{22}\boldsymbol{v}_2 \tag{4.35b}$$
$$\boldsymbol{u}_2 = \boldsymbol{T}_{12}\boldsymbol{v}_1 \tag{4.35c}$$
$$\boldsymbol{v}_2 = \boldsymbol{T}_{22}\boldsymbol{v}_1, \tag{4.35d}$$

which gives $\boldsymbol{T}_{22} = \boldsymbol{S}_{12}^{-1}$ and $\boldsymbol{T}_{12} = \boldsymbol{S}_{22}\boldsymbol{S}_{12}^{-1}$. With $\boldsymbol{v}_1 = 0$,

$$\mathbf{0} = \boldsymbol{S}_{11}\boldsymbol{u}_1 + \boldsymbol{S}_{12}\boldsymbol{v}_2 \tag{4.36a}$$
$$\boldsymbol{u}_2 = \boldsymbol{S}_{21}\boldsymbol{u}_1 + \boldsymbol{S}_{22}\boldsymbol{v}_2 \tag{4.36b}$$
$$\boldsymbol{u}_2 = \boldsymbol{T}_{11}\boldsymbol{u}_1 \tag{4.36c}$$
$$\boldsymbol{v}_2 = \boldsymbol{T}_{21}\boldsymbol{u}_1, \tag{4.36d}$$

which gives $\boldsymbol{T}_{21} = -\boldsymbol{S}_{12}^{-1}\boldsymbol{S}_{11}$ and $\boldsymbol{T}_{11} = \boldsymbol{S}_{21} - \boldsymbol{S}_{22}\boldsymbol{S}_{12}^{-1}\boldsymbol{S}_{11}$. Thus,

$$\mathbf{T} = \begin{bmatrix} \boldsymbol{S}_{21} - \boldsymbol{S}_{22}\boldsymbol{S}_{12}^{-1}\boldsymbol{S}_{11} & \boldsymbol{S}_{22}\boldsymbol{S}_{12}^{-1} \\ -\boldsymbol{S}_{12}^{-1}\boldsymbol{S}_{11} & \boldsymbol{S}_{12}^{-1} \end{bmatrix}. \tag{4.37}$$

For a device to be described with a transfer matrix, $\boldsymbol{S}_{12}$ must be invertible; that is the transmission from the right cannot be zero for any input field vector. Thus, ideal mirrors and ideal polarizers cannot be described by a transfer matrix.

Similarly, the scattering matrix relates to the transfer matrix as follows:

$$\mathbf{S} = \begin{bmatrix} -\boldsymbol{T}_{22}^{-1}\boldsymbol{T}_{21} & \boldsymbol{T}_{22}^{-1} \\ \boldsymbol{T}_{11} - \boldsymbol{T}_{12}\boldsymbol{T}_{22}^{-1}\boldsymbol{T}_{21} & \boldsymbol{T}_{12}\boldsymbol{T}_{22}^{-1} \end{bmatrix}. \tag{4.38}$$

4.B Reciprocity and lossless conditions

If the linear device described by the scattering matrix $\mathbf{S}$ is reciprocal and each block is expressed is expressed in a linear basis, $\mathbf{S}$ must be symmetric ($\mathbf{S} = \mathbf{S}^{\mathrm{T}}$), i.e.,

$$\boldsymbol{S}_{21} = \boldsymbol{S}_{12}^{\mathrm{T}} \tag{4.39a}$$
$$\boldsymbol{S}_{11} = \boldsymbol{S}_{11}^{\mathrm{T}} \tag{4.39b}$$
$$\boldsymbol{S}_{22} = \boldsymbol{S}_{22}^{\mathrm{T}}. \tag{4.39c}$$

In transfer matrix formalism, (4.39) gives

$$\boldsymbol{T}_{11} - \boldsymbol{T}_{12}\boldsymbol{T}_{22}^{-1}\boldsymbol{T}_{21} = \boldsymbol{T}_{22}^{\mathrm{T}-1} \tag{4.40a}$$
$$\boldsymbol{T}_{22}^{-1}\boldsymbol{T}_{21} = \boldsymbol{T}_{21}^{\mathrm{T}}\boldsymbol{T}_{22}^{\mathrm{T}-1} \tag{4.40b}$$
$$\boldsymbol{T}_{12}\boldsymbol{T}_{22}^{-1} = \boldsymbol{T}_{22}^{\mathrm{T}-1}\boldsymbol{T}_{12}^{\mathrm{T}}. \tag{4.40c}$$

Combining (4.40a) and (4.40b) leads to

$$\boldsymbol{T}_{11}\boldsymbol{T}_{22}^{\mathrm{T}} - \boldsymbol{T}_{12}\boldsymbol{T}_{21}^{\mathrm{T}} = \boldsymbol{T}_{22}\boldsymbol{T}_{11}^{\mathrm{T}} - \boldsymbol{T}_{21}\boldsymbol{T}_{12}^{\mathrm{T}} = \boldsymbol{I}, \tag{4.41a}$$

while combining (4.40a) and (4.40c) yields

$$\boldsymbol{T}_{22}^{\mathrm{T}}\boldsymbol{T}_{11} - \boldsymbol{T}_{12}^{\mathrm{T}}\boldsymbol{T}_{21} = \boldsymbol{T}_{11}^{\mathrm{T}}\boldsymbol{T}_{22} - \boldsymbol{T}_{21}^{\mathrm{T}}\boldsymbol{T}_{12} = \boldsymbol{I}. \tag{4.41b}$$

(4.40b) and (4.40c) can be simplified to

$$\boldsymbol{T}_{22}\boldsymbol{T}_{21}^{\mathrm{T}} - \boldsymbol{T}_{21}\boldsymbol{T}_{22}^{\mathrm{T}} = \mathbf{0} \tag{4.41c}$$
$$\boldsymbol{T}_{22}^{\mathrm{T}}\boldsymbol{T}_{12} - \boldsymbol{T}_{12}^{\mathrm{T}}\boldsymbol{T}_{22} = \mathbf{0}. \tag{4.41d}$$

Additional limitations are forced on the scattering matrix and the transfer matrix if the device is lossless. For a lossless device, the total incident power must be equal to the total emitted power. In scattering matrix formalism, this is expressed as $\mathbf{S}^{\dagger}\mathbf{S} = \mathbf{I}$. Thus,

$$\boldsymbol{S}_{11}^{\dagger}\boldsymbol{S}_{11} + \boldsymbol{S}_{21}^{\dagger}\boldsymbol{S}_{21} = \boldsymbol{I} \tag{4.42a}$$
$$\boldsymbol{S}_{12}^{\dagger}\boldsymbol{S}_{12} + \boldsymbol{S}_{22}^{\dagger}\boldsymbol{S}_{22} = \boldsymbol{I} \tag{4.42b}$$
$$\boldsymbol{S}_{12}^{\dagger}\boldsymbol{S}_{11} + \boldsymbol{S}_{22}^{\dagger}\boldsymbol{S}_{21} = \mathbf{0}. \tag{4.42c}$$

Using (4.37) and the reciprocity relations (4.41), (4.42) can be expressed in transfer matrix formalism as

$$\boldsymbol{T}_{22}\boldsymbol{T}_{22}^{\dagger} - \boldsymbol{T}_{21}\boldsymbol{T}_{21}^{\dagger} = \boldsymbol{I} \tag{4.43a}$$
$$\boldsymbol{T}_{22}^{\dagger}\boldsymbol{T}_{22} - \boldsymbol{T}_{12}^{\dagger}\boldsymbol{T}_{12} = \boldsymbol{I} \tag{4.43b}$$
$$\boldsymbol{T}_{22}\boldsymbol{T}_{21}^{\mathrm{T}} - \boldsymbol{T}_{12}^{*}\boldsymbol{T}_{22}^{\mathrm{T}} = \mathbf{0}. \tag{4.43c}$$

Comparing (4.43c) with (4.41c) gives $\boldsymbol{T}_{12}^{*}\boldsymbol{T}_{22}^{\mathrm{T}} = \boldsymbol{T}_{21}\boldsymbol{T}_{22}^{\mathrm{T}}$; thus $\boldsymbol{T}_{12} = \boldsymbol{T}_{21}^{*}$. So (4.41a) can be written $\boldsymbol{T}_{22}\boldsymbol{T}_{11}^{\mathrm{T}} - \boldsymbol{T}_{21}\boldsymbol{T}_{21}^{\dagger} = \boldsymbol{I}$. Comparing this result with (4.43a) gives that $\boldsymbol{T}_{11} = \boldsymbol{T}_{22}^{*}$. Thus, provided that the matrix describing the transmission from the right is nonsingular, any reciprocal lossless two-port device can be described by a transfer matrix on the form

$$\mathbf{T} = \begin{bmatrix} \boldsymbol{A}^{*} & \boldsymbol{B}^{*} \\ \boldsymbol{B} & \boldsymbol{A} \end{bmatrix}, \tag{4.44}$$

where the block matrices $\boldsymbol{A}$ and $\boldsymbol{B}$ satisfy

$$\boldsymbol{A}\boldsymbol{A}^{\dagger} - \boldsymbol{B}\boldsymbol{B}^{\dagger} = \boldsymbol{I} \tag{4.45a}$$
$$\boldsymbol{A}\boldsymbol{B}^{\mathrm{T}} - \boldsymbol{B}\boldsymbol{A}^{\mathrm{T}} = \mathbf{0} \tag{4.45b}$$
$$\boldsymbol{A}^{\mathrm{T}}\boldsymbol{B}^{*} - \boldsymbol{B}^{\dagger}\boldsymbol{A} = \mathbf{0}. \tag{4.45c}$$

To facilitate the interpretation of (4.45) we introduce the singular value decompositions of $\boldsymbol{A}$ and $\boldsymbol{B}$. In the following, we will for simplicity assume that the $\boldsymbol{A}$ and $\boldsymbol{B}$ matrices have the dimension 2×2.

$$\boldsymbol{A} = \boldsymbol{U}_{\boldsymbol{A}}\boldsymbol{\Sigma}_{\boldsymbol{A}}\boldsymbol{V}_{\boldsymbol{A}} \tag{4.46a}$$
$$\boldsymbol{B} = \boldsymbol{U}_{\boldsymbol{B}}\boldsymbol{\Sigma}_{\boldsymbol{B}}\boldsymbol{V}_{\boldsymbol{B}}, \tag{4.46b}$$

In (4.46), $\boldsymbol{U_A}$, $\boldsymbol{U_B}$, $\boldsymbol{V_A}$ and $\boldsymbol{V_B}$ are unitary matrices, and $\boldsymbol{\Sigma_A}$ and $\boldsymbol{\Sigma_B}$ are real and non-negative diagonal matrices. Equation (4.43b) (or a combination of the three equations in (4.45) gives $\boldsymbol{A}^\dagger\boldsymbol{A} - \boldsymbol{B}^{\mathrm{T}}\boldsymbol{B}^* = \boldsymbol{I}$, leading to

$$\boldsymbol{V}_{\boldsymbol{A}}^\dagger\boldsymbol{\Sigma}_{\boldsymbol{A}}^2\boldsymbol{V_A} - \boldsymbol{V}_{\boldsymbol{B}}^{\mathrm{T}}\boldsymbol{\Sigma}_{\boldsymbol{B}}^2\boldsymbol{V}_{\boldsymbol{B}}^* = \boldsymbol{I}. \tag{4.47}$$

From (4.47) it follows that

$$\boldsymbol{\Sigma_A} = \boldsymbol{V_A}\boldsymbol{V}_{\boldsymbol{B}}^{\mathrm{T}}(\boldsymbol{I} + \boldsymbol{\Sigma}_{\boldsymbol{B}}^2)^{1/2}\boldsymbol{V}_{\boldsymbol{B}}^*\boldsymbol{V}_{\boldsymbol{A}}^\dagger, \tag{4.48}$$

and with the help of (4.46a) we obtain

$$\boldsymbol{A} = \boldsymbol{U_A}\boldsymbol{V_A}\boldsymbol{V}_{\boldsymbol{B}}^{\mathrm{T}}(\boldsymbol{I} + \boldsymbol{\Sigma}_{\boldsymbol{B}}^2)^{1/2}\boldsymbol{V}_{\boldsymbol{B}}^*. \tag{4.49}$$

Eq. (4.49) represents a new singular value decomposition of $\boldsymbol{A}$. Substituting (4.49) and (4.46b) into (4.45a) leads to the commutator relation

$$\boldsymbol{D}^2\boldsymbol{\Sigma}_{\boldsymbol{B}}^2 = \boldsymbol{\Sigma}_{\boldsymbol{B}}^2\boldsymbol{D}^2, \tag{4.50}$$

where $\boldsymbol{D}^2 \equiv \boldsymbol{U}_{\boldsymbol{B}}^\dagger\boldsymbol{U_A}\boldsymbol{V_A}\boldsymbol{V}_{\boldsymbol{B}}^{\mathrm{T}}$ is unitary. If the two singular values of $\boldsymbol{B}$ (i.e. the elements of $\boldsymbol{\Sigma_B}$) are different, the only solution to (4.50) is that $\boldsymbol{D}^2$ is diagonal. By (4.49) this means that $\boldsymbol{A} = \boldsymbol{U_B}\boldsymbol{D}(\boldsymbol{I}+\boldsymbol{\Sigma}_{\boldsymbol{B}}^2)^{1/2}\boldsymbol{D}\boldsymbol{V}_{\boldsymbol{B}}^*$. We also have $\boldsymbol{B} = \boldsymbol{U_B}\boldsymbol{\Sigma_B}\boldsymbol{V_B}$, so we can write

$$\boldsymbol{A} = \boldsymbol{\Phi}_r^*\boldsymbol{t}^{-1}\boldsymbol{\Phi}_l^* \tag{4.51a}$$

$$\boldsymbol{B} = -\boldsymbol{\Phi}_r^*\boldsymbol{t}^{-1}\boldsymbol{\rho}\boldsymbol{\Phi}_l, \tag{4.51b}$$

where $\boldsymbol{\Phi}_r \equiv i\boldsymbol{U}_{\boldsymbol{B}}^*\boldsymbol{D}^*$ and $\boldsymbol{\Phi}_l \equiv -i\boldsymbol{D}^*\boldsymbol{V_B}$ are unitary matrices, and $\boldsymbol{\rho} \equiv (\boldsymbol{I} + \boldsymbol{\Sigma}_{\boldsymbol{B}}^2)^{-1/2}\boldsymbol{\Sigma_B}$ and $\boldsymbol{t} \equiv (\boldsymbol{I} + \boldsymbol{\Sigma}_B^2)^{-1/2} = (\boldsymbol{I} - \boldsymbol{\rho}^2)^{1/2}$. In the case where the singular values of $\boldsymbol{B}$ are equal, we can with no loss of generality set $\boldsymbol{V_B} = \boldsymbol{V_A} = \boldsymbol{I}$. By substituting into (4.45b), we find $\boldsymbol{U_A}\boldsymbol{U}_{\boldsymbol{B}}^{\mathrm{T}} = \boldsymbol{U_B}\boldsymbol{U}_{\boldsymbol{A}}^{\mathrm{T}}$ which implies that $\boldsymbol{U}_{\boldsymbol{A}}^{-1}\boldsymbol{U_B}$ is symmetric. Any symmetric, unitary matrix can be written on the form $\boldsymbol{\Phi}_l^{\mathrm{T}}\boldsymbol{\Phi}_l$, where $\boldsymbol{\Phi}_l$ is unitary, see Appendix 4.D.2. Thus we can represent $-\boldsymbol{U}_{\boldsymbol{A}}^{-1}\boldsymbol{U_B} = \boldsymbol{\Phi}_l^{\mathrm{T}}\boldsymbol{\Phi}_l$ and $\boldsymbol{U_A} = \boldsymbol{\Phi}_r^*\boldsymbol{\Phi}_l^*$, where $\boldsymbol{\Phi}_r$ is unitary, yielding (4.51).

We conclude that the lossless and reciprocity conditions (4.45) are satisfied if and only if the matrices $\boldsymbol{A}$ and $\boldsymbol{B}$ can be written in the form of (4.51), with $\boldsymbol{\Phi}_r$ and $\boldsymbol{\Phi}_l$ unitary, and $\boldsymbol{\rho}$ diagonal and nonnegative satisfying $\|\boldsymbol{\rho}\| < 1$ (and $\boldsymbol{t} = (\boldsymbol{I} - \boldsymbol{\rho}^2)^{1/2}$). According to (4.38), the associated reflection matrices can be expressed as $\boldsymbol{S}_{11} = \boldsymbol{\Phi}_l^{\mathrm{T}}\boldsymbol{\rho}\boldsymbol{\Phi}_l$ (from the left), and $\boldsymbol{S}_{22} = \boldsymbol{\Phi}_r(-\boldsymbol{\rho})\boldsymbol{\Phi}_r^{\mathrm{T}}$ (from the right), and the transmission from the left to the right is $\boldsymbol{S}_{21} = \boldsymbol{S}_{12}^{\mathrm{T}} = \boldsymbol{\Phi}_r\boldsymbol{t}\boldsymbol{\Phi}_l$. Hence, the interpretation of (4.51) is a discrete reflector $\boldsymbol{\rho}$ sandwiched between two retardation sections $\boldsymbol{\Phi}_l$ and $\boldsymbol{\Phi}_r$.

4.C Proof of the realizability conditions

Here we will prove that an overall transfer matrix (filter response) is realizable as a discrete, birefringent grating if and only if it can be written in the form of (4.22)-(4.23) and satisfies (4.24)-(4.25). For clarity in the proof, it turns out that it is convenient to rename the layers so that layer 0 becomes layer N, layer 1 becomes layer $N-1$, etc.

4.C.1 Necessity

The entire grating has the response

$$\mathbf{M}_N = \mathbf{T}_0\mathbf{T}_1\cdots\mathbf{T}_{N-1}\mathbf{T}_N, \tag{4.52}$$

where the transfer matrices $\mathbf{T}_j$ are given by

$$\mathbf{T}_j = \begin{bmatrix} z^{-1/2}\boldsymbol{t}_j^{-1}\boldsymbol{\Phi}_j & -z^{-1/2}\boldsymbol{t}_j^{-1}\boldsymbol{\rho}_j\boldsymbol{\Phi}_j^* \\ -z^{1/2}\boldsymbol{t}_j^{-1}\boldsymbol{\rho}_j\boldsymbol{\Phi}_j & z^{1/2}\boldsymbol{t}_j^{-1}\boldsymbol{\Phi}_j^* \end{bmatrix}, \tag{4.53}$$

for $1 \le j \le N$, and

$$\mathbf{T}_0 = \begin{bmatrix} \boldsymbol{\Phi}\boldsymbol{t}_0^{-1}\boldsymbol{\Phi}_0 & -\boldsymbol{\Phi}\boldsymbol{t}_0^{-1}\boldsymbol{\rho}_0\boldsymbol{\Phi}_0^* \\ -\boldsymbol{\Phi}^*\boldsymbol{t}_0^{-1}\boldsymbol{\rho}_0\boldsymbol{\Phi}_0 & \boldsymbol{\Phi}^*\boldsymbol{t}_0^{-1}\boldsymbol{\Phi}_0^* \end{bmatrix}. \tag{4.54}$$

The local reflection matrices $\boldsymbol{\rho}_j$ are real and symmetric, and satisfy $\|\boldsymbol{\rho}_j\| < 1$. The local transmission matrices are defined as $\boldsymbol{t}_j = (\boldsymbol{I} - \boldsymbol{\rho}_j^2)^{1/2}$. The retardation matrices $\boldsymbol{\Phi}_j$ and $\boldsymbol{\Phi}$ are unitary.

It is clear that the overall grating is lossless and satisfies the reciprocity conditions. From Appendix 4.B we therefore find that form (4.22) and relations (4.24) are valid for real frequencies, i.e., on the unit circle $|z| = 1$. In general, the necessity of (4.22)-(4.25) can be proved by induction. Notice that the transfer matrices of time delay sections, retardation sections and discrete reflectors all can be written in the form of (4.22) and satisfies (4.24). It is straightforward to prove that if two matrices in the form of (4.22) both satisfy (4.24), then the product also is in the form of (4.22) and satisfies (4.24). It is therefore clear that the overall matrix in (4.52) can be written in the form of (4.22) and satisfies (4.24).

It remains to prove (4.23) and (4.25). We observe that the elements in $\mathbf{M}_0 = \mathbf{T}_0$ are in the form of (4.23) for $N = 0$, and that the determinant of the (2,2)-entry of $\mathbf{M}_0$ has no zeros and thus satisfies (4.25). Assuming that $\mathbf{M}_N$ (as given by (4.22) satisfies (4.23)-(4.25), we must now prove that the elements of $\mathbf{M}_{N+1} = \mathbf{M}_N\mathbf{T}_{N+1}$ satisfy (4.23) and (4.25). We find that

$$\mathbf{M}_{N+1} = \begin{bmatrix} z^{-1/2}\boldsymbol{A}_*\boldsymbol{t}^{-1}\boldsymbol{\Phi} - z^{1/2}\boldsymbol{B}_*\boldsymbol{t}^{-1}\boldsymbol{\rho}\boldsymbol{\Phi} & -z^{-1/2}\boldsymbol{A}_*\boldsymbol{t}^{-1}\boldsymbol{\rho}\boldsymbol{\Phi}^* + z^{1/2}\boldsymbol{B}_*\boldsymbol{t}^{-1}\boldsymbol{\Phi}^* \\ -z^{1/2}\boldsymbol{A}\boldsymbol{t}^{-1}\boldsymbol{\rho}\boldsymbol{\Phi} + z^{-1/2}\boldsymbol{B}\boldsymbol{t}^{-1}\boldsymbol{\Phi} & z^{1/2}\boldsymbol{A}\boldsymbol{t}^{-1}\boldsymbol{\Phi}^* - z^{-1/2}\boldsymbol{B}\boldsymbol{t}^{-1}\boldsymbol{\rho}\boldsymbol{\Phi}^* \end{bmatrix}. \tag{4.55}$$

For simplicity, we have suppressed the subscript index of $\boldsymbol{t}_{N+1}$, $\boldsymbol{\rho}_{N+1}$ and $\boldsymbol{\Phi}_{N+1}$. It is now clear that the elements in the new matrix $\mathbf{M}_{N+1}$ are $(N+1)$th order polynomials in the form of (4.23). Physically, (4.25) must be satisfied for the $N+1$ layer structure, since the inverse of the matrix polynomial in the (2,2)-entry of $\mathbf{M}_{N+1}$ is the transmission response from the right, and therefore has to exist, be causal and stable. Rigorously, the property can be proven by induction by considering the (2,2)-entry of (4.55):

$$z^{1/2}\boldsymbol{A}\boldsymbol{t}^{-1}\boldsymbol{\Phi}^* - z^{-1/2}\boldsymbol{B}\boldsymbol{t}^{-1}\boldsymbol{\rho}\boldsymbol{\Phi}^* = z^{1/2}\boldsymbol{A}(\boldsymbol{I} - z^{-1}\boldsymbol{A}^{-1}\boldsymbol{B}\boldsymbol{\rho})\boldsymbol{t}^{-1}\boldsymbol{\Phi}^*. \tag{4.56}$$

Define $\boldsymbol{R} = -\boldsymbol{A}^{-1}\boldsymbol{B}$ (physically, this is the reflection response from the left). From (4.24a) we obtain on the unit circle $\boldsymbol{R}\boldsymbol{R}^\dagger + \boldsymbol{A}^{-1}\boldsymbol{A}^{-1\dagger} = \boldsymbol{I}$ and therefore $\|\boldsymbol{R}\| < 1$.

Now, let the matrix $\boldsymbol{R} = \boldsymbol{R}(z)$ act on a constant vector $\boldsymbol{v}$ of unit norm. By writing out the product in an obvious notation we obtain $\|\boldsymbol{R}(z)\boldsymbol{v}\|^2 = |R_{11}(z)v_1 + R_{12}(z)v_2|^2 + |R_{21}(z)v_1 + R_{22}(z)v_2|^2$. Since the elements of $\boldsymbol{R}(z)$ are analytic outside the unit circle, the real-valued function $\|\boldsymbol{R}(z)\boldsymbol{v}\|$ is a subharmonic function of z [38]. Thus the maximum principle states that $\|\boldsymbol{R}(z)\boldsymbol{v}\|$ takes its maximum on the unit circle. We have already argued that this maximum is less than 1, so for $|z| \geq 1$ we obtain $\|z^{-1}\boldsymbol{A}^{-1}\boldsymbol{B}\boldsymbol{\rho}\| \leq |z^{-1}|\|\boldsymbol{R}\|\|\boldsymbol{\rho}\| < 1$, and as a result $\boldsymbol{I} - z^{-1}\boldsymbol{A}^{-1}\boldsymbol{B}\boldsymbol{\rho}$ is nonsingular on and outside the unit circle.

4.C.2 Sufficiency

To prove that (4.22)-(4.25) are sufficient for realizability, we will show by induction that the total transfer matrix (4.22) can be factorized into $N+1$ "unit cell" matrices as in (4.52).

For $N = 0$ the factorization is trivial, and we must show that any matrix $\mathbf{M}_0$ given by (4.22)-(4.25) can be expressed in the form of (4.54). In this case the $\boldsymbol{A}$ and $\boldsymbol{B}$ matrices are independent of z, and $\boldsymbol{A}_* = \boldsymbol{A}^*$, $\boldsymbol{B}_* = \boldsymbol{B}^*$. Thus (4.24) reduces to (4.45). From the discussion following (4.45), we can express $\mathbf{M}_0$ in the form of (4.54) with a real, symmetric $\boldsymbol{\rho}_0$ satisfying $\|\boldsymbol{\rho}_0\| < 1$.

To proceed, assume $N \geq 1$. Defining $\mathbf{M}_{N-1} \equiv \mathbf{M}_N\mathbf{T}_N^{-1}$, we obtain with the help of

$$\mathbf{T}_N^{-1} = \begin{bmatrix} z^{1/2}\boldsymbol{\Phi}_N^\dagger\boldsymbol{t}_N^{-1} & z^{-1/2}\boldsymbol{\Phi}_N^\dagger\boldsymbol{t}_N^{-1}\boldsymbol{\rho}_N \\ z^{1/2}\boldsymbol{\Phi}_N^{\mathrm{T}}\boldsymbol{t}_N^{-1}\boldsymbol{\rho}_N & z^{-1/2}\boldsymbol{\Phi}_N^{\mathrm{T}}\boldsymbol{t}_N^{-1} \end{bmatrix} \tag{4.57}$$

that

$$\mathbf{M}_{N-1} = \begin{bmatrix} z^{1/2}(\boldsymbol{A}_* + \boldsymbol{B}_*\boldsymbol{\Phi}_N^{\mathrm{T}}\boldsymbol{\rho}_N\boldsymbol{\Phi}_N)\boldsymbol{\Phi}_N^\dagger\boldsymbol{t}_N^{-1} & z^{-1/2}(\boldsymbol{B}_* + \boldsymbol{A}_*\boldsymbol{\Phi}_N^\dagger\boldsymbol{\rho}_N\boldsymbol{\Phi}_N^*)\boldsymbol{\Phi}_N^{\mathrm{T}}\boldsymbol{t}_N^{-1} \\ z^{1/2}(\boldsymbol{B} + \boldsymbol{A}\boldsymbol{\Phi}_N^{\mathrm{T}}\boldsymbol{\rho}_N\boldsymbol{\Phi}_N)\boldsymbol{\Phi}_N^\dagger\boldsymbol{t}_N^{-1} & z^{-1/2}(\boldsymbol{A} + \boldsymbol{B}\boldsymbol{\Phi}_N^\dagger\boldsymbol{\rho}_N\boldsymbol{\Phi}_N^*)\boldsymbol{\Phi}_N^{\mathrm{T}}\boldsymbol{t}_N^{-1} \end{bmatrix}. \tag{4.58}$$

Substituting (4.23) into (4.58) makes it straightforward to show that $\mathbf{M}_{N-1}$ can be written in the form of (4.22), where the entries have been reduced to $(N-1)$th order polynomials, provided we choose that $\boldsymbol{\rho}_N$ so that

$$\boldsymbol{b}(0) + \boldsymbol{a}(0)\boldsymbol{\Phi}_N^{\mathrm{T}}\boldsymbol{\rho}_N\boldsymbol{\Phi}_N = \boldsymbol{a}(N) + \boldsymbol{b}(N)\boldsymbol{\Phi}_N^\dagger\boldsymbol{\rho}_N\boldsymbol{\Phi}_N^* = \mathbf{0}. \tag{4.59}$$

Noting that $\boldsymbol{a}(0)$ is invertible, we find that (4.59) can be fulfilled only if we choose

$$\boldsymbol{\Phi}_N^{\mathrm{T}}\boldsymbol{\rho}_N\boldsymbol{\Phi}_N = -\boldsymbol{a}(0)^{-1}\boldsymbol{b}(0), \tag{4.60}$$

and if

$$\boldsymbol{a}(N) - \boldsymbol{b}(N)\boldsymbol{a}^*(0)^{-1}\boldsymbol{b}^*(0) = \mathbf{0}. \tag{4.61}$$

By substituting (4.23) into (4.24a) and (4.24b) and considering the highest power of z, we obtain $\boldsymbol{a}(0)\boldsymbol{a}(N)^\dagger = \boldsymbol{b}(0)\boldsymbol{b}(N)^\dagger$ and $\boldsymbol{a}(0)\boldsymbol{b}(0)^{\mathrm{T}} = \boldsymbol{b}(0)\boldsymbol{a}(0)^{\mathrm{T}}$, ensuring that (4.61) is satisfied.

Before we can show that conditions (4.24)-(4.25) are valid for the reduced system, we must prove that $\|\boldsymbol{\rho}_N\| < 1$ and that $\boldsymbol{\rho}_N$ can be chosen real and symmetric. Define

$\boldsymbol{R}(z) = -\boldsymbol{A}^{-1}(z)\boldsymbol{B}(z)$. Since $\boldsymbol{A}(z)$ is nonsingular on and outside the unit circle of the z-plane, it is clear that $\boldsymbol{R}(z)$ can be written as a power series:

$$\boldsymbol{R}(z) \equiv -\left(\sum_{k=0}^{N} \boldsymbol{a}(k) z^{-k}\right)^{-1} \left(\sum_{k=0}^{N} \boldsymbol{b}(k) z^{-k}\right) = \sum_{k=0}^{\infty} \boldsymbol{h}(k) z^{-k}. \tag{4.62}$$

Letting $z \to \infty$ we find that $\boldsymbol{h}(0) = -\boldsymbol{a}(0)^{-1}\boldsymbol{b}(0)$, and with the help of (4.60)

$$\|\boldsymbol{\rho}_N\| = \|\boldsymbol{a}(0)^{-1}\boldsymbol{b}(0)\| = \|\boldsymbol{h}(0)\| = \left\| \frac{1}{2\pi} \int_{-\pi}^{\pi} \boldsymbol{R}(e^{i\theta}) \mathrm{d}\theta \right\| \leq \frac{1}{2\pi} \int_{-\pi}^{\pi} \|\boldsymbol{R}(e^{i\theta})\| \mathrm{d}\theta. \tag{4.63}$$

The norm $\|\boldsymbol{R}(z)\|$ is less than 1 on the unit circle according to (4.24), and we can therefore conclude that $\|\boldsymbol{\rho}_N\| < 1$.

Letting $z \to \infty$ in (4.24b) gives that $\boldsymbol{h}(0)$ is symmetric. The matrix $\boldsymbol{h}(0)$ can therefore be represented by $\boldsymbol{U}^T\boldsymbol{\Lambda}\boldsymbol{U}$ by using singular value decomposition, where $\boldsymbol{U}$ is a unitary matrix and $\boldsymbol{\Lambda}$ is a diagonal matrix with real nonnegative components (see Appendix 4.D.2). Any unitary 2×2 matrix $\boldsymbol{U}$ can be represented by a product $\boldsymbol{U} = \boldsymbol{P}\boldsymbol{Q}$, where $\boldsymbol{P}$ is a unitary matrix with real entries (orthonormal matrix) so that $\boldsymbol{P}^\dagger = \boldsymbol{P}^{\mathrm{T}} = \boldsymbol{P}^{-1}$ and $\boldsymbol{Q}$ is symmetric unitary matrix ($\boldsymbol{Q}^T = \boldsymbol{Q}$), see Appendix 4.D.3. This gives

$$\boldsymbol{h}(0) = -\boldsymbol{a}(0)^{-1}\boldsymbol{b}(0) = \boldsymbol{Q}\boldsymbol{P}^T\boldsymbol{\Lambda}\boldsymbol{P}\boldsymbol{Q}, \tag{4.64}$$

Thus, by comparing (4.64) and (4.60), $\boldsymbol{\Phi}_N$ we can choose to be symmetric and equal to $\boldsymbol{Q}$ and $\boldsymbol{\rho}_N = \boldsymbol{P}^T\boldsymbol{\Lambda}\boldsymbol{P}$. It follows that $\boldsymbol{\rho}_N$ is real and symmetric.

Returning to the reduced transfer matrix in (4.58), we can now realize that $\mathbf{T}_N^{-1}$ is in the form of (4.22), and that (4.24) is valid for its entries, so that (4.24) is also valid for the reduced matrix $\mathbf{M}_{N-1}$. Finally, it is possible to prove that the reduced $\boldsymbol{A}(z)$ matrix is nonsingular on and outside the unit circle with use of the maximum principle. Since all conditions (4.22)-(4.25) remain valid for the reduced system, we can continue the process until we have reached the 0th layer.

4.D Some 2×2 matrix properties

4.D.1 Spectral decomposition of symmetrical normal matrices

A matrix is said to be normal if and only if the eigenvectors are orthonormal. Thus, any normal matrix $\boldsymbol{N}$ can be decomposed by using spectral decomposition,

$$\boldsymbol{N} = \boldsymbol{U}\boldsymbol{\Lambda}\boldsymbol{U}^\dagger, \tag{4.65}$$

where $\boldsymbol{\Lambda}$ is diagonal and $\boldsymbol{U}$ is unitary. We first assume that the eigenvalues of $\boldsymbol{N}$ (the elements of $\boldsymbol{\Lambda}$) are different. Since $\boldsymbol{N}$ is symmetric,

$$\boldsymbol{U}\boldsymbol{\Lambda}\boldsymbol{U}^\dagger = \boldsymbol{U}^*\boldsymbol{\Lambda}\boldsymbol{U}^{\mathrm{T}}, \tag{4.66}$$

which leads to

$$\boldsymbol{U}^{\mathrm{T}}\boldsymbol{U}\boldsymbol{\Lambda} = \boldsymbol{\Lambda}\boldsymbol{U}^{\mathrm{T}}\boldsymbol{U}. \tag{4.67}$$

Since $\boldsymbol{U}^{\mathrm{T}}\boldsymbol{U}$ commutes with $\boldsymbol{\Lambda}$, $\boldsymbol{U}^{\mathrm{T}}\boldsymbol{U} = \boldsymbol{D}$ where $\boldsymbol{D}$ is a unitary diagonal matrix. This gives $\boldsymbol{U}\sqrt{\boldsymbol{D}^*} = \boldsymbol{U}^*\sqrt{\boldsymbol{D}}$, so $\boldsymbol{P} \equiv \boldsymbol{U}\sqrt{\boldsymbol{D}^*}$ is real. It is straightforward to realize that

$$\boldsymbol{N} = \boldsymbol{P}\boldsymbol{\Lambda}\boldsymbol{P}^{\mathrm{T}}, \tag{4.68}$$

so $\boldsymbol{P}$ is a real unitary eigenvector matrix. If the eigenvalues are equal, $\boldsymbol{N}$ is diagonal in any basis, and $\boldsymbol{U}$ can be chosen to be some real unitary $\boldsymbol{P}$. Thus, the orthogonal eigenvectors of any symmetrical normal matrix $\boldsymbol{N}$ can be assumed real. With no loss of generality, we can assume $\det \boldsymbol{P} = 1$.

4.D.2 Singular value decomposition of symmetrical matrices

We are interested in the most general form of an arbitrary, complex, symmetric matrix $\boldsymbol{\Upsilon}$. By using singular value decomposition, we can write

$$\boldsymbol{\Upsilon} = \boldsymbol{V}_1\boldsymbol{\Sigma}\boldsymbol{V}_2, \tag{4.69}$$

where $\boldsymbol{V}_{1,2}$ are unitary, and $\boldsymbol{\Sigma}$ is diagonal and nonnegative. Since $\boldsymbol{\Upsilon}$ is symmetric, we find that $(\boldsymbol{\Upsilon}\boldsymbol{\Upsilon}^\dagger)^{\mathrm{T}} = \boldsymbol{\Upsilon}^\dagger\boldsymbol{\Upsilon}$, and therefore

$$\boldsymbol{W}\boldsymbol{\Sigma}^2 = \boldsymbol{\Sigma}^2\boldsymbol{W}, \tag{4.70}$$

where $\boldsymbol{W} \equiv \boldsymbol{V}_2^*\boldsymbol{V}_1$. Since $\boldsymbol{W}$ and $\boldsymbol{\Sigma}^2$ commute, they can be diagonalized in the same basis, yielding

$$\sqrt{\boldsymbol{W}}\boldsymbol{\Sigma} = \boldsymbol{\Sigma}\sqrt{\boldsymbol{W}}. \tag{4.71}$$

This means that either $\sqrt{\boldsymbol{W}}$ is diagonal, or $\boldsymbol{\Sigma} = s\boldsymbol{I}$, where s is a real number. In the first case we obtain $\boldsymbol{\Upsilon} = \boldsymbol{V}_2^{\mathrm{T}}\boldsymbol{W}\boldsymbol{\Sigma}\boldsymbol{V}_2 = (\sqrt{\boldsymbol{W}}\boldsymbol{V}_2)^{\mathrm{T}}\boldsymbol{\Sigma}\sqrt{\boldsymbol{W}}\boldsymbol{V}_2$. Thus we can write

$$\boldsymbol{\Upsilon} = \boldsymbol{U}^{\mathrm{T}}\boldsymbol{\Sigma}\boldsymbol{U}, \tag{4.72}$$

where $\boldsymbol{U} \equiv \sqrt{\boldsymbol{W}}\boldsymbol{V}_2$ is unitary and $\boldsymbol{\Sigma}$ is diagonal and positive. For the case $\boldsymbol{\Sigma} = s\boldsymbol{I}$ we must prove that any unitary, symmetric matrix can be written $\boldsymbol{U}^{\mathrm{T}}\boldsymbol{U}$. Noting that unitary matrices are normal, we introduce a spectral decomposition $\boldsymbol{\Upsilon}/s = \boldsymbol{P}\boldsymbol{D}\boldsymbol{P}^{\mathrm{T}}$ with unitary $\boldsymbol{P}$ and unitary and diagonal $\boldsymbol{D}$. In the case where the eigenvalues are equal, let $\boldsymbol{P} = \boldsymbol{I}$. We obtain

$$\boldsymbol{\Upsilon}/s = \boldsymbol{U}^{\mathrm{T}}\boldsymbol{U}, \tag{4.73}$$

where $\boldsymbol{U} = \sqrt{\boldsymbol{D}}\boldsymbol{P}^{\mathrm{T}}$.

The decomposition in Eq. (4.72) is not unique: First of all the order of the singular values in $\boldsymbol{\Sigma}$ is in principle arbitrary. Once the order has been established, the remaining ambiguities are described by the multiplicative $\boldsymbol{J}$ matrix ($\boldsymbol{U} \to \boldsymbol{J}\boldsymbol{U}$): For distinct singular values, $\boldsymbol{J}$ is diagonal; moreover when both singular values are nonzero, the elements are ± 1. If one of the singular values is zero, the corresponding diagonal element of $\boldsymbol{J}$ is an arbitrary complex number of modulus 1. When the two singular values are equal and nonzero, $\boldsymbol{J}$ is an arbitrary, real unitary matrix; when the two singular values are zero, $\boldsymbol{J}$ is an arbitrary, unitary matrix.

4.D.3 Factorization of a unitary matrix into a symmetrical matrix and a rotation matrix

Any 2×2 unitary matrix can be written as $\boldsymbol{U}=\boldsymbol{P}\boldsymbol{Q}$, where $\boldsymbol{P}$ is a real, special unitary matrix (rotation matrix with the properties $\boldsymbol{P}^{-1}=\boldsymbol{P}^{\dagger}=\boldsymbol{P}^{\mathrm{T}}$ and $\det\boldsymbol{P}=1$), and $\boldsymbol{Q}$ is a symmetric, unitary matrix ($\boldsymbol{Q}^{\mathrm{T}}=\boldsymbol{Q}$). Physically, this means that a general retardation section (or a combination of several linear and circular birefringence sections) can be described as a cascade of a linear and a circular birefringence section.

A matrix $\boldsymbol{U}$ is said to be unitary if and only if the columns are orthonormal, which means that $\boldsymbol{U}$ must satisfy $\boldsymbol{U}^{\dagger}\boldsymbol{U}=\boldsymbol{I}$ or equivalently $\boldsymbol{U}^{-1}=\boldsymbol{U}^{\dagger}$. Thus, a 2×2 unitary matrix $\boldsymbol{U}$ is given by

$$\boldsymbol{U}=\begin{bmatrix} u_1 & u_2 \\ -u_2^* & u_1^* \end{bmatrix} e^{i\phi}, \tag{4.74}$$

where u_1 and u_2 are complex numbers that satisfy $|u_1|^2+|u_2|^2=1$, and ϕ is an arbitrary global phase.

Let $\boldsymbol{P}$ be a 2×2 matrix characterized by $\boldsymbol{P}^{-1}=\boldsymbol{P}^{\mathrm{T}}$ and $\det\boldsymbol{P}=1$. This means that

$$\boldsymbol{P}=\begin{bmatrix} p_1 & p_2 \\ -p_2 & p_1 \end{bmatrix}, \qquad p_1^2+p_2^2=1. \tag{4.75}$$

By comparing (4.75) and (4.74), we can see clearly that the matrix $\boldsymbol{P}$ is unitary if and only if p_1 and p_2 are real numbers.

Define

$$\boldsymbol{Q}\equiv\boldsymbol{P}^{-1}\boldsymbol{U}=\boldsymbol{P}^{\mathrm{T}}\boldsymbol{U}=\begin{bmatrix} p_1u_1+p_2u_2^* & p_1u_2-p_2u_1^* \\ p_2u_1-p_1u_2^* & p_2u_2+p_1u_1^* \end{bmatrix} e^{i\phi} \tag{4.76}$$

The matrix $\boldsymbol{Q}$ is symmetric if

$$p_1(u_2+u_2^*)=p_2(u_1+u_1^*). \tag{4.77}$$

Thus, the numbers p_1 and p_2 can be chosen to be real, which gives that $\boldsymbol{P}$ is unitary. Since $\boldsymbol{Q}^{\dagger}\boldsymbol{Q}=\boldsymbol{U}^{\dagger}\boldsymbol{P}\boldsymbol{P}^{\mathrm{T}}\boldsymbol{U}=\boldsymbol{U}^{\dagger}\boldsymbol{U}=\boldsymbol{I}$, $\boldsymbol{Q}$ is unitary. Note that $\boldsymbol{U}$ is symmetric and $\boldsymbol{P}=\boldsymbol{I}$ if $\mathrm{Re}(u_2)=0$.

The factorization is usually unique up to the global sign of $\boldsymbol{P}$ and $\boldsymbol{Q}$. An exception occurs if u_1 and u_2 are imaginary; then $\boldsymbol{P}$ is arbitrary. If $q_{1,2}$ denote the eigenvalues of $\boldsymbol{Q}$, it can be shown that when $q_1\neq -q_2$, the factorization is unique.

Chapter 5

Inverse scattering in multi-mode structures*

We consider the inverse scattering problem associated with any number of interacting modes. The coupling between the modes is contradirectional in addition to codirectional, and may be distributed continuously or in discrete points. The local coupling as a function of position is obtained from reflection data using a layer-stripping (layer-peeling) type method, and the separate identification of the contradirectional and codirectional coupling is obtained using matrix factorization. Ambiguities are discussed in detail, and different a priori information that can resolve the ambiguities is suggested. Applications to multimode optical waveguides and 3D problems are outlined.

5.1 Introduction

In waveguides that support several modes, scattering, or coupling between the different modes, may appear due to different kinds of perturbations. Possible perturbations are reflectors, gratings, bends, tapering, and other kind of geometrical or material modulation along the waveguide. The coupling may be both codirectional (coupling between modes that propagate in the same direction) or contradirectional (coupling between modes that propagate in opposite directions). The direct scattering problem of computing the scattered field when the probing waves and the scatter structure are known has been extensively discussed in the literature [56, 6, 57]. The inverse scattering problem associated with two interacting modes is also well understood, and has been treated in several contexts since the pioneering work by Gel'fand and Levitan [7], Marchenko [58], and Krein [59]. In geophysics the so-called dynamic deconvolution or layer-stripping (layer-peeling) methods emerged, for the identification of layered-earth models from acoustic scatter data [60, 61, 62, 9, 10]. More recently the inverse scattering methods have been applied to the design and characterization of optical devices involving two interacting modes. Both contradi-

*This chapter has been submitted to SIAM Journal of Applied Mathematics for publication. Authors: Ole Henrik Waagaard and Johannes Skaar.

rectional coupling and codirectional coupling have been treated. Optical components based on contradirectional coupling include thin-film filters and fiber Bragg gratings [13, 16, 26, 63, 40], while codirectional coupling is present in e.g. grating-assisted codirectional couplers and long-period gratings [36, 64, 65, 66, 67]. While the inverse-scattering problem associated with two interacting modes is well-known, the inverse-scattering problem of several, possibly non-degenerate modes (i.e., with different propagation constants) has not attracted much attention. Some work has been done in the case of 4 degenerate modes, that is, two polarization modes in each direction [19, 68], and several degenerate modes with only contradirectional coupling [69].

On the other hand, several methods for the inverse scattering of acoustical or electromagnetic waves in 2D and 3D have been reported. In particular, Yagle *et al.* have developed layer-stripping methods for the multidimensional case [70, 71, 72]. By Fourier transforming the problem with respect to the transversal coordinates, the 2D or 3D problem may be regarded as one-dimensional with several interacting modes.

In this paper we will extend these lines of thought to cover the general inverse scattering problem associated with any number of interacting modes in one-dimensional, reciprocal structures. In the model (Section II) both codirectional and contradirectional coupling may be present simultaneously. We limit ourselves to the case where the known probing waves and the scattered waves propagate in opposite directions. In other words the scattered wave is considered as a reflection from the unknown structure. Ambiguities related to the simultaneous presence of co- and contradirectional coupling will be discussed in detail. Possible *a priori* information that can resolve these ambiguities will be suggested. The layer-stripping algorithm, including a separate identification of the co- and contradirectional coupling, is presented in Section III. Finally, we will outline applications to quasi-periodical waveguide structures and 3D problems in Section IV. The formalism is particularly useful for the quasi-periodical case since only the (slowly varying) envelope needs to be represented, yielding an efficient algorithm.

5.2 Continuous and discrete coupling model

Consider a reciprocal structure with P modes in each direction along the x-axis. We visualize the x-axis as being directed to the right, and say that the $+x$-direction is the forward direction. The propagation constant of the pth mode is $\pm n_p\omega/c$, i.e., the x-dependence of the complex field associated with mode p is $\exp(\pm in_p\omega x/c)$, where the upper (lower) sign applies to forward (backward) propagating modes. Here ω is the angular frequency, c is some fixed reference velocity (common for all modes), and n_p accounts for the actual phase velocity. For electromagnetic waves, it is natural to set c equal to the vacuum velocity, and consequently we will refer to n_p as the effective index associated with mode p. Note that the effective indices of different modes may or may not be different. In principle, the effective indices may be complex and dependent on frequency, meaning that modal loss and dispersion are permitted in the model. However, the modal field profiles are assumed to have

uniform phases such that they can be written real.

Coupling may occur due to a continuous or discrete scatter structure. In the first case, the field is assumed to be governed by the coupled-mode equation

$$\frac{\mathrm{d}\mathbf{E}}{\mathrm{d}x} = i\mathbf{C}\mathbf{E}, \tag{5.1}$$

where $\mathbf{E}$ is a column vector containing the $2P$ mode amplitudes. The first P elements are the mode amplitudes of the forward propagating modes (propagating in the $+x$ direction) and the last P elements are those of the backward propagating modes. The coupling matrix $\mathbf{C}$ can be decomposed into three contributions:

$$\mathbf{C} = \mathbf{D} + \mathbf{C}_{\boldsymbol{\sigma}} + \mathbf{C}_{\boldsymbol{\kappa}}. \tag{5.2}$$

The contributions can be expressed as 2×2 block matrices consisting of $P \times P$ blocks:

$$\mathbf{D} = \begin{bmatrix} \boldsymbol{\beta} & \mathbf{0} \\ \mathbf{0} & -\boldsymbol{\beta} \end{bmatrix}, \tag{5.3a}$$

$$\mathbf{C}_{\boldsymbol{\kappa}} = \begin{bmatrix} \mathbf{0} & \boldsymbol{\kappa} \\ -\boldsymbol{\kappa}^* & \mathbf{0} \end{bmatrix}, \tag{5.3b}$$

$$\mathbf{C}_{\boldsymbol{\sigma}} = \begin{bmatrix} \boldsymbol{\sigma} & \mathbf{0} \\ \mathbf{0} & -\boldsymbol{\sigma}^* \end{bmatrix}, \tag{5.3c}$$

where * denotes complex conjugate. The first term $\mathbf{D}$ describes the frequency dependence due to the propagation of the different modes ("self-coupling"), and is independent on x:

$$\boldsymbol{\beta} = \frac{\omega}{c} \begin{bmatrix} n_1 & 0 & 0 & \dots & 0 \\ 0 & n_2 & 0 & \dots & 0 \\ & & & \ddots & \\ 0 & 0 & 0 & \dots & n_P \end{bmatrix}. \tag{5.4}$$

Only this term is permitted to be lossy in the model ($\boldsymbol{\beta}$ may be complex). The second term $\mathbf{C}_{\boldsymbol{\kappa}}$ describes the coupling between counterpropagating modes, whereas the last term $\mathbf{C}_{\boldsymbol{\sigma}}$ accounts for the coupling between copropagating modes. The coupling coefficients $\boldsymbol{\kappa}$ and $\boldsymbol{\sigma}$ are dependent on x but assumed independent on frequency. As will become clear shortly, the above forms of $\mathbf{C}_{\boldsymbol{\kappa}}$ and $\mathbf{C}_{\boldsymbol{\sigma}}$ are consequences of reciprocity and losslessness.

The coupling region in the waveguide is discretized into $N+1$ layers, each of thickness $\Delta x = L/(N+1)$, where L is the total length. If N is sufficiently large so that the matrices in (5.3) can be treated as constants in each layer, we can solve (5.1):

$$\mathbf{E}(x_j + \Delta x) = \exp\left(i\mathbf{C}\Delta x\right)\mathbf{E}(x_j), \quad x_j = j\Delta x. \tag{5.5}$$

This transfer matrix relation can be used to propagate the fields through the piecewise uniform structure. With the help of the connection between the transfer matrix and the scattering matrix (Appendix 5.B) we can find the reflection and transmission response from the total transfer matrix, obtained as a product of the transfer matrices $\exp\left(i\mathbf{C}\Delta x\right)$ of each layer (direct scattering).

While direct scattering is achieved straightforwardly using the piecewise-uniform discretization, for inverse scattering it is convenient to push the discretization further, to identify the different contributions to the transfer matrix $\exp(i\mathbf{C}\Delta x)$. To first order in Δx, we have $\exp(i\mathbf{C}\Delta x) = \exp(i\mathbf{D}\Delta x)\exp(i\mathbf{C}_{\boldsymbol{\kappa}}\Delta x)\exp(i\mathbf{C}_{\boldsymbol{\sigma}}\Delta x)$. For a continuous structure of finite thickness, the bandwidth where the reflection spectrum is significantly different from zero is finite. Thus we need only be concerned with frequencies satisfying $|\omega| \leq \omega_{\mathrm{b}}$ for some positive constant ω_{b}. For inverse scattering, the reflection spectrum and therefore ω_{b} are known. Therefore, provided Δx is chosen sufficiently small we can approximate each layer by a cascade of three sections: a section with codirectional coupling, a section with contradirectional coupling (discrete reflector), and time-delay section. The transfer matrix of the jth layer becomes

$$\mathbf{T}_j = \mathbf{T}_{\boldsymbol{Z}}\mathbf{T}_{\boldsymbol{\rho}_j}\mathbf{T}_{\boldsymbol{\Phi}_j}, \tag{5.6}$$

where

$$\mathbf{T}_{\boldsymbol{Z}} \equiv \exp(i\mathbf{D}\Delta x) = \begin{bmatrix} \boldsymbol{Z}^{-1} & \mathbf{0} \\ \mathbf{0} & \boldsymbol{Z} \end{bmatrix}, \quad \boldsymbol{Z}^{-1} = \exp(i\boldsymbol{\beta}\Delta x), \tag{5.7a}$$

$$\mathbf{T}_{\boldsymbol{\rho}_j} \equiv \exp(i\mathbf{C}_{\boldsymbol{\kappa}}\Delta x) = \begin{bmatrix} \boldsymbol{t}_j^{-1*} & -\boldsymbol{t}_j^{-1*}\boldsymbol{\rho}_j^* \\ -\boldsymbol{t}_j^{-1}\boldsymbol{\rho}_j & \boldsymbol{t}_j^{-1} \end{bmatrix}, \quad \begin{array}{l} \boldsymbol{\rho}_j = i\tanh[(\boldsymbol{\kappa}^*\boldsymbol{\kappa})^{1/2}\Delta x](\boldsymbol{\kappa}^*\boldsymbol{\kappa})^{-1/2}\boldsymbol{\kappa}^*, \\ \boldsymbol{t}_j = \cosh[(\boldsymbol{\kappa}^*\boldsymbol{\kappa})^{1/2}\Delta x]^{-1}, \end{array} \tag{5.7b}$$

$$\mathbf{T}_{\boldsymbol{\Phi}_j} \equiv \exp(i\mathbf{C}_{\boldsymbol{\sigma}}\Delta x) = \begin{bmatrix} \boldsymbol{\Phi}_j & \mathbf{0} \\ \mathbf{0} & \boldsymbol{\Phi}_j^* \end{bmatrix}, \quad \boldsymbol{\Phi}_j = \exp(i\boldsymbol{\sigma}\Delta x). \tag{5.7c}$$

The form of the matrix in (5.7b) may for example be verified by evaluating the power series expansion of the matrix exponential. In principle, it suffices to express (5.7) to first order in Δx; however, the exact form is kept to emphasize the properties of each of the three sections, and to retain the correspondence to the discrete case (below).

We are now in the position that we can argue for the forms of the coupling matrices (5.3). Note that while we have permitted loss in the propagation section $\boldsymbol{Z}^{-1}$, the coupling sections are assumed lossless. Since the coupling sections also are assumed to be reciprocal, their transfer matrices satisfy (5.64) and (5.65) (Appendix 5.B). Allowing a more general $\mathbf{C}_{\boldsymbol{\kappa}}$ by substituting $\boldsymbol{\kappa}^* \to \boldsymbol{\kappa}_{21}$ in the (2,1) block, and expanding $\exp(i\mathbf{C}_{\boldsymbol{\kappa}}\Delta x)$ to first order in Δx, the lossless and reciprocity conditions give $\boldsymbol{\kappa}_{12} = -\boldsymbol{\kappa}^*$ and dictate $\boldsymbol{\kappa}$ to be symmetric. Similarly, we can derive the form of $\mathbf{C}_{\boldsymbol{\sigma}}$ and establish that $\boldsymbol{\Phi}_j$ must be unitary, i.e., $\boldsymbol{\sigma}$ is hermitian.

From the discussion above, each layer is characterized by a unitary codirectional coupling matrix $\boldsymbol{\Phi}_j$ and a discrete reflector. Let superscript T denote transpose and let $\|\cdot\|$ be the usual matrix 2-norm. The discrete reflector satisfies $\boldsymbol{\rho}_j = \boldsymbol{\rho}_j^{\mathrm{T}}$, and has an associated, positive definite transmission matrix $\boldsymbol{t}_j$ with $\boldsymbol{t}_j^2 = \boldsymbol{I} - \boldsymbol{\rho}_j\boldsymbol{\rho}_j^*$. We restrict ourselves to reflectors that satisfy $\|\boldsymbol{\rho}_j\| < 1$; otherwise the reflector will mask the later part of the structure such that the inverse scattering procedure will not be possible.

So far we have considered a continuous scatter structure, and discretized it into a cascade of codirectional coupling, reflection, and pure propagation. Obviously, we

can also describe discrete coupling directly. The most general, lossless, reciprocal coupling element can be described as a discrete reflector sandwiched between two codirectional coupling sections (Appendix 5.B). Compared to our discrete model above, there is an extra codirectional coupling section on the right-hand side of the reflector. In the special case where all modes have equal effective index, $\boldsymbol{Z}^{-1} \propto \boldsymbol{I}$, this coupling section commutes with the delay section, and as a result it can be absorbed into the next, adjacent layer on the right-hand side. However, in the general case this extra coupling section does not commute with the delay section and cannot be ignored. For inverse scattering, this coupling section should therefore not be present since it prevents unique reconstruction, at least when only using the reflection response as the starting point. Moreover, we will assume that $\boldsymbol{t}_j$ is positive definite such that $\boldsymbol{t}_j$ can be determined uniquely by $\boldsymbol{t}_j = (\boldsymbol{I} - \boldsymbol{\rho}_j\boldsymbol{\rho}_j^*)^{1/2}$.

Writing out the transfer matrix (5.6) of each layer, we obtain

$$\mathbf{T}_j = \begin{bmatrix} \boldsymbol{Z}^{-1}\boldsymbol{t}_j^{-1*}\boldsymbol{\Phi}_j & -\boldsymbol{Z}^{-1}\boldsymbol{t}_j^{-1*}\boldsymbol{\rho}_j^*\boldsymbol{\Phi}_j^* \\ -\boldsymbol{Z}\boldsymbol{t}_j^{-1}\boldsymbol{\rho}_j\boldsymbol{\Phi}_j & \boldsymbol{Z}\boldsymbol{t}_j^{-1}\boldsymbol{\Phi}_j^* \end{bmatrix} = \begin{bmatrix} \boldsymbol{Z}^{-1}\boldsymbol{K}_j & \mathbf{0} \\ \mathbf{0} & \boldsymbol{Z}\boldsymbol{K}_j^* \end{bmatrix} \begin{bmatrix} \boldsymbol{I} & -\boldsymbol{\Upsilon}_j^* \\ -\boldsymbol{\Upsilon}_j & \boldsymbol{I} \end{bmatrix}, \quad (5.8)$$

where $\boldsymbol{\Upsilon}_j = \boldsymbol{\Phi}_j^{\mathrm{T}}\boldsymbol{\rho}_j\boldsymbol{\Phi}_j$ and $\boldsymbol{K}_j = \boldsymbol{t}_j^{-1*}\boldsymbol{\Phi}_j$. The transfer matrix can be converted into a scattering matrix (Appendix 5.B):

$$\mathbf{S}_j = \begin{bmatrix} \boldsymbol{\Phi}_j^{\mathrm{T}}\boldsymbol{\rho}_j\boldsymbol{\Phi}_j & \boldsymbol{\Phi}_j^{\mathrm{T}}\boldsymbol{t}_j\boldsymbol{Z}^{-1} \\ \boldsymbol{Z}^{-1}\boldsymbol{t}_j^*\boldsymbol{\Phi}_j & -\boldsymbol{Z}^{-1}\boldsymbol{t}_j^{-1*}\boldsymbol{\rho}_j^*\boldsymbol{t}_j\boldsymbol{Z}^{-1} \end{bmatrix}. \quad (5.9)$$

Thus, $\boldsymbol{\Upsilon}_j$ represents the reflection response from the left of layer j.

The combined transfer matrix describing the total structure with $N+1$ layers is given by

$$\mathbf{T} = \mathbf{T}_N\mathbf{T}_{N-1}\cdots\mathbf{T}_1\mathbf{T}_0. \quad (5.10)$$

From this matrix we can determine the reflection and transmission response using (5.57). For example, the reflection response from the left is

$$\boldsymbol{R}(\omega) \equiv \boldsymbol{S}_{11} = -\boldsymbol{T}_{22}^{-1}\boldsymbol{T}_{21}, \quad (5.11)$$

where $\boldsymbol{T}_{kl}$ are the $P \times P$ blocks in $\mathbf{T}$. Assuming $\|\boldsymbol{\rho}_j\| < 1$ for all j, it can be proven by induction that $\boldsymbol{T}_{22}$ is invertible on and above the real frequency axis in the complex ω-plane, for any number of layers. Physically this is obvious since $\boldsymbol{T}_{22}^{-1}$ is the transmission response from the right, and therefore it must exist and be causal and stable.

Reciprocity (5.58a) gives $\boldsymbol{R}(\omega) = \boldsymbol{R}(\omega)^{\mathrm{T}}$. Using $\|\boldsymbol{\rho}_j\| < 1$ for all j, it can be shown by induction that $\|\boldsymbol{R}\| < 1$ for a passive structure (a passive structure is characterized by $\operatorname{Im} n_p \geq 0$ for all p). By causality the reflection response can be written in the form

$$\boldsymbol{R}(\omega) = \int_0^\infty \boldsymbol{h}(t)\exp(i\omega t)\mathrm{d}t, \quad (5.12)$$

where $\boldsymbol{h}(t)$ is the time-domain impulse response.

When the modes are nondispersive, $\boldsymbol{h}(t)$ contains a train of non-equally spaced, weighted delta pulses, i.e.,

$$\boldsymbol{h}(t) = \sum_{k=0}^{\infty} \boldsymbol{h}^k\delta(t - t^k), \quad (5.13)$$

where $\boldsymbol{h}^k$ and t^k are the weight and arrival time of the kth pulse, respectively. Substituting (5.13) into (5.12) gives

$$\boldsymbol{R}(\omega) = \sum_{k=0}^{\infty} \boldsymbol{h}^k \exp(i\omega t^k). \tag{5.14}$$

The weights $\boldsymbol{h}^k$ can in principle be calculated from $\boldsymbol{R}(\omega)$ using an inverse transform of the form

$$\boldsymbol{h}^k = \lim_{\omega_{\max}\to\infty} \frac{1}{2\omega_{\max}} \int_{-\omega_{\max}}^{\omega_{\max}} \boldsymbol{R}(\omega) \exp(-i\omega t^k) \mathrm{d}\omega. \tag{5.15}$$

The valid arrival times are determined by the delay from a layer to the next of each mode. Let $\Delta t_p = n_p \Delta x/c$ be the delay of mode p through a single layer. A delta pulse at $t = 0$ is incident to the structure on the left-hand side. Consider the reflection from the different layers, as seen from left-hand side of the structure. From layer 0, the arrival times in all modes will be zero. An impulse in mode p reflected from layer 1 into mode q, will arrive at $\Delta t_p + \Delta t_q$. Thus, considering layer 1, the arrival times are any combinations of two unit delays Δt_p. Considering layer 2, the arrival times are any combinations of four unit delays, and so forth.

When the modes are dispersive, the impulse response is no longer a train of delta functions. Nevertheless, at $t = 0$ it can still be written as $\boldsymbol{h}^0\delta(t)$, and the weight $\boldsymbol{h}^0$ can be found from (5.15).

Eq. (5.14) clearly demonstrate that, in principle, for a discrete structure the reflection response $\boldsymbol{R}(\omega)$ does not approach zero for large frequencies. Only in the special case where the modal effective indices are rational numbers, the reflection spectrum is periodic. Fortunately, in practice, it is not necessary to represent the entire bandwidth to enable inverse scattering for a discrete structure. As shown in the next section, what is needed in the layer-stripping algorithm is the zeroth point of the impulse response, at time $t = 0$. Since the next nonzero value is for $t = 2\min_p \Delta t_p$ [1], the zeroth point is computed accurately provided the represented bandwidth $\omega_{\max}$ satisfies $\omega_{\max} \gg 1/\min_p \Delta t_p = c/(\Delta x \min_p n_p)$. Then, if the true reflection spectrum is multiplied by a smooth window function $W(\omega)$ that goes to zero at $\omega = \pm\omega_{\max}$, the inverse Fourier transform evaluated around zero is approximately $w(t)\boldsymbol{h}^0$, where $w(t)$ is the inverse Fourier transform of $W(\omega)$. Since $w(0)\boldsymbol{h}^0 \approx \frac{1}{2\pi}\int_{-\omega_{\max}}^{\omega_{\max}} W(\omega)\boldsymbol{R}(\omega)\mathrm{d}\omega$, we can find $\boldsymbol{h}^0$ from a measurement of $\boldsymbol{R}(\omega)$ in the bandwidth $(-\omega_{\max}, \omega_{\max})$:

$$\boldsymbol{h}^0 \approx \frac{\int_{-\omega_{\max}}^{\omega_{\max}} W(\omega)\boldsymbol{R}(\omega)\mathrm{d}\omega}{\int_{-\omega_{\max}}^{\omega_{\max}} W(\omega)\mathrm{d}\omega}. \tag{5.16}$$

If the scatter structure is continuous, at least under certain circumstances, one can use the true reflection spectrum as input to the layer-stripping algorithm even though each layer is modeled discrete. This can be realized by the following argument: The layer thickness Δx is chosen small such that the first order approximations of $\exp(i\mathbf{C}_{\boldsymbol{\kappa}}\Delta x)$ and $\exp(i\mathbf{C}_{\boldsymbol{\sigma}}\Delta x)$ are valid. (Thus an upper bound on $\|\mathbf{C}_{\boldsymbol{\kappa}}\|$ and

[1] For simplicity it is here and in the next paragraph assumed a nondispersive structure.

$\|\mathbf{C}_{\boldsymbol{\sigma}}\|$ should be known *a priori*.) If the resulting Δx satisfies $\Delta x \ll c/(\omega_{\mathrm{b}} \max_p n_p)$ for some $\omega_{\mathrm{b}} > 0$, the first order approximation of $\exp(i\mathbf{D}\Delta x)$ is valid, and the true reflection spectrum is approximately equal to that of the corresponding discrete model in the bandwidth $\omega \leq \omega_{\mathrm{b}}$. We can therefore use the true reflection spectrum for $\omega \leq \omega_{\mathrm{b}}$ as input to the layer-stripping algorithm instead of the (unknown) spectrum of the discrete model. Outside this interval, the spectrum can be set to zero, at the expense of limiting the spatial resolution (Δx_{res}): $\Delta x_{\mathrm{res}} \sim c/(\omega_{\mathrm{b}} \min_p n_p)$. By measuring the reflection spectrum in a sufficiently large bandwidth, any spatial resolution can be achieved. For most waveguides, in the bandwidth of interest the effective indices are similar. While the phase relation between the modes may still yield a nontrivial reflection matrix, the spectrum is roughly periodic. Since the round-trip time from a reflector to the next is $2\Delta t_1 = 2\Delta x n_1/c$, the spectral period is $2\omega_{\max} = \pi c/(\Delta x n_1)$. This bandwidth should now be represented in the layer-stripping; the zeroth point of the impulse response is found as the mean value of the spectrum.

Due to the differences between the discrete and continuous models, the local impulse responses in the layer-stripping algorithm will have (small) noncausal parts. These errors get amplified through the layer-stripping process. By forcing the intermediate impulse responses to be causal (removing the noncausal parts) the stability of the scalar algorithm has been shown to be improved considerably [73]. A similar approach can be used straightforwardly in the vector layer-stripping algorithm described in Section 5.3.

In many practical cases, the structure to be reconstructed is quasi-sinusoidal. More generally, the structure is often quasi-periodic, and e.g. the first "Fourier component" is to be reconstructed. In such cases, one can define modal field envelopes which are slowly varying with respect to x (compared to a wavelength). Similarly, one can extract slowly varying coupling coefficient envelopes. As a result, all quantities in (5.1) are varying slowly with x. The relevant bandwidth in (5.16) will then be centered about a chosen "design frequency". The main advantage of this procedure is that it leads to considerably less requirements on the spatial resolution, and as a result efficient inverse scattering. This modification to the model is detailed in Section 5.4.1.

5.3 Layer-stripping method

The inverse scattering problem can now be stated as follows: Given a structure consisting of $N+1$ layers. Each layer consists of three sections (sublayers), the first ($\boldsymbol{\Phi}_j$) responsible for coupling between copropagating modes, the second ($\boldsymbol{\rho}_j$) responsible for coupling between counterpropagating modes, and the third a pure propagating section ($\boldsymbol{Z}^{-1}$). The effective indices of the involved modes are known and specified in terms of $\boldsymbol{Z}^{-1}$. [2] From a set of excitation-response pairs ($\boldsymbol{R}(\omega)$), we

[2] The effective indices may contain small, unknown parts Δn_p, i.e., $n_p = n_{p,\mathrm{known}} + \Delta n_p$, where $n_{p,\mathrm{known}}$ are the known parts. Provided Δn_p is sufficiently small, the variation of the associated phase factor $\exp(i\omega\Delta n_p \Delta x/c)$ may be small over the relevant bandwidth. In such cases the unknown parts can be absorbed into the $\boldsymbol{\Phi}_j$'s.

want to reconstruct $\boldsymbol{\rho}_j$ and $\boldsymbol{\Phi}_j$ for all j.

The structure itself and the medium to the right are assumed to be at rest at time $t = 0$. For incident waves from the left, the reflection response from the structure is described by the matrix $\boldsymbol{R}(\omega)$ of dimension $P \times P$. This matrix can be viewed as the operator which takes the excitation field vector to the reflected field vector. Its columns can be interpreted as the responses for orthonormal excitation basis vectors $\boldsymbol{e}_1, \boldsymbol{e}_2, \ldots, \boldsymbol{e}_P$, respectively. Here $\boldsymbol{e}_p$ has only one nonzero element (equal to unity) at position p. Similarly, we can define the forward ($\boldsymbol{u}_j(\omega)$) and backward ($\boldsymbol{v}_j(\omega)$) propagating field matrices as $P \times P$ matrices where the columns are the fields for orthonormal excitations $\boldsymbol{e}_1, \boldsymbol{e}_2, \ldots, \boldsymbol{e}_P$. A subscript j is specified to emphasize that $\boldsymbol{u}_j(\omega)$ and $\boldsymbol{v}_j(\omega)$ are the fields at the beginning (left-hand side) of layer j. The field matrices of layer $j+1$ are related to the field matrices of layer j by

$$\begin{bmatrix} \boldsymbol{u}_{j+1}(\omega) \\ \boldsymbol{v}_{j+1}(\omega) \end{bmatrix} = \mathbf{T}_j \begin{bmatrix} \boldsymbol{u}_j(\omega) \\ \boldsymbol{v}_j(\omega) \end{bmatrix}, \tag{5.17}$$

where $\mathbf{T}_j$ is given by (5.8).

The layer-stripping algorithm is based on the simple fact that the leading edge of the impulse response is independent on later parts of the structure due to causality. Hence, one can identify the first layer of the structure, and subsequently remove its effect using the associated transfer matrix.

For layer 0, we initialize $\boldsymbol{u}_0(\omega) = \boldsymbol{I}$ and $\boldsymbol{v}_0(\omega) = \boldsymbol{R}(\omega)$. We define a local reflection spectrum $\boldsymbol{R}_j(\omega) = \boldsymbol{v}_j(\omega)\boldsymbol{u}_j(\omega)^{-1}$ and the associated impulse response $\boldsymbol{h}_j(t)$ as the response of the structure after removing the first $j-1$ layers. Similarly to the impulse response of the entire structure, $\boldsymbol{h}_j(t)$ contains an isolated delta function at $t = 0$. Due to causality, this pulse is equal to the reflection from the zeroth layer alone. Denoting the weight of this pulse $\boldsymbol{h}_j^0$, we find from (5.9) that

$$\boldsymbol{h}_j^0 = \boldsymbol{\Upsilon}_j \equiv \boldsymbol{\Phi}_j^{\mathrm{T}} \boldsymbol{\rho}_j \boldsymbol{\Phi}_j. \tag{5.18}$$

Note that $\boldsymbol{R}_j(\omega)$ is symmetric for all ω as a result of reciprocity; thus $\boldsymbol{h}_j^0$ is symmetric as well. Writing out (5.17) and (5.8), and substituting $\boldsymbol{v}_j(\omega) = \boldsymbol{R}_j(\omega)\boldsymbol{u}_j(\omega)$, we obtain

$$\boldsymbol{u}_{j+1}(\omega) = \boldsymbol{Z}^{-1}\boldsymbol{K}_j \left[\boldsymbol{I} - \boldsymbol{\Upsilon}_j^* \boldsymbol{R}_j(\omega)\right] \boldsymbol{u}_j(\omega), \tag{5.19a}$$

$$\boldsymbol{v}_{j+1}(\omega) = \boldsymbol{Z}\boldsymbol{K}_j^* \left[\boldsymbol{R}_j(\omega) - \boldsymbol{\Upsilon}_j\right] \boldsymbol{u}_j(\omega), \tag{5.19b}$$

and therefore

$$\boldsymbol{R}_{j+1}(\omega) = \boldsymbol{Z}\boldsymbol{K}_j^* \left[\boldsymbol{R}_j(\omega) - \boldsymbol{\Upsilon}_j\right] \left[\boldsymbol{I} - \boldsymbol{\Upsilon}_j^* \boldsymbol{R}_j(\omega)\right]^{-1} \boldsymbol{K}_j^{-1} \boldsymbol{Z}. \tag{5.20}$$

Provided $\boldsymbol{\Upsilon}_j$ and $\boldsymbol{K}_j$ are known, (5.20) shows that the local reflection spectrum of layer $j+1$ can be calculated directly from the local reflection spectrum of layer j without calculating the fields $\boldsymbol{u}_{j+1}$ and $\boldsymbol{v}_{j+1}$. Note the similarity to the Schur formula used in scalar layer-stripping [9].

To characterize layer j completely, and to identify $\boldsymbol{K}_j$, we must determine $\boldsymbol{\rho}_j$ and $\boldsymbol{\Phi}_j$. By counting the available degrees of freedom (in $\boldsymbol{\Upsilon}_j$), we immediately find that

this cannot be done uniquely. It is therefore necessary to use *a priori* information on $\boldsymbol{\rho}_j$ and/or $\boldsymbol{\Phi}_j$. The available information may vary from situation to situation. Here we will consider the following situations, where $\boldsymbol{\rho}_j$ and $\boldsymbol{\Phi}_j$ can be found using the methods in the Appendices 5.A.2 and 5.A.3.

a) $\boldsymbol{\Phi}_j = \boldsymbol{I}$. In this case there is no codirectional coupling. The identification of the layer is now particularly simple, as $\boldsymbol{\rho}_j = \boldsymbol{\Upsilon}_j$ uniquely. Note that while there is no codirectional coupling, $\boldsymbol{\rho}_j$ describes reflection from all modes into all modes. Thus the different modes may still interact.

b) $\boldsymbol{\rho}_j$ is diagonal and nonnegative. Now $\boldsymbol{\rho}_j$ is a simple partial reflector which only reflects light into the same mode as the incident field (no reflection into other modes). The coupling between different modes is instead described by $\boldsymbol{\Phi}_j$. Since $\boldsymbol{\Upsilon}_j = \boldsymbol{\Phi}_j^{\mathrm{T}} \boldsymbol{\rho}_j \boldsymbol{\Phi}_j$, $\boldsymbol{\rho}_j$ is found uniquely as the singular value matrix associated with $\boldsymbol{\Upsilon}_j$, up to reordering of the singular values. Once the order of the singular values has been established, the unitary $\boldsymbol{\Phi}_j$ is found uniquely up to the sign of its rows, provided all singular values are distinct and nonzero (see Appendix 5.A.2). When one or more singular values of $\boldsymbol{\Upsilon}_j$ are zero, the corresponding row(s) of $\boldsymbol{\Phi}_j$ cannot be determined uniquely. More precisely, $\boldsymbol{\Phi}_j$ is determined up to a premultiplicative unitary matrix $\boldsymbol{J}$ operating on the associated mode(s). Physically, this is obvious since when a singular value is zero, the associated mode is not reflected from the layer. When two or more nonvanishing singular values are equal, $\boldsymbol{\Phi}_j$ is determined up to a premultiplicative, real unitary $\boldsymbol{J}$ operating on the associated modes. Physically, this means that these modes experience the same reflection and thus an arbitrary (real) "rotation" of the modes is not detected. In such cases, the unitary section $\boldsymbol{\Phi}_j$, as determined by the method in Appendix 5.A.2, does not necessarily correspond to the physical section. This error will propagate to the next layers according to (5.20).

c) $\boldsymbol{\Phi}_j$ is symmetrical and $\boldsymbol{\rho}_j$ is real and positive semidefinite. A special case in which there are only two degenerate modes in each direction is treated in [68]. The reflector matrix $\boldsymbol{\rho}_j$ can be written $\boldsymbol{P}_j \boldsymbol{\Sigma}_j \boldsymbol{P}_j^{\mathrm{T}}$, where $\boldsymbol{P}_j$ is a real, special unitary matrix and $\boldsymbol{\Sigma}_j$ is diagonal and nonnegative. Since $\boldsymbol{\Upsilon}_j = \boldsymbol{\Phi}_j^{\mathrm{T}} \boldsymbol{\rho}_j \boldsymbol{\Phi}_j = \boldsymbol{\Phi}_j^{\mathrm{T}} \boldsymbol{P}_j \boldsymbol{\Sigma}_j \boldsymbol{P}_j^{\mathrm{T}} \boldsymbol{\Phi}_j$, we find $\boldsymbol{\Sigma}_j$ and $\boldsymbol{P}_j^{\mathrm{T}} \boldsymbol{\Phi}_j$ as in the previous case, with the identical ambiguity issues. The separate identification of $\boldsymbol{P}_j^{\mathrm{T}}$ and $\boldsymbol{\Phi}_j$ is accomplished using the factorization method in Appendix 5.A.3, with certain ambiguities related to the sign of the eigenvalues of $\boldsymbol{\Phi}_j$.

The ambiguities when determining $\boldsymbol{\Phi}_j$ in situation b) are in fact very similar to the well-known ambiguities in the scalar case with a single mode in each direction. In the scalar case any π phase-shift sections between the reflectors cannot be identified since the associated round-trip phase accumulated to and from a reflector becomes 2π. In our multimode case, the sign of the rows of the "phase-delay" section ($\boldsymbol{\Phi}_j$) between two reflectors cannot be identified. Similarly, in the scalar case, any phase-shift section preceeding a zero reflector cannot be determined uniquely. Instead it

is chosen arbitrarily (e.g. removed), and instead attributed to the next layer with a nonzero reflector.

When the structure to be reconstructed is a discretized version of a smooth structure, the smoothness can be used to resolve ambiguites. First we consider situation b). For small Δx, $\boldsymbol{\Phi}_j$ is close to identity; thus the sign of the rows of $\boldsymbol{\Phi}_j$ can be determined uniquely. If $\boldsymbol{\rho}_j$ has distinct eigenvalues, valid for all j, the order of the eigenvalues of $\boldsymbol{\rho}_j$ can be determined from the order of the eigenvalues of $\boldsymbol{\rho}_{j-1}$ using the smoothness of $\boldsymbol{\kappa} = \boldsymbol{\kappa}(x)$. If there are equal eigenvalues for a certain reflector $\boldsymbol{\rho}_j$, or if $\boldsymbol{\rho}_j$ is singular, the ambiguities of $\boldsymbol{\Phi}_j$ are characterized by the premultiplicative $\boldsymbol{J}$ matrix (Appendix 5.A.2). In other words, the chosen $\boldsymbol{\Phi}_j$ is related to the corresponding true matrix ($\boldsymbol{\Phi}_{j,\mathrm{true}}$) by $\boldsymbol{\Phi}_j = \boldsymbol{J}\boldsymbol{\Phi}_{j,\mathrm{true}}$. By choosing $\boldsymbol{J}$ such that $\|\boldsymbol{\Phi}_j - \boldsymbol{\Phi}_{j-1}\|$ is minimum, the resulting $\boldsymbol{J}$ is close to identity (that is, $\|\boldsymbol{J} - \boldsymbol{I}\| \leq \|\boldsymbol{\Phi}_{j,\mathrm{true}} - \boldsymbol{\Phi}_{j-1}\|$). Since $\boldsymbol{t}_j$ and $\boldsymbol{Z}^{-1}$ are close to identity as well, the order of three sections $\boldsymbol{J}$, $\boldsymbol{t}_j$, and $\boldsymbol{Z}^{-1}$ can be interchanged (see Section 5.2). Thus the error due to wrong choice of $\boldsymbol{\Phi}_j$ can be absorbed into $\boldsymbol{\Phi}_{j+1}$. More generally, provided only a few neighboring layers have singular or degenerate $\boldsymbol{\rho}_j$'s, only the corresponding and following $\boldsymbol{\Phi}_j$ sections may be determined erroneously, and the determination of the later part of the structure is (approximately) unaffected.

In situation c), the matrix $\boldsymbol{P}_j^{\mathrm{T}}\boldsymbol{\Phi}_j$ is not necessarily close to identity. Nevertheless, the sign of its rows can be determined from $\boldsymbol{P}_{j-1}^{\mathrm{T}}\boldsymbol{\Phi}_{j-1}$ if $\boldsymbol{\kappa} = \boldsymbol{\kappa}(x)$ and $\boldsymbol{\sigma} = \boldsymbol{\sigma}(x)$ are sufficiently smooth. (Recall that the matrix $\boldsymbol{P}_j^{\mathrm{T}}\boldsymbol{\Phi}_j$ is unitary, which means that there exists at least one element of magnitude $\geq 1/\sqrt{P}$.) The order of eigenvalues of $\boldsymbol{\rho}_j$ can be determined as in situation b). Finally, since $\boldsymbol{\Phi}_j$ is close to identity, its eigenvalues are close to unity. It follows that the factorization of $\boldsymbol{P}_j^{\mathrm{T}}\boldsymbol{\Phi}_j$ into $\boldsymbol{P}_j^{\mathrm{T}}$ and $\boldsymbol{\Phi}_j$ is unique (Appendix 5.A.3).

From the discussion above, we summarize the layer-stripping algorithm, analogously to the scalar version described in ref. [9, 10], that can be applied to identify a structure supporting multiple modes:

1) Initialize $j = 0$. Set $\boldsymbol{R}_j(\omega) = \boldsymbol{R}(\omega)$.

2) Compute the zeroth weight $\boldsymbol{h}_j^0$ of the impulse response. In practice this is achieved by the substitutions $\boldsymbol{h}^0 \to \boldsymbol{h}_j^0$ and $\boldsymbol{R}(\omega) \to \boldsymbol{R}_j(\omega)$ in (5.16).

3) Use a model-specific factorization of $\boldsymbol{h}_j^0 = \boldsymbol{\Phi}_j^{\mathrm{T}}\boldsymbol{\rho}_j\boldsymbol{\Phi}_j$ to find $\boldsymbol{\Phi}_j$ and $\boldsymbol{\rho}_j$.

4) Calculate $\boldsymbol{t}_j = (\boldsymbol{I} - \boldsymbol{\rho}_j\boldsymbol{\rho}_j^*)^{1/2}$ such that the associated eigenvalues are positive, and set $\boldsymbol{K}_j = \boldsymbol{t}_j^{-1}\boldsymbol{\Phi}_j$.

5) Calculate the next, local reflection response $\boldsymbol{R}_{j+1}(\omega)$ using (5.20).

6) Increase j and return to 2.

5.4 Examples of multi-mode coupling structures

5.4.1 Quasi-sinusoidal 1D coupling structures

Continuous coupling in acoustical, radio frequency, or optical waveguides may be obtained by perturbation of the effective indices n_p associated with each mode. This can be achieved by modulation of the wall profile or waveguide medium properties. As a concrete example, we will discuss fiber Bragg gratings [11], which have attracted large interest recently due to their applications in fiber optical communications and sensors. A fiber grating is formed in an optical fiber by modulating the refractive index of the core periodically or quasi-periodically. The main peak of the reflection spectrum appears for the frequency where the reflection from a crest in the index modulation is in phase with the next reflection. Permanent gratings are fabricated by UV-illumination. In fibers doped with certain dopants such as germanium, the UV-illumination will permanently rise the refractive index of the core. Advanced fabrication methods have made it possible to manufacture complex gratings with varying index modulation amplitude and period. The layer-stripping algorithm is the most widely used method for designing the index profile to obtain a given reflection spectrum [16, 26, 40].

In most cases, the fiber grating is formed in a single-mode fiber, and coupling is only considered between the forward-propagating and backward-propagating fundamental mode. The field matrices $\boldsymbol{u}_j(\omega)$ and $\boldsymbol{v}_j(\omega)$ are then scalar functions. However, in some cases it is not sufficient to consider only one forward-propagating mode and one backward-propagating mode. For instance, a single mode fiber is always slightly birefringent, and the photosensitivity can be polarization-dependent [42]. In this case, two forward-propagating and two backward-propagating polarization modes must be considered. An inverse scattering algorithm that takes into account polarization mode coupling is described in [68]. The coupling between the two polarization modes are described by Jones matrices [51]. Both polarization modes have approximately the same effective index, so $\boldsymbol{Z}^{-1} = \exp(i\beta\Delta x)\boldsymbol{I}$, where the common propagation constant β is scalar.

In a multi-mode fiber, the modulation of the refractive index may result in coupling between the fundamental mode and other modes. Each mode has a transversal field profile $\Psi_p(r,\phi)$ which is a solution to the scalar wave equation in polar coordinates r and ϕ [6][3]:

$$\left\{\nabla_{\mathrm{t}}^2 + k^2(\bar{n}^2(r) - n_p^2)\right\}\Psi_p(r,\phi) = 0. \tag{5.21}$$

Here $\bar{n}(r)$ is the unperturbed, refractive index profile of the fiber, which is assumed to be real, ∇_{t} is the transversal nabla operator, and $k = \omega/c$. The field $\Psi_p(r,\phi)$ and its first derivatives are continuous. For bound modes, the fields are real and orthonormal such that $\int_{A_\infty}\Psi_p(r,\phi)\Psi_q(r,\phi)\mathrm{d}A = \delta(p-q)$, where $\delta(p-q)$ denotes the Kronecker delta, and A_∞ is the entire transversal plane. The effective indices n_p

[3]To find the exact electromagnetic modes, the vector wave equation must be solved. However, for weakly guiding waveguides (waveguides with small difference between the refractive index of the core and the cladding), the scalar wave equation can be used. This is the case for most conventional fibers.

are eigenvalue solutions to (5.21). A mode p is bounded when $n_{\rm cl} < n_p \leq n_{\rm co}$, where $n_{\rm co}$ and $n_{\rm cl}$ are the refractive indices of the fiber core and cladding, respectively. Ignoring radiation modes, which in the vicinity of the core decay rapidly away from the excitation source, the total electric field $E(r,\phi,x)$ can be written as a superposition of forward- and backward-propagating bound modes:

$$E(r,\phi,x) = \sum_{p=1}^{P} (b_p^+(x) + b_p^-(x))\Psi_p(r,\phi). \tag{5.22}$$

Here $b_p^{\pm}(x)$ contain all x-dependence including the harmonic propagation factor $\exp(\pm i\beta_p x)$, where $\beta_p = kn_p$.

Coupling between the modes originates from longitudinal modulation of the refractive index. Let the refractive index be perturbed quasi-periodically with a spatial period Λ,

$$n(r,\phi,x) = \bar{n}(r) + \Delta n_{\rm ac}(r,\phi,x)\cos\left(\frac{2\pi}{\Lambda}x + \theta(x)\right) + \Delta n_{\rm dc}(r,\phi,x), \tag{5.23}$$

where $\Delta n_{\rm ac}(r,\phi,x)$, $\Delta n_{\rm dc}(r,\phi,x)$, and $\theta(x)$ are slowly varying with x over a distance Λ. We assume that $\Delta n_{\rm ac}(r,\phi,x) \ll \bar{n}$, and $\Delta n_{\rm dc}(r,\phi,x) \ll \bar{n}$, which is the case for practical fiber gratings. The total electric field must satisfy the scalar wave-equation for the perturbed fiber, i.e.,

$$\left\{\nabla_{\rm t}^2 + \frac{\partial^2}{\partial x^2} + k^2 n^2(r,\phi,x)\right\} E(r,\phi,x) = 0. \tag{5.24}$$

We now substitute (5.22) into (5.24), take (5.21) into account, and multiply the resulting equation by $\Psi_q(r,\phi)$. By integration over the entire transversal plane, and recalling that the modes are orthonormal, the resulting set of second order differential equations can be decomposed into first order coupled mode equations [6],

$$\frac{{\rm d}b_p^+}{{\rm d}x} - i\beta_p b_p^+ = i\sum_{q=1}^{P} \mathcal{C}_{pq}(x)(b_q^+(x) + b_q^-(x)), \tag{5.25a}$$

$$\frac{{\rm d}b_p^-}{{\rm d}x} + i\beta_p b_p^- = -i\sum_{q=1}^{P} \mathcal{C}_{pq}(x)(b_q^+(x) + b_q^-(x)), \tag{5.25b}$$

where

$$\mathcal{C}_{pq}(x) = \frac{k}{2n_p}\int_{A_\infty} (n^2(r,\phi,x) - \bar{n}^2(r))\Psi_p(r,\phi)\Psi_q(r,\phi){\rm d}A. \tag{5.26}$$

Note that the frequency-dependence of (5.26) can be ignored in practice, since the normalized bandwidth of interest is usually much less than unity, and the field profiles and effective indices are approximately constant in this bandwidth. Also note that since the fiber is assumed to be weakly guiding, n_p can be set equal to $n_{\rm co}$; thus $\mathcal{C}_{pq} = \mathcal{C}_{qp}$.

In the case of a quasi-periodic structure it is natural to write the coupling coefficient as a quasi-Fourier series:

$$\begin{aligned}\mathcal{C}_{pq}(x) = \sigma_{pq}(x) + \kappa_{pq}(x)\exp\left(i\frac{2\pi}{\Lambda}x\right) + \kappa_{pq}^{*}(x)\exp\left(-i\frac{2\pi}{\Lambda}x\right) \\ + \sum_{|m|\geq 2}\kappa_{pq}^{(m)}(x)\exp\left(i\frac{2\pi m}{\Lambda}x\right),\end{aligned} \tag{5.27}$$

where the "Fourier coefficients" $\kappa_{pq}(x)$, $\sigma_{pq}(x)$, and $\kappa_{pq}^{(m)}(x)$ are slowly varying over a period Λ. For a fiber grating the index modulation $n(r,\phi,x)-\bar{n}(r)$ is given by (5.23) and is small compared to $\bar{n}(r)$, so the zeroth and first order Fourier components dominate. Note that $\arg\{\kappa_{pq}(x)\} = \theta(x)$.

The field amplitudes $b_p^{\pm}(x)$ vary rapidly; it is therefore convenient to introduce the slowly varying field envelopes $u_p(x)$ and $v_p(x)$ by setting

$$b_p^{+}(x) = i^{1/2}u_p(x)\exp\left(i\frac{\pi}{\Lambda}x\right)\exp\left(i\frac{\theta(x)}{2}\right), \tag{5.28a}$$

$$b_p^{-}(x) = i^{-1/2}v_p(x)\exp\left(-i\frac{\pi}{\Lambda}x\right)\exp\left(-i\frac{\theta(x)}{2}\right). \tag{5.28b}$$

Since an identical phase factor is removed from all modes, the reflection response as calculated from b_p^{+} and b_q^{-} will only differ from that calculated from u_p and v_q by a constant phase factor not dependent on p and q. Inserting (5.27) and (5.28) into (5.25), and ignoring rapidly oscillating terms (since they contribute little to $\mathrm{d}u_p/\mathrm{d}x$ and $\mathrm{d}v_p/\mathrm{d}x$), we obtain an alternative set of coupled-mode equations

$$\begin{aligned}\frac{\mathrm{d}u_p(x;\omega)}{\mathrm{d}x} &= i\delta_p(\omega)u_p(x;\omega) - i\frac{1}{2}\frac{\mathrm{d}\theta(x)}{\mathrm{d}x}u_p(x;\omega) \\ &\quad + i\sum_{q=1}^{P}\sigma_{pq}(x)u_q(x;\omega) + \sum_{q=1}^{P}|\kappa_{pq}(x)|v_q(x;\omega),\end{aligned} \tag{5.29a}$$

$$\begin{aligned}\frac{\mathrm{d}v_p(x;\omega)}{\mathrm{d}x} &= -i\delta_p(\omega)v_p(x;\omega) + i\frac{1}{2}\frac{\mathrm{d}\theta(x)}{\mathrm{d}x}v_p(x;\omega) \\ &\quad - i\sum_{q=1}^{P}\sigma_{pq}(x)v_q(x;\omega) + \sum_{q=1}^{P}|\kappa_{pq}(x)|u_q(x;\omega),\end{aligned} \tag{5.29b}$$

where $\delta_p = \beta_p - \pi/\Lambda = n_p\omega/c - \pi/\Lambda$ is the wavenumber detuning of mode p. Thus, $-i|\kappa_{pq}(x)|$ is the coupling coefficient between modes p and q propagating in opposite directions, while $\sigma_{pq}(x) - \delta(p-q)(\mathrm{d}\theta(x)/\mathrm{d}x)/2$ is the coupling coefficient between modes p and q in the same direction. With $\boldsymbol{E} = [u_1, u_2, \ldots, u_P, v_1, v_2, \ldots, v_P]^{\mathrm{T}}$ we find that (5.29) coincides with (5.1), where $\sigma_{pq}(x) - \delta(p-q)(\mathrm{d}\theta(x)/\mathrm{d}x)/2$ and $-i|\kappa_{pq}(x)|$ are the (p,q)-elements of $\boldsymbol{\sigma}$ and $\boldsymbol{\kappa}$, respectively, and δ_p are the diagonal elements of $\boldsymbol{\beta}$. Note that (5.4) no longer is valid since δ_p are not the actual propagation constants but rather their detuning from π/Λ. Approximating the effective indices by n_{co}, this means that the bandwidth of interest is not centered about zero

but rather about the "design frequency" $\omega_0 \equiv \pi c/(n_{\rm co}\Lambda)$. The frequency interval of integration in (5.16) should be centered about ω_0. As in the scalar case [40], we also note that in general, the geometrical phase variation $\theta(x)$ cannot be distinguished from the phase variation associated with the dc index term $\Delta n_{\rm dc}(r,\phi,x)$.

We observe that $\boldsymbol{\sigma}$ is real and symmetric, and $\boldsymbol{\kappa}$ is imaginary and symmetric. Moreover, it is not difficult to realize that $i\boldsymbol{\kappa}$ is positive semidefinite.[4] Thus $\boldsymbol{\Phi}_j$ defined in (5.7) is unitary and symmetric, and $-\boldsymbol{\rho}_j$ is real and positive semidefinite. It follows that we can use the layer-stripping method together with the factorization approach c), as given in Section 5.3, to identify the coupling sections $\boldsymbol{\rho}_j$ and $\boldsymbol{\Phi}_j$ (and therefore the coupling matrices $\boldsymbol{\kappa}$ and $\boldsymbol{\sigma}$ as a function of position x). Since $(i\boldsymbol{\Phi}_j)^{\rm T}(-\boldsymbol{\rho}_j)(i\boldsymbol{\Phi}_j) = \boldsymbol{\Phi}_j^{\rm T}\boldsymbol{\rho}_j\boldsymbol{\Phi}_j$, the factorization approach gives $-\boldsymbol{\rho}_j$ and $i\boldsymbol{\Phi}_j$.

For a fiber grating it is usually reasonable to assume that the ac and dc index modulations can be written in the forms $\Delta n_{\rm ac}(r,\phi,x) = \Delta n(r,\phi)\Delta n_{\rm ac}(x)$ and $\Delta n_{\rm dc}(r,\phi,x) = \Delta n(r,\phi)\Delta n_{\rm dc}(x)$, respectively. Here $\Delta n(r,\phi)$ accounts for the transversal variation of the index modulation profile, and $\Delta n_{\rm ac}(x)$ and $\Delta n_{\rm dc}(x)$ are the ac and dc modulations as a function of x. As before, we assume that the index modulation and $n_{\rm co} - n_{\rm cl}$ are small, yielding

$$\boldsymbol{\kappa}(x) = -i\Delta n_{\rm ac}(x)\boldsymbol{\eta}, \tag{5.30a}$$

$$\boldsymbol{\sigma}(x) = \Delta n_{\rm dc}(x)\boldsymbol{\eta} - \frac{1}{2}\frac{{\rm d}\theta(x)}{{\rm d}x}\boldsymbol{I}, \tag{5.30b}$$

where $\boldsymbol{\eta}$ is independent on x. The elements of $\boldsymbol{\eta}$ are

$$\eta_{pq} = k\int_{A_\infty} \Delta n(r,\phi)\Psi_p\Psi_q {\rm d}A. \tag{5.31}$$

When the mode profiles and $\Delta n(r,\phi)$ are known, this means that the entire coupling matrix $\boldsymbol{\kappa}(x)$ is determined from only a single nonvanishing element. For $\boldsymbol{\sigma}$, two elements are needed (one diagonal and one off-diagonal element). Note that in this case, it is indeed possible to distinguish between the dc index modulation $\Delta n_{\rm dc}(x)$ and the geometrical phase variation ${\rm d}\theta(x)/{\rm d}x$.

A potential application of the multimode layer-stripping method is to characterize coupling from the core mode to cladding modes in a single mode fiber. Cladding modes are modes that not bounded with in the core of the fiber, but by the cladding/air boundary [74]. The power in these modes will eventually be lost to the environment. The resonant wavelength of the core-cladding mode coupling is shorter than that of the core-core mode coupling, and will not affect the reflection spectrum of a narrow-band grating. However, the core-cladding mode coupling can be seen clearly in the transmission spectra of strong gratings. For chirped gratings [75] and chirped, sampled gratings [76] for filtering and dispersion compensation in dense wavelength-division multiplexed optical communication systems, the bandwidth may become larger than the separation in wavelength between the core-core

[4]The real matrix given by the elements $\Psi_p\Psi_q$ is clearly positive semidefinite, since $\sum_{p,q} a_p\Psi_p\Psi_q a_q = (\sum_p \Psi_p a_p)^2 \geq 0$ for any real a_p. For a fiber grating $\Delta n_{\rm ac}(r,\phi,x) \geq 0$ for all r and ϕ; thus $|\kappa_{pq}(x)|$ adopts the positive semidefinite property from $\Psi_p\Psi_q$.

mode coupling and the core-cladding mode coupling. Then the core-cladding mode coupling will also affect the reflection spectrum of the grating [77]. This unwanted coupling is often handled by writing the grating in fibers with depressed cladding modes [78]. There has also been some attempts of taking into account the core-cladding mode coupling in the design of the grating [79, 80]. Here, direct scattering is treated with multiple mode coupling, but the inverse scattering is purely single-mode. The layer-stripping algorithm described in Section 5.3 can both be used for characterization of such coupling and possibly for design. In contrast to the methods in [79, 80], multiple modes can be taken into account in the inverse scattering part of an iterative design process.

5.4.2 Discrete coupling structures

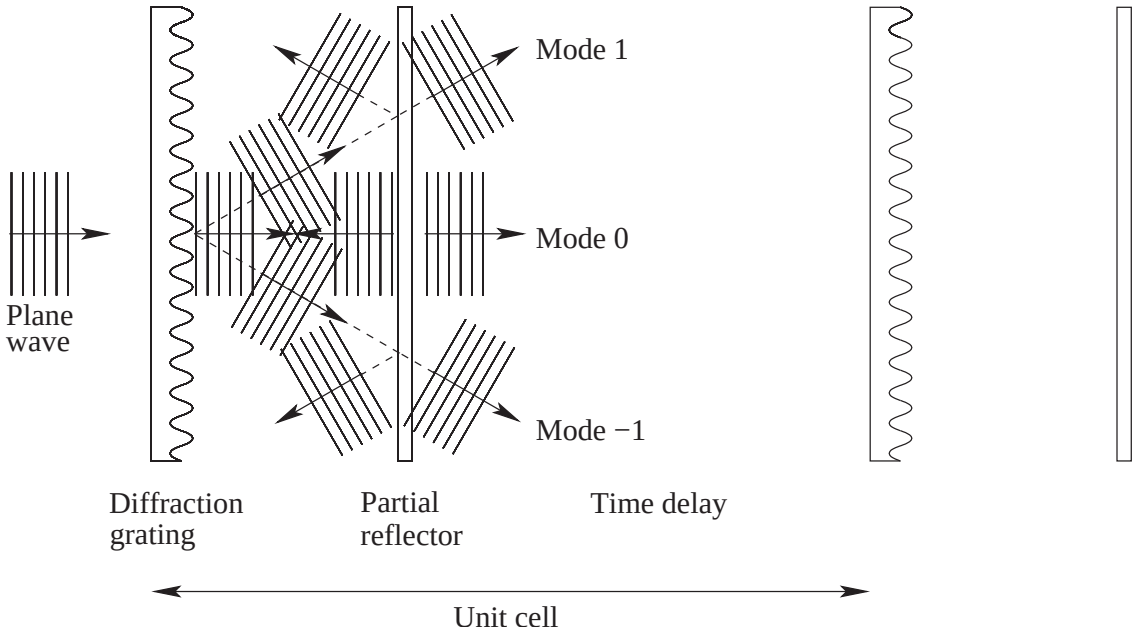

Figure 5.1: Coupling in 2D discrete diffraction/reflection structure.

A true discrete, multimode scattering structure can be viewed as an arrayed digital lattice filter structure. To illustrate discrete scattering in a physical example, consider the 2D structure depicted in Fig. 5.1. A plane wave is transmitted through a diffraction grating. The diffraction grating is assumed periodic and infinite in the vertical direction. The wave is diffracted into a finite number of propagating modes, characterized by their vertical (transversal) wavenumber. The diffraction grating is immediately followed by a partial reflector, which partially reflects the field in a particular mode into the same mode in the opposite x-direction. The waves transmitted through the reflector are transmitted through a free-space section of length Δx.

The total structure consists of a cascade of such layers. The reflectivity of the reflectors may be different from layer to layer. The detailed structure of the diffrac-

tion gratings may also be different; however, the period should be identical. Also the free-space sections are assumed identical for all layers.

Although the structure is 2D, the field is only contained in a discrete set of directions. Thus in practice, the scattering can be treated as 1D with a finite number of modes, characterized by their transversal wavenumber. The diffraction gratings, the reflectors, and the free-space sections represent $\boldsymbol{\Phi}_j$, $\boldsymbol{\rho}_j$, and $\boldsymbol{Z}^{-1}$, respectively. Here $\boldsymbol{\Phi}_j$ is unitary, and $\boldsymbol{\rho}_j$ is diagonal and negative; thus in the layer-stripping algorithm, the factorization b) is applicable (yielding $-\boldsymbol{\rho}_j$ and $i\boldsymbol{\Phi}_j$). In the absence of diffraction gratings, we simply obtain $\boldsymbol{\Upsilon}_j = \boldsymbol{\rho}_j$ (factorization a)).

There are two complications. First, we must choose the modes such that the transversal mode profiles can be written real. This is done to ensure that reciprocity implies symmetrical scattering matrices (see the next example for details). Second, to use the layer-peeling algorithm, $\boldsymbol{\rho}_j$ and $\boldsymbol{\Phi}_j$ must be approximately independent on frequency in the bandwidth of interest.

5.4.3 Analogies to 3D inverse scattering

An important inverse scattering problem is the three-dimensional problem associated with the Schrödinger equation [81],

$$\left\{\nabla^2 + k^2 - V(x,y,z)\right\}\psi(x,y,z;k) = 0, \tag{5.32}$$

where $\psi(x,y,z,k)$ is the wave function and $V(x,y,z)$ is a smooth and positive potential with compact support. In particular, solutions to this problem is applicable to inverse seismic scattering. This problem has been solved using a generalized Marchenko method in [81] and [82], while layer-stripping solutions are suggested in [70] and [71]. The example in Section 5.4.2 indicates that inverse scattering in more than one dimension is possible with the algorithm in Section 5.3. When the diffraction grating is not periodic, the incident light will be scattered in all directions. By representing each direction as a mode, an infinite number of modes are involved in the scattering. Note the close resemblance between (5.32) and (5.24), indicating that a similar method as that in Subsection 5.4.1 can be used.

We express the solution as a superposition of the eigenmodes of the Schrödinger equation with $V(x,y,z) = 0$. Writing $\psi(x,y,z;k) = \Psi(y,z;k_y,k_z)\exp(ik_x x)$, these eigenmodes are given by

$$\Psi(y,z;k_y,k_z) = \exp(i(k_y y + k_z z)), \tag{5.33}$$

where k_y and k_z are the wave numbers in y-direction and z-direction, respectively, and $k^2 = k_x^2 + k_y^2 + k_z^2$.

In a discrete model, the wavenumbers k_y and k_z can for example be discretized in equal intervals Δk, such that $k_y = p\Delta k$ and $k_z = q\Delta k$. In the yz-plane, this means that only a principal range $(-\pi/\Delta k, \pi/\Delta k)$ is considered, and the fields are extended periodically outside this range. The integers p and q are the modal indices satisfying $p^2 + q^2 \leq (k/\Delta k)^2$ for propagating (not evanescent) modes. The modal field profiles are written in normalized form $\Psi_{pq}(y,z) = (\Delta k/2\pi)\Psi(y,z;p\Delta k, q\Delta k)$.

The total field $\psi(x, y, z; k)$ is expressed as the superposition

$$\psi(x, y, z; k) = \sum_{p,q} (b^+_{pq}(x; k) + b^-_{pq}(x; k))\Psi_{pq}(y, z), \tag{5.34}$$

where $b^\pm_{pq}(x; k)$ includes all x-dependence of the fields, and $\pm$ indicate the sign of k_x, i.e, the propagation direction of the mode.

As in Section 5.4.1, we insert (5.34) into (5.32), multiply by $\Psi^*_{pq}(y, z)$ and integrate over the principal range of the yz-plane. This leads to the coupled mode equations

$$\frac{\mathrm{d}b^+_{pq}(x; k)}{\mathrm{d}x} - ik_{x,pq}b^+_{pq}(x; k) = i\sum_{r,s} \mathcal{C}_{pq,rs}(x)(b^+_{rs}(x; k) + b^-_{rs}(x; k)), \tag{5.35a}$$

$$\frac{\mathrm{d}b^-_{pq}(x; k)}{\mathrm{d}x} + ik_{x,pq}b^-_{pq}(x; k) = -i\sum_{r,s} \mathcal{C}_{pq,rs}(x)(b^+_{rs}(x; k) + b^-_{rs}(x; k)), \tag{5.35b}$$

where the coupling coefficients are given by

$$\begin{aligned} \mathcal{C}_{pq,rs}(x) &= -\frac{1}{2k_x}\int \Psi^*_{pq}(y, z)V(x, y, z)\Psi_{rs}(y, z)\mathrm{d}y\mathrm{d}z \\ &= -\frac{1}{2k_x}\left(\frac{\Delta k}{2\pi}\right)^2 \int V(x, y, z)\exp\left[i\Delta k((r - p)y + (s - q)z)\right]\mathrm{d}y\mathrm{d}z, \end{aligned} \tag{5.36}$$

and $k_{x,pq} = [k^2 - (\Delta k)^2(p^2 + q^2)]^{1/2}$. In the case where $V(x, y, z)$ is quasi-periodic along the x-direction, expansions of $b_{pq}(x; k)$ as in (5.27) together with the transformation (5.28) can be used. We assume that $C_{pq,rs}(x)$ is approximately independent on frequency in the bandwidth of interest (i.e., that this bandwidth is small). Moreover, in order to use the physical reflection spectrum as input to the discrete algorithm in a straightforward manner, the involved modes should have similar $k_{x,pq}$'s (see Section 5.2).

The coupled mode equations in (5.35) can be written in vectorized form as in Section 5.2; then $k_{x,pq}$ are the diagonal elements of $\boldsymbol{\beta}$. However, in order to use the factorization methods developed in Section 5.3, we must ensure that the reciprocity theorem implies symmetrical scattering matrices. This is guaranteed when the mode profiles can be written real. Thus we should define real mode fields $\tilde{\Psi}_{pq}$ by the transformation

$$\begin{bmatrix} \tilde{\boldsymbol{\Psi}}_{++} \\ \tilde{\boldsymbol{\Psi}}_{-+} \\ \tilde{\boldsymbol{\Psi}}_{+-} \\ \tilde{\boldsymbol{\Psi}}_{--} \end{bmatrix} = \mathbf{M}\begin{bmatrix} \boldsymbol{\Psi}_{++} \\ \boldsymbol{\Psi}_{-+} \\ \boldsymbol{\Psi}_{+-} \\ \boldsymbol{\Psi}_{--} \end{bmatrix}, \quad \mathbf{M} = \frac{1}{2}\begin{bmatrix} \boldsymbol{I} & \boldsymbol{I} & \boldsymbol{I} & \boldsymbol{I} \\ -i\boldsymbol{I} & +i\boldsymbol{I} & -i\boldsymbol{I} & +i\boldsymbol{I} \\ -i\boldsymbol{I} & -i\boldsymbol{I} & +i\boldsymbol{I} & +i\boldsymbol{I} \\ -\boldsymbol{I} & \boldsymbol{I} & \boldsymbol{I} & -\boldsymbol{I} \end{bmatrix}. \tag{5.37}$$

Here, $\boldsymbol{\Psi}_{++}$ denotes a column vector containing the modal field amplitudes with positive p and q; $\boldsymbol{\Psi}_{-+}$ denotes a column vector containing the modal field amplitudes with negative p and positive q, and so forth. The dimension of the identity matrices in the blocks of $\mathbf{M}$ corresponds to the dimension of $\boldsymbol{\Psi}_{++}$. In the transformed basis,

we can express (5.35) in vector form. By comparing to (5.1), we obtain that $\boldsymbol{\kappa} = \boldsymbol{\sigma} = \mathbf{M}^*\mathcal{C}\mathbf{M}^{\mathrm{T}}$, where $\mathcal{C}$ is the matrix formed by the elements $\mathcal{C}_{pq,rs}$. Eq. (5.36) shows that $\boldsymbol{\kappa} = \boldsymbol{\sigma}$ is real. Further inspection of (5.36) gives that $-\mathcal{C}$ and therefore $-\boldsymbol{\kappa} = -\boldsymbol{\sigma}$ are positive semidefinite (recall that $V(x, y, z) \geq 0$). Thus $\boldsymbol{\Phi}_j$ is unitary and symmetric, and $i\boldsymbol{\rho}_j$ is real and positive semidefinite. The layer-stripping method with the factorization c), as described in Section 5.3, can therefore be applied to the identification of $\boldsymbol{\rho}_j$ and $\boldsymbol{\Phi}_j$. (The factorization method gives $i\boldsymbol{\rho}_j$ and $\sqrt{-i}\boldsymbol{\Phi}_j$.) The required input data is the reflection response upon excitation of the different plane waves onto the plane $x = 0$. The scattering potential $V(x, y, z)$ is found from the inverse of (5.36).

The multimode layer-stripping algorithm applied to the 3D case has similarities to the method in [72]. Although the present method is somewhat more complex, it may be useful in the case where the potential is quasi-periodic. By performing a transformation similar to that in Section 5.4.1, the spatial resolution in x-direction does only be sufficiently large to represent the slowly varying potential envelope, not the potential itself.

5.5 Conclusion

A layer-stripping method for the inverse scattering of multi-mode structures has been proposed. Ambiguities related to factorization of each layer's response into codirectional and contradirectional coupling have been discussed. When there are no codirectional coupling, the ambiguities disappear. Also, when the structure to be reconstructed is smooth, there are important cases with simultaneous co- and contradirectional coupling that can be reconstructed uniquely, provided the reflector eigenvalues are nonzero and nondegenerate. Applications to quasi-periodical structures and 3D structures have been discussed.

5.A Some matrix properties

5.A.1 Spectral decomposition of symmetrical normal matrices

Any normal matrix $\boldsymbol{N}$ can be written

$$\boldsymbol{N} = \boldsymbol{U}\boldsymbol{\Lambda}\boldsymbol{U}^{\dagger}, \tag{5.38}$$

where $\boldsymbol{\Lambda}$ is diagonal and $\boldsymbol{U}$ is unitary (spectral decomposition), and the superscript $\dagger$ denotes Hermitian conjugate. Since $\boldsymbol{N}$ is assumed to be symmetric, $\boldsymbol{U}\boldsymbol{\Lambda}\boldsymbol{U}^{\dagger} = \boldsymbol{U}^*\boldsymbol{\Lambda}\boldsymbol{U}^{\mathrm{T}}$, which leads to

$$\boldsymbol{U}^{\dagger}\boldsymbol{U}^*\boldsymbol{\Lambda} = \boldsymbol{\Lambda}\boldsymbol{U}^{\dagger}\boldsymbol{U}^*. \tag{5.39}$$

Define the unitary, symmetric matrix $\boldsymbol{V} \equiv \boldsymbol{U}^{\dagger}\boldsymbol{U}^*$. According to (5.39), $\boldsymbol{V}$ and $\boldsymbol{\Lambda}$ can be diagonalized in the same basis. Expressing the square root of $\boldsymbol{V}$ in this basis, we find

$$\sqrt{\boldsymbol{V}}\boldsymbol{\Lambda} = \boldsymbol{\Lambda}\sqrt{\boldsymbol{V}}. \tag{5.40}$$

Note that $\sqrt{\boldsymbol{V}}$ can be chosen symmetric since $\boldsymbol{V}$ is symmetric. Thus from $\boldsymbol{V} = \boldsymbol{U}^\dagger\boldsymbol{U}^*$ we find that $\boldsymbol{U}\sqrt{\boldsymbol{V}} = \boldsymbol{U}^*\sqrt{\boldsymbol{V}}^*$, so $\boldsymbol{P} \equiv \boldsymbol{U}\sqrt{\boldsymbol{V}}$ is real. Using (5.40),

$$\boldsymbol{N} = \boldsymbol{U}\boldsymbol{\Lambda}\boldsymbol{V}\boldsymbol{U}^{\mathrm{T}} = \boldsymbol{U}\sqrt{\boldsymbol{V}}\boldsymbol{\Lambda}\sqrt{\boldsymbol{V}}\boldsymbol{U}^{\mathrm{T}} = \boldsymbol{P}\boldsymbol{\Lambda}\boldsymbol{P}^{\mathrm{T}}. \tag{5.41}$$

The eigenvalue matrix $\boldsymbol{\Lambda}$ is unique up to reordering of the eigenvalues. When the order of the eigenvalues is established, $\boldsymbol{P}$ is unique up to the replacement $\boldsymbol{P}\boldsymbol{J} \to \boldsymbol{P}$, where $\boldsymbol{J}$ is a real, unitary matrix satisfying $\boldsymbol{P}\boldsymbol{J}\boldsymbol{\Lambda}(\boldsymbol{P}\boldsymbol{J})^{\mathrm{T}} = \boldsymbol{P}\boldsymbol{\Lambda}\boldsymbol{P}^{\mathrm{T}}$. This leads to that $\boldsymbol{J}$ commutes with $\boldsymbol{\Lambda}$. Thus, $\boldsymbol{J}$ operates nontrivially only on dimensions corresponding to repeated eigenvalues. If the eigenvalues in $\boldsymbol{\Lambda}$ is sorted in, say, descending order, $\boldsymbol{J}$ is a block-diagonal matrix, where each block is a real unitary matrix with a dimension equal to the number of corresponding repeated eigenvalues. For a non-repeated eigenvalue, the corresponding block of $\boldsymbol{J}$ is either 1 or -1.

5.A.2 Singular value decomposition of symmetrical matrices

We are interested in the most general form of an arbitrary, complex, symmetric matrix $\boldsymbol{\Upsilon}$. By using singular value decomposition, we can write

$$\boldsymbol{\Upsilon} = \boldsymbol{V}_1\boldsymbol{\Sigma}\boldsymbol{V}_2, \tag{5.42}$$

where $\boldsymbol{V}_{1,2}$ are unitary, and $\boldsymbol{\Sigma}$ is diagonal and nonnegative. Since $\boldsymbol{\Upsilon}$ is symmetric, we find that

$$\boldsymbol{W}\boldsymbol{\Sigma} = \boldsymbol{\Sigma}\boldsymbol{W}^{\mathrm{T}}, \tag{5.43}$$

where $\boldsymbol{W} \equiv \boldsymbol{V}_2^*\boldsymbol{V}_1$. We also have that $(\boldsymbol{\Upsilon}\boldsymbol{\Upsilon}^\dagger)^{\mathrm{T}} = \boldsymbol{\Upsilon}^\dagger\boldsymbol{\Upsilon}$, which gives $\boldsymbol{W}\boldsymbol{\Sigma}^2 = \boldsymbol{\Sigma}^2\boldsymbol{W}$ and therefore

$$\boldsymbol{W}\boldsymbol{\Sigma} = \boldsymbol{\Sigma}\boldsymbol{W}. \tag{5.44}$$

By comparing this result with (5.43),

$$\boldsymbol{\Sigma}\boldsymbol{W} = \boldsymbol{\Sigma}\boldsymbol{W}^{\mathrm{T}}. \tag{5.45}$$

Thus, provided all singular values are non-zero, $\boldsymbol{W}$ is symmetric. Since $\sqrt{\boldsymbol{W}}$ can be chosen such that it commutes with $\boldsymbol{\Sigma}$ and is symmetric, we obtain $\boldsymbol{\Upsilon} = \boldsymbol{V}_2^{\mathrm{T}}\boldsymbol{W}\boldsymbol{\Sigma}\boldsymbol{V}_2 = (\sqrt{\boldsymbol{W}}\boldsymbol{V}_2)^{\mathrm{T}}\boldsymbol{\Sigma}\sqrt{\boldsymbol{W}}\boldsymbol{V}_2$. Thus we can write

$$\boldsymbol{\Upsilon} = \boldsymbol{U}^{\mathrm{T}}\boldsymbol{\Sigma}\boldsymbol{U}, \tag{5.46}$$

where $\boldsymbol{U} \equiv \sqrt{\boldsymbol{W}}\boldsymbol{V}_2$ is unitary and $\boldsymbol{\Sigma}$ is diagonal and positive.

If one or more of the singular values are zero, i.e. the matrix $\boldsymbol{\Upsilon}$ is singular, we write

$$\boldsymbol{\Sigma} = \begin{bmatrix} \boldsymbol{\Sigma}' & \boldsymbol{0} \\ \boldsymbol{0} & \boldsymbol{0} \end{bmatrix} \qquad \text{and} \qquad \boldsymbol{W} = \begin{bmatrix} \boldsymbol{W}_{11} & \boldsymbol{W}_{12} \\ \boldsymbol{W}_{21} & \boldsymbol{W}_{22} \end{bmatrix}, \tag{5.47}$$

where we have arranged $\boldsymbol{\Sigma}$ so that the zero singular values are the last ones, $\boldsymbol{\Sigma}'$ is a diagonal matrix with the nonzero singular values, and $\boldsymbol{W}_{11}$ has the same dimension as $\boldsymbol{\Sigma}'$. Using (5.44) we find $\boldsymbol{\Sigma}'\boldsymbol{W}_{11} = \boldsymbol{W}_{11}\boldsymbol{\Sigma}'$ and $\boldsymbol{W}_{12} = \boldsymbol{W}_{21} = \boldsymbol{0}$, and (5.45)

gives that $\boldsymbol{W}_{11} = \boldsymbol{W}_{11}^{\mathrm{T}}$. The commutation relations do not provide any information on $\boldsymbol{W}_{22}$. Choose $\sqrt{\boldsymbol{W}}$ such that

$$\sqrt{\boldsymbol{W}} = \begin{bmatrix} \sqrt{\boldsymbol{W}_{11}} & \boldsymbol{0} \\ \boldsymbol{0} & \sqrt{\boldsymbol{W}_{22}} \end{bmatrix}, \tag{5.48}$$

where $\sqrt{\boldsymbol{W}_{11}}$ is symmetric and $\sqrt{\boldsymbol{W}_{11}}$ and $\boldsymbol{\Sigma}'$ commute. Write $\boldsymbol{\Upsilon} = \boldsymbol{U}_1^{\mathrm{T}} \boldsymbol{\Sigma} \boldsymbol{U}_2$, with

$$\boldsymbol{U}_1 = \sqrt{\boldsymbol{W}}^{\mathrm{T}} \boldsymbol{V}_2 = \begin{bmatrix} \boldsymbol{U}' \\ \boldsymbol{U}_1'' \end{bmatrix} \tag{5.49}$$

$$\boldsymbol{U}_2 = \sqrt{\boldsymbol{W}} \boldsymbol{V}_2 = \begin{bmatrix} \boldsymbol{U}' \\ \boldsymbol{U}_2'' \end{bmatrix}. \tag{5.50}$$

The matrices $\boldsymbol{U}_1''$ and $\boldsymbol{U}_2''$ are the rows of $\boldsymbol{U}_1$ and $\boldsymbol{U}_2$ that correspond to the zero singular values, and they do not give any contribution to $\boldsymbol{\Upsilon}$. We may therefore replace the rows $\boldsymbol{U}_1''$ by $\boldsymbol{U}_2''$, which gives $\boldsymbol{U}_1 = \boldsymbol{U}_2 = \boldsymbol{U}$.

The matrix $\boldsymbol{\Sigma}$ is unique up to reordering of the singular values. When the order of the singular values is established, $\boldsymbol{U}$ is unique up to the replacement $\boldsymbol{J}\boldsymbol{U} \rightarrow \boldsymbol{U}$, where $\boldsymbol{J}$ is a unitary matrix satisfying $(\boldsymbol{J}\boldsymbol{U})^{\mathrm{T}} \boldsymbol{\Sigma} \boldsymbol{J} \boldsymbol{U} = \boldsymbol{U}^{\mathrm{T}} \boldsymbol{\Sigma} \boldsymbol{U}$. This leads to $\boldsymbol{J}^{\mathrm{T}} \boldsymbol{\Sigma} \boldsymbol{J} = \boldsymbol{\Sigma}$. Assuming the singular values are sorted in, say, descending order, we find that $\boldsymbol{J}$ is a unitary block-diagonal matrix, where each block has a dimension equal to the number of corresponding repeated singular values. For zero singular values, the corresponding block in $\boldsymbol{J}$ is an arbitrary unitary matrix. For repeated non-zero singular values, the corresponding block in $\boldsymbol{J}$ is real. For a distinct, non-zero singular value, the corresponding block of $\boldsymbol{J}$ is either 1 or -1.

5.A.3 Factorization of a unitary matrix into a symmetrical matrix and a orthogonal matrix

We will show that a unitary matrix $\boldsymbol{U}$ can be factorized into $\boldsymbol{U} = \boldsymbol{P}\boldsymbol{Q}$, where $\boldsymbol{P}$ is a real unitary matrix (orthogonal matrix) and $\boldsymbol{Q}$ is a symmetrical unitary matrix. The matrix $\boldsymbol{Q}$ can be factorized into $\boldsymbol{Q} = \boldsymbol{P}_1 \boldsymbol{D} \boldsymbol{P}_1^{\mathrm{T}}$ using spectral decomposition (Appendix 5.A.1) where $\boldsymbol{D}$ is a diagonal unitary matrix and $\boldsymbol{P}_1$ is a real unitary matrix. Thus, an equivalent problem is to show that

$$\boldsymbol{U} = \boldsymbol{P}_2 \boldsymbol{D} \boldsymbol{P}_1^{\mathrm{T}}, \tag{5.51}$$

where $\boldsymbol{P}_2 = \boldsymbol{P}\boldsymbol{P}_1$. The decomposition in (5.51) is very similar to singular value decomposition of real matrices, except that $\boldsymbol{D}$ may have complex elements.

The matrix $\boldsymbol{U}^{\mathrm{T}}\boldsymbol{U}$ is symmetric; thus using spectral decomposition (Appendix 5.A.1), we have

$$\boldsymbol{U}^{\mathrm{T}} \boldsymbol{U} = \boldsymbol{P}_1 \boldsymbol{\Lambda} \boldsymbol{P}_1^{\mathrm{T}}, \tag{5.52}$$

where $\boldsymbol{P}_1$ is a real unitary matrix and $\boldsymbol{\Lambda}$ is a diagonal unitary matrix. Define

$$\boldsymbol{P}_2 = \boldsymbol{U} \boldsymbol{P}_1 \boldsymbol{D}^*, \tag{5.53}$$

where the diagonal matrix $\boldsymbol{D}$ is a solution to $\boldsymbol{D}^2 = \boldsymbol{\Lambda}$. The matrix $\boldsymbol{P}_2$ is unitary since it is produced by multiplication of unitary matrices. The matrix is also real since

$$\boldsymbol{P}_2 = \boldsymbol{P}_2^* \boldsymbol{P}_2^{\mathrm{T}} \boldsymbol{P}_2 = \boldsymbol{P}_2^* \boldsymbol{D}^* \boldsymbol{P}_1^{\mathrm{T}} \boldsymbol{U}^{\mathrm{T}} \boldsymbol{U} \boldsymbol{P}_1 \boldsymbol{D}^* = \boldsymbol{P}_2^* \boldsymbol{D}^* \boldsymbol{P}_1^{\mathrm{T}} \boldsymbol{P}_1 \boldsymbol{D}^2 \boldsymbol{P}_1^{\mathrm{T}} \boldsymbol{P}_1 \boldsymbol{D}^* = \boldsymbol{P}_2^*. \quad (5.54)$$

From (5.53) we therefore conclude that the decomposition (5.51), with real unitary $\boldsymbol{P}_1$ and $\boldsymbol{P}_2$ and diagonal $\boldsymbol{D}$, is always possible. It follows that any unitary matrix can be written $\boldsymbol{U} = \boldsymbol{P}\boldsymbol{Q}$, where $\boldsymbol{P}$ is real and unitary, and $\boldsymbol{Q}$ is symmetric and unitary. Note that any global phase of $\boldsymbol{P}$ can instead be assigned to $\boldsymbol{Q}$, so without loss of generality we can assume that $\boldsymbol{P}$ is special ($\det \boldsymbol{P} = 1$ and $\det \boldsymbol{Q} = \det \boldsymbol{U}$).

Since $\boldsymbol{D}$ is calculated from $\boldsymbol{D}^2 = \boldsymbol{\Lambda}$, the sign of its elements are arbitrary. The ambiguities when determining $\boldsymbol{P}_1$ in (5.52) give rise to ambiguities in $\boldsymbol{P}$ and $\boldsymbol{Q}$. The possible $\boldsymbol{P}$ and $\boldsymbol{Q}$ can be expressed as $\boldsymbol{P} = \boldsymbol{U}\boldsymbol{P}_1\boldsymbol{J}\boldsymbol{D}^*\boldsymbol{J}^{\mathrm{T}}\boldsymbol{P}_1^{\mathrm{T}}$ and $\boldsymbol{Q} = \boldsymbol{P}_1\boldsymbol{J}\boldsymbol{D}\boldsymbol{J}^T\boldsymbol{P}_1^{\mathrm{T}}$ for a real unitary $\boldsymbol{J}$ that commutes with $\boldsymbol{D}^2$. Here $\boldsymbol{P}_1$ is fixed. If the signs of the elements of $\boldsymbol{D}$ are known to be such that any equal elements of $\boldsymbol{D}^2$ correspond to equal elements of $\boldsymbol{D}$, then $\boldsymbol{J}$ commutes with $\boldsymbol{D}$ and can be ignored.

5.B Linear, reciprocal and lossless components

Consider a linear component with P input and P output modes on the left-hand side, and also P input and P output modes on the right-hand side, see Fig. 5.2. The component is completely characterized by the $2P \times 2P$ dimensional scattering

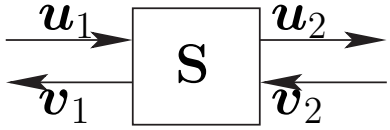

Figure 5.2: A linear component with P input and P output modes on each side.

matrix $\mathbf{S}$ which relates the input and output fields:

$$\begin{bmatrix} \boldsymbol{v}_1 \\ \boldsymbol{u}_2 \end{bmatrix} = \mathbf{S} \begin{bmatrix} \boldsymbol{u}_1 \\ \boldsymbol{v}_2 \end{bmatrix} = \begin{bmatrix} \boldsymbol{S}_{11} & \boldsymbol{S}_{12} \\ \boldsymbol{S}_{21} & \boldsymbol{S}_{22} \end{bmatrix} \begin{bmatrix} \boldsymbol{u}_1 \\ \boldsymbol{v}_2 \end{bmatrix}. \quad (5.55)$$

The field vectors that propagate to the right and left are denoted $\boldsymbol{u}$ and $\boldsymbol{v}$, respectively, and the subscripts 1 and 2 indicate the left- and right-hand side of the component. The scattering matrix is a block matrix; the blocks $\boldsymbol{S}_{11}$ and $\boldsymbol{S}_{22}$ being the reflection from the left and right side of the device, respectively, and $\boldsymbol{S}_{21}$ and $\boldsymbol{S}_{12}$ the transmission through the device from the left and right, respectively. These blocks have the dimension $P \times P$.

There exists a similar relation, a transfer matrix relation, that connects the fields on the left-hand side to the fields on the right-hand side:

$$\begin{bmatrix} \boldsymbol{u}_2 \\ \boldsymbol{v}_2 \end{bmatrix} = \mathbf{T} \begin{bmatrix} \boldsymbol{u}_1 \\ \boldsymbol{v}_1 \end{bmatrix}. \quad (5.56)$$

Comparing (5.55) and (5.56) we find the blocks of $\mathbf{T}$:

$$\mathbf{T} = \begin{bmatrix} \boldsymbol{S}_{21} - \boldsymbol{S}_{22}\boldsymbol{S}_{12}^{-1}\boldsymbol{S}_{11} & \boldsymbol{S}_{22}\boldsymbol{S}_{12}^{-1} \\ -\boldsymbol{S}_{12}^{-1}\boldsymbol{S}_{11} & \boldsymbol{S}_{12}^{-1} \end{bmatrix}. \tag{5.57}$$

To describe a device with a transfer matrix, $\boldsymbol{S}_{12}$ must be invertible, that is the transmission from the right cannot be zero for any input field vector. Thus, ideal mirrors, for example, cannot be described by a transfer matrix.

Provided the mode profiles can be written real, reciprocity means that the scattering matrix is symmetric [83, 84], i.e.,

$$\boldsymbol{S}_{11} = \boldsymbol{S}_{11}^{\mathrm{T}} \tag{5.58a}$$
$$\boldsymbol{S}_{22} = \boldsymbol{S}_{22}^{\mathrm{T}} \tag{5.58b}$$
$$\boldsymbol{S}_{21} = \boldsymbol{S}_{12}^{\mathrm{T}}. \tag{5.58c}$$

Moreover, the lossless condition is expressed as the unitarity condition $\mathbf{S}^{\dagger}\mathbf{S} = \mathbf{I}$:

$$\boldsymbol{S}_{11}^{\dagger}\boldsymbol{S}_{11} + \boldsymbol{S}_{21}^{\dagger}\boldsymbol{S}_{21} = \boldsymbol{I} \tag{5.59a}$$
$$\boldsymbol{S}_{12}^{\dagger}\boldsymbol{S}_{12} + \boldsymbol{S}_{22}^{\dagger}\boldsymbol{S}_{22} = \boldsymbol{I} \tag{5.59b}$$
$$\boldsymbol{S}_{12}^{\dagger}\boldsymbol{S}_{11} + \boldsymbol{S}_{22}^{\dagger}\boldsymbol{S}_{21} = \boldsymbol{0}. \tag{5.59c}$$

With (5.58) in mind, we introduce singular value decompositions of the symmetrical matrices $\boldsymbol{S}_{11}$ and $-\boldsymbol{S}_{22}$ (see Appendix 5.A.2):

$$\boldsymbol{S}_{11} = \boldsymbol{\Phi}_{\mathrm{l}}^{\mathrm{T}}\boldsymbol{\rho}\boldsymbol{\Phi}_{\mathrm{l}} \tag{5.60a}$$
$$\boldsymbol{S}_{22} = \boldsymbol{\Phi}_{\mathrm{r}}(-\boldsymbol{\rho}')\boldsymbol{\Phi}_{\mathrm{r}}^{\mathrm{T}} \tag{5.60b}$$
$$\boldsymbol{S}_{21} = \boldsymbol{\Phi}_{\mathrm{r}}\boldsymbol{t}'\boldsymbol{\Phi}_{\mathrm{l}}. \tag{5.60c}$$

Here, $\boldsymbol{\Phi}_{\mathrm{l}}$ and $\boldsymbol{\Phi}_{\mathrm{r}}$ are unitary matrices, $\boldsymbol{\rho}$ and $\boldsymbol{\rho}'$ are diagonal and nonnegative, and $\boldsymbol{t}' = \boldsymbol{\Phi}_{\mathrm{r}}^{\dagger}\boldsymbol{S}_{21}\boldsymbol{\Phi}_{\mathrm{l}}^{\dagger}$. By substituting into (5.59) and using (5.58) we obtain

$$\boldsymbol{t}'^{\dagger}\boldsymbol{t}' = \boldsymbol{I} - \boldsymbol{\rho}^2 \tag{5.61a}$$
$$\boldsymbol{t}'\boldsymbol{t}'^{\dagger} = \boldsymbol{I} - \boldsymbol{\rho}'^2 \tag{5.61b}$$
$$\boldsymbol{\rho}' = \boldsymbol{t}'^{*}\boldsymbol{\rho}\boldsymbol{t}'^{-1}. \tag{5.61c}$$

Introducing the singular value decomposition $\boldsymbol{t}' = \boldsymbol{U}'\boldsymbol{t}\boldsymbol{V}'$, we obtain from (5.61a) that $\boldsymbol{t}^2 = \boldsymbol{V}'(\boldsymbol{I} - \boldsymbol{\rho}^2)\boldsymbol{V}'^{\dagger}$, which means $\boldsymbol{t} = \boldsymbol{V}'\sqrt{\boldsymbol{I} - \boldsymbol{\rho}^2}\boldsymbol{V}'^{\dagger}$. Backsubstitution shows that $\boldsymbol{t}'$ can be written $\boldsymbol{t}' = \boldsymbol{U}\sqrt{\boldsymbol{I} - \boldsymbol{\rho}^2}$ for a unitary $\boldsymbol{U}$. With $\boldsymbol{t}'$ on this form, (5.61b) and (5.61c) reduce to $\boldsymbol{\rho}'^2 = \boldsymbol{U}\boldsymbol{\rho}^2\boldsymbol{U}^{\dagger}$ and $\boldsymbol{\rho}' = \boldsymbol{U}^{*}\boldsymbol{\rho}\boldsymbol{U}^{\dagger}$, respectively. Taking the root of the first equation and comparing, we find $\boldsymbol{U}\boldsymbol{\rho} = \boldsymbol{U}^{*}\boldsymbol{\rho}$ and equivalently $\boldsymbol{\rho}\boldsymbol{U}^{\dagger} = \boldsymbol{\rho}\boldsymbol{U}^{\mathrm{T}}$. With these properties, it is straightforward to show that (5.60) can be written

$$\boldsymbol{S}_{11} = \boldsymbol{\Phi}_{\mathrm{l}}^{\mathrm{T}}\boldsymbol{\rho}\boldsymbol{\Phi}_{\mathrm{l}} \tag{5.62a}$$
$$\boldsymbol{S}_{22} = \boldsymbol{\Phi}_{\mathrm{r}}(-\boldsymbol{\rho})\boldsymbol{\Phi}_{\mathrm{r}}^{\mathrm{T}} \tag{5.62b}$$
$$\boldsymbol{S}_{21} = \boldsymbol{S}_{12}^{\mathrm{T}} = \boldsymbol{\Phi}_{\mathrm{r}}\boldsymbol{t}\boldsymbol{\Phi}_{\mathrm{l}}, \tag{5.62c}$$

where $\boldsymbol{U}$ has been absorbed into $\boldsymbol{\Phi}_{\mathrm{r}}$, $\boldsymbol{\Phi}_{\mathrm{r}}\boldsymbol{U} \to \boldsymbol{\Phi}_{\mathrm{r}}$, and

$$\boldsymbol{t} = \sqrt{\boldsymbol{I} - \boldsymbol{\rho}^2}. \tag{5.63}$$

Note that (5.61) implies that $\|\boldsymbol{\rho}\| \leq 1$.

Eq. (5.62) and (5.63) can be interpreted as follows: The component can be viewed as a discrete reflector sandwiched between two unitary transmission sections. The discrete reflector provides coupling between equal modes that propagate in opposite directions, and the unitary sections provide coupling between different modes in the same direction. For the discrete reflector, the reflection response from the left and right is $\boldsymbol{\rho}$ and $-\boldsymbol{\rho}$, respectively, and the transmission is $\boldsymbol{t}$. For the two unitary sections, there are no reflections, and the transmission responses from the left are $\boldsymbol{\Phi}_{\mathrm{l}}$ and $\boldsymbol{\Phi}_{\mathrm{r}}$, while the transmission responses from the right are $\boldsymbol{\Phi}_{\mathrm{l}}^{\mathrm{T}}$ and $\boldsymbol{\Phi}_{\mathrm{r}}^{\mathrm{T}}$. Note that this interpretation is consistent with the reciprocity and lossless conditions (5.58) and (5.59), for each of the three sections separately.

Using (5.62), the transfer matrix (5.57) can be written

$$\mathbf{T} = \begin{bmatrix} \boldsymbol{A}^* & \boldsymbol{B}^* \\ \boldsymbol{B} & \boldsymbol{A} \end{bmatrix}, \tag{5.64}$$

where the blocks $\boldsymbol{A} = \boldsymbol{\Phi}_r^* \boldsymbol{t}^{-1} \boldsymbol{\Phi}_l^*$ and $\boldsymbol{B} = -\boldsymbol{\Phi}_r^* \boldsymbol{t}^{-1} \boldsymbol{\rho} \boldsymbol{\Phi}_l$ satisfy

$$\boldsymbol{A}^\dagger \boldsymbol{A} - \boldsymbol{B}^{\mathrm{T}} \boldsymbol{B}^* = \boldsymbol{I} \tag{5.65a}$$

$$\boldsymbol{A}\boldsymbol{B}^{\mathrm{T}} - \boldsymbol{B}\boldsymbol{A}^{\mathrm{T}} = \mathbf{0} \tag{5.65b}$$

$$\boldsymbol{A}^{\mathrm{T}} \boldsymbol{B}^* - \boldsymbol{B}^\dagger \boldsymbol{A} = \mathbf{0}. \tag{5.65c}$$

Part II

Spatial characterization of fiber Bragg gratings

Chapter 6

Spatial characterization of optical components

Spatial characterization is used to find the attenuation, gain or coupling between propagation modes (e.g. reflection) along an optical fiber or within an optical component. The source light is reflected from different positions within the fiber, and different reflected light components will have different delays from the source to the receiver. Several measurement techniques are developed to separate these reflections components, including optical time-domain reflectometry (OTDR), optical coherence-domain reflectometry (OCDR), optical space-domain reflectometry (OSDR) and optical frequency domain reflectometry (OFDR).

OTDR [85, 86, 87, 88] is the most established spatial characterization technique. The device under test (DUT) is interrogated by short laser pulses generated with separation that is at least the total dual-pass delay of the fiber. The backscattered light is detected and processed. The delay of a scattered signal component is then directly measured. OTDR is particularly useful for finding reflection points along long fiber sections. The Rayleigh scattering gives continuous scattering from the fiber. The decay of Rayleigh scattering can be used to find the attenuation along the fiber. The OTDR method has its shortcomings, since the spatial resolution is typically in the range of 1 m, limited by the width of the interrogation pulses and the required dynamic range [85]. OTDR is based on direct detection of the backscattered light. The method has therefore limited dynamic range, and does not provide information about the reflection phase. OTDR is therefore not suitable for spatial characterization of fiber Bragg gratings.

OCDR [89, 90, 91, 92] is an interferometric measurement technique. The measurement setup includes a Michelson interferometer with a movable reference mirror in one path, and the DUT in the other. OCDR is based on a low-coherent source, and is therefore often called optical low coherence reflectometry (OLCR). Superluminescent diodes [89, 93] or broad-band fiber lasers [92, 94] are often used. The interference between the reflection reference mirror and reflections within the DUT is suppressed when the delay difference between the reflections are more than the coherence time of the source. As the mirror is moved, reflections from different positions within the component are detected. The interference signal as function of

position is proportional to the impulse response of the DUT. The spatial resolution is limited by the coherence length of the source, and the range is limited by the movable distance of the reference mirror. OCDR has typically a spatial resolution of 10-50 μm [89, 93] and a range of 0.1-1 m A sensitivity of -161 dB has been demonstrated using a broad-band fiber laser [92]. OCDR is therefore in an entirely different regime in terms of spatial resolution, range and sensitivity compared to OTDR. OCDR was first used for spatial characterization of FBGs by Lambelet *et.al.* [95], and has later been used by several other groups [96, 97, 93]. By measuring the impulse response from both sides of a grating, Keren *et.al* [94] demonstrated successful characterization of a grating with 99.91 % reflectivity.

In OSDR, a perturbation of the refractive index is applied along the DUT, and the reflection or transmission response as function of position within the DUT is detected. The refractive index is usually perturbed by heat scan [98, 99, 100, 100, 101], but also pressure can be used [102]. Brinkmeyer *et.al.* [100] used this technique to measure the spatial profile of gratings by measuring the transmission in a side lobe as function of position of the perturbation. A related technique is the side-scattering technique [103, 104, 105], where the grating is illuminated from the side and the intensity of the scattered light is detected. The advantage of these methods is that the spatial profile is measured directly, whereas with OCDR and OFDR the reflection spectrum or the impulse response is measured and inverse scattering has to be applied to extract the spatial profile. However, it requires complex mechanical arrangements, and the spatial resolution is limited by the size of the perturbation.

OFDR [106, 107, 108] is based on coherent detection of the reflected light from the DUT with the light reflected from a fixed reference. To do this, the DUT is often placed in one of the arms of a Michelson interferometer, while the other end is terminated by a fixed mirror. Alternatively, a Mach-Zehnder interferometer can be used. The optical frequency of a highly coherent laser source is swept, and the interference pattern is detected as function of optical frequency. The impulse response of the DUT can be found by Fourier transforming the detected interference pattern and extracting the signal band starting at the dual-pass delay difference between the two arms of the interferometer. The length range is given by the coherence of the laser and how dense the interference signal can be sampled in optical frequency, while the spatial resolution is given by the tuning range of the laser. Thus, depending on the type of laser used, slow and smooth tuning of the optical frequency will give a long range, while sweeping the laser over a large frequency span will give high spatial resolution. The spatial range can be improved by using a trigger interferometer to generate sampling pulses equidistant in optical frequency [107]. Oberson *et.al.* [109] demonstrated spatial characterization over a range of 150 m with a resolution of 16 cm using a PZT-tuned DFB fiber laser over a wavelength range of 1 nm. In the other extreme, commercial external cavity lasers can be tuned up to 100 nm. Thus in principle, the spatial resolution can be as low as 8 μm. The ratio between range and resolution is often bounded by how many spectral points that can be sampled and processed. OFDR is therefore much more flexible in terms of range and resolution compared to the other techniques. This method was first used for spatial characterization of FBGs by Froggatt [110]. The OFDR technique

is highly practical for spatial characterization of FBGs. In comparison with OCDR, the setup is simpler, since it does not require a sweeping mirror, and the length of fiber into the FBG is allowed to vary with several meters. However, OCDR appears to be superior in terms of sensitivity.

In chapter 7, we use OFDR to measure the complex reflection spectrum of an FBG and feed this into the layer-peeling inverse scattering algorithm to calculate the spatial profile of the grating. Issues concerning scaling of the reflection response and birefringence of FBGs are discussed. We will demonstrate that this method can be used for characterization of FBGs up to 98-99 % reflectivity ($-17 - 20$ dB minimum transmission).

In chapter 8, the maximum reflectivity of the gratings that can be spatial characterized using OFDR is extended beyond the limitations in chapter 7. Here, a thermal chirp is applied to the grating so that the spectral information is spread over a much wider bandwidth, and so that the maximum reflectivity is reduced. In this way, a grating with a minimum transmission of -66 dB is successfully spatially characterized.

In chapter 9, a polarization-resolved spatial characterization technique based on OFDR is developed. A strain-tuned fiber DFB laser with closed-loop control of the laser sweep is used as source. Excellent sweep linearity is achieved with this method. The fiber laser is followed by a polarization-modulation interferometer that modulates the state of polarization of the interrogation light. The information about the grating impulse response is spread into different bands in the optical delay domain, and these bands are combined to find the polarization-resolved grating impulse response. This impulse response is fed into the polarization-resolved layer-peeling algorithm of chapter 4 to obtain the spatial profile. This method is used to investigate the polarization-dependent index modulation as function of the polarization of the uv-light used to fabricate the grating.

Chapter 7

Spatial characterization of FBGs using OFDR*

Characterization of the complex reflection spectrum and the spatial profile of fiber Bragg gratings using optical frequency domain reflectometry and the layer peeling algorithm is presented. The importance of correct scaling and polarization effects are discussed. The method gives accurate measurement of the spatial profile for gratings with reflectivity < 98-99 %. Immunity to spurious reflections and high dynamic range in spectral measurements are achieved.

7.1 Introduction

Fiber Bragg gratings (FBGs) are one of the most used passive component in fiber optical communication systems today. Advanced writing techniques [12, 111] have made it possible to write long gratings with arbitrary profile. The gratings are usually spectrally characterized using an optical spectrum analyzer or a tunable laser combined with powermeters. The spectrum gives information on the quality of the grating, however it does not give information about the origin of the spectral errors. With a measurement of the spatial profile of the grating, one can look for errors in the writing process, and if these errors are systematic, they can be compensated.

Previously reported methods measure the spatial profile directly [112]. The spatial profile is measured by introducing phase shifts using thermal perturbation along the grating and measuring the transmission in one of the side lobes as a function of the position of the perturbation [100]. Another reported method illuminates the grating from the side, and the intensity of the scattered light is measured [103, 105]. These methods can measure the spatial profile of arbitrary strong gratings, however they require complex mechanical arrangements and the spatial resolution is limited by the size of the perturbation.

*This chapter is published as O.H. Waagaard, E. Rønnekleiv and J.T. Kringlebotn, "Spatial characterization of strong fiber Bragg gratings" in Proceedings of SPIE, Fiber-Based Components Fabrication, Testing, and Connectorization, vol. 4943: pp 16-24, 2003.

Here we will use an indirect measurement of the spatial profile. The complex reflection spectrum is measured by optical frequency domain reflectometry (OFDR) [106, 107, 108, 113][1]. OFDR is based on coherent detection of the reflected light from the device under test when the optical frequency of the light source is swept. This measurement method provides the grating impulse response calculated as the Fourier transform of the complex reflection spectrum. For weak gratings, the first Born approximation can be applied, and the grating profile and the grating impulse response will be equal. For stronger gratings, the first Born approximation will give inaccurate results due to multiple reflection within the grating, and an inverse scattering algorithm must be applied to calculate the correct spatial profile. We will use the time-domain layer peeling algorithm [16, 26] to calculate the spatial profile. This algorithm has been used extensively over the last years for synthesis of Bragg gratings, and we demonstrate that the algorithm can be applied for characterization. The noise amplification in the layer-peeling algorithm is proportional to the inverse of the minimum transmissivity [37]. This limits the reflectivity of the gratings that can be characterized using this method to 98-99 %.

7.2 Measurement setup

The optical frequency domain reflectometry setup is shown in Figure 7.1. The measurement is based on a narrow band tunable laser source which sweeps the wavelength continuously over the grating spectrum. In order to achieve a sufficient optical frequency resolution, a reference Michelson interferometer is used to linearize the scan. The 120° phase shifted fringe outputs D3 and D4 are used to calculate the exact evolution of the optical frequency. This information is used to resample the outputs D1 and D2 to an accurate equidistant frequency grid for further processing. The reference interferometer is packed acoustically and thermally stable so that the imbalance does not fluctuate. The laser frequency can be calculated using

$$\nu(t) = \frac{c}{2\pi n 2 L_{\text{ref}}} \phi_{\text{ref}}(t) \tag{7.1}$$

where L_{ref} is the imbalance of the reference interferometer, n is the group index of the fibers in the interferometer and ϕ_{ref} is the measured phase with detectors D3 and D4. The factor 2 accounts for the two passes of the light through the arms of the interferometer. The imbalance of the reference interferometer is approximately 1.4 m, which gives a free spectral range of 75 MHz. With 16 bit ADC-resolution, the theoretical optical frequency resolution is less than 1 kHz, however the actual resolution is given by the linewidth of the laser, detector noise, the sampling jitter and the wavelength dependence of the phase difference between the two outputs of the 3x3 coupler. If the calibration of the imbalance is not correct, the optical frequency sampling interval will be wrong. In the spatial domain, the grating profile will appear expanded or compressed compared with the actual profile. By simultaneous characterization of two gratings with known and sufficiently spaced center wavelengths, the reference interferometer can be accurately calibrated.

[1] Ref. [106] and [107] have been added after the publication of the paper.

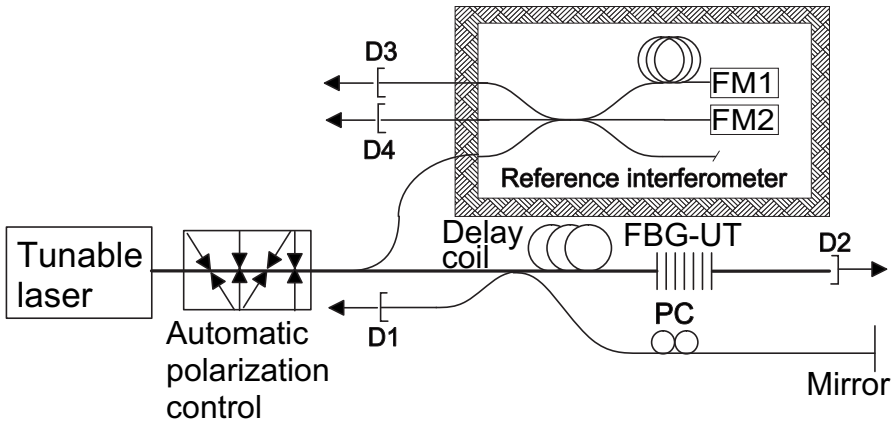

Figure 7.1: Interferometric measurement of the complex reflection spectrum. FBG-UT, FBG under test; PC, manual polarization controller; FM1-2, Faraday rotation mirrors; D1-4, detectors.

The FBG constitutes one of the reflectors in a Michelson interferometer at the bottom of Figure 7.1. The power measured at the output D1 of the interferometer is given by,

$$P(\nu) = P_0(|r_r|^2 + |r_{\mathrm{fbg}}(\nu)|^2 + 2V|r_r||r_{\mathrm{fbg}}(\nu)|\cos(2\pi\nu\tau + \phi_{\mathrm{fbg}}(\nu))) \tag{7.2}$$

where $r_{\mathrm{fbg}}(\nu) = |r_{\mathrm{fbg}}(\nu)|\exp(i\phi_{\mathrm{fbg}}(\nu))$ is the complex reflection spectrum of the FBG, $|r_r|$ is the reflection amplitude of the mirror, P_0 is a constant given by the output power of the laser, the coupling ratio of the coupler and the responsivity of detection circuits, V is the visibility of the interferometer and $\tau = 2nL/c$ is the group delay difference between the two arms of the interferometer, where L is the imbalance of the interferometer.

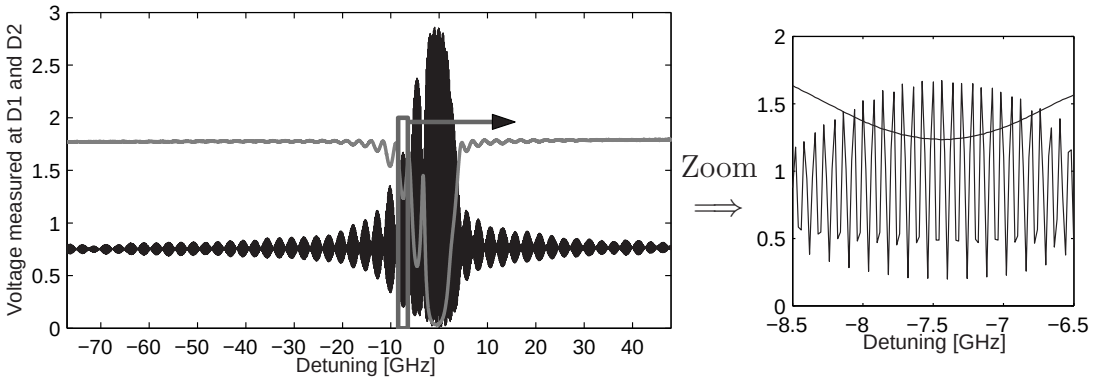

Figure 7.2: Response at detectors D1 and D2. The left figure shows the response within the whole wavelength range of which the grating has been characterized. The right figure shows a 2 GHz zoom of the same response.

Typical measured responses at D1 and D2 are shown in Figure 7.2. The figure shows the responses after resampling of the sampled data that are equidistant in time

to a equidistant optical frequency grid using the reference interferometer. From this figure it is possible to separate the three terms in (7.2). The first term, $P_0|r_r|^2$ should be constant and is the mean of the fringe signal of D1 far from the center wavelength of the grating (where $|r_{\text{fbg}}(\nu)|^2$ is negligible compared to $|r_r|^2$). A normalized fringe signal is calculated as

$$\tilde{P}(\nu) = P(\nu)/(P_0|r_r|^2) - 1 = \left|\frac{r_{\text{fbg}}(\nu)}{r_r}\right|^2 + 2V\left|\frac{r_{\text{fbg}}(\nu)}{r_r}\right|\cos(2\pi\nu\tau + \phi_{\text{fbg}}(\nu))) \quad (7.3)$$

The first term in the normalized fringe signal, $|r_{\text{fbg}}(\nu)/r_r|^2$ is the low frequency part. This term causes the asymmetry of the fringe signal, and will give the same as a direct reflection measurement without the interferometer. The last term, $2V|r_{\text{fbg}}(\nu)/r_r|\cos(2\pi\nu\tau + \phi_{\text{fbg}}(\nu))$ is the interference between the reflection from the grating and the mirror, and has a carrier frequency given by the imbalance of the interferometer.

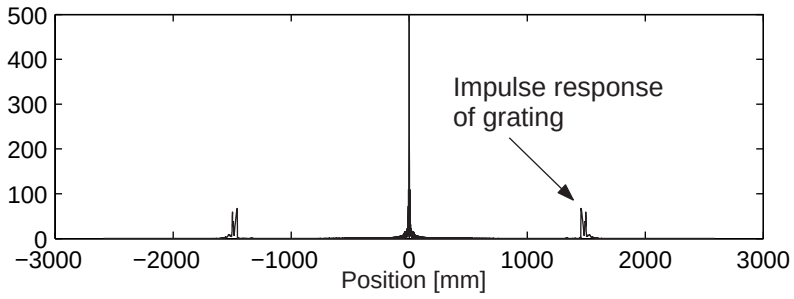

Figure 7.3: The Fourier transform of the normalized fringe signal.

Figure 7.3 shows the Fourier transform of the normalized fringe signal. The horizontal axis shows the position along the fiber of the interferometer. The Fourier transform of $\tilde{P}(\nu)$ has three bands. There is one band at a position equal to the imbalance $c\tau/(2n)$ of the interferometer. This is proportional to the impulse response of the grating which is the Fourier transform of the complex reflection spectrum. The grating impulse response will be used as input to the inverse scattering algorithm which calculates the spatial profile of the grating. A mirrored and complex conjugated version of the grating impulse response appears at negative imbalance. The band at zero delay is proportional to the Fourier transform of $|r_{\text{fbg}}(\nu)|^2$ which equals the autocorrelation of the impulse response.

Correct scaling of the impulse response is essential for correct results from the inverse scattering algorithm. The effect of multiple reflections inside the grating is enhanced when the grating is made stronger, thus a weak and a strong grating with proportional spatial profiles will have different reflection spectra. The same applies in the reverse direction, a reflection spectrum that is incorrectly scaled gives an incorrect spatial profile. The accuracy of the scaling becomes more critical for stronger gratings.

Equation (7.3) shows that V and $|r_r|$ must be known in order to calculate the correctly scaled complex reflection spectrum. $|r_r|$ depends on the reflectivity of

the mirror, the loss in the fiber and the splitting ratio of the coupler, while the visibility V depends greatly on the angle between the polarizations reflected from the two arms of the interferometer. $|r_r|^2$ can be found if the measurement of the transmission is available. The power measured at detector D2 is proportional to the transmission spectrum of the grating. The scaling factor is calculated so that the variance of the sum of the reflection and the transmission spectrum are minimum and the mean value equal to 1. This gives,

$$|r_r|^2 = \bar{R}(\nu) - \frac{\mathrm{Var}(R(\nu))}{\mathrm{Covar}(T(\nu), R(\nu))}\bar{T}(\nu) \qquad \Rightarrow \qquad |r_{\mathrm{fbg}}(\nu)|^2 = R(\nu)|r_r|^2 \tag{7.4}$$

where $R(\nu)$ is the first term in (7.3), $T(\nu)$ is the measured transmission spectrum. $\bar{R}(\nu)$, $\bar{T}(\nu)$ are the mean values, $\mathrm{Var}(R(\nu))$ is the variance and $\mathrm{Covar}(T(\nu), R(\nu))$ is the covariance of $R(\nu)$ and $T(\nu)$. If the transmission spectrum is not available, one can measure $|r_r|^2$ and assume it is constant, however especially the coupling ratio of the coupler may fluctuate with temperature and the wavelength range of the measurement.

If the visibility of the interferometer is independent of wavelength, one can compare the squared amplitude of the second term in (7.3) with the first term. Then the complex reflection spectrum $r_{\mathrm{fbg}}(\nu)e^{i\phi_{\mathrm{fbg}}(\nu)}$ has been found. If the grating is birefringent, the reflected polarization will generally vary along the grating. This may cause errors in the measured impulse response, since the visibility of the interferometer is polarization dependent. To overcome this problem, the interrogating polarization should be aligned with one of the polarization eigenaxes of the grating. If the grating fiber has constant birefringence, and the grating coupling coefficient is polarization independent, the measured reflection spectrum is a linear combination of two spectra, one in each of the eigenaxes of the fiber. The grating in the slow axis will be a replica of the grating in the fast axis but shifted in wavelength. Thus, by maximizing or minimizing the transmissivity on an edge of the FBG transmission spectrum using an automatic polarization controller, one has found one of the eigenaxes of the fiber.

A schematic overview of the commercial automatic polarization controller used is shown in Figure 7.4 [114]. The automatic polarization controller is based on changing the birefringence of a fiber using PZT-plates. Four modulators are used with alternating orientation of 0° and 45°, so that any input polarization can be converted to an arbitrary output polarization using three modulators.

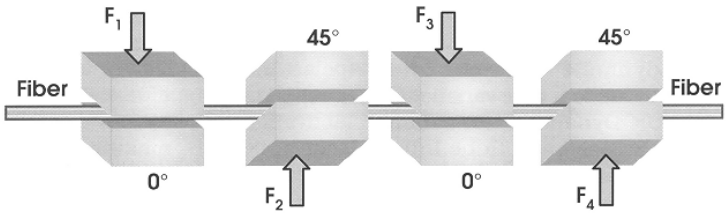

Figure 7.4: The automatic polarization controller squeezes the fiber with PZT-plates which changes the birefringence of the fiber section.

We have implemented a search algorithm based on dithering two modulators and calculate the optimization of the transmitted power by quadratic approximation [115]. A simulation of a polarization optimization is shown in Figure 7.5. The axes are the retardation generated by the two polarization modulators, and mesh indicates the measured power at D2. The dashed line shows how the algorithm searches for a maximum. In the neighborhood of a particular point $\boldsymbol{\Omega} = \boldsymbol{\Omega}_0$, where $\boldsymbol{\Omega} = \begin{bmatrix}\Omega_1 & \Omega_2\end{bmatrix}^{\mathrm{T}}$ is the retardance generated by the polarization modulators, the transmitted power can approximated by Taylor expansion [115],

$$P(\boldsymbol{\Omega}) = P(\boldsymbol{\Omega}_0) + \boldsymbol{\nabla} P|_{\boldsymbol{\Omega}=\boldsymbol{\Omega}_0}(\boldsymbol{\Omega} - \boldsymbol{\Omega}_0) + \frac{1}{2}(\boldsymbol{\Omega} - \boldsymbol{\Omega}_0)^T \boldsymbol{H}|_{\boldsymbol{\Omega}=\boldsymbol{\Omega}_0}(\boldsymbol{\Omega} - \boldsymbol{\Omega}_0) + \cdots , \quad (7.5)$$

where $\boldsymbol{\nabla} P = [\partial P/\partial \Omega_i]$ is the gradient vector and $\boldsymbol{H} = [H_{ij}] = [\partial^2 P/\partial \Omega_i \partial \Omega_j]$ is the second derivative matrix (Hessian matrix). A necessary requirement for a maximum or a minimum at a point $\boldsymbol{\Omega}'$ is that $\boldsymbol{\nabla} P(\boldsymbol{\Omega}') = \mathbf{0}$. This gives,

$$\boldsymbol{\nabla} P(\boldsymbol{\Omega}') \approx \boldsymbol{\nabla} P|_{\boldsymbol{\Omega}=\boldsymbol{\Omega}_0} + \boldsymbol{H}|_{\boldsymbol{\Omega}=\boldsymbol{\Omega}_0}(\boldsymbol{\Omega}' - \boldsymbol{\Omega}_0) = \mathbf{0} \quad \Rightarrow \quad \boldsymbol{\Omega}' = \boldsymbol{\Omega}_0 - \boldsymbol{H}^{-1} \boldsymbol{\nabla} P|_{\boldsymbol{\Omega}=\boldsymbol{\Omega}_0}. \quad (7.6)$$

Not all points where the length of the gradient vector is zero, are maxima or minima. Saddle points are points which are local minima for one parameter and local maxima for the other. The point $\boldsymbol{\Omega}'$=[1.2,2.1] in Figure 7.5 is a saddle point. The search algorithm finds a maximum or a minimum if and only if $\boldsymbol{H}$ has a positive determinant [116]. If this is not the case, the algorithm jumps to another point and checks the determinant of $\boldsymbol{H}$.

Once $\boldsymbol{\Omega}'$ is calculated, the operation point of the modulators $\boldsymbol{\Omega}_0$ is set to $\boldsymbol{\Omega}'$. The modulators are again dithered and a new $\boldsymbol{\Omega}'$ is calculated using (7.6). The iteration stops when the length of the vector $\boldsymbol{\Omega}' - \boldsymbol{\Omega}_0$ is less than some predefined value.

The gradient vector and the Hessian matrix are found by dithering the polarization modulators with different frequencies around the operation point $\boldsymbol{\Omega}_0$. The gradient vector components are given by the measured amplitude at the modulation frequencies, while the components of $\boldsymbol{H}$ are found at twice the modulation frequencies and the sum frequency.

If the input polarization is parallel to one of the eigenaxis of the first modulator, the modulator will not change the polarization. If that is the case, one can convert the input polarization to any output polarization using modulator 2 and 3. Therefore once the optimum using modulator 1 and 2 is found, the same algorithm is applied to modulator 2 and 3. This ensures that the real maximum or minimum has been found.

The last part of the signal processing is to apply the layer peeling inverse scattering algorithm [16, 26]. The spatial profile of the grating is calculated from the grating impulse response. The discrete version of the layer peeling algorithm [26] approximate the grating as a stack of discrete complex reflectors as shown in Figure 7.6. The forward propagation field in the section before the first grating layer is initialized as an impulse $\delta(t)$, while the backward propagation field is initialized as the impulse response $h(t)$. The algorithm is based on the fact the first point of the impulse response represents the reflection from the first grating layer of the reflector stack. Thus, the reflectivity of this grating layer has been found, and the fields in

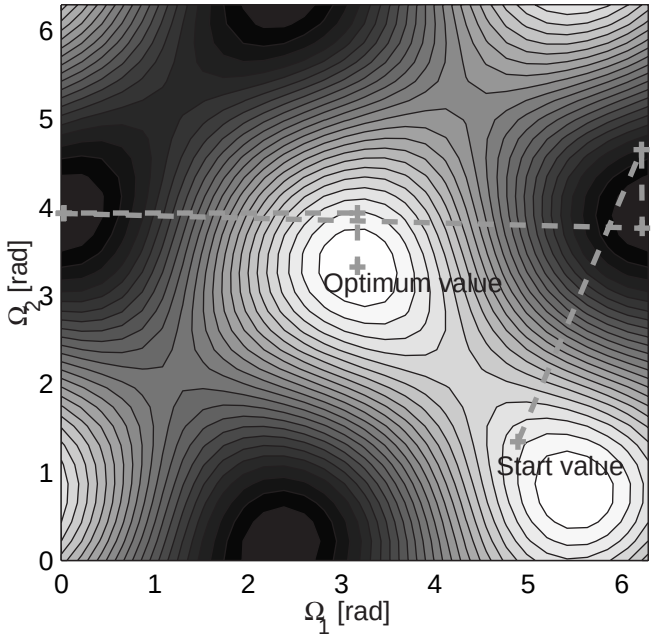

Figure 7.5: Polarization optimalization search algorithm. The axes are the birefringence generated by the modulators which are proportional to the applied voltage. White is maximum value, while black is the minimum value. The dashed curve is the path of the search algorithm.

the next section can be calculated. Once the fields in the next grating section are calculated, the previous section can be removed. The algorithm is applied successively until the whole spatial profile i.e. the reflectivities ρ_i of the grating layers are calculated.

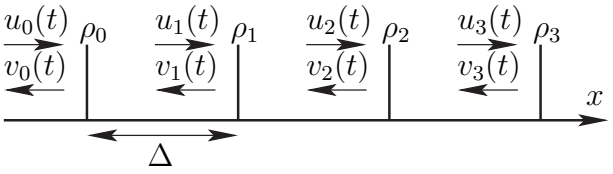

Figure 7.6: The grating model used by the time-domain discrete layer peeling algorithm [26]. The grating is described by a stack of reflectors with reflectivity ρ_i which are spaced by a distance Δ. $u_i(t)$ and $v_i(t)$ are the forward and backward propagating fields, respectively. The algorithm initialize $u_0(t) = \delta(t)$ and $v_0(t) = h(t)$.

The signal processing for extracting the spatial profile of an FBG from an OFDR measurement can be summarized as follows,

1) Interrogate the grating on an edge of the transmission spectrum and apply the polarization optimization procedure.

2) Execute the OFDR measurement.

3) Resample the sampled data at detector D1 and D2, using the optical frequency measured by the reference interferometer.

4) Calculate a normalized fringe signal using equation (7.3).

5) Apply the Fourier transform, and separate the components at zero delay and the components at the delay given by the imbalance of the interferometer.

6) Calculate the scaling of the complex reflection spectrum and the grating impulse response using the transmission measurement.

7) Apply the layer peeling algorithm to calculate the spatial profile.

8) Calculate the amplitude/power and phase/group delay spectra from the inverse Fourier transform of the grating impulse response.

7.3 Results

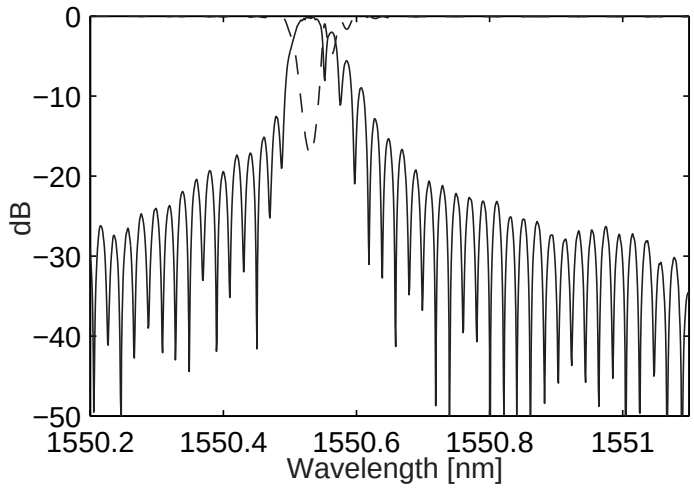

Figure 7.7: The characterized transmission and reflection spectra of a 42 mm uniform grating with maximum reflectivity 98%.

Figure 7.7 shows the characterized transmission and reflection spectra of a 42 mm uniform grating with maximum reflectivity 98 % calculated from the fringe signal shown in Figure 7.2. Figure 7.8 shows the impulse response (versus dual path delay) and the grating coupling coefficient κ calculated based on the impulse response using the time-domain layer-peeling algorithm. The resolution in optical frequency and space is 20 MHz (0.16 pm) and 0.6 mm, respectively. The spatial resolution distance is inversely proportional to the optical frequency span, which can easily be increased by a factor of 10 from the value of 1 nm used here.

Figure 7.8 shows that the first Born approximation cannot be applied for this grating. The first Born approximation gives a spatial profile that is equal to the impulse response which is clearly not the case.

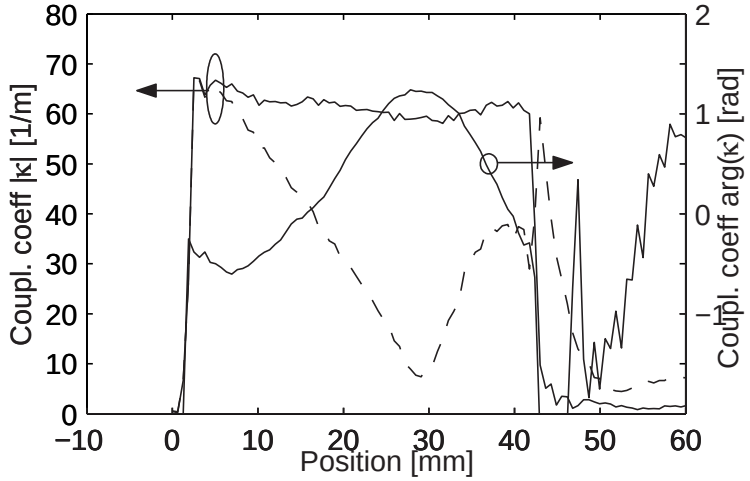

Figure 7.8: The impulse response(- -) and the spatial profile(–) calculated using the time-domain layer-peeling algorithm.

Because most of the power is reflected from the first part of the grating, the impulse response drops quite rapidly for the first 26 mm, it then increases due to multiple reflections. The sharp transition seen at 42 mm is due to the sudden absence of destructive interference from first order reflections.

The calculated spatial profile has steep edges at both grating ends and is quite uniform within the grating. This indicates that the layer peeling algorithm is working well. For such strong gratings, low noise and accurate scaling of the impulse response are critical for obtaining accurate results from the layer peeling. If the reflection spectrum is scaled poorly or the noise contribution is significant, the tail of the spatial profile after the end of the grating (here after 42 mm) will not go to zero. The characterized profile in Figure 7.8 does not reach zero, however the extinction is more than 10 times. The error amplification is exponential with κL (where L is the grating length) [37], and we believe that gratings with reflectivity >98-99% cannot be characterized using this method with realistic sampling accuracies.

Figure 7.7 shows that the grating is not symmetric. A grating with quadratic frequency chirp will be asymmetric. The grating phase calculated in Figure 7.8 is a 3rd-order function, corresponding to a quadratic chirp. This explains the asymmetry of the spectrum.

Figure 7.9 shows the spectrum of a 11 mm low reflectivity chirped apodized grating. This grating was designed as broadband reflector with 4 % reflectivity. The first Born approximation gives sufficient accurate results for this grating, thus the impulse response and the grating profile calculated using the layer peeling algorithm will be equal. Figure 7.10 shows the spatial profile of the grating. The grating was apodized using a $\exp(-(x/a)^6)$-window, and the figure shows a good fit between the designed and the measured apodization.

The local wavelength of the grating can be calculated from the phase profile

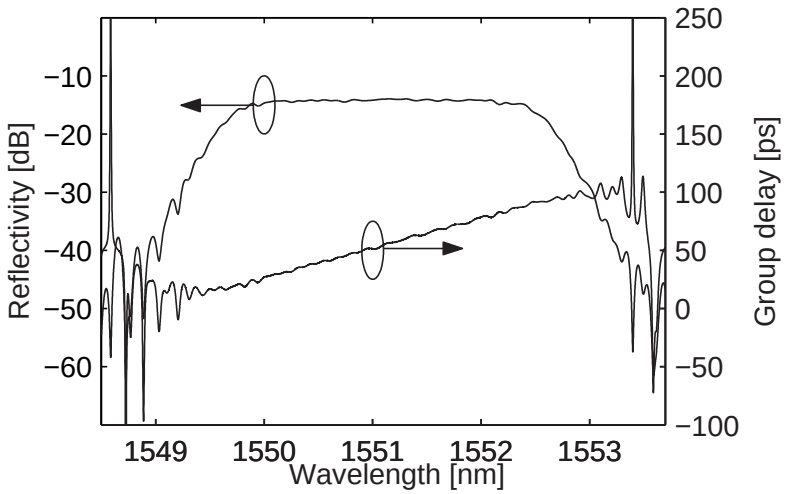

Figure 7.9: Characterized reflection and group delay spectra of a 11 mm chirped apodized grating.

using

$$\frac{1}{\lambda_{\text{local}}} = \frac{1}{\lambda_b} + \frac{c}{4\pi n_{\text{eff}}} \frac{d\arg(\kappa)}{dx}, \tag{7.7}$$

where λ_b is the Bragg wavelength and n_{eff} is the effective refractive index of the grating. Figure 7.10 shows that the grating is linearly chirped, thus the different wavelength components are reflected from different part of the grating. The low wavelength components are reflected from the first part of the grating while the high wavelength components are reflected from the last part.

Figure 7.9 also demonstrate that the measurement method also provides the group delay spectrum. The measured group delay at the longest wavelengths are about 100 ps, which equals the dual-path delay between the start and the end of the grating.

Provided that the phase errors are repeatable from one writing session to another, the measured profiles can be used to compensate for systematic errors in the writing setup [117]. The measurement setup shown in Figure 7.1 provides very high dynamic range in the spectral measurements. This is due to the coherent homodyne detection technique used, where the fringe amplitudes are proportional to the optical field reflectivity of the FBG. With a 16-bit ADC resolution, the quantization noise floor will be as low as –96 dB optical, as compared to –48 dB with direct power measurements.

Another advantage of the presented method is that responses from spurious reflections can be efficiently removed by using only the duration of the FBG impulse response as input to the inverse Fourier transform when calculating the reflection spectrum. This immunity against spurious reflections has been verified experimentally. The fact that only a part of the full impulse response is extracted also leads to an effective smoothening of detector noise etc. In this example about 1% of the full impulse response length was extracted, resulting in a noise reduction of 20 dB when assuming white noise.

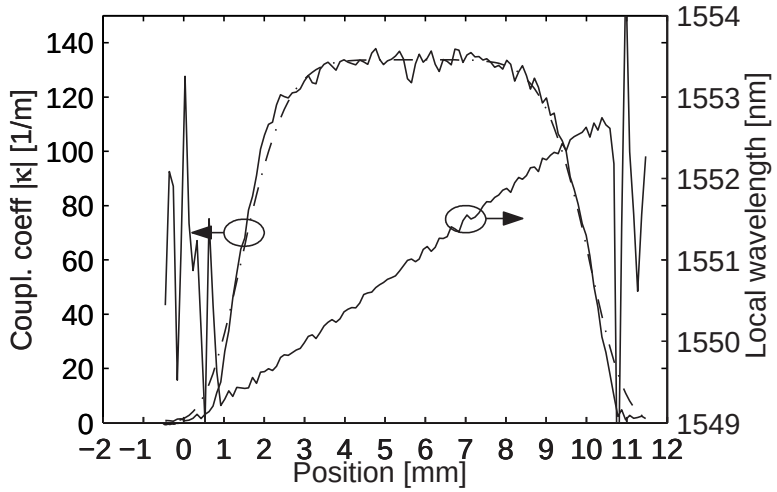

Figure 7.10: The spatial profile(–) and local wavelength of the chirped apodized grating. The designed apodization (-·) of the grating is also shown.

7.4 Conclusions

We have demonstrated a measurement method which gives both the complex reflection spectrum and the complex spatial profile based on optical frequency domain reflectometry. A spectral resolution less than 0.01 pm and a spatial resolution less than 0.1 mm are possible. The coherent measurement method also provides high dynamic range in spectral reflection measurements, and allows spurious reflections outside the grating to be removed from the measurements.

The polarization reflected from the grating is generally wavelength dependent, which gives a wavelength dependent interferometer visibility. This problem has been solved by maximizing or minimizing the grating transmissivity at the edge of the transmission spectrum using an automatic polarization controller.

The spatial profile of gratings with reflectivity less than 98-99 % has successfully calculated from the coherent homodyne measurement data using the time-domain layer peeling algorithm. This method is a valuable tool supporting the writing process, and makes it possible to compensate for systematic writing errors.

Chapter 8

Spatial characterization of strong FBGs using thermal chirp and OFDR*

A method that can spatially characterize gratings with grating strength $|\kappa|L$ up to 10 is presented. The grating is thermally chirped to increase the transmissivity through the grating. The complex reflectivity spectrum is measured using optical frequency domain reflectometry, and the spatial profile is reconstructed using the time-domain layer-peeling algorithm. The spatial profiles of an uniform grating with grating strength $|\kappa|L = 8.25$ (-66 dB minimum transmissivity) and a distributed feedback fiber laser (DFB-FL) grating with grating strength $|\kappa|L = 7.5$ are accurately reconstructed from the measured complex reflection spectrum.

8.1 Introduction

Fiber Bragg gratings (FBGs) are attractive components in fiber optical communication and sensing systems. Advanced writing techniques [12, 111] have made it possible to write long gratings with arbitrary profile. A grating is usually spectrally characterized using an optical spectrum analyzer or a tunable laser combined with power meters. The spectrum gives information on the quality of the grating; however, it does not give information about the origin of the spectral errors. By measuring the spatial profile (complex coupling coefficient profile) of the grating, the errors in the writing process can be determined. If these errors are systematic, they can be compensated [117].

The spatial profile can be measured directly by introducing phase shifts along the grating using a thermal perturbation and by measuring the transmission in one of the sidelobes as a function of the position of the perturbation [100, 112]. This method has also been used for characterization of the intensity distribution in the

*This chapter is published as O.H. Waagaard, "Spatial characterization of strong fiber Bragg gratings using thermal chirp and optical-frequency-domain reflectometry" in *IEEE Journal Lightwave Technology* vol. 23, pp. 909-914, 2005

cavity of distributed feedback fiber lasers (DFB-FL) [101]. Another reported method illuminates the grating through the side onto its core, and the intensity of the scattered light is measured [103, 105]. These methods can measure the spatial profile of arbitrary strong gratings; however, they require complex mechanical arrangements, and the spatial resolution is limited by the size of the perturbation.

The spatial profile can also be found indirectly from the complex reflectivity spectrum, which can be measured using optical frequency domain reflectometry (OFDR) [106, 107, 108, 113, 118, 119][1] or optical coherence domain reflectometry (OCDR) [95, 120, 97, 93]. In both methods, the grating constitutes one of the reflectors in a Michelson interferometer. In OFDR, the optical frequency of a highly coherent light source is swept, and the interference signal from the interferometer is detected. In OCDR, a low-coherent source with a coherence length shorter than the required spatial resolution is used, and an interference signal is detected while scanning the position of the reference reflector.

Once the complex reflectivity spectrum is measured, the spatial profile can be reconstructed from the complex reflectivity spectrum using an inverse scattering algorithm such as the layer-peeling algorithm [16, 26, 40]. This algorithm is based on the simple fact that the leading edge of the impulse response is independent of the later part of the grating due to causality. Hence, one can identify the first layer of the grating and remove its effect using the associated transfer matrix. Theoretically, the spatial profile can be exactly reconstructed from the complex reflection spectrum using this algorithm. Unfortunately, noise in a measured reflection spectrum will be amplified in the inverse scattering process with a factor that grows exponentially with grating strength [37]. The reconstruction of the spatial profile from a measured complex reflectivity spectrum is therefore limited to gratings with a transmission minimum larger than about -20 dB (99 % reflectivity) [119]. For a uniform grating, this corresponds to a grating strength (coupling coefficient-length product) $|\kappa|L < 3$. In [94], it is suggested that the measurement results can be improved by combining the measured spatial profile of the grating from both sides, and the spatial profile for an apodized grating with 99.91 % maximum reflectivity has been successfully reconstructed. By combining the spatial profile measured from both ends, it should be possible to characterize gratings with grating strength $|\kappa|L < 6$.

DFB-FLs are attractive sources both in sensing, instrumentation and telecommunication because of their narrow linewidths in the order of 1-10 kHz. Grating errors in a DFB-FL grating may cause the DFB-FL not to lase, a reduction of the finesse and the stability, and lasing in higher order modes [121]. Spatial characterization of DFB-FL grating can give valuable information concerning the (unexpected) behavior of the laser. However, DFB-FL gratings have a grating strength in the range $|\kappa|L$=6-16, and these gratings are therefore too strong for the spatial profile to be reconstructed from a measurement of the complex reflectivity spectrum.

In this paper, a technique that can characterize such strong gratings is presented. A chirp is applied to the grating using a temperature gradient [122]. This sufficiently increase the transmission through the grating and spreads the spectral information over a much larger bandwidth. Thus, the spatial profile can be reconstructed from

[1]Ref. [106] and [107] have been added after the publication of the paper.

a measurement of the reflection spectrum using OFDR [108].

8.2 Spatial profile reconstruction

The OFDR setup [123, 119] is shown in Figure 8.1. The FBG constitutes one of the reflectors in the Michelson interferometer to the right hand side of this figure. The other reflector is a highly reflective dielectric mirror. The polarization controller PC1 is used to adjust the input polarization to the grating, while PC2 is used to maximize the visibility of the measurement. A narrow band tunable laser source (Ando AQ4320B) sweeps the wavelength continuously across the grating bandwidth of typically 5-10 nm in ∼1 s. A fringe spectrum is measured at detector output D1, while the transmission through the grating is measured at detector output D2. In order to achieve a sufficient optical frequency resolution, a reference Michelson interferometer is used to linearize the scan. The 120° phase-shifted fringe outputs D3 and D4 are used to calculate the exact evolution of the optical frequency. This information is used to resample the outputs D1 and D2 to an accurate equidistant frequency grid for further processing.

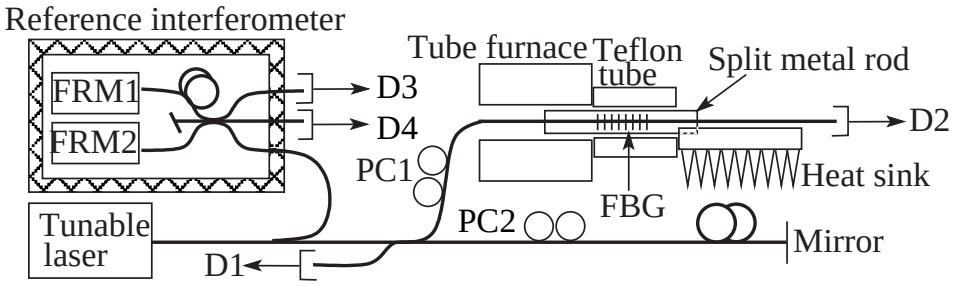

Figure 8.1: Interferometric measurement of the complex reflection spectrum with thermal chirping device. PC1-2: manual polarization controllers; FRM1-2: Faraday rotation mirrors; D1-4: detectors.

The grating is placed in a groove at the center of a split metal rod, which is thermally isolated with a Teflon tube. One end of the metal rod is placed within a tube furnace, and the other end is connected to a heat sink. When the metal rod is heated by the tube furnace, there will be a temperature gradient along the metal rod, which will chirp the grating. This will effectively increase the transmission through the grating.

Typical measured responses at detector outputs D1 and D2 are shown in Figure 8.2. The power measured as a function of optical frequency ν at D1 is given by,

$$\begin{aligned} P(\nu) = P_0\{&|r_r|^2 + |r_{\text{fbg}}(\nu)|^2 \\ &+ 2V|r_r||r_{\text{fbg}}(\nu)|\cos(2\pi\nu\tau + \phi_{\text{fbg}}(\nu))\}, \end{aligned} \tag{8.1}$$

where $r_{\text{fbg}}(\nu) = |r_{\text{fbg}}(\nu)|\exp(i\phi_{\text{fbg}}(\nu))$ is the complex reflection spectrum of the FBG, $|r_r|$ is the field reflectivity of the mirror, V is the visibility of the interferometer and $\tau = 2nL_{\text{if}}/c$ is the group-delay difference between the two arms of the interferometer,

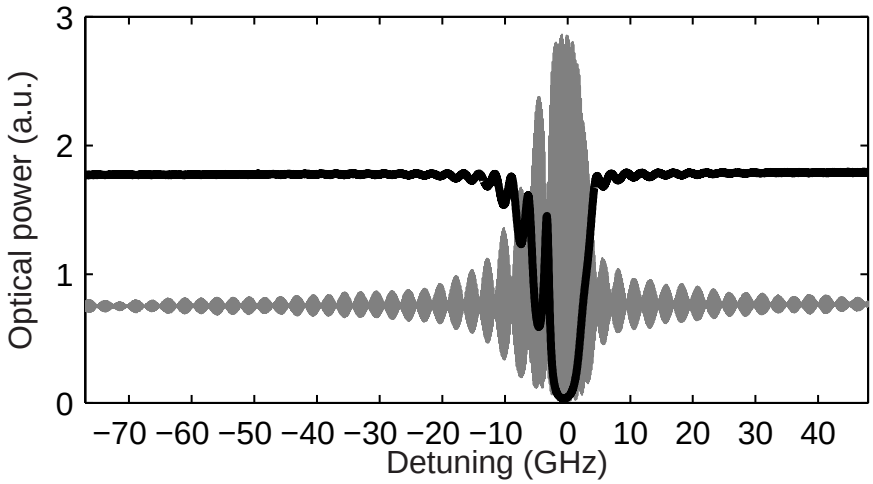

Figure 8.2: Response at detectors D1(grey) and D2(black).

where L_{if} is the imbalance of the interferometer, and c/n is the group velocity of light in the fiber. The fiber arm with the FBG is the longest, and the imbalance of the interferometer is in the range 0.1-4 m.

The first term in (8.1), $P_0|r_r|^2$ is assumed independent on ν, and is calculated as the mean of the fringe signal of D1 far from the center wavelength of the grating (where $|r_{\text{fbg}}(\nu)|^2$ is negligible compared to $|r_r|^2$). A normalized fringe signal is then calculated as

$$\begin{aligned}\tilde{P}(\nu) &= P(\nu)/(P_0|r_r|^2) - 1 \\ &= \left|\frac{r_{\text{fbg}}(\nu)}{r_r}\right|^2 + 2V\left|\frac{r_{\text{fbg}}(\nu)}{r_r}\right|\cos(2\pi\nu\tau + \phi_{\text{fbg}}(\nu)))\end{aligned} \tag{8.2}$$

The first term in (8.2), $|r_{\text{fbg}}(\nu)/r_r|^2$, varies slowly with ν, and causes the vertical asymmetry of the fringe signal shown in Fig. 8.2. This term should be proportional to a direct reflection measurement of the grating without the interferometer. The last term, $2V|r_{\text{fbg}}(\nu)/r_r|\cos(2\pi\nu\tau + \phi_{\text{fbg}}(\nu))$ is the interference between the reflections from the grating and the mirror and may be viewed as a carrier signal versus optical frequency that is modulated by the amplitude and phase of the FBG reflectivity spectrum. The number of cycles per unit optical frequency change equals the delay imbalance of the interferometer at the measurement optical frequency.

Figure 8.3 shows the Fourier transform of the normalized fringe signal. The horizontal axis represents the position along the FBG fiber in the interferometer. The Fourier transform of $\tilde{P}(\nu)$ has three bands. There is one band at a position equal to the imbalance $c\tau/(2n)$ of the interferometer. This band is proportional to the impulse response of the grating, which is the Fourier transform of the complex reflectivity spectrum. The grating impulse response will be used as input to the inverse scattering algorithm that calculates the spatial profile of the grating. A mirrored and complex conjugated version of the grating impulse response appears at negative imbalance. The band around zero delay is proportional to the Fourier transform of $|r_{\text{fbg}}(\nu)|^2$, which is the autocorrelation of the impulse response.

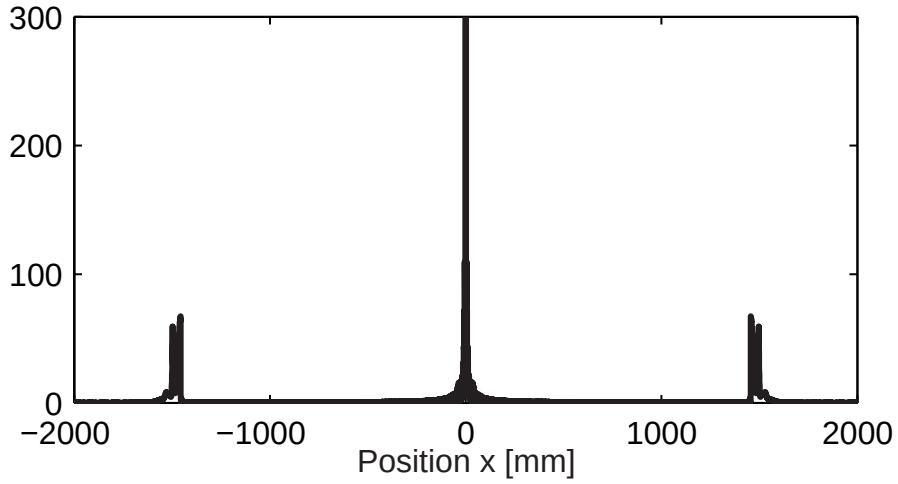

Figure 8.3: Fourier transform of the normalized fringe signal.

Correct scaling of the grating impulse response is essential for correct results from the inverse scattering algorithm. Correct scaling becomes increasingly critical as the strength of the gratings increase. If the grating is lossless, the scaling factor $|r_r|$ is determined by requiring that the sum of the reflection spectrum given by the slowly varying part of (8.2) and the transmission measured at detector D2 should be 1 for all optical frequencies [119]. If the visibility of the interferometer is independent of optical frequency, one can determine V by comparing the squared amplitude of the second term in (8.2) with the first term. Thus, the complex reflectivity spectrum $r_{\mathrm{fbg}}(\nu)e^{j\phi_{\mathrm{fbg}}(\nu)}$ can be extracted.

If the grating is birefringent, the reflected polarization state will generally vary along the grating. This may cause errors in the measured impulse response, since the visibility of the interferometer depends on the polarization state of the interfering light components. To overcome this problem, the interrogating polarization should be aligned with one of the polarization eigenaxes of the grating. If the grating birefringence is position independent and the grating coupling coefficient is polarization independent, the reflection spectra measured with the input polarization state parallel to the two polarization eigenaxes of the grating are equal except for a shift in center frequency. The input polarization state is therefore aligned to one of the polarization eigenaxes when the transmissivity through the FBG at a flank of the spectrum is either minimum or maximum as function of input polarization state. An automatic polarization controller [114] can be placed between the laser and the Michelson interferometer. This controller can be used to search for the input polarization state that gives the minimum or maximum transmissivity at the flank [119]. Another method that can be used is to compare the spectrum calculated from the first term in (8.2) and the square amplitude calculated from the second term in (8.2) while adjusting polarization controller PC1. When these two spectra are proportional, the visibility is constant, and the input polarization is aligned to one of the polarization eigenaxes of the grating. Both methods were tested, and the latter method gave best results.

It will be more difficult to reconstruct the spatial profile of an Er-doped DFB-FL grating than a uniform grating in a lossless fiber with the same grating strength. Light will resonate near the discrete phase shift at the center of the grating. As more light resonate around the phase shift, it becomes more difficult to extract information about the spatial profile after the resonator. In addition, the DFB-FL grating is written in an Er-doped fiber, and there will be absorption within the grating. For gratings in fibers with absorption, the reflection spectrum and the transmission spectrum no longer add to 1, and it is more difficult to calculate the correct scaling factor for the impulse response. However, the following procedure should give a good estimate of the scaling factor for a grating in an Er-doped fiber: Far from the Bragg wavelength, the power transmissivity equals $\exp(-\alpha L)$, where α is the absorption coefficient of the fiber, and L is the length of the grating. If the grating has such a low reflectivity that the first Born approximation applies, i.e. the spatial profile is approximately proportional to the impulse response, and that the mean group delay is equal to the dual pass delay to the center of the grating, one can use as a first-order approximation that the sum of the reflection spectrum and the transmission spectrum equals $\exp(-\alpha L)$. This condition is satisfied when the grating is sufficiently chirped.

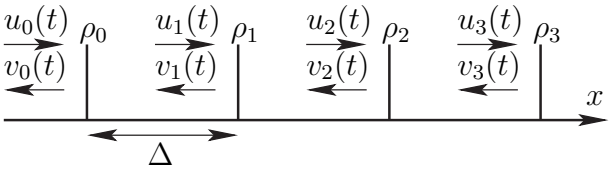

Figure 8.4: Grating model used by the time-domain discrete layer-peeling algorithm.

The calculated impulse response is the input to the time-domain layer-peeling algorithm. In this algorithm, the grating is represented by a stack of N discrete complex reflectors separated by a distance $\Delta = c/(2n\nu_{\text{span}})$ as shown in Figure 8.4, where ν_{span} is the optical-frequency scanning range of the measurement. Within each layer $j = 0, 1, \ldots, N-1$ there are a time-dependent forward-propagating optical field u_j and a backward propagating optical field v_j. Due to the discrete grating model, the fields u_j and v_j are discrete in time as well, and the sampling period is equal to the dual-pass delay within a layer, 2Δ (normalized). The relation between the fields in layer j and the corresponding fields in layer $j+1$ at time-step k is described by [26]

$$\begin{bmatrix} u_{j+1}(k) \\ v_{j+1}(k-1) \end{bmatrix} = \mathbf{T}_{\rho_j} \begin{bmatrix} u_j(k) \\ v_j(k) \end{bmatrix}, \tag{8.3}$$

where,

$$\mathbf{T}_{\rho_j} = (1 - |\rho_j|^2)^{-1/2} \begin{bmatrix} 1 & -\rho_j^* \\ -\rho_j & 1 \end{bmatrix}. \tag{8.4}$$

Here, $\rho_j = -\tanh(|\kappa_j|\Delta x)\kappa_j/|\kappa_j|$ is the local complex reflection coefficient of reflector j.

In the layer-peeling algorithm, the grating will be evaluated layer by layer, and the time reference may be chosen differently for each layer. In (8.3), we have there-

fore omitted the time delay for the forward-propagating field from a layer to the next so that the first nonzero elements of the fields are always $u_j(0)$ and $v_j(0)$.

In gratings with absorption such as DFB-FL gratings, the absorption must be incorporated in the grating model. The absorption in each layer is described by a transfer matrix,

$$\mathbf{T}_a = a^{1/2} \begin{bmatrix} 1 & 0 \\ 0 & a^{-1} \end{bmatrix}, \tag{8.5}$$

where $a = \exp(-\alpha \Delta x)$ is the power loss factor for transmission through each layer in the discrete grating model. This factor is assumed to be known and equal for all layers. The combined transfer matrix of layer j is then represented by $\mathbf{T}_{\rho_j} \mathbf{T}_a$.

Thus, by incorporating absorption, (8.3) can be written,

$$\begin{bmatrix} u_{j+1}(k) \\ v_{j+1}(k-1) \end{bmatrix} = \begin{bmatrix} 1 & -\rho_j^* \\ -\rho_j & 1 \end{bmatrix} \begin{bmatrix} u_j(k) \\ v_j(k)/a \end{bmatrix}. \tag{8.6}$$

Since we are only interested in the ratio between the backward- and forward-propagation fields, we have in (8.6) omitted the common factor $(1 - |\rho_j|^2)^{-1/2} a^{1/2}$.

The layer-peeling algorithm is a recursive algorithm. The forward and backward propagating field of the first layer are initialized as an impulse $\delta(k)$ and the measured impulse response $h(k)$, respectively, where $k = 0, 1, \ldots, N-1$. Causality implies that $-\rho_j u_j(0) + v_j(0)/a = v_{j+1}(-1) \equiv 0$, and the local reflection coefficient can therefore be calculated as $\rho_j = v_j(0)/u_j(0)/a$. For the first layer, the local reflection coefficient is simply given by $\rho_0 = h(0)/a$. Once ρ_0 has been calculated, (8.6) can be used to calculate the fields of layer 1, and the same procedure can be used to find ρ_1. This procedure is repeated for $j = 1, \ldots, N-1$.

A time-domain layer-peeling algorithm that calculates the local reflection coefficients for a grating with absorption can be summarized as follows:

Initialize $u(k) = \delta(k)$, $v(k) = h(k)$, $k = 0, 1, \ldots, N-1$
FOR $j = 0$ TO $N-1$,
    Calculate $v(k) = v(k)/a$, $k = 0, 1, \ldots, N-1$
    Calculate $\rho_j = v(0)/u(0)$
    FOR $k = 0$ TO $N-j-1$,
        $u(k) = u(k) - \rho_j^* v(k)$
        $v(k) = v(k+1) - \rho_j u(k+1)$
    END
END

The spatial index j of u and v is omitted since the algorithm only operates on one layer at the time, and u and v do not need to be saved.

The last step of the measurement procedure is to measure the thermally induced coupling phase and remove it from the measured coupling phase of the grating. This can be done using a grating with such a low reflectivity that the spatial profile can be reconstructed both when the grating is unchirped and when it is thermally chirped. The difference in measured coupling phase with and without chirp gives the thermally induced coupling phase, which can be subtracted from the measured

coupling phase of the strong grating. The weak grating can either be co-located with the strong grating but in another fiber, or can be superimposed on the strong grating, but with a different center wavelength.

8.3 Results

The measurement method was tested both with and without an applied thermal chirp on a $L = 50$ mm strong uniform grating at 1550 nm, which was annealed at 200°C for 30 min. The grating was placed in the groove inside the split metal rod of aluminum centered on the 90 mm insulated section between the tube furnace and the heat sink. A second much weaker grating at 1565 nm with max reflectivity of 2% was superimposed on the strong grating.

The weak superimposed grating was used to find the temperature profile along the rod. The difference between the measured local detuning with and without thermally induced chirp is proportional to the temperature profile. We found that the Bragg wavelength temperature sensitivity was 8.9 pm/°C. The measurement setup was also tested for a split metal rod of stainless steel. The measured temperature profiles that were measured along these two rods after the temperature was stabilized, are shown with 0.8 mm resolution in Figure 8.5. Also shown is a fourth order polynomial fit. We choose to fit the temperature profile to a polynomial since we do not expect that the temperature chirping induces fast variations in local detuning. The average temperature gradient was 1.0 °C/mm along the aluminum rod and 1.9 °C/mm along the stainless steel rod. The temperature gradient is larger along the stainless steel rod, due to the lower thermal conductivity. Thus, the stainless steel rod will chirp the grating and increase the transmission through the grating more than an aluminum rod. The maximum strength of a grating that can be spatially characterized with this method is limited by the maximum temperature gradient possible in the setup. With the present setup we believe that the spatial profile of gratings with strength $|\kappa|L \leq 10$ can be reconstructed. We also found that the temperature gradient along the aluminum rod decreased with time, while it remained constant along the stainless steel rod. Since there is more heat transfer along the aluminum rod, more heat has to be dissipated at the heat sink. The capacity of the heat sink was not sufficient, and the temperature on the cold end increased. While the stainless steel rod provided the largest temperature gradient, the temperature profile along this rod is also the most nonlinear. This is because the amount of heat transfer along the rod is more comparable to the heat transfer to the environment. Thus there is a tradeoff between linearity of the thermally induced chirp and the maximum available temperature gradient. As the temperature profile becomes more nonlinear, temperature measurements with higher resolution are required in order to find the thermally induced coupling phase. It should be possible to generate a more linear temperature profile along the stainless steel with better isolation to the environment. This will also improve the stability of the temperature profile. Another improvement would be to use Peltier elements for both heating and cooling instead of the furnace and the heat sink. The Peltier elements should provide better control of the temperature profile, and since the Peltier elements can cool the cold

end below room temperature, a larger temperature gradient can be induced without damaging the grating.

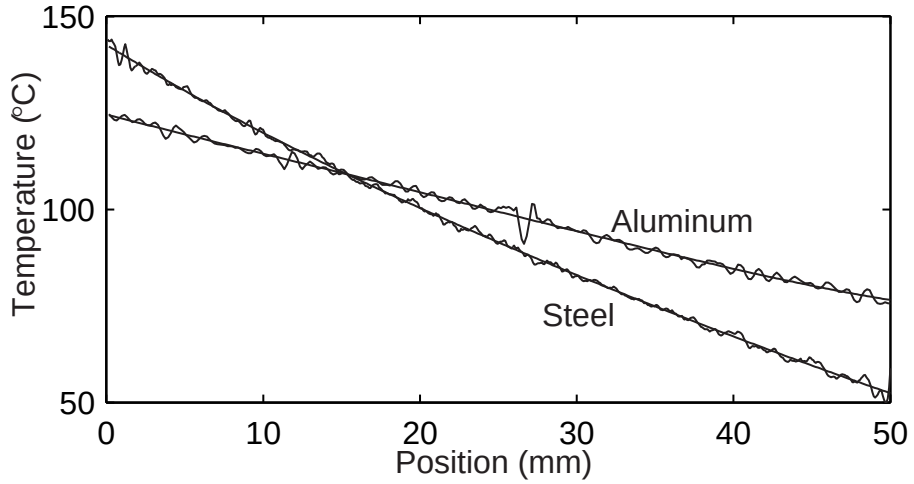

Figure 8.5: Measured temperature profile with aluminum and stainless steel rod. fourth order fits are also shown.

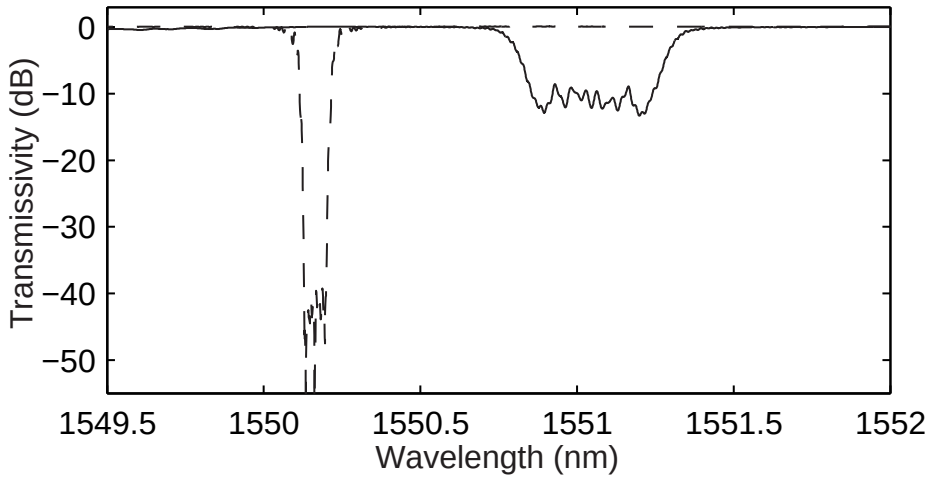

Figure 8.6: Transmissivity of the unchirped strong grating (- -) and when the grating is thermally chirped (—).

Figure 8.6 shows the transmission spectrum of the strong grating with and without the applied thermal chirp. Without the thermal chirp, the Bragg wavelength is 1550.15 nm and the 3 dB bandwidth is 0.122 nm. The measured minimum transmission is limited by the resolution of the analog-to-digital converter (ADC), however a comparison between the theoretical bandwidth of a 50 mm uniform grating and the measured bandwidth indicates −66 dB minimum transmission. With an applied thermal chirp, the Bragg wavelength is 1551.05 nm, the 3 dB bandwidth is 0.498 nm and the transmission minimum is increased to −13 dB, which is sufficient for measuring the spatial profile using OFDR.

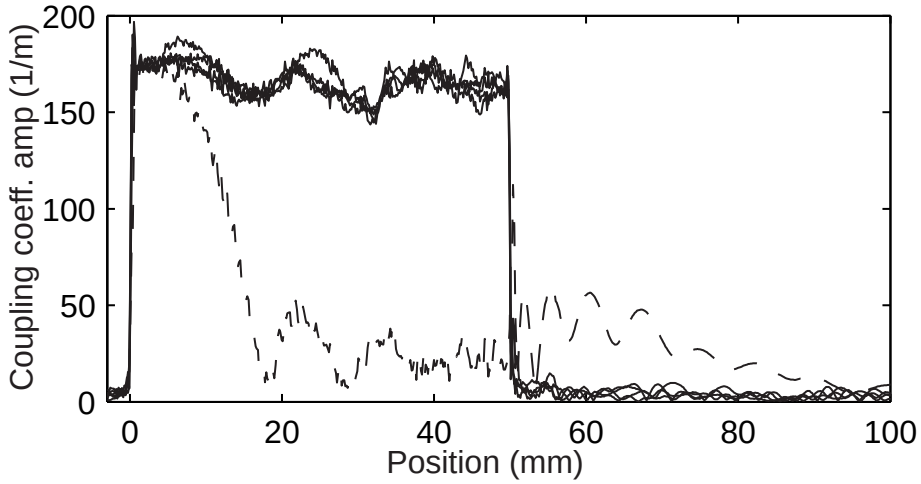

Figure 8.7: Measurement of the coupling strength profile $|\kappa|$ for the unchirped strong grating(- -) and four measurements with thermal chirp(—).

Fig. 8.7 shows the reconstruction of the coupling strength profile $|\kappa|$ of the strong grating measured with and without the applied thermal chirp. Four measurements were done with thermal chirp to evaluate the repeatability of the method. The spatial resolution of 0.16 mm is determined by the 5 nm wavelength span of the measurement. Without the thermal chirp, only the first 3 mm of the grating are correctly reconstructed. After 3 mm, the reconstructed coupling coefficient is dominated by noise amplified by the reconstruction algorithm. The reconstructed $|\kappa|$ of the grating with applied thermal chirp is 165 ± 15 m^{-1}, corresponding to a effective grating strength $|\kappa|L$ of about 8.25. The periodic variations in $|\kappa|$ may be real variations; however, such periodic variations has been observed when the input polarization to the grating was not aligned to one of the eigenpolarizations of the grating. The repeatability is less than 10% of the maximum coupling strength, except for a larger variation at about 23 mm in one of the measurements.

Figure 8.8 shows the reconstructed coupling phase profile $\arg(\kappa)$ of the strong grating after subtracting the thermally induced coupling phase found from the polynomial fit of the temperature profile along the aluminum rod shown in Figure 8.5. The weak grating was characterized immediately after the strong grating. This should accurately remove the thermally induced grating phase from the measured phase profile. The figure shows minimum 0.1 rad repeatability in reconstructed $\arg(\kappa)$, and even less for high frequency phase errors.

The method was also tested on a 50 mm long DFB-FL grating that lased at 1524.28 nm with 250 μW output power. The discussion in Section 8.2 indicates that due to the resonance around the phase shift and absorption, a DFB-FL must be more thermally chirped than an equally strong uniform grating to get correct measurements. By placing the DFB-FL grating within the stainless steel rod, the transmission through the grating was sufficiently increased. A weak grating in another fiber was co-located with the DFB-FL grating and was used to measure the temperature profile. The measured temperature profile is shown in Figure 8.5.

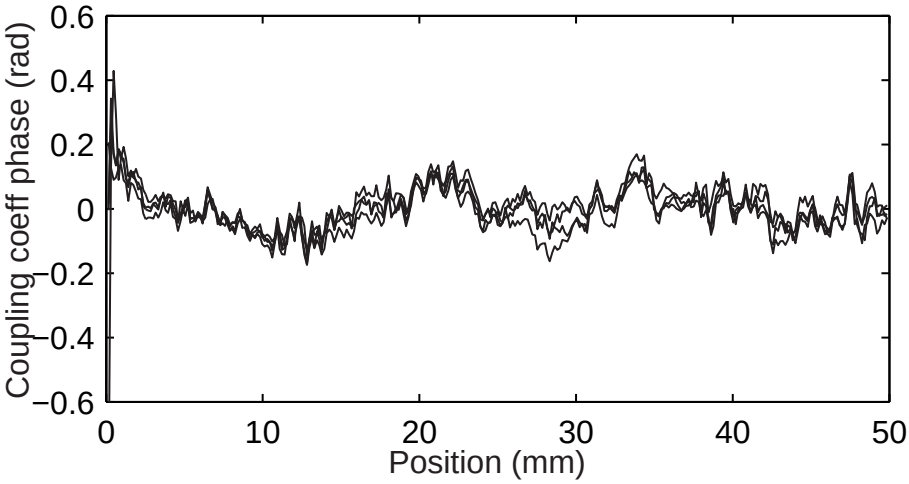

Figure 8.8: Reconstructed coupling phase profile $\arg(\kappa)$ for four measurements with thermal chirp.

Figure 8.9 shows the reconstructed coupling strength profile from four measurements of the DFB-FL grating. The modified layer-peeling algorithm that incorporates absorption was used for the reconstruction, and the absorption of the Er-fiber at the lasing wavelength was measured to 20 dB/m. The measured coupling strength was found to be in the range $|\kappa| = 150 \pm 30$ m^{-1}, except for a significant dip around the phase shift of the grating. This corresponds to a grating strength $|\kappa|L$ of about 7.5. Also shown is a reconstruction of the coupling strength without incorporating absorption. Here, the coupling strength descend from 200 m^{-1} at the start to 120 m^{-1} at the end. The decrease in reconstructed $|\kappa|$ is due to the increasing attenuation with propagated distance within the Er-fiber. The dip in coupling strength is also found in the measured coupling phase. The DFB-FL grating is a distributed optical resonator around the phase shift. Even though the chirping of the grating reduces the strength of the optical resonator, a significant portion of the light will resonate several roundtrips around the phase shift. Due to noise and scaling error, some of this resonate light is not removed by the layer-peeling algorithm, and the coupling coefficient in this region is not correctly reconstructed. This resonate light only has an effect on a section after the phase shift, and the length of this section is given by the strength of the resonator.

Figure 8.10 shows the coupling phase profile $\arg(\kappa)$ after the measured temperature-induced coupling phase has been subtracted. The grating has a phase shift of -0.8π at position 23 mm, which is in agreement with the design of the grating. The measured coupling phase shows also here 0.1 rad repeatability. Since the temperature gradient along the stainless steel rod was less linear and the temperature sensitivity may be different for the two gratings, one cannot expect that the thermally induced grating phase is as accurately determined as for the uniform grating in Figure 8.8 where the superimposed weak grating was used as reference. Thus, there may be a small slowly varying phase component that is caused by errors in the measured temperature profile.

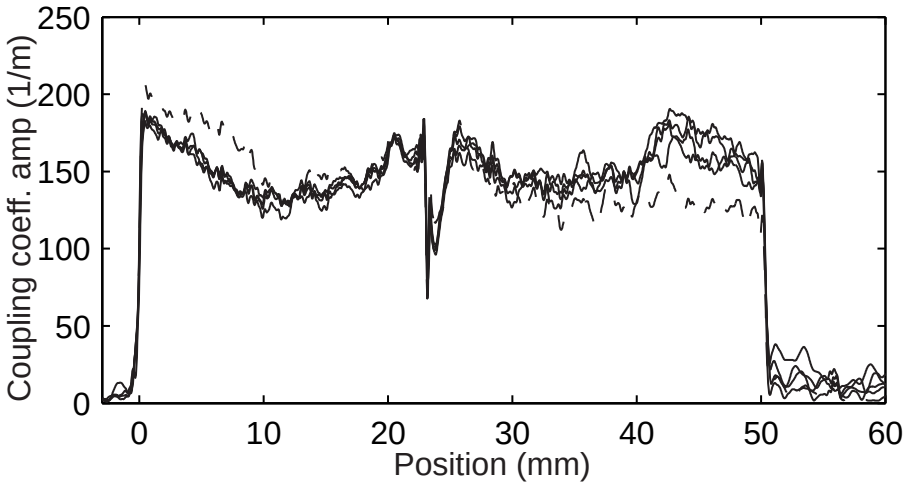

Figure 8.9: Reconstructed coupling strength profile $|\kappa|$ of a DFB fiber laser (four measurements) incorporating 20 dB/m absorption (—) and one reconstruction without incorporating absorption(- -).

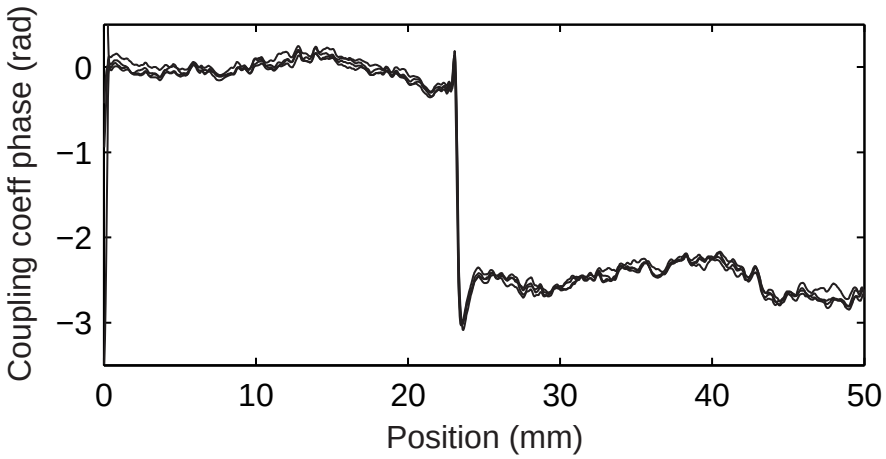

Figure 8.10: Reconstructed coupling phase profile $\arg(\kappa)$ of a DFB fiber laser (four measurements).

8.4 Conclusions

In this paper, an experimental technique for measuring the spatial profile of very strong gratings using an applied thermal chirp and optical frequency domain reflectometry. This method enables spatial characterization of gratings with much higher strength and higher spatial resolution than previously reported methods. The thermal chirping equipment is simple and can be used to enhance the applicability of both OFDR- and OCDR-based grating characterization systems. An accurate measurement of the thermally induced grating phase is achieved using a weaker grating that can be characterized both with and without thermal chirp. This grating can either be superimposed on the strong grating or co-located with the strong grating

but in a different fiber. Spatial reconstruction of a uniform grating with grating strength $|\kappa|L$=8.25 (−66 dB minimum transmissivity) and a DFB-FL grating with grating strength $|\kappa|L$=7.5 was demonstrated. A coupling phase repeatability of 0.1 rad and coupling strength repeatability of 10 % are demonstrated. The method allows for measuring the spatial profile of even stronger gratings, and is only limited by the maximum chirp range of the setup.

Chapter 9

Polarization-resolved spatial characterization of birefringent Fiber Bragg Gratings*

A method that enables polarization-resolved spatial characterization of fiber Bragg gratings is presented. The polarization-resolved reflection spectrum of the grating is measured using optical-frequency domain reflectometry. A polarization-resolved layer-peeling algorithm is used to compute the spatial profile, including the local birefringence and the local polarization-dependent index modulation. A strain-tuned distributed feedback fiber laser is used as source. With closed-loop control of the laser sweep, 0.14 % maximum deviation from constant sweep rate is achieved, which is much better than commercial available tunable lasers. The polarization of the source is modulated synchronous with the laser sweep by passing the light through a three-armed Mach-Zehnder-type interferometer having different retardation. The method is used to investigate the polarization-dependence of the index modulation amplitude of a fiber Bragg grating.

9.1 Introduction

Spatial characterization of fabricated fiber Bragg gratings (FBGs) is a useful tool because it provides direct information of the noise in the fabrication of the FBG or fiber properties. The spatial profile of the FBG can be found by first measuring the complex reflectivity spectrum, and then reconstruct the spatial profile using an inverse scattering algorithm such as the layer peeling algorithm [120, 97, 93, 118, 119, 124].

A method for measuring the complex reflectivity spectrum is the optical frequency domain reflectometry (OFDR) [106, 107, 108]. In OFDR, the optical frequency of a highly coherent tunable laser source (TLS) is swept, and the light is launched into a measurement interferometer consisting of one arm containing the

*This chapter will be submitted to Optics Express for publication. Author: Ole Henrik Waagaard

FBG and one reference arm. The interference signal from the interferometer is detected, and the complex reflection spectrum can be extracted from the interference signal.

In previous methods the grating is assumed to be polarization independent, that is the reflection and transmission spectra are treated as scalar functions. However, the fiber in which the FBG is fabricated will always have some intrinsic birefringence, and the fabrication using uv-light may also induce birefringence as well as polarization-dependent index modulation [41, 42, 43, 44].

If the intrinsic birefringence is constant and there is no uv-induced birefringence or polarization-dependent index modulation, the FBG can be represented as two decoupled scalar spectra in the two eigenaxes of the fiber. Thus, as long as the interrogation state of polarization (SOP) is along one of the eigenaxes of the fiber, only a scalar measurement of the reflection spectrum is required. The interrogation SOP can be oriented along one of the eigenaxes of the fiber by maximizing or minimizing the transmissivity at an edge of the FBG stop band [119]. Alternatively, a polarization diversity receiver can be used [125]. Here, one take advantage of that the sum of the power reflectivities in any two orthogonal polarization states equals the square sum of the two decoupled scalar spectra.

In cases where both intrinsic and uv-induced birefringence contribute, the combined birefringence may have eigenpolarizations that depends on position [68]. Then, the reflectivity spectrum of the FBG can no longer be treated as two decoupled scalar spectra, and a measurement of the full reflection Jones matrix using a polarization-resolved characterization method is required.

In [118], a polarization-resolved spectral characterization method is presented, where polarization controllers are placed in both arms of the measurement interferometer. This method has the disadvantage that 16 laser sweeps are required with different settings for the polarization controllers. There are also commercial instruments that are able to measure the reflection Jones matrix, such as the Luna Technologies Optical Vector Analyzer [126] and the Agilent 81910A Photonic All-parameter Analyzer [127]. Both these instruments include a polarization-diversity receiver.

In this paper we will present and demonstrate a new a method for spectral measurements of the reflection Jones matrix of an FBG using a polarization modulation interferometer between the TLS and the measurement interferometer. In this may a polarization-diversity receiver is not required. This polarization modulation interferometer has three paths with different delays, where the SOPs out of two of the paths are parallel, while the third is orthogonal to the two other SOPs. The polarization modulation interferometer spreads the information about the reflection Jones matrix elements into multiple frequency bands in the detected signal. The polarization-dependent layer-peeling algorithm [68] can be used to find spatial distribution of the index modulation and phase, and also the birefringence and the polarization-dependence of the index modulation from the measured spectrum of the reflection Jones matrix.

9.2 Theory

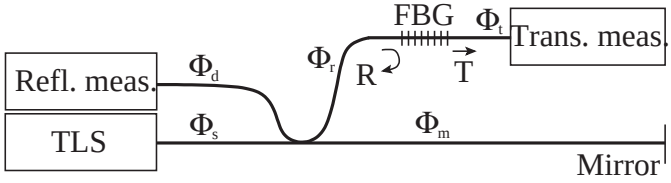

Figure 9.1: Optical frequency domain reflectometry setup for measuring the reflection Jones matrix of a FBG. TLS: Tunable laser source.

Fig. 9.1 shows the basic setup for measuring complex reflection spectrum of an FBG using an OFDR measurement [119]. The tunable laser source (TLS) sweeps the wavelength across the bandwidth of the FBG. The FBG constitutes one of the reflectors in a Michelson interferometer and a highly reflective mirror the other. The light that has been reflected from the FBG and the mirror will interfere. By extracting the phase and amplitude of this interference signal, the complex reflection spectrum can be found, which serves as an input to the layer-peeling algorithm [16, 26, 40] that calculates the spatial profile of the grating. The light that is transmitted through the grating can also be measured, and can be used to scale the measured reflectivity so that the sum of power reflectivity and the power transmissivity is unity across the whole grating bandwidth [119].

We will now analyze the requirement for spectral measurement of all Jones matrix elements of the FBG reflection and transmission. The optical frequency dependent reflection Jones matrix of the grating is denoted $\boldsymbol{R}(\nu)$ and the transmission Jones matrix is denoted $\boldsymbol{T}(\nu)$. Let $\boldsymbol{E}_\mathrm{s}(t) = \hat{\boldsymbol{E}}_\mathrm{s}\mathrm{e}^{-i2\pi\nu t}$ be the electric field vector of light from the TLS, where $\hat{\boldsymbol{E}}_\mathrm{s} = \begin{bmatrix} E_1 & E_2 \end{bmatrix}^\mathrm{T}$ is the Jones vector describing the state of polarization (SOP) and the superscript T represents the matrix transpose operation. The polarization reflected from the FBG and the reflector is altered by the birefringence of the fibers in the interferometer. Let the retardation Jones matrices $\boldsymbol{\Phi}_\mathrm{s}$, $\boldsymbol{\Phi}_\mathrm{r}$, $\boldsymbol{\Phi}_\mathrm{m}$ and $\boldsymbol{\Phi}_\mathrm{d}$ describe the birefringence of the four fibers into and out of the coupler as shown in Fig. 9.1. We assume that these fiber sections are lossless so that these corresponding matrices are unitary.

The electric field vectors $\boldsymbol{E}_\mathrm{m}(t)$ and $\boldsymbol{E}_\mathrm{r}(t)$ reaching the reflection measurement detector after reflection from the FBG and the mirror, respectively, are given by

$$\boldsymbol{E}_\mathrm{m}(t) = k_\mathrm{m}\hat{\boldsymbol{E}}_\mathrm{m}\mathrm{e}^{-i2\pi\nu t} = k_\mathrm{m}\boldsymbol{\Phi}_\mathrm{d}^\mathrm{T}\boldsymbol{\Phi}_\mathrm{m}^\mathrm{T}\boldsymbol{\Phi}_\mathrm{m}\boldsymbol{\Phi}_\mathrm{s}\boldsymbol{E}_\mathrm{s}(t-\tau_\mathrm{m}), \tag{9.1}$$

$$\boldsymbol{E}_\mathrm{r}(t) = k_\mathrm{r}\hat{\boldsymbol{E}}_\mathrm{r}\mathrm{e}^{-i2\pi\nu t} = k_\mathrm{r}\boldsymbol{\Phi}_\mathrm{d}^\mathrm{T}\boldsymbol{\Phi}_\mathrm{r}^\mathrm{T}\boldsymbol{R}(\nu)\boldsymbol{\Phi}_\mathrm{r}\boldsymbol{\Phi}_\mathrm{s}\boldsymbol{E}_\mathrm{s}(t-\tau_\mathrm{r}), \tag{9.2}$$

where τ_m and τ_r account for the optical delays of the two paths, and k_m and k_r are scalar constants given by the coupling ratios of the coupler and the reflectivity of the mirror. (Due to reciprocity, a retardation Jones matrix in the backward direction is given by the transpose of the retardation Jones matrix in the forward direction

[68].) The two light signals interfere, and the detected power is given by

$$\begin{aligned} P_{\mathrm{r}}(\nu) =& k_{\mathrm{m}}^2 \boldsymbol{E}_{\mathrm{m}}(t)^\dagger \boldsymbol{E}_{\mathrm{m}}(t) + k_{\mathrm{r}}^2 \boldsymbol{E}_{\mathrm{r}}(t)^\dagger \boldsymbol{E}_{\mathrm{r}}(t) \\ &+ 2k_{\mathrm{m}}k_{\mathrm{r}}\mathrm{Re}\left\{\boldsymbol{E}_{\mathrm{m}}(t)^\dagger \boldsymbol{E}_{\mathrm{r}}(t)\right\} \\ =& k_{\mathrm{m}}^2 \hat{\boldsymbol{E}}_{\mathrm{m}}^\dagger \hat{\boldsymbol{E}}_{\mathrm{m}} + k_{\mathrm{r}}^2 \hat{\boldsymbol{E}}_{\mathrm{r}}^\dagger \hat{\boldsymbol{E}}_{\mathrm{r}} + 2k_{\mathrm{m}}k_{\mathrm{r}}\mathrm{Re}\left\{\hat{\boldsymbol{E}}_{\mathrm{m}}^\dagger \hat{\boldsymbol{E}}_{\mathrm{r}} \mathrm{e}^{i2\pi\nu\tau_0}\right\} \end{aligned} \tag{9.3}$$

where $\dagger = \mathrm{T}*$ is the transpose conjugate operation, and $\tau_0 = \tau_{\mathrm{r}} - \tau_{\mathrm{m}}$ is the imbalance of the interferometer. The term $\mathrm{e}^{i2\pi\nu\tau_0}$, may be viewed as a carrier signal oscillating versus optical frequency. The interference part of $P_{\mathrm{r}}(\nu)$ can be extracted in the Fourier domain (i.e. the optical delay-domain) around delay τ_0:

$$\begin{aligned} P_{\mathrm{i}}(\nu) &= \hat{\boldsymbol{E}}_{\mathrm{m}}^\dagger \hat{\boldsymbol{E}}_{\mathrm{r}} \mathrm{e}^{i2\pi\nu\tau_0} \\ &= \hat{\boldsymbol{E}}_{\mathrm{s}}^\dagger \boldsymbol{\Phi}_{\mathrm{s}}^\dagger \boldsymbol{\Phi}_{\mathrm{m}}^\dagger \boldsymbol{\Phi}_{\mathrm{m}}^* \boldsymbol{\Phi}_{\mathrm{r}}^{\mathrm{T}} \boldsymbol{R}(\nu) \boldsymbol{\Phi}_{\mathrm{r}} \boldsymbol{\Phi}_{\mathrm{s}} \hat{\boldsymbol{E}}_{\mathrm{s}} \mathrm{e}^{i2\pi\nu\tau_0} \\ &= \hat{\boldsymbol{E}}_{\mathrm{s}}^\dagger \boldsymbol{\Phi}_{\mathrm{o}} \boldsymbol{R}(\nu) \boldsymbol{\Phi}_{\mathrm{i}} \hat{\boldsymbol{E}}_{\mathrm{s}} \mathrm{e}^{i2\pi\nu\tau_0}. \end{aligned} \tag{9.4}$$

Here, we have left out the constant $k_{\mathrm{m}}k_{\mathrm{r}}$. Note that P_{i} is complex since we have only extracted the signal for positive delay. Since $\boldsymbol{\Phi}_{\mathrm{d}}$ is unitary, we have used that $\boldsymbol{\Phi}_{\mathrm{d}}^* \boldsymbol{\Phi}_{\mathrm{d}}^{\mathrm{T}} = \boldsymbol{I}$, where $\boldsymbol{I}$ is the identity matrix. The Jones matrices $\boldsymbol{\Phi}_{\mathrm{o}}$ and $\boldsymbol{\Phi}_{\mathrm{i}}$ are the products of Jones matrices before and after $\boldsymbol{R}(\nu)$ in the second line in (9.4) and represent the effective birefringence from the TLS to the grating and from the grating to the detector.

A more explicit expression for $P_{\mathrm{i}}(\nu)$ can be found by writing (9.4) in terms of the components of $\hat{\boldsymbol{E}}_{\mathrm{s}}$ and $\tilde{\boldsymbol{R}} = \boldsymbol{\Phi}_{\mathrm{o}} \boldsymbol{R}(\nu) \boldsymbol{\Phi}_{\mathrm{i}}$:

$$\begin{aligned} P_{\mathrm{i}}(\nu) &= \left(\tilde{R}_{11}|E_1|^2 + \tilde{R}_{12}E_1^*E_2 + \tilde{R}_{21}E_2^*E_1 + \tilde{R}_{22}|E_2|^2\right)\mathrm{e}^{i2\pi\nu\tau_0} \\ &= \boldsymbol{C}_{\mathrm{s}}^{\mathrm{T}} \begin{bmatrix} \tilde{R}_{11} \\ \tilde{R}_{21} \\ \tilde{R}_{12} \\ \tilde{R}_{22} \end{bmatrix} \mathrm{e}^{i2\pi\tau_0\nu}, \end{aligned} \tag{9.5}$$

where $\boldsymbol{C}_{\mathrm{s}} = \begin{bmatrix} |E_1|^2 & E_2^*E_1 & E_1^*E_2 & |E_2|^2 \end{bmatrix}^{\mathrm{T}}$ is the coherency vector [128] of $\hat{\boldsymbol{E}}_{\mathrm{s}}$ (similar to the coherency matrix, except that the elements are collected into a 4×1 column vector rather than a 2×2 matrix). Note that there is a linear and invertible relationship between the coherency vector $\boldsymbol{C}_{\mathrm{s}}$ and the 4-component Stokes vector [128].

Extracting the four components of $\tilde{\boldsymbol{R}}$ from (9.5), requires four measurements of P_{i} with different source SOPs. These 4 measurements can be put together by writing

$$\begin{bmatrix} P_{\mathrm{i},1}(\nu) \\ P_{\mathrm{i},2}(\nu) \\ P_{\mathrm{i},3}(\nu) \\ P_{\mathrm{i},4}(\nu) \end{bmatrix} = \begin{bmatrix} \boldsymbol{C}_{\mathrm{s},1} & \boldsymbol{C}_{\mathrm{s},2} & \boldsymbol{C}_{\mathrm{s},3} & \boldsymbol{C}_{\mathrm{s},4} \end{bmatrix}^{\mathrm{T}} \begin{bmatrix} \tilde{R}_{11} \\ \tilde{R}_{21} \\ \tilde{R}_{12} \\ \tilde{R}_{22} \end{bmatrix} \mathrm{e}^{i2\pi\tau_0\nu}, \tag{9.6}$$

where $P_{\mathrm{i},j}(\nu)$, $j = 1, \ldots, 4$ are the detected interference signal with the four different coherency vectors $\boldsymbol{C}_{\mathrm{s},j}$. By inverting the matrix $\begin{bmatrix} \boldsymbol{C}_{\mathrm{s},1} & \boldsymbol{C}_{\mathrm{s},2} & \boldsymbol{C}_{\mathrm{s},3} & \boldsymbol{C}_{\mathrm{s},4} \end{bmatrix}^{\mathrm{T}}$, $\tilde{\boldsymbol{R}}$ can

be found from $\begin{bmatrix} P_{\mathrm{i},1}(\nu) & P_{\mathrm{i},2}(\nu) & P_{\mathrm{i},3}(\nu) & P_{\mathrm{i},4}(\nu) \end{bmatrix}^{\mathrm{T}}$. In order to do that, the matrix must be invertible. This means that the four coherency vectors $\boldsymbol{C}_{\mathrm{s},j}$, $j = 1, \ldots, 4$ (or the four corresponding Stokes vectors), must be linearly independent. One example of such a set of SOPs is horizontal polarization, vertical polarization, linear 45° polarization and right circular polarization.

The four measurements can be made by sweeping the laser four times with different polarization settings. However, this may lead to offsets in optical frequencies between the measurements, due to the uncertainty in absolute wavelength of the TLS. An alternative is to continuously modulate the SOP so that components of $\tilde{\boldsymbol{R}}$ have different carrier frequencies [126]. This method is more elaborated in Sec. 9.3. Using this method, only one sweep is required and there will be no problems with frequency offsets between the components of $\tilde{\boldsymbol{R}}$.

The transmission measurement is not used directly to calculated the spatial profile of the FBG, but can be used for proper scaling of $\tilde{\boldsymbol{R}}$. From Fig. 9.1 we find that the SOP of the light reaching the transmission measurement detector is given by

$$\hat{\boldsymbol{E}}_{\mathrm{t}} = k_{\mathrm{t}} \boldsymbol{\Phi}_{\mathrm{t}} \boldsymbol{T}(\nu) \boldsymbol{\Phi}_{\mathrm{r}} \boldsymbol{\Phi}_{\mathrm{s}} \hat{\boldsymbol{E}}_{\mathrm{s}}, \tag{9.7}$$

where k_{t} accounts for loss and detector responsivity. The detected power becomes

$$\begin{aligned} P_{\mathrm{t}}(\nu) &= k_{\mathrm{t}}^2 \hat{\boldsymbol{E}}_{\mathrm{t}}^{\dagger} \hat{\boldsymbol{E}}_{\mathrm{t}} = k_{\mathrm{t}}^2 \hat{\boldsymbol{E}}_{\mathrm{s}}^{\dagger} \boldsymbol{\Phi}_{\mathrm{s}}^{\dagger} \boldsymbol{\Phi}_{\mathrm{r}}^{\dagger} \boldsymbol{T}(\nu)^{\dagger} \boldsymbol{T}(\nu) \boldsymbol{\Phi}_{\mathrm{r}} \boldsymbol{\Phi}_{\mathrm{s}} \hat{\boldsymbol{E}}_{\mathrm{s}} \\ &= k_{\mathrm{t}}^2 \hat{\boldsymbol{E}}_{\mathrm{s}}^{\dagger} \boldsymbol{\Phi}_{\mathrm{i}}^{\dagger} \boldsymbol{T}(\nu)^{\dagger} \boldsymbol{T}(\nu) \boldsymbol{\Phi}_{\mathrm{i}} \hat{\boldsymbol{E}}_{\mathrm{s}} = k_{\mathrm{t}}^2 \hat{\boldsymbol{E}}_{\mathrm{s}}^{\dagger} \tilde{\boldsymbol{T}}(\nu)^{\dagger} \tilde{\boldsymbol{T}}(\nu) \hat{\boldsymbol{E}}_{\mathrm{s}} \end{aligned} \tag{9.8}$$

where we have used that $\boldsymbol{\Phi}_{\mathrm{t}}^{\dagger} \boldsymbol{\Phi}_{\mathrm{t}} = \boldsymbol{I}$.

Assuming that the FBG is lossless [68],

$$\tilde{\boldsymbol{R}}(\nu)^{\dagger} \tilde{\boldsymbol{R}}(\nu) + \tilde{\boldsymbol{T}}(\nu)^{\dagger} \tilde{\boldsymbol{T}}(\nu) = \boldsymbol{I}. \tag{9.9}$$

This relation is used to find $k_{\mathrm{m}} k_{\mathrm{r}}$ in (9.3) so that $\tilde{\boldsymbol{R}}$ is scaled correctly.

The polarization-resolved layer-peeling algorithm in [68] will be used to calculate the spatial profile of the grating from the grating impulse response (the Fourier transform of the reflection spectrum.) However this algorithm requires that the grating is reciprocal and measured in a linear basis, which means that the reflection Jones matrix is symmetric for all optical frequencies ν. This is not the case since the reflection Jones matrix seen from the detector, $\tilde{\boldsymbol{R}}(\nu) = \boldsymbol{\Phi}_{\mathrm{o}} \boldsymbol{R}(\nu) \boldsymbol{\Phi}_{\mathrm{i}}$ is only symmetric when $\boldsymbol{\Phi}_{\mathrm{o}} = \boldsymbol{\Phi}_{\mathrm{i}}^{\mathrm{T}}$.

We calculate the grating impulse response $\boldsymbol{h}(\tau) = \mathrm{FT}\{\boldsymbol{R}(\nu)\}$, as $\boldsymbol{h}(\tau) = \tilde{\boldsymbol{\Phi}}_{\mathrm{o}}^{\dagger} \tilde{\boldsymbol{h}}(\tau) \tilde{\boldsymbol{\Phi}}_{\mathrm{i}}^{\dagger}$, where $\tilde{\boldsymbol{h}}(\tau) = \mathrm{FT}\{\tilde{\boldsymbol{R}}(\nu)\}$. Here, FT denotes the Fourier transform. The matrices $\tilde{\boldsymbol{\Phi}}_{\mathrm{o}}$ and $\tilde{\boldsymbol{\Phi}}_{\mathrm{i}}$ must be chosen so that $\boldsymbol{h}(\tau)$ is symmetric for all τ, which means that $\tilde{\boldsymbol{\Phi}}_{\mathrm{o}} = \boldsymbol{\Phi}_{\mathrm{o}} \tilde{\boldsymbol{\Phi}}$ and $\tilde{\boldsymbol{\Phi}}_{\mathrm{i}} = \tilde{\boldsymbol{\Phi}}^{\mathrm{T}} \boldsymbol{\Phi}_{\mathrm{i}}$ where $\tilde{\boldsymbol{\Phi}}$ is an arbitrary and constant unitary matrix. To remove the effect of $\tilde{\boldsymbol{\Phi}}_{\mathrm{o}}$ and $\tilde{\boldsymbol{\Phi}}_{\mathrm{i}}$, select a delay $\tau = \tau'$ where the singular values of $\tilde{\boldsymbol{h}}(\tau')$ do not degenerate. Using singular decomposition we may factorize $\tilde{\boldsymbol{h}}(\tau') = \boldsymbol{U} \boldsymbol{\Sigma} \boldsymbol{V}$, where $\boldsymbol{U}$ and $\boldsymbol{V}$ are unitary and $\boldsymbol{\Sigma}$ is diagonal and non-negative. Since the singular values are different, the $\boldsymbol{U}$ and $\boldsymbol{V}$ are unique up to a matrix

$$\boldsymbol{D} = \begin{bmatrix} \mathrm{e}^{i\theta} & 0 \\ 0 & \mathrm{e}^{-i\theta} \end{bmatrix}, \tag{9.10}$$

where θ is real but otherwise arbitrary, since $\boldsymbol{U}\boldsymbol{D}\boldsymbol{\Sigma}\boldsymbol{D}^*\boldsymbol{V} = \boldsymbol{U}\boldsymbol{\Sigma}\boldsymbol{V}$. We choose $\tilde{\boldsymbol{\Phi}}_{\mathrm{o}} = \boldsymbol{U}\boldsymbol{D}$ and $\tilde{\boldsymbol{\Phi}}_{\mathrm{i}} = \boldsymbol{D}^*\boldsymbol{V}$, which gives

$$\boldsymbol{h}(\tau) = \boldsymbol{D}^*\boldsymbol{U}^\dagger\tilde{\boldsymbol{h}}(\tau)\boldsymbol{V}^\dagger\boldsymbol{D} = \begin{bmatrix} \hat{h}_{11} & \hat{h}_{12}\mathrm{e}^{-i2\theta} \\ \hat{h}_{21}\mathrm{e}^{i2\theta} & \hat{h}_{22} \end{bmatrix}, \tag{9.11}$$

where $\hat{h}_{nm}$ are the components of the matrix $\boldsymbol{U}^\dagger\tilde{\boldsymbol{h}}(\tau)\boldsymbol{V}^\dagger$. By evaluating this equation for all $\tau \neq \tau'$, the phase constant θ can be found as the phase in $\boldsymbol{D}$ that minimizes the difference $\hat{h}_{12}\mathrm{e}^{-i2\theta} - \hat{h}_{21}\mathrm{e}^{i2\theta}$ for all τ.

The polarization-resolved layer-peeling algorithm [68] can now be used to calculate the polarization-dependent spatial profile of the FBG from $\boldsymbol{h}(\tau)$. In [68], the grating is discretized into N layers, where each layer is a cascade of a retardation section, a discrete reflector and a time-delay section. From $\boldsymbol{h}(0)$, the retardation and the discrete reflector of the first layer can be found. Once the first layer is characterized, the transfer matrix of the layer can be computed, and the effect of the layer on the FBG can be removed using the calculated transfer matrix. Then, the retardance and the discrete reflector of the next layer can be found from the reduced grating. This procedure is repeated until all layers are characterized.

In the polarization-resolved layer-peeling algorithm, let $\boldsymbol{\Upsilon}_j$ represent the reflection response from layer j alone. $\boldsymbol{\Upsilon}_j$ should be symmetric due to reciprocity, and given by $\boldsymbol{\Phi}_j^{\mathrm{T}}\boldsymbol{\rho}_j\boldsymbol{\Phi}_j$, where $\boldsymbol{\Phi}_j$ is the Jones matrix describing the retardation from layer $j-1$ to layer j and $\boldsymbol{\rho}_j$ the reflection from discrete reflector j.

When the grating reflection response is measured, and not synthesized as in [68], measurement noise and calibration errors may lead to a measured response that is not symmetric. In Appendix 9.A it is shown how to factorize $\boldsymbol{\Upsilon}_j$ when it is not symmetric. The asymmetry is handled by adding an extra retardation $\boldsymbol{\Phi}_{\mathrm{as},j}$ for the forward propagating field, so that $\boldsymbol{\Upsilon}_j = \boldsymbol{\Phi}_j^{\mathrm{T}}\boldsymbol{\rho}_j\boldsymbol{\Phi}_j\boldsymbol{\Phi}_{\mathrm{as},j}$.

9.3 Measurement of the grating impulse response

9.3.1 Optical frequency modulation

The setup used for measuring the optical-frequency dependent reflection Jones matrix of a fiber Bragg grating (FBG) is shown in Fig. 9.2. The reflection of the FBG is detected at detector output D1, while detector output D2 gives the transmissivity. These two waveforms are sampled with a National Instrument NI-6052 data acquisition (DAQ) card, and processed in LabView$^{\mathrm{TM}}$ and Matlab$^{\mathrm{TM}}$.

A distributed-feedback fiber laser (DFB-FL) at 1549 nm is used as the tunable laser source. This source provides both low frequency and intensity noise and mode-hop free operation [129]. The linewidth is typically in the order of 1-10 kHz. By using this source, superior sensitivity and length range can be obtained [109]. The DFB-FL is arranged in a master oscillator power amplifier (MOPA) configuration. The laser is pumped by a 100 mW 1480 nm laser diode, and an EDFA boosts up the power from the laser and removes the remaining pump light. The power at the output of the MOPA is detected with D5. The detected power provides negative

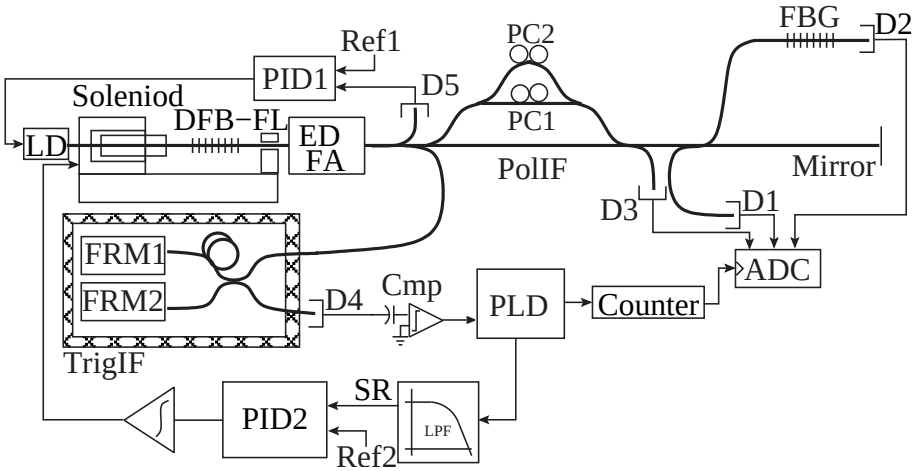

Figure 9.2: Optical frequency domain reflectometry of a FBG's reflection Jones matrix. DFB-FL: Distributed-feedback fiber laser; LD: Diode pump laser; EDFA: Erbium doped fiber amplifier; TrigIF: Trigger interferometer; D1-4: Detectors; PolIF: Polarization modulation interferometer; PC1-2: Manual polarization controllers; FRM1-2: Faraday rotation mirrors; ADC: Analog-to-digital converter (NI-6052); PLD: Programmable logic device; Cmp: Comparator; PID1-2: Proportional-integrate-derivate controllers; SR: Sweep rate; Ref1-2: Reference signals; LPF: low-pass filter.

feedback to the laser diode current to minimize the intensity noise of the laser output [129].

One end of the DFB-FL is fixed, while the other end is mounted to the armature (the moving part) of a solenoid. When voltage is applied to the solenoid, the fiber is strained. This provides tuning of the wavelength of the laser across the grating bandwidth. We apply at maximum 1.2% stain to the fiber, and the available wavelength range becomes 1549 nm to 1563 nm.

A trigger Michelson interferometer with ∼100 m imbalance is used to keep track of the exact evolution of the optical frequency during the sweep of the laser. We use the fringe output D4 of this interferometer to generate a sampling clock to the NI-6052 card for sampling the detector outputs D1-3 equidistant in optical frequency [107]. The phase of the fringe signal at detector D4 is $\phi_3(t) = 2\pi\nu(t)\tau_{\text{trig}}$, where $\nu(t)$ is the optical frequency and τ_{trig} is the dual pass delay difference of the interferometer. The fringe output D4 is connected to an ac-coupled comparator, which produces 0V or 5V dependent on the sign of the fringe signal. The PLD produces a 30 ns short trigger pulse from this signal. This pulse train can be used as a sampling clock for D1-3. However, in order to make the system more flexible, this pulse train is fed to a counter integrated on the NI-6052 card. This counter enables software-selectable down-sampling so that D1-3 can be sampled equidistant in optical frequency with a sampling interval that is any multiple of $1/(2\tau_{\text{trig}}) \sim 0.5$ MHz.

In practice, the interference signal at D1 will not be sampled exactly equidistant in optical frequency; there will always be some sampling jitter associated with the generation of trigger pulses. Let the interference signal be sampled at a frequency

$k\Delta\nu + \delta\nu(k)$, where k is an integer and $\delta\nu(k)$ is the sampling jitter. Then the detected interference power in (9.3) is given by

$$\mathrm{Re}\{P_\mathrm{i}(k\Delta\nu + \delta\nu(k)\} \approx \mathrm{Re}\{P_\mathrm{i}(k\Delta\nu)\} + \frac{d\mathrm{Re}\{P_\mathrm{i}(k\Delta\nu)\}}{d\nu}\delta\nu(k). \tag{9.12}$$

Here, we assume for simplicity that $2k_\mathrm{m}k_\mathrm{r} = 1$. With sufficiently large trigger interferometer delays, the last term in this equation will typically give a noise contribution to the measured value for $P_\mathrm{i}(\nu)$ that exceeds the quantum noise with several orders of magnitude [107]. It is therefore essential to minimize this sampling jitter in order to minimize noise in the characterization results. Assuming that $\mathrm{Re}\{P_\mathrm{i}(k\Delta\nu)\}$ and $\delta\nu(k)$ are uncorrelated, the rms of this noise contribution is given by

$$\Delta P_\mathrm{i,rms} = \sqrt{\left\langle \left| \frac{d\mathrm{Re}\{P_\mathrm{i}(k\Delta\nu)\}}{d\nu} \right|^2 \right\rangle} \sqrt{\left\langle |\delta\nu(k)|^2 \right\rangle} = \sqrt{\left\langle \left| \frac{d\mathrm{Re}\{P_\mathrm{i}(k\Delta\nu)\}}{d\nu} \right|^2 \right\rangle} \delta\nu_\mathrm{rms}. \tag{9.13}$$

Improved signal-to-noise ratio (SNR) can be obtained by reducing $\delta\nu_\mathrm{rms}$. The sampling jitter is a function of the product of the fluctuations in laser sweep rate and the difference in delay to the AD converter between the trigger pulses and the sampled signal. If the laser sweep is completely linear and the delay is constant, this delay is unimportant since the delay transforms to a constant $\delta\nu$. If the laser sweep is not completely linear, it can be compensated by adding fiber before detector D4. However, the delays have to be very well matched when the fluctuations in sweep rate is large. In addition, group delay ripple in filters may give a delay difference that is not constant. The laser sweep should therefore be as linear as possible.

To linearize the sweep, the trigger interferometer enables closed-loop control of the laser sweep [130]. The PLD in Fig. 9.2 produces a 120 ns long pulse every time the fringe signal at D4 crosses zero. The delay between subsequent pulses is given by the actual sweep rate SR=$d\nu(t)/dt$ of the DFB-FL. This pulse train is low-pass filtered using a 4-pole Butterworth active filter with 60 kHz bandwidth. The resulting voltage amplitude is proportional to the sweep rate. Using a PID controller, we lock the measured sweep rate to a reference sweep rate. The optical frequency of the DFB-FL is a (nonlinear) function of the voltage applied to the solenoid. The output of the PID controller is therefore integrated to generate a signal that is proportional to optical frequency. This signal is applied to the solenoid.

9.3.2 Polarization modulation

The polarization modulation interferometer (PolIF) comprises four 3 dB couplers and the three paths 1, 2 and 3 with delays τ_1, τ_2 and τ_3, respectively. These delays are chosen so that $\tau_\mathrm{a} = \tau_2 - \tau_1 = 10$ ns and $\tau_\mathrm{b} = \tau_3 - \tau_1 = 15$ ns. The SOP out of the PolIF depends on the birefringence of the paths and the optical frequency.

The electric field vector at the output of the PolIF is given by

$$\begin{aligned} \boldsymbol{E}_\mathrm{s}(t) &= \hat{\boldsymbol{E}}_\mathrm{s}\mathrm{e}^{-i2\pi\nu t} = \hat{\boldsymbol{E}}_1\mathrm{e}^{-i(2\pi\nu(t-\tau_1))} + \hat{\boldsymbol{E}}_2\mathrm{e}^{-i(2\pi\nu(t-\tau_2))} + \hat{\boldsymbol{E}}_3\mathrm{e}^{-i(2\pi\nu(t-\tau_3))} \\ &= k_1\boldsymbol{\Phi}_1\mathrm{e}^{-i(2\pi\nu(t-\tau_1))}\left(\hat{\boldsymbol{e}}_1 + \hat{\boldsymbol{E}}_\mathrm{a}\mathrm{e}^{i2\pi\nu\tau_\mathrm{a}} + \hat{\boldsymbol{E}}_\mathrm{b}\mathrm{e}^{i2\pi\nu\tau_\mathrm{b}}\right), \end{aligned} \tag{9.14}$$

where $\hat{\boldsymbol{E}}_1$, $\hat{\boldsymbol{E}}_2$ and $\hat{\boldsymbol{E}}_3$ are the Jones vectors describing the SOP out of each of the three paths, respectively, and $\hat{\boldsymbol{e}}_1 = \begin{bmatrix}1 & 0\end{bmatrix}^{\mathrm{T}}$.

The matrix $\boldsymbol{\Phi}_1$ is a unitary matrix with the first column equal to $\hat{\boldsymbol{E}}_1$, so that $\boldsymbol{\Phi}_1\hat{\boldsymbol{e}}_1 = \hat{\boldsymbol{E}}_1$. We write,

$$\hat{\boldsymbol{E}}_{\mathrm{a}} = \boldsymbol{\Phi}_1^{\dagger}\hat{\boldsymbol{E}}_2 = k_{\mathrm{a}}\begin{bmatrix}\sin\theta_{\mathrm{a}}\mathrm{e}^{i\alpha_{\mathrm{a}}}\\ \cos\theta_{\mathrm{a}}\mathrm{e}^{i\beta_{\mathrm{a}}}\end{bmatrix} = \begin{bmatrix}\mathrm{s_a}\\ \mathrm{c_a}\end{bmatrix} \tag{9.15}$$

$$\hat{\boldsymbol{E}}_{\mathrm{b}} = \boldsymbol{\Phi}_1^{\dagger}\hat{\boldsymbol{E}}_3 = k_{\mathrm{b}}\begin{bmatrix}\sin\theta_{\mathrm{b}}\mathrm{e}^{i\alpha_{\mathrm{b}}}\\ \cos\theta_{\mathrm{b}}\mathrm{e}^{i\beta_{\mathrm{b}}}\end{bmatrix} = \begin{bmatrix}\mathrm{s_b}\\ \mathrm{c_b}\end{bmatrix}. \tag{9.16}$$

The second column of $\boldsymbol{\Phi}_1$ must be orthonormal to the first column, but can have an arbitrary common mode phase. This common mode phase will be chosen so that $\beta_{\mathrm{a}} = -\beta_{\mathrm{b}} = \beta$. When the coupler has 50/50 % coupling ratio and there is no loss neither in the couplers nor the fibers within PolIF, $k_{\mathrm{a}} = k_{\mathrm{b}} = 1/2$.

By inserting (9.14) into (9.4) we find that the matrix $\boldsymbol{\Phi}_1$ may be absorbed into the matrices $\boldsymbol{\Phi}_{\mathrm{i}}$ and $\boldsymbol{\Phi}_{\mathrm{o}}$, and k_1 can be absorbed into k_{m} and k_{r}, which is left out in (9.4). Without loss of generality we may therefore set $k_1 = 1$, $\boldsymbol{\Phi}_1 = \boldsymbol{I}$ and $\tau_1 = 0$.

The coherence vector found by inserting (9.15) and (9.16) into (9.14) then becomes,

$$\boldsymbol{C}_{\mathrm{s}} = \boldsymbol{M}\begin{bmatrix}1\\ \mathrm{e}^{-i2\pi\nu(\tau_{\mathrm{b}}-\tau_{\mathrm{a}})}\\ \mathrm{e}^{i2\pi\nu(\tau_{\mathrm{b}}-\tau_{\mathrm{a}})}\\ \mathrm{e}^{-i2\pi\nu\tau_{\mathrm{a}}}\\ \mathrm{e}^{i2\pi\nu\tau_{\mathrm{a}}}\\ \mathrm{e}^{-i2\pi\nu\tau_{\mathrm{b}}}\\ \mathrm{e}^{i2\pi\nu\tau_{\mathrm{b}}}\end{bmatrix}, \tag{9.17}$$

where

$$\boldsymbol{M} = \begin{bmatrix}1+|\mathrm{s_a}|^2+|\mathrm{s_b}|^2 & \mathrm{s_a}\mathrm{s_b}^* & \mathrm{s_a}^*\mathrm{s_b} & \mathrm{s_a}^* & \mathrm{s_a} & \mathrm{s_b}^* & \mathrm{s_b}\\ \mathrm{s_a}\mathrm{c_a}^*+\mathrm{s_b}\mathrm{c_b}^* & \mathrm{s_a}\mathrm{c_b}^* & \mathrm{c_a}^*\mathrm{s_b} & \mathrm{c_a}^* & 0 & \mathrm{c_b}^* & 0\\ \mathrm{s_a}^*\mathrm{c_a}+\mathrm{s_b}^*\mathrm{c_b} & \mathrm{c_a}\mathrm{s_b}^* & \mathrm{s_a}^*\mathrm{c_b} & 0 & \mathrm{c_a} & 0 & \mathrm{c_b}\\ |\mathrm{c_a}|^2+|\mathrm{c_b}|^2 & \mathrm{c_a}\mathrm{c_b}^* & \mathrm{c_a}^*\mathrm{c_b} & 0 & 0 & 0 & 0\end{bmatrix}. \tag{9.18}$$

In Section 9.2 we found that the reflection Jones matrix can be extracted if the SOP in (9.17) is modulated through 4 SOPs represented by 4 linearly independent coherence vectors (or equally 4 linearly independent Stokes vectors). This will be the case as long as $\tau_{\mathrm{a}} \neq \tau_{\mathrm{b}} \neq \tau_{\mathrm{b}} - \tau_{\mathrm{a}} \neq 0$, $k_{\mathrm{a}}, k_{\mathrm{b}} \neq 0$ and $\boldsymbol{M}$ has linearly independent rows. $\boldsymbol{M}$ will only have linear dependent rows when $\hat{\boldsymbol{E}}_{\mathrm{a}}, \hat{\boldsymbol{E}}_{\mathrm{b}} \| \hat{\boldsymbol{e}}_1$. The optimum configuration is when $\hat{\boldsymbol{E}}_{\mathrm{a}}, \hat{\boldsymbol{E}}_{\mathrm{b}} \perp \hat{\boldsymbol{e}}_1$, which gives

$$\boldsymbol{M} = \begin{bmatrix}1 & 0 & 0 & 0 & 0 & 0 & 0\\ 0 & 0 & 0 & k_{\mathrm{a}}\mathrm{e}^{-i\beta} & 0 & k_{\mathrm{b}}\mathrm{e}^{i\beta} & 0\\ 0 & 0 & 0 & 0 & k_{\mathrm{a}}\mathrm{e}^{i\beta} & 0 & k_{\mathrm{b}}\mathrm{e}^{-i\beta}\\ k_{\mathrm{a}}^2+k_{\mathrm{b}}^2 & k_{\mathrm{a}}k_{\mathrm{b}}\mathrm{e}^{i2\beta} & k_{\mathrm{a}}k_{\mathrm{b}}\mathrm{e}^{-i2\beta} & 0 & 0 & 0 & 0\end{bmatrix}. \tag{9.19}$$

Inserting (9.17) into (9.5) gives the detected interference power at D1:

$$P_{\mathrm{i}}(\nu) = \begin{bmatrix} 1 \\ \mathrm{e}^{-i2\pi\nu(\tau_{\mathrm{b}}-\tau_{\mathrm{a}})} \\ \mathrm{e}^{i2\pi\nu(\tau_{\mathrm{b}}-\tau_{\mathrm{a}})} \\ \mathrm{e}^{-i2\pi\nu\tau_{\mathrm{a}}} \\ \mathrm{e}^{i2\pi\nu\tau_{\mathrm{a}}} \\ \mathrm{e}^{-i2\pi\nu\tau_{\mathrm{b}}} \\ \mathrm{e}^{i2\pi\nu\tau_{\mathrm{b}}} \end{bmatrix}^{\mathrm{T}} \boldsymbol{M}^{\mathrm{T}} \begin{bmatrix} \tilde{R}_{11}(\nu) \\ \tilde{R}_{21}(\nu) \\ \tilde{R}_{12}(\nu) \\ \tilde{R}_{22}(\nu) \end{bmatrix} \mathrm{e}^{i2\pi\tau_0\nu}. \tag{9.20}$$

Now, let $\tilde{\boldsymbol{h}}(\tau)$ be the Fourier transform of $\tilde{\boldsymbol{R}}(\nu)$, and $\zeta(\tau)$ be the Fourier transform of $P_r(\nu)$. Even though the impulse response $\tilde{\boldsymbol{h}}(\tau)$ is infinitely long, we assume that the amplitude is insignificant outside the range $[0, \tau_l]$. The Fourier transform of the leftmost vector in (9.20) is a column of delta functions $\delta(\tau - \tau')$ with different delays τ'. In the delay-domain, this factor is convolved with the Fourier transform of the remaining factors to produce the signal $\zeta(\tau)$, where the matrix components of $\tilde{\boldsymbol{h}}$ is divided into separable bands starting at τ_0, $\tau_0 \pm (\tau_{\mathrm{b}} - \tau_{\mathrm{a}})$, $\tau_0 \pm \tau_{\mathrm{a}}$ and $\tau_0 \pm \tau_{\mathrm{b}}$. To avoid overlap between these bands, we must require that $\tau_l < \tau_{\mathrm{a}} - \tau_{\mathrm{b}}$=5 ns. We may extract these bands and shift them to zero delay, yielding the vector

$$\begin{bmatrix} \zeta(\tau - \tau_0) \\ \zeta(\tau - \tau_0 + (\tau_{\mathrm{b}} - \tau_{\mathrm{a}})) \\ \zeta(\tau - \tau_0 - (\tau_{\mathrm{b}} - \tau_{\mathrm{a}})) \\ \zeta(\tau - \tau_0 + \tau_{\mathrm{a}}) \\ \zeta(\tau - \tau_0 - \tau_{\mathrm{a}}) \\ \zeta(\tau - \tau_0 + \tau_{\mathrm{b}}) \\ \zeta(\tau - \tau_0 - \tau_{\mathrm{b}}) \end{bmatrix} = \boldsymbol{M}^{\mathrm{T}} \begin{bmatrix} \tilde{h}_{11}(\tau) \\ \tilde{h}_{21}(\tau) \\ \tilde{h}_{12}(\tau) \\ \tilde{h}_{22}(\tau) \end{bmatrix}, \tag{9.21}$$

which is valid for $0 \leq \tau \leq \tau_l$. The components of $\tilde{\boldsymbol{h}}(\tau)$ can be found this equation. Note that there is 4 unknowns and 7 equations, i.e. the system is over-determined. A least square solution can be found by multiplying each side of (9.21) with the pseudo-inverse $\boldsymbol{M}^{+}$ of $\boldsymbol{M}^{\mathrm{T}}$, which satisfy $\boldsymbol{M}^{+}\boldsymbol{M}^{\mathrm{T}} = \boldsymbol{I}$.

9.3.3 Calibration

Detector D3 is used for monitoring of the polarization modulation and calculation of the matrix $\boldsymbol{M}$. The Jones vector at detector D3 is proportional to $\hat{\boldsymbol{e}}_1 - k_{\mathrm{c}}\left(\hat{\boldsymbol{E}}_{\mathrm{a}} \exp[i2\pi\nu\tau_{\mathrm{a}}] + \hat{\boldsymbol{E}}_{\mathrm{b}} \exp[i2\pi\nu\tau_{\mathrm{b}}]\right)$, where k_{c} is given by the power coupling ratio of the coupler at the output of the PolIF. Thus, the detected power becomes,

$$\begin{aligned} P_{\mathrm{D3}}(\nu) &= k_{\mathrm{D3}}\left[\hat{\boldsymbol{e}}_1 - k_{\mathrm{c}}\left(\hat{\boldsymbol{E}}_{\mathrm{a}}\mathrm{e}^{i2\pi\nu\tau_{\mathrm{a}}} + \hat{\boldsymbol{E}}_{\mathrm{b}}\mathrm{e}^{i2\pi\nu\tau_{\mathrm{b}}}\right)\right]^{\dagger}\left[\hat{\boldsymbol{e}}_1 - k_{\mathrm{c}}\left(\hat{\boldsymbol{E}}_{\mathrm{a}}\mathrm{e}^{i2\pi\nu\tau_{\mathrm{a}}} + \hat{\boldsymbol{E}}_{\mathrm{b}}\mathrm{e}^{i2\pi\nu\tau_{\mathrm{b}}}\right)\right] \\ &= k_{\mathrm{D3}}\Big[1 + k_{\mathrm{c}}^2\left(k_{\mathrm{a}}^2 + k_{\mathrm{b}}^2 + 2\mathrm{Re}\left\{(\mathrm{s}_{\mathrm{a}}^{*}\mathrm{s}_{\mathrm{b}} + \mathrm{c}_{\mathrm{a}}^{*}\mathrm{c}_{\mathrm{b}})\mathrm{e}^{i2\pi\nu(\tau_{\mathrm{b}}-\tau_{\mathrm{a}})}\right\}\right) \\ &\qquad - 2k_{\mathrm{c}}\left(\mathrm{Re}\left\{\mathrm{s}_{\mathrm{a}}\mathrm{e}^{i2\pi\nu\tau_{\mathrm{a}}}\right\} + \mathrm{Re}\left\{\mathrm{s}_{\mathrm{b}}\mathrm{e}^{i2\pi\nu\tau_{\mathrm{b}}}\right\}\right)\Big], \end{aligned} \tag{9.22}$$

where k_{D3} is a scaling constant.

The PolIF can be set in the optimum mode of operation by adjusting polarization controllers PC1 and PC2, while repeatedly sweeping the laser, measure the response at detector D3, and calculate the Fourier transform $\zeta_{\mathrm{D3}}(\tau) = \mathrm{FT}\{P_{\mathrm{D3}}(\nu)\}$. PC1 should be adjusted until $\zeta_{\mathrm{D3}}(\tau_{\mathrm{a}}) = 0$ and PC2 so that $\zeta_{\mathrm{D3}}(\tau_{\mathrm{b}}) = 0$. This will ensure that $\hat{\boldsymbol{E}}_{\mathrm{a}}, \hat{\boldsymbol{E}}_{\mathrm{b}} \| \begin{bmatrix} 0 & 1 \end{bmatrix}^{\mathrm{T}}$, which is the wanted mode of operation.

Even though the PolIF is calibrated so that the SOP out of the second and third path is orthogonal to the SOP out of the first path, the birefringence in the paths may fluctuate between measurements. Instead of readjusting PC1 and PC2 to compensate for the drift in birefringence, the response at detector D3 is measured simultaneously with the responses at detectors D1 and D2 to find the matrix $\boldsymbol{M}$ in (9.18).

Provided that the constants k_{a}, k_{b} and k_{c} are known (see below), k_{D3} can be found from $\zeta_{\mathrm{D3}}(0)$. We may then calculate

$$\mathrm{s_a} = -\zeta_{\mathrm{D3}}(\tau_{\mathrm{a}})/(k_{\mathrm{D3}}k_{\mathrm{c}}) \tag{9.23a}$$

$$\mathrm{s_b} = -\zeta_{\mathrm{D3}}(\tau_{\mathrm{b}})/(k_{\mathrm{D3}}k_{\mathrm{c}}) \tag{9.23b}$$

$$|\mathrm{c_a}| = \sqrt{k_{\mathrm{a}}^2 - |\mathrm{s_a}|^2} \tag{9.23c}$$

$$|\mathrm{c_b}| = \sqrt{k_{\mathrm{b}}^2 - |\mathrm{s_b}|^2} \tag{9.23d}$$

$$\beta = \arg(\mathrm{c_a c_b^*})/2 = \arg(\zeta_{\mathrm{D3}}(\tau_{\mathrm{b}} - \tau_{\mathrm{a}})^* k_{\mathrm{D3}} - \zeta_{\mathrm{D3}}(\tau_{\mathrm{a}})^* \zeta_{\mathrm{D3}}(\tau_{\mathrm{b}}))/2. \tag{9.23e}$$

Thus, we have obtained all the components required for calculation of $\boldsymbol{M}$.

The constants k_{a}, k_{b} and k_{c} depend only on the coupling ratios of the couplers and the loss in the interferometer path, and we can therefore assume that they do not fluctuate with time.

When the FBG replaced is replaced by a patch-cord, the resulting detected power at D2 will be proportional to (9.22) but with $k_{\mathrm{c}} = -1$. The constant k_{c} can therefore be found by comparing the measured responses at D3 and D2.

Eq. (9.22) provides measurement of seven independent real parameters, whereas eqs. (9.23) only use six. The remaining independent parameter gives rise to the equation

$$\begin{aligned} &|\zeta'_{\mathrm{D3}}(\tau_{\mathrm{b}} - \tau_{\mathrm{a}})|^2 + k_{\mathrm{a}}'^2 |\zeta'_{\mathrm{D3}}(\tau_{\mathrm{b}})|^2 + k_{\mathrm{b}}'^2 |\zeta'_{\mathrm{D3}}(\tau_{\mathrm{a}})|^2 \\ &= \frac{k_{\mathrm{a}}'^2 k_{\mathrm{b}}'^2}{(1 + k_{\mathrm{a}}'^2 + k_{\mathrm{b}}'^2)^2} + 2(1 + k_{\mathrm{a}}'^2 + k_{\mathrm{b}}'^2)\mathrm{Re}\{\zeta'_{\mathrm{D3}}(\tau_{\mathrm{b}} - \tau_{\mathrm{a}})\zeta'_{\mathrm{D3}}(\tau_{\mathrm{a}})\zeta'^*_{\mathrm{D3}}(\tau_{\mathrm{b}})\}, \end{aligned} \tag{9.24}$$

where $\zeta'_{\mathrm{D3}}(\tau) = \zeta_{\mathrm{D3}}(\tau)/\zeta_{\mathrm{D3}}(0)$, $k'_{\mathrm{a}} = k_{\mathrm{c}}k_{\mathrm{a}}$ and $k'_{\mathrm{b}} = k_{\mathrm{c}}k_{\mathrm{b}}$. Measuring the response at D3 two or more times with different settings of PC1 and PC2, and inserting the measured responses into (9.24), gives a set of nonlinear equations, from which the constants k_{a} and k_{b} can be found.

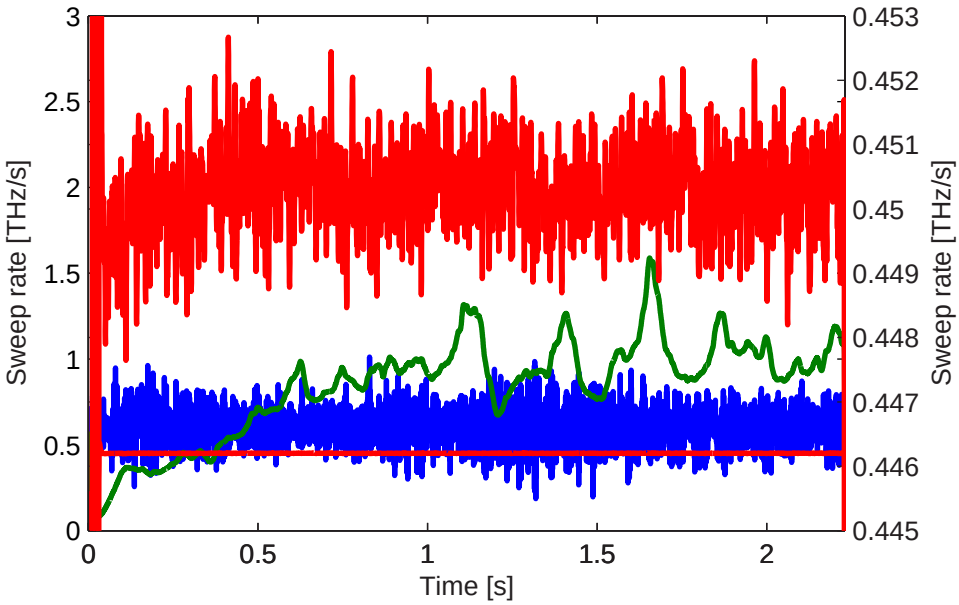

Figure 9.3: Measured instantaneous sweep rate of a Ando AQ4320B TLS (blue), open-loop fiber laser sweep (green) and closed-loop fiber laser sweep (red). In the upper red graph, the variations is sweep rate of the closed-loop fiber sweep is zoomed, and refers to the right vertical axis.

9.4 Results

9.4.1 Swept fiber laser with high sweep linearity

The output SR in Fig. 9.2 provides measurements of the laser sweep rate. Fig. 9.3 shows the measured sweep rate for a commercial tunable laser (Ando AQ4320B), and our fiber laser both with and without closed-loop control of the laser sweep. The Ando laser has large high-frequency fluctuations in sweep rate, but with almost constant mean. The sweep rate fluctuations for the open-loop swept fiber laser is large but much more low frequent than the Ando laser. The sweep rate has a increasing trend, which is caused by the increased force applied to the armature of solenoid when a larger part of the armature is within the coil. The more rapid fluctuations are probably caused by varying friction between the armature and the inner walls of the solenoid.

When the sweep of the fiber laser is controlled using the PID-controller, most of the sweep rate fluctuations are eliminated. The sweep rate has an overshoot of 3.5 THz/s the first 30 ms (not shown), but is constant throughout the rest of the sweep with a rms variation of 0.63 GHz/s or 0.14 % of mean sweep rate. The large bandwidth of the measured sweep rate, may indicate that a larger part of the remaining fluctuations in the measured sweep rate are measurement noise, since the bandwidth of the mechanical response is low. Nevertheless, the sweep rate fluctuations of the closed-loop controlled fiber laser are more than two orders of magnitude lower than that of the Ando laser (16 %) and the open-loop controlled

fiber laser (30 %).

9.4.2 Reconstruction of the polarization-dependent spatial profile of an FBG

The measurement setup was tested on a 10 mm uniform grating at 1554.5 mn with a reflectivity of 35 % written by scanning the uv-light [12] along a Nufern GF3 photosensitive fiber. The polarization of the uv-light was varied between p- and s-polarization during production.

Before measuring the grating response, the polarization controllers PC1 and PC2 were adjusted to minimize $|\zeta_{\mathrm{D3}}(\tau_{\mathrm{a}})|$ and $|\zeta_{\mathrm{D3}}(\tau_{\mathrm{b}})|$, so that the SOP out of path 2 and 3 is approximately orthogonal to the SOP out of path 1 of the PolIF. Then, the DFB-FL was swept from 1550 nm to 1557 nm, which provides a theoretical spatial resolution of 0.15 mm. The interference signal at D1 and the PolIF calibration output at D3 were sampled equidistant in optical frequency as described in Section 9.3.1. Both signals were then multiplied with a Blackman window, which reduced the effective spatial resolution to 0.45 mm. The PolIF calibration output signal was used to calculate the matrix $\boldsymbol{M}$ using (9.23). The transmission spectrum was not measured, instead the maximum reflectivity was set equal to the reflectivity measured with an optical spectrum analyzer in transmission mode.

Fig. 9.4 shows a segment of $|\zeta(\tau)|$, which is the Fourier transform of the measured interference pattern $P_r(\nu)$ at detector D1. There are in total ten signal bands. The peaks at 5, 10 and 15 ns corresponds to the imbalances of the PolIF, and is the Fourier transform of the sum of the (non-interfering) reflected power from the mirror and the FBG. Note that the peaks at 5 ns, 10 ns and 15 ns are actually beyond the vertical scale in this figure. This is not shown since the other signal bands are much weaker. The amplitudes in these bands were $12.5 \cdot 10^{-3}$, $3.0 \cdot 10^{-3}$ and $2.9 \cdot 10^{-3}$, respectively. The remaining seven signal bands originate from the interference between the reflections from the reference mirror and the FBG, and are the signal bands that will be used for calculation of the spatial profile of the FBG. The delay to the center band equals τ_0=21.3 ns, which is the imbalance of the measurement interferometer. If PolIF is removed, this would be the only signal band in Fig. 9.4. The remaining signal bands at $\tau_0 \pm (\tau_{\mathrm{b}} - \tau_{\mathrm{a}})$, $\tau_0 \pm \tau_{\mathrm{a}}$ and $\tau_0 \pm \tau_{\mathrm{b}}$ have offsets from τ_0 that equals the imbalances of the PolIF.

The signal bands extracted from $\zeta(\tau)$ are shown to the left in Fig. 9.5. From these signals, the pseudo-inverse $\boldsymbol{M}^{+}$ of $\boldsymbol{M}^{\mathrm{T}}$ is used to calculate $\tilde{\boldsymbol{h}}(\tau)$. The grating impulse response matrix $\boldsymbol{h}(\tau)$ is calculated from $\tilde{\boldsymbol{h}}(\tau)$, using the method described in the paragraph before (9.10) to remove the effect of the matrices $\boldsymbol{\Phi}_{\mathrm{i}}$ and $\boldsymbol{\Phi}_{\mathrm{o}}$. The resulting impulse response is shown on the right. This procedure will make $h_{12}(\tau') = h_{21}(\tau') = 0$ for a chosen delay $\tau = \tau'$. We observe that $|h_{12}(\tau)|$ and $|h_{21}(\tau)|$ is nearly equal to zero over the whole length of the grating. This means that the grating has almost constant orthogonal eigenpolarizations. Beating between the intrinsic and uv-induced birefringence of the fiber may cause non-orthogonal eigenpolarizations [68]. This is therefore an indication that such beating does not take place. Since, $h_{12}(\tau), h_{21}(\tau) \approx 0$, $h_{11}(\tau)$ and $h_{22}(\tau)$ are the impulse response of

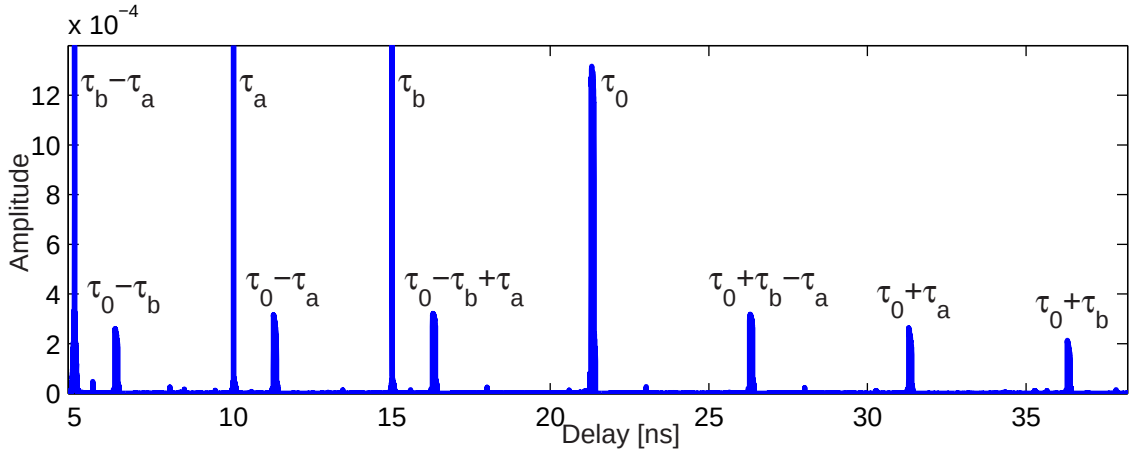

Figure 9.4: Fourier transform of the measured response at detector D1.

the two eigenpolarizations. There is an observable difference between $|h_{11}(\tau)|$ and $|h_{22}(\tau)|$, indicating polarization-dependent index modulation.

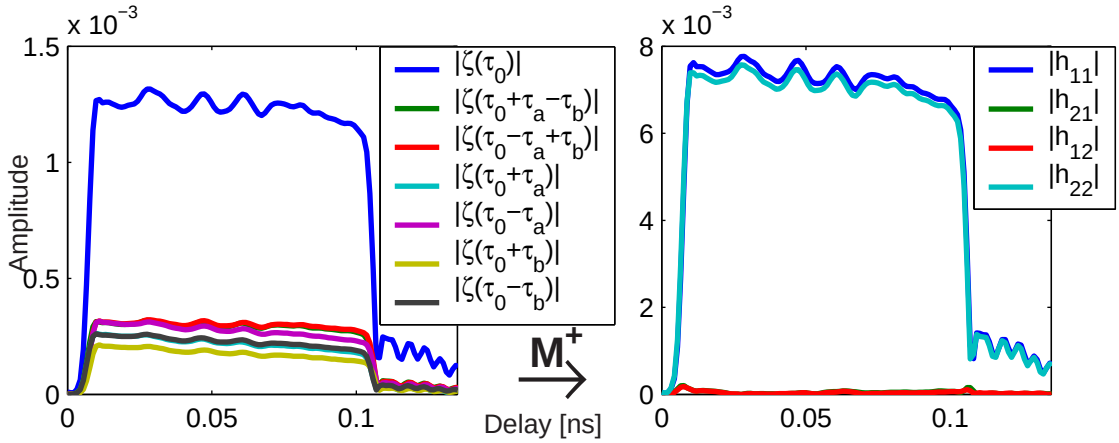

Figure 9.5: Amplitude of extracted signal bands of ζ (left) and the amplitude of components of the impulse response matrix $\boldsymbol{h}$ (right).

The upper plot in Fig. 9.6 shows the reconstructed index modulation eigenmode amplitudes $n_{\mathrm{ac},x}$ and $n_{\mathrm{ac},y}$ versus position calculated by the polarization-resolved layer-peeling algorithm. The impulse response amplitudes in Fig. 9.5 has a clear negative slope versus position, and there is significant amplitude at delays larger 0.1 ns, which is the dual-pass delay through the grating. The index modulation amplitudes in Fig. 9.6 are reasonable flat, as one should expect for a uniform grating. In addition, the relative amplitude beyond the grating is reduced. This indicates that the polarization-resolved layer-peeling algorithm removes higher-order multiple reflections from the scattering data.

The index modulation amplitudes have a pronounced common mode dependence of the uv-polarization. At the end of the grating, s-polarization was used. We find that the common mode index modulation for p-polarization is about 7 % lower.

Most of this difference is due to the dependence of visibility on the angle between the uv-beams. The reduction in visibility for p-polarization becomes 5.2 % for a grating at 1550 nm [43]. Additional common mode amplitude difference may be caused by polarization-dependent loss of the bulk optics in the writing setup and difference in photosensitivity due to stress effects.

The upper plot of Fig. 9.6 shows an average differential index modulation amplitude $n_{\mathrm{ac},x} - n_{\mathrm{ac},y}$ of $1 \cdot 10^{-6}$ (2.9 % of common mode index modulation), which is independent of uv-polarization. The middle plot shows the orientation of the eigenaxis that corresponds to $n_{\mathrm{ac},x}$. We find that the eigenaxis is approximately constant throughout the whole grating. One explanation of the photosensitivity of Ge-doped fiber without H_2-loading, is the modification of the glass structure leading to a volume change of the glass. These volume changes lead to uv-induced birefringence [131], and birefringence has been calculated to be 6 % of the index modulation amplitude at the fiber center with $n_{\mathrm{ac}} = 1.7 \cdot 10^{-4}$. The effective average birefringence across the mode field should be smaller than this. It should be noted that the resolution in differential index modulation depends on PDL in couplers and detectors. The couplers used had a PDL as low as 0.2 %, while the detectors are specified to have a maximum PDL of 2 %. Thus, the uncertainty in the measurement of differential index modulation amplitude is lower than 2 %.

The fluctuations in differential index modulation amplitude is $\pm 0.2 \cdot 10^{-6}$. It is tempting to assume that these fluctuations are due to the dependence of the uv-polarization. However, by closer inspection, we find that the fluctuations are proportional to the derivative of common mode index modulation amplitude. This may be caused by a horizontal offsets between the reconstructed $n_{\mathrm{ac},x}$ and $n_{\mathrm{ac},y}$. When extracting the seven bands from $\zeta(\tau)$, the bands may have offsets that are fractions of a sample. Such small offsets may give an offset between the two index modulation profiles. Assume that the two index modulation profiles are equal but the second is slightly shifted in vertically an amount of ϵ from the position z. Then,

$$n_{\mathrm{ac},y}(z) = n_{\mathrm{ac},x}(z+\epsilon) = n_{\mathrm{ac},x}(z) + \epsilon \frac{dn_{\mathrm{ac},x}(z)}{dz}. \tag{9.25}$$

The reconstructed differential index modulation amplitude in (9.25) shows that it will be proportional to the derivative of the common mode index modulation amplitude. A scaled version of the derivative of the common mode index was calculated so that the best fit to the differential index modulation amplitude was obtained. This signal was subtracted from the differential index modulation amplitude. Assuming that none of the components in the differential index modulation amplitude that are proportional to derivative of the common mode index modulation amplitude are real, we then find that the uv-dependence of the index modulation difference is $\sim 0.1 \cdot 10^{-6}$ for this fiber.

The lower plot in Fig. 9.6 shows the measured change in dc-index in the two birefringence eigenaxes. We find a common mode peak-to-peak variation of about $9 \cdot 10^{-5}$. When integrating along the grating length, this corresponds to a grating phase variation of 60 mrad. In comparison, the relative peak-to-peak variation in index modulation amplitude between 8 and 10 mm, where the uv-polarization was

constant equal to s, was about 1.5 %. By combining the index modulation and phase into a phasor, one should expect that white measurement noise contributes equally in all directions around this phasor. In this case, the relative noise in index modulation should be approximately equal to the phase noise. Since the grating phase variations are 4 times larger, we can conclude that measured dc-index are originating from the writing setup or the fiber. The measured difference in grating phase between the two axes is in the same range as the relative variations in index modulation amplitude. Thus, the low birefringence of this fiber could not be measured with this setup. However, the birefringence is less than $1 \cdot 10^{-5}$, corresponding to wavelength shift of less than 10 pm. The rapid variations of the orientation of the dc-index eigenaxis shown in the middle plot, also indicates that this measurement is dominated by noise.

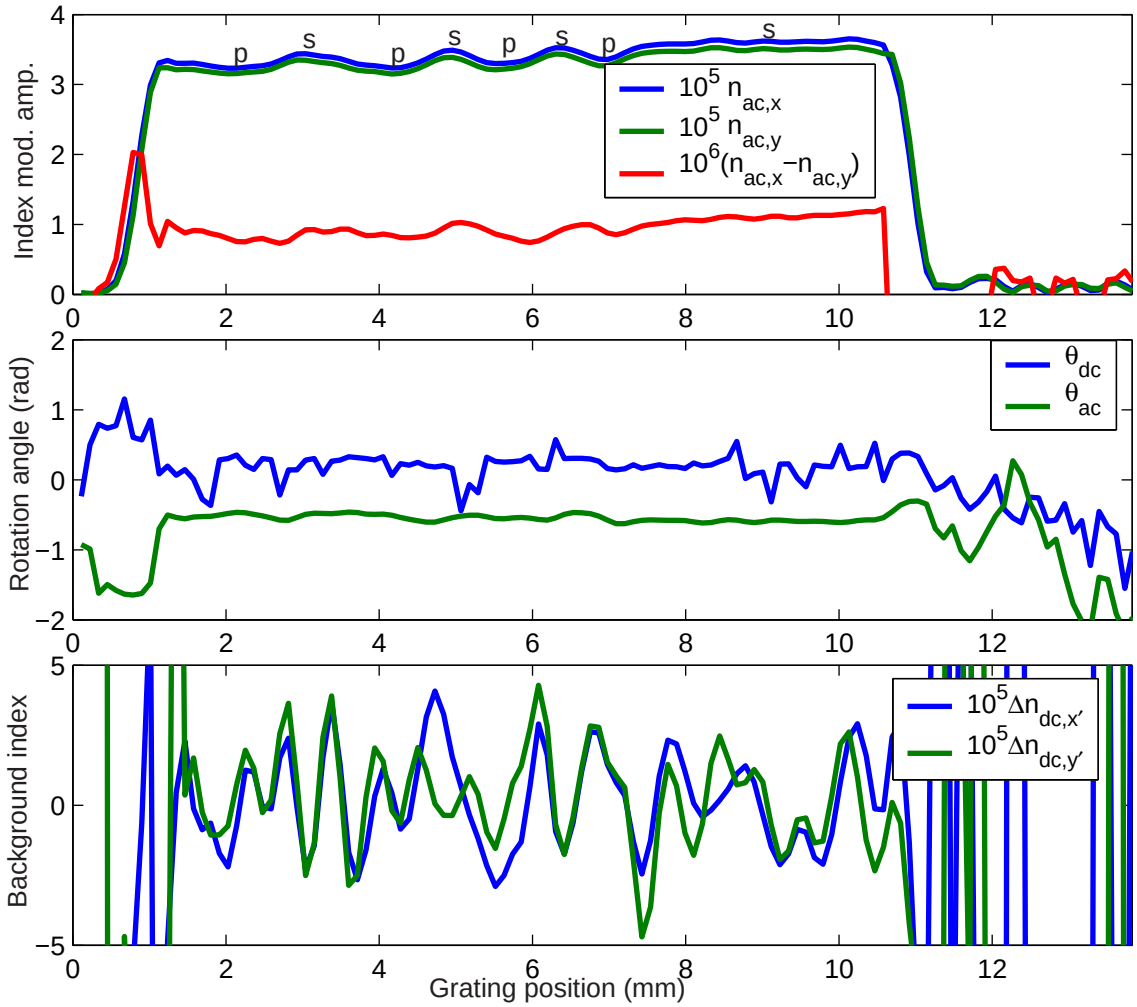

Figure 9.6: Spatial characterization of an FBG written with varying uv-polarization. Top: Index modulation amplitudes and differential modulation amplitude. s and p indicates the positions with s- and p-polarization was used to fabricate the grating. Middle: Orientation angles of the first index modulation eigenmode and of the first birefringence eigenmode. Bottom: dc-index change.

9.5 Conclusions

We have developed a method for polarization-resolved characterization of fiber Bragg gratings using OFDR. A strain-tuned fiber laser was used as source. With closed-loop control of the sweep rate, the sweep in optical frequency was made highly linear, with a rms variation of 0.14 % from constant sweep rate. The state of polarization of the light interrogating the FBG was modulated using a polarization modulation interferometer. In this way, the different components of the grating impulse response was spread in the optical delay-domain. From these bands, the grating impulse response matrix was calculated. This grating impulse response was fed into the layer-peeling algorithm to calculate the birefringence, the common mode index modulation amplitude and differential index modulation amplitude. The measurement setup was tested on a grating that was written with varying uv-polarization. A differential index modulation amplitude of $1 \cdot 10^{-6}$ was observed, but insignificant dependence on uv-polarization was found.

9.A Factorization of $\boldsymbol{\Upsilon}$

In Appendix D.2 in [68] it is shown that a symmetric matrix $\boldsymbol{\Upsilon}$ can be written $\boldsymbol{U}^{\mathrm{T}}\boldsymbol{\Sigma}\boldsymbol{U}$, where $\boldsymbol{U}$ is unitary and $\boldsymbol{\Sigma}$ is diagonal and nonnegative.

We must find a relevant factorization of a general non-symmetric matrix $\boldsymbol{\Upsilon}$ that can be used in the layer-peeling algorithm to handle non-reciprocity.

Using singular value decomposition (svd), $\boldsymbol{\Upsilon} = \boldsymbol{V}_1\boldsymbol{\Sigma}\boldsymbol{V}_2$, where $\boldsymbol{V}_1$ and $\boldsymbol{V}_2$ is unitary and $\boldsymbol{\Sigma}$ is diagonal and nonnegative. Let the matrix $\boldsymbol{\Phi}_{\mathrm{as}}$ be a unitary matrix with $\det \boldsymbol{\Phi}_{\mathrm{as}} = 1$, and is such that $\tilde{\boldsymbol{\Upsilon}} = \boldsymbol{\Upsilon}\boldsymbol{\Phi}_{\mathrm{as}}^{\dagger} = \boldsymbol{V}_1\boldsymbol{\Sigma}\boldsymbol{V}_2\boldsymbol{\Phi}_{\mathrm{as}}^{\dagger}$ is symmetric. By evaluating $(\tilde{\boldsymbol{\Upsilon}}^{\dagger}\tilde{\boldsymbol{\Upsilon}})^{\mathrm{T}} = \tilde{\boldsymbol{\Upsilon}}\tilde{\boldsymbol{\Upsilon}}^{\dagger}$, we find that $\boldsymbol{D}\boldsymbol{\Sigma}^2 = \boldsymbol{\Sigma}^2\boldsymbol{D}$, where $\boldsymbol{D} = \boldsymbol{V}_2^{*}\boldsymbol{\Phi}_{\mathrm{as}}^{\mathrm{T}}\boldsymbol{V}_1$. Since $\boldsymbol{D}$ commutes with $\boldsymbol{\Sigma}^2$, $\boldsymbol{D}$ is diagonal and unitary when the singular values are unequal. We may write

$$\tilde{\boldsymbol{\Phi}}_{\mathrm{as}} = \boldsymbol{V}_2\boldsymbol{\Phi}_{\mathrm{as}}\boldsymbol{V}_2^{\dagger} = \boldsymbol{W}^{*}\boldsymbol{D}, \tag{9.26}$$

where $\boldsymbol{W} = \boldsymbol{V}_2^{*}\boldsymbol{V}_1$. Since $\det \tilde{\boldsymbol{\Phi}}_{\mathrm{as}} = \det \boldsymbol{\Phi}_{\mathrm{as}} = 1$, $\det \boldsymbol{D} = \det \boldsymbol{W}$. Thus, $\boldsymbol{\Phi}_{\mathrm{as}}$ can be calculated from (9.26) where

$$\boldsymbol{D} = \begin{bmatrix} \mathrm{e}^{i\theta} & 0 \\ 0 & \mathrm{e}^{-i\theta}\det \boldsymbol{W} \end{bmatrix}, \tag{9.27}$$

and θ is real but otherwise arbitrary.

The matrix $\boldsymbol{D}$ should be chosen so that the phase eigenvalues of $\boldsymbol{\Phi}_{\mathrm{as}}$ are minimum. This can be done by maximizing the real parts of its eigenvalues. The matrices $\boldsymbol{\Phi}_{\mathrm{as}}$ and $\tilde{\boldsymbol{\Phi}}_{\mathrm{as}}$ have the same eigenvalues, which is given by $\mathrm{Re}\{\tilde{\Phi}_{\mathrm{as},11}\} \pm i\sqrt{1 - \mathrm{Re}\{\tilde{\Phi}_{\mathrm{as},11}\}^2}$, where the index 11 denotes the upper left component. Maximizing $\mathrm{Re}\{\tilde{\Phi}_{\mathrm{as},11}\}$ gives,

$$\mathrm{e}^{i\theta} = \frac{W_{11}}{|W_{11}|}. \tag{9.28}$$

Chapter 10

Summary and future work

In this chapter we summerize the previous chapters and draw lines for future work.

10.1 Summary

In chapter 2 of the first part of the thesis, the one dimensional inverse scattering problem was presented. It was shown that there is a close connection between quantum mechanical potential scattering and electromagnetic and acoustical wave scattering. Different inverse scattering algorithms were reviewed, and the differences between the two most used inverse scattering algorithms; the Gel'fand-Levitan-Machenko (GLM) method and the layer-peeling algorithm, were discussed. It was shown that the layer-peeling algorithm had a simpler physical interpretation and lower computation complexity. We ended this chapter by reviewing the use of inverse scattering for the design of fiber Bragg gratings. The shortcomings in previous methods were discussed, and the motivation for the work of part I was obtained.

Chapter 3 was devoted to the design of gratings in single mode fibers with a finite length. First, the grating was model as a stack of $N+1$ discrete reflectors placed a distance L/N apart, were L is the length of the grating. It was shown that the reflection spectrum can be represented as a digital infinite-duration impulse response (IIR) filter of order N. By using some additional conditions on the nominator and the denominator polynomial, a method for designing the reflection spectrum of gratings with finite length was developed. Once the realizable reflection spectrum has been obtained, the spatial profile was found using the layer-peeling algorithm. It was demonstrated that the proposed method gave grating designs with better side lobe suppression and less ripple than gratings designed by windowing.

In chapter 4, the treatment was extended to the case of birefringent reflective gratings with polarization-dependent background index and polarization-dependent effective index contrast. In this case, scattering involved two forward-propagating and two backward-propagating modes, and the grating was characterized by a frequency-dependent reflection Jones matrix. Based on reciprocity and losslessness, a discrete model was obtained for grating. Each layer was divided into three sections; a retardation section, a discrete reflector and a time-delay section. A time-domain layer-peeling algorithm similar to the algorithm used for polarization-independent

gratings was developed. In order to differentiate the response from the retardation section and the reflector, different matrix factorizations were used. The realizability criteria of chapter 3 were extended to the case of birefringent gratings, and a similar design algorithm was developed. However, this design algorithms had its limitations, since it does not take into account physical constraints such as the maximum allowable polarization-dependent index difference, and since there was an additional phase factor that could not be easily found. The algorithms were tested numerically, especially on reconstruction of a fiber grating written in a slightly birefringent fiber and with uv-induced birefringence and index modulation. It was demonstrated that the developed polarization-resolved layer-peeling could reconstruct the spatial profile correctly, while the scalar version could not.

Chapter 5 was devoted to the general case of inverse scattering with any number of interacting modes. The coupling between the interacting modes could be both codirectional or contradirectional in a continuous or a discrete structure. The scattering model in chapter 4 was generalized to include any number of interacting modes. In chapter 4, it was assumed that the interacting polarization modes had approximately the same propagation constant, while in chapter 5, they could be entirely different. A frequency-domain layer-peeling algorithm for any number of interacting modes were developed. The reflection response from a single layer cannot be uniquely factorized into a retardation section and discrete reflector. Various factorizations were discussed, and the correct factorization can be chosen based on the physical model of the scattering structure. Finally, some applications to multimode, optical waveguides and 3D structures were outlined.

The second part of the thesis was devoted to spatial characterization of gratings, and in chapter 6, different spatial characterization techniques were reviewed.

In chapter 7, it was demonstrated that OFDR can be used to spatially characterize a fiber Bragg grating. While sweeping a tunable laser, the response from a Michelson interferometer where the FBG constituted one of the reflectors, was measured. From the Fourier transform of this response, the impulse response of the grating was obtained. This impulse response was fed to the layer-peeling algorithm for calculation of the spatial profile. The measurement technique was satisfactorily demonstrated by reconstruction of the spatial profile of a 98 % reflectivity uniform grating.

In chapter 8, the characterization method in chapter 7 was extended for the use on very strong gratings. The method of chapter 7 was limited to gratings with maximum reflectivity of 98-99 % due to uncertainty in scaling and measurement noise. Stronger gratings can be spatially characterized by thermally chirping of the grating so that the spectral information is spread over a much wider bandwidth and so that the reflectivity is reduced. This was achieved by placing the grating in a metal rod connected to a tube furnace in one end and a heat sink in the other. The method was demonstrated by measuring the spatial profile of a uniform grating with grating strength 8.25 ($-$ 66 dB minimum transmission) and a distributed feedback fiber laser (DFB-FL) with grating strength 7.5.

In chapter 9, a polarization-resolved spatial characterization method was developed. A strain-tuned DFB-FL was used as source. With closed-loop control of the

laser sweep, 0.14 % deviation from mean sweep rate and a sweep range of 14 nm was achieved. A trigger interferometer was used to generate trigger pulses so that the samples became equidistant in optical frequency. By continuously modulating the polarization state of the source through four polarization states that can be represented by four linearly independent Stokes vectors, the reflection Jones matrix of the grating could be measured. Modulation of the polarization state was done by a Mach-Zehnder-type polarization modulation interferometer in between the source and the interferometer containing the grating. The polarization modulation interferometer had three paths with different delay and retardation. The different components of the impulse response of the grating was spread into different bands in the optical delay domain. The impulse response Jones matrix was found from the signal in these bands using a matrix given by the measured polarization modulation. This impulse response served as an input to the polarization-resolved layer-peeling algorithm in chapter 4 to calculate the spatial profile of the grating, including the polarization-dependent index modulation and birefringence. The measurement system was used to characterize a uniform grating that was fabricated by varying the polarization of the uv-light between s-polarization and p-polarization. For the particular tested fiber grating a differential index modulation amplitude of 2.9 % was found, which was independent of the uv-polarization used.

10.2 Future work

It would be interesting to move further with the general case of multi-mode inverse scattering. First of all, the layer-peeling algorithm should be tested numerically. Especially, the effect of discretization should be tested further. As indicated, an interesting application of this theory is design of fiber Bragg gratings with many interacting modes, such as long, chirped gratings in which the core mode interacts with the cladding modes. It is reasonable to assume that the index modulation can be separated into a longitudinal and a transverse factor. In this case, it was shown that the number of physical degrees of freedom becomes quite limited. It will therefore be interesting to study how these new constrains can be handled in the layer-peeling algorithm. Hopefully, this will lead to an efficient method for designing gratings in fibers with many interacting modes. Another interesting subject is to find out whether a similar algorithm can be used to design or characterize long period gratings with more than two interacting modes, where the coupling is purely codirectional.

In chapter 7 and chapter 8 an external cavity tunable laser was used and the response was sampled equidistant in time. In chapter 9 a fiber laser was used as source and the response was sampled equidistant in optical frequency. It should be tested which of these methods that gives best results in terms of noise and resolution. The sensitivity to fluctuations in laser sweep rate should be evaluated experimentally.

With use of closed-loop control of the sweep rate, the fiber laser is a very attractive source for OFDR in general, and not only for spatial characterization of Bragg gratings. This laser both provides a relative large tuning range (2 % = 24

nm should be feasible without braking the fiber), and a long measurement range, since the laser can be tuned very smoothly. It is therefore interesting to use the fiber laser in a more general OFDR setup. The maximum range for OFDR with this laser should be investigated.

The OFDR setup also have potentials for distributed sensing. For instance may the setup be used for distributed sensing of strain and temperature along a grating. With the use of the polarization-resolved measurement technique, both transverse and longitudinal strain can be measured.

The setup in chapter 9 should be tested with other gratings, having different properties in terms of strength, profile and fiber type. This may be gratings in birefringent fibers, twisted gratings and gratings with an applied transversal load.

The resolution of the measurement of polarization-dependent index modulation and birefringence in chapter 9 may depend on the polarization-dependent loss of couplers, mirrors and detectors. The resolution of the present system should be evaluated, and if necessary, methods for improving this resolution should be considered.

Bibliography

[1] K. O. Hill, Y. Fujii, D. C. Johnsen, and B. S. Kawasaki. Photosensitivity in optical fiber waveguides: Application to reflection filter fabrication. *Appl. Phys. Lett.*, 32:647–649, 1978.

[2] G. Meltz, W. W. Morey, and W. H. Glenn. Formation of Bragg gratings in optical fibers by a transverse holographic method. *Opt. Lett.*, 14:823–825, 1989.

[3] A. D. Kersey, M. A. Davis, H. J. Patrick, M. LeBlanc, K. P. Koo, C. G. Askins, M. A. Putnam, and E. J. Friebele. Fiber grating sensors. *J. Lightwave Technol.*, 15:1442–1463, 1997.

[4] R. Pike and P. Sabatier, editors. *Scattering: Scattering and Inverse Scattering in Pure and Applied Science*, volume 1. Academic Press, London, UK, 2002.

[5] R. Pike and P. Sabatier, editors. *Scattering: Scattering and Inverse Scattering in Pure and Applied Science*, volume 2. Academic Press, London, UK, 2002.

[6] A. W. Snyder and J. D. Love. *Optical Waveguide Theory.* Chapman & Hall, 1983.

[7] I. M. Gel'fand and B. M. Levitan. On the determination of a differential equation from its spectral function. *Amer. Math. Soc. Transl. (2)*, 1:253–304, 1955.

[8] P. V. Frangos and D. L. Jaggard. A numerical solution to the Zakharov-Shabat inverse scattering problem. *IEEE Trans. Antennas. Propagat.*, 39:74–79, 1991.

[9] A. M. Bruckstein, B. C. Levy, and T. Kailath. Differential methods in inverse scattering. *SIAM J. Appl. Math.*, 45:312–335, 1985.

[10] A. M. Bruckstein and T. Kailath. Inverse scattering for discrete transmission-line models. *SIAM Rev.*, 29:359–389, 1987.

[11] K. O. Hill and G. Meltz. Fiber Bragg grating technology: Fundamentals and overview. *J. Lightwave Technol.*, 15:1263–1276, 1997.

[12] A. Asseh, H. Storøy, B.E. Sahlgren, S. Sandgren, and R.A.H. Stubbe. A writing technique for long fiber Bragg gratings with complex reflectivity profiles. *IEEE J. Lightwave Techn.*, 15(8):1419–1423, 1997.

[13] G.-H Song and S.-Y Shin. Design of corrugated waveguide filters by the Gel'fand-Levitan-Marchenko inverse-scattering method. *J. Opt. Soc. Am. A*, 2:1905–1915, 1985.

[14] P. V. Frangos and D. L. Jaggard. Inverse scattering: Solution of coupled Gel'fand-Levitan-Marchenko integral equations using succesive kernel approximations. *IEEE Trans. Antennas. Propagat.*, 43:547–552, 1995.

[15] E. Peral, J. Capmany, and J. Marti. Iterative solution to the Gel'fand-Levitan-Marchenko equations and application to synthesis of fiber gratings. *IEEE J. Quantum Electron.*, 32:2078–2084, 1996.

[16] R. Feced, M. N. Zervas, and M. A. Muriel. An efficient inverse scattering algorithm for the design of nonuniform fiber Bragg gratings. *IEEE J. Quantum Electron.*, 35:1105–1115, 1999.

[17] L. Poladian. Simple grating synthesis algorithm. *Opt. Lett.*, 25:787–789, 2000.

[18] J. Skaar, L. Wang, and T. Erdogan. Synthesis of thick optical thin-film filters with a layer-peeling inverse-scattering algorithm. *Appl. Opt.*, 40:2183–2189, 2001.

[19] D. Sandel, R. Noé, G. Heise, and B. Borchert. Optical network analysis and longitudinal structure characterization of fiber Bragg grating. *J. Lightwave Technol.*, 16:2435–2442, 1998.

[20] H. Kogelnik. Filter response of nonuniform almost-periodic structures. *Bell Sys. Tech. J.*, 55:109–126, 1976.

[21] D. L. Jaggard and Y. Kim. Accurate one-dimensional inverse scattering using a nonlinear renormalization technique. *J. Opt. Soc. Am. A*, 2:1922–1930, 1985.

[22] K. A. Winick and J. E. Roman. Design of corrugated waveguide filters by Fourier-transform techniques. *IEEE J. Quantum Electron.*, 26:1918–1929, 1990.

[23] M. C. Parker, R. J. Mears, and S. D. Walker. A Fourier transform theory for photon localization and evanescence in photonic bandgap structures. *J. Opt. A: Pure Appl. Opt.*, 3:171–183, 2001.

[24] Ch. Papachristos and P. Frangos. Synthesis of single- and multi-mode planar optical waveguides by a direct numerical solution of the Gel'fand-Levitan-Marchenko integral equations. *Optics Communications*, 203:27–37, 2002.

[25] Ch. Papachristos and P. Frangos. Design of corrugated optical waveguide filters through a direct numerical solution of the coupled Gel'fand-Levitan-Marchenko intergral equations. *J. Opt. Soc. Am. A*, 19:1005–1012, 2002.

[26] J. Skaar, L. Wang, and T. Erdogan. On the synthesis of fiber Bragg gratings by layer peeling. *IEEE J. Quantum Electron.*, 37:165–173, 2001.

[27] A. V. Oppenheim and R. W. Schafer. *Digital signal processing*. Prentice-Hall, 1975.

[28] J. Skaar and K. M. Risvik. A genetic algorithm for the inverse problem in synthesis of fiber gratings. *J. Lightwave Tech.*, 16:1928–1932, 1998.

[29] L. Poladian. Resonance mode expansions and exact solutions for nonuniform gratings. *Phys. Rev. E*, 54:2963–2975, 1996.

[30] J. Skaar. *Synthesis and characterization of fiber Bragg gratings*. Ph.D. dissertation, Norwegian University of Science and Technology, Trondheim, Norway, available online at http://www.fysel.ntnu.no/Department/Avhandlinger/dring/, 2000.

[31] E. M. Dowling and D. L. MacFarlane. Lightwave lattice filters for optically multiplexed communication systems. *J. Lightwave Tech.*, 12:471–486, 1994.

[32] J. L. Frolik and A. E. Yagle. An asymmetric discrete-time approach for the design and analysis of periodic waveguide gratings. *J. Lightwave Tech.*, 13:175–185, 1994.

[33] C. K. Madsen and J. H. Zhao. *Optical filter design and analysis: a signal processing approach*. New York: Wiley & Sons, 1999.

[34] G. Lenz, B. J. Eggleton, C. R. Giles, C. K. Madsen, and R. E. Slusher. Dispersive properties of optical filters for WDM systems. *IEEE J. Quantum Electron.*, 34:1390–1402, 1998.

[35] T. Kudou, K. Shimizu, K. Harada, and T. Ozeki. Synthesis of grating lattice circuits. *J. Lightwave Tech.*, 17:347–353, 1999.

[36] K. Jinguji and M. Kawachi. Synthesis of coherent two-port lattice-form optical delay-line circuit. *J. Lightwave Tech.*, 13:73–82, 1995.

[37] J. Skaar and R. Feced. Reconstruction of gratings from noisy reflection data. *J. Opt. Soc. Am. A*, 19:2229–2237, 2002.

[38] L. V. Ahlfors. *Complex analysis*. McGraw-Hill International Editions, 1979.

[39] M. Yamada and K Saduka. Analysis of almost periodic distributed feedback slab waveguides via a fundamental matrix approach. *Appl. Opt.*, 26:3474–3478, 1987.

[40] J. Skaar and O. H. Waagaard. Design and characterization of finite length fiber gratings. *IEEE J. Quantum Electron.*, 39:1238–1245, 2003. See chapter 3.

[41] G. Meltz and W. W. Morey. Bragg grating formation and germanosilicate fiber photosensitivity. *in International workshop on photoinduced self-organization effects in optical fiber, Proc. Soc. Photo-Opt. Instrum. Eng.*, 1516:185–199, 1991.

[42] K. O. Hill, F. Bilodeau, B. Malo, and D. C. Johnson. Birefringent photosensitivity in monomode optical fibre: application to external writing of rocking filters. *Electron. Lett.*, 27:1548–1550, 1991.

[43] T. Erdogan and V. Mizrahi. Characterization of UV-induced birefringence in photosensitive Ge-doped silica optical fibers. *J. Opt. Soc. Am. B*, 11:2100–2105, 1994.

[44] S. Pereira, J. E. Sipe, R. E. Slusher, and S. Spälter. Enhanced and suppressed birefringence in fiber Bragg gratings. *J. Opt. Soc. Am. B*, 19:1509–1515, 2002.

[45] P. Niay, P. Bernage, T. Taunay, M. Douay, E. Delevaque, S. Boj, and B. Poumellec. Polarization selectivitiy of gratings written in Hi-Bi fibers by the external method. *IEEE Photon. Technol. Lett*, 7:391–393, 1995.

[46] L. Bjerkan, K. Johannessen, and X. Guo. Measurements of Bragg grating birefringence due to transverse compressive forces. *in 12th International Conference on Optical Fiber Sensors, OSA Technical Digest Series*, 16:60–63, 1997.

[47] C. M. Lawrence, D. V. Nelson, E. Udd, and T. Bennett. A fiber optic sensor for transverse strain measurement. *Experimental mechanics*, 39:202–209, 1999.

[48] R. Gafsi and M. A. El-Sherif. Analysis of induced-birefringence effects on fiber Bragg gratings. *Optical Fiber Technology*, 6:299–323, 2000.

[49] A.-P Zhang, B.-O Guan, X.-M Tao, and H.-Y Tam. Experimental and theoretical analysis of fiber Bragg gratings under lateral compression. *Opt. Comm.*, 206:81–87, 2002.

[50] M.-J Li and S. I. Najafi. Polarization dependence of grating-assisted waveguide Bragg reflectors. *Appl. Opt.*, 32:4517–4521, 1993.

[51] R. C. Jones. A new calculus for the treatment of optical systems. *J. Opt. Soc. Am.*, 31:488–503, 1941.

[52] E. Rønnekleiv, M. N. Zervas, and J. T. Kringlebotn. Modeling of polarization-mode competition in fiber DFB lasers. *J. Quantum Electron.*, 34:1559–1569, 1998.

[53] A. Yariv and P. Yeh. *Optical Waves in Crystals: Propagation and control of laser radiation*, chapter 6.4. John Wiley and sons, 1983.

[54] Raman Kashyap. *Fiber Bragg Gratings*, chapter 5. Academic Press, 1999.

[55] A. Buryak. Iterative schema for "mixed" scattering problems. In *Bragg Gratings, Photosensitivity, and Poling in glass waveguides (BGPP)*, volume 94 of *OSA Topic in Optics and Photonics Series*, page MB3, Washington, D.C., 2003. Optical Society of America.

[56] D. Marcuse. *Theory of Dielectric Optical Waveguides*. New York: Academic, 1991.

[57] H. Kogelnik. *Theory of Optical Waveguides, Guided-Wave Optoelectronics*. New York: Springer-Verlag, 1990.

[58] Anne Boutet de Monvel and Vladimir Marchenko. New inverse spectral problem and its application. In *Inverse and algebraic quantum scattering theory (Lake Balaton, 1996)*, volume 488 of *Lecture Notes in Phys.*, pages 1–12. Springer, Berlin, 1997.

[59] M. Kreĭ n. On a method of effective solution of an inverse boundary problem. *Doklady Akad. Nauk SSSR (N.S.)*, 94:987–990, 1954.

[60] C. L. Pekeris. Direct method of interpretation in resistivity prospecting. *Geophysics*, 5:31–42, 1940.

[61] E. A. Robinson. Dynamic predictive deconvolution. *Geophys. Prosp.*, 23:779–797, 1975.

[62] V. Bardan. Comments on dynamic predictive deconvolution. *Geophys. Prosp.*, 25:569–572, 1977.

[63] Rakesh. A one-dimensional inverse problem for a hyperbolic system with complex coefficients. *Inv. Prob.*, 17:1401–1417, 2001.

[64] G.-H Song. Toward the ideal codirectional Bragg filter with an acousto-optic-filter design. *J. Lightwave Technol.*, 13:470–480, 1995.

[65] R. Feced and M. N. Zervas. Efficient inverse scattering algorithm for the design of grating-assisted codirectional mode couplers. *J. Opt. Soc. Am. A*, 17:1573–1582, 2000.

[66] L. Wang and T. Erdogan. Layer peeling algorithm for reconstruction of long-period fibre gratings. *Electron. Lett.*, 37:154–156, 2001.

[67] J. K. Brenne and J. Skaar. Design of grating-assisted codirectional couplers with discrete inverse-scattering algorithms. *J. Lightwave Technol.*, 21:254–263, 2003.

[68] O.H. Waagaard and J. Skaar. Synthesis of birefringent reflective gratings. *J. Opt. Soc. Am. A*, 21(7):1207–1220, 2004. See chapter 4.

[69] T. Aktosun, M. Klaus, and C van der Mee. Direct and inverse scattering for selfadjoint Hamiltonian systems on the line. *Integr. Equ. Oper. Theory*, 38:129–171, 2000.

[70] A. E. Yagle and B. C. Levy. Layer-stripping solutions of multidimensional inverse scattering problems. *Journal of Mathematical Physics*, 27(6):1701–1710, 1986.

[71] A. E. Yagle. Differential and integral methods for multidimensional inverse scattering problems. *Journal of Mathematical Physics*, 27(10):2584–2591, 1986.

[72] A. E. Yagle and J. L. Frolik. On the feasibility of impulse reflection response data for the two-dimensional inverse scattering problem. *IEEE Transactions on Antennas and Propagation*, 44(12):1551–1564, 1996.

[73] A. Rosenthal and M. Horowitz. Inverse scattering algorithm for reconstructing strongly reflecting fiber Bragg gratings. *IEEE J. Quantum Electron.*, 39:1018–1026, 2003.

[74] T. Erdogan. Cladding-mode resonances in short- and long-period fiber grating filters. *Journal Of The Optical Society Of America A-Optics Image Science And Vision*, 14(8):1760–1773, 1997.

[75] F. Ouellette. Dispersion cancellation using linearly chirped Bragg grating filters in optical wave-guides. *Optics Letters*, 12(10):847–849, 1987.

[76] F. Ouellette, P. A. Krug, T. Stephens, G. Dhosi, and B. Eggleton. Broad-band and wdm dispersion compensation using chirped sampled fiber Bragg gratings. *Electronics Letters*, 31(11):899–901, 1995.

[77] V. Finazzi and M. Zervas. Cladding mode losses in chirped Bragg gratings. In *Bragg Gratings, Photosensitivity, and Poling in glass waveguides (BGPP)*, OSA Technical Digest, page BMG16, Washington, D.C., 2001. Optical Society of America.

[78] L. Dong, L. Reekie, J. L. Cruz, J. E. Caplen, J. P. deSandro, and D. N. Payne. Optical fibers with depressed claddings for suppression of coupling into cladding modes in fiber Bragg gratings. *IEEE Photonics Technology Letters*, 9(1):64–66, 1997.

[79] H. P. Li, Y. Nakamura, K. Ogusu, Y. L. Sheng, and J. E. Rothenberg. Influence of cladding-mode coupling losses on the spectrum of a linearly chirped multi-channel fiber Bragg grating. *Optics Express*, 13(4):1281–1290, 2005.

[80] F. Ghiringhelli and M. Zervas. Inverse scattering design of fiber Bragg gratings with cladding mode losses compensation. In *Bragg Gratings, Photosensitivity, and Poling in glass waveguides (BGPP)*, volume 94 of *OSA Topic in Optics and Photonics Series*, page TuD2, Washington, D.C., 2003. Optical Society of America.

[81] R.G. Newton. Inverse scattering. II. Three dimensions. *Journal of Mathematical Physics*, 21(7):1698–1715, 1980.

[82] J.H. Rose. The connection between time- and frequency-domain three-dimensional inverse scattering methods. *Journal of Mathematical Physics*, 25(10):2995–3000, 1984.

[83] David M. Pozar. *Microwave engineering.* Addison-Wesley, 1993.

[84] H. A. Haus. *Electromagnetic noise and quantum optical measurements.* Springer, 2000.

[85] G. Cancellieri, editor. *Single-mode optical fiber measurement: Characterization and sensing.* Artech House, Boston, USA, 1993.

[86] M. K. Barnoski and S. M. Jensen. Fiber waveguides - novel technique for investigating attenuation characteristics. *Applied Optics*, 15(9):2112–2115, 1976.

[87] S. D. Personick. Photon probe - optical-fiber time-domain reflectometer. *Bell System Technical Journal*, 56(3):355–366, 1977.

[88] B. L. Danielson. Optical time-domain reflectometer specifications and performance testing. *Applied Optics*, 24(15):2313–2322, 1985.

[89] K. Takada, I. Yokohama, K. Chida, and J. Noda. New measurement system for fault location in optical waveguide devices based on an interferometric technique. *Applied Optics*, 26(9):1603–1606, 1987.

[90] H. H. Gilgen, R. P. Novak, R. P. Salathe, W. Hodel, and P. Beaud. Submillimeter optical reflectometry. *Journal Of Lightwave Technology*, 7(8):1225–1233, 1989.

[91] E. Brinkmeyer and R. Ulrich. High-resolution OCDR in dispersive waveguides. *Electron. Lett.*, 26(6):413–414, 1990.

[92] K. Takada, T. Kitagawa, M. Shimizu, and M. Horiguchi. High-sensitivity low coherence reflectometer using erbium-doped superfluorescent fiber source and erbium-doped power-amplifier. *Electronics Letters*, 29(4):365–367, 1993.

[93] Ph. Giaccari, H.G. Limberger, and R.P. Salathé. Local coupling-coefficient characterization in fiber Bragg gratings. *Optics Letters*, 28(8):598–600, 2003.

[94] S. Keren, A. Rosenthal, and M. Horowitz. Measuring the structure of highly reflecting fiber Bragg gratings. *IEEE Photonics Technology Letters*, 15(4):575–577, 2003.

[95] P. Lambelet, P.Y. Fonjallaz, H.G. Limberger, R.P. Salathé, C. Zimmer, and H.H. Gilgen. Bragg grating characterization by optical low-coherence reflectometry. *IEEE Photonics Technology Letters*, 5(5):565–567, 1993.

[96] E. Petermann, J. Skaar, B. Sahlgren, R. Stubbe, and A. Friberg. Characterization of fiber Bragg gratings by use of optical coherence-domain reflectometry. *IEEE J. Lightw. Technol.*, 17(11):2371–2378, 1999.

[97] S. Keren and M. Horowitz. Interrogation of fiber gratings by use of low-coherence spectral interferometry of noiselike pulses. *Optics Letters*, 26(6):328–330, 2001.

[98] W. Margulis, I.C.S. Carvalho, P.M.P Gouvêa, and B. Lesche. Heat scan: a simple technique to characterize gratings in fibers. *Opt. Lett.*, 18:1016–1018, 1993.

[99] S. Sandgren, B. Sahlgren, A. Asseh, W. Margulis, F. Laurell, and R. Stubbe. Characterization of Bragg gratings in fibers using the heat-scan technique. *Electron. Lett.*, 31:665–666, 1995.

[100] E. Brinkmeyer, G. Stolze, and D. Johlen. Optical space domain reflectometry of determination of strength and chirp distribution along optical fiber gratings. In *Bragg grating, photosensitivity and poling in glass fibers and waveguides: Fundamentals and Applications*, page BSuC2, Williamsburg, USA, 1997.

[101] E. Rønnekleiv, M. Ibsen, M.N. Zervas, and R.I. Lamming. Characterization of fiber distributed-feedback lasers with perturbation method. *Applied Optics*, 38:4558–4565, 1999.

[102] C.J.S. de Matos, P. Torres, L.C.G. Valente, W. Margulis, and R. Stubbe. Fiber Bragg grating characterization and shaping by local pressure. *IEEE J. Lightwave Techn.*, 19(8):1206–1211, 2001.

[103] P. A. Krug, R. Stolte, and R. Ulrich. Measurement of index modulation along an optical fiber Bragg gratings. *Optics Letters*, 20(17):1767–1769, 1995.

[104] J. Canning, D. C. Psaila, Z. Brodzeli, A. Higley, and M. Janos. Charaterization of apodized fiber Bragg gratings for rejection filter application. *Applied Optics*, 36(36):9378–9382, 1997.

[105] P.-Y. Fonjallaz and P. Börjel. Interferometric side diffraction technique for characterization of fiber gratings. *OSA TOPS*, 33:179–182, 1999.

[106] W. Eickhoff and R. Ulrich. Optical frequency-domain reflectometry in single-mode fiber. *Applied Physics Letters*, 39(9):693–695, 1981.

[107] U. Glombitza and E. Brinkmeyer. Coherent frequency-domain reflectometry for characterization of single-mode integrated-optical waveguides. *J. Lightwave Technol.*, 11(8):1377–1384, 1993.

[108] J.P. von der Weid, R. Passy, G. Mussi, and N. Gisin. On the characterization of optical network componenents with optical frequency domain reflectometry. *IEEE J. Lightwave Techn.*, 15(7):1131–1141, 1997.

[109] P. Oberson, B. Hutter, O. Guinnard, L. Guinnard, G. Ribordy, and N. Gisin. Optical frequency domain reflectometry with a narrow linwidth fiber laser. *IEEE Photon. Technol. Lett.*, 12(7):867–869, 2000.

[110] M. Froggatt. Distributed measurement of the complex modulation of a photoinduced Bragg grating in an optical fiber. *Applied Optics*, 35(25):5162–5164, 1996.

[111] I. Peterman, B. Sahlgren, S. Helmfrid, and A.T. Friberg adn P.-Y. Fonjallaz. Fabrication of advanced fiber Bragg gratings by use of sequential writing with a continuous-wave ultraviolet laser source. *Applied Optics*, 41(6), 2002.

[112] E. Brinkmeyer, D. Johlen, F. Knappe, and H. Renner. Methods for experimental characterization of uv-written gratings and waveguides. *OSA TOPS*, 33:155–175, 1999.

[113] M. Foggatt, T. Erdogan, J. Moore, and S. Shenk. Optical frequency domain characterization of dispersion in optical fiber Bragg gratings. *OSA TOPS*, 33:176–178, 1999.

[114] S. Yao. Have you hugged your fiber today? *Photonics spectra*, February 2001.

[115] W.H. Press, S.A. Teukolsky, W. T. Vetterling, and B. P. Flannery. *Numerical recipies in C*. Cambrige university press, second edition, 1992.

[116] G. Stang. *Linear algebra and its applications*. Harcourt Brace Jovanovitch College Publishers, third edition, 1988.

[117] A.V. Buryak and D.Y. Stepanov. Correction of systematic errors in the fabrication of fiber Bragg gratings. *Optics Letters*, 27(13):1099–1101, 2002.

[118] D. Sandel, R. Noé, G. Heise, and B. Borchert. Optical network analysis and longitunal structure characterization of fiber Bragg gratings. *IEEE J. Lightwave Techn.*, 16(12):2435–2442, 1998.

[119] O.H. Waagaard, E. Rønnekleiv, and J.T.Kringlebotn. Spatial characterization of strong fiber Bragg gatings. In V. Pruneri, R.P. Dahlgren, and G.M. Sanger, editors, *Proceedings of SPIE, Fiber-Based Components Fabrication, Testing, and Connectorization*, volume 4943, pages 16–24, 2003. See chapter 7.

[120] D.-W. Huang and C.-C. Yang. Reconstruction of fiber grating refractive-index profiles from complex Bragg reflection spectra. *Applied Optics*, 38(21):4494–4498, 1999.

[121] S. Løvseth and E. Rønnekleiv. Fundamental and higher order mode thresholds of DFB fiber lasers. *IEEE Journal of Lightwave Technology*, 20(3):494–501, 2002.

[122] J. Lauzon, S. Thibault, J. Martin, and F. Ouellette. Implementation and characterization of fiber Bragg gratings linearly chirped by a temperature gradient. *Optics Letters*, 19(23):2027–2029, 1994.

[123] O.H. Waagaard, Erlend Rønnekleiv, and J.T. Kringlebotn. Spatial characterization of FBGs using layer-peeling. In *Proceeding of the 28th European Conference on Optical Communication*, page P1.32, September 2002.

[124] O.H. Waagaard. Spatial characterization of strong fiber Bragg gratings using thermal chirp and optical-frequency-domain reflectometry. *J. Lightwave Technol.*, 23(2):909–914, 2005. See chapter 8.

[125] B.J. Soller, D.K. Gifford, M.S. Wolfe, and M.E. Foggatt. High resolution optical frequency domain reflectometry for characterization of components and assemblies. *Optics Express*, 13(2):666–674, 2005.

[126] Luna Technologies white paper. Optical vector network analyzer for single scan measurements of loss, group delay and polarization mode dispersion. http://www.lunatechnologies.com/products/ova/files/OVAwhitePaper.pdf, Luna Technologies, 2005.

[127] Agilent Technologies white paper. Agilent 81910a photonic all-parameter analyzer user guide. http://www.home.agilent.com/agilent/facet.jspx?kt=1&cc=US&lc=eng&k=81910, Agilent, 2005.

[128] R.M.A. Azzam and N.M. Bashara. *Ellipsometry and polarized light*. North-Holland, 1977.

[129] E. Rønnekleiv. Frequency and intensity noise of single frequency fiber Bragg grating lasers. *Optical Fiber Technology*, 7(3):206–235, 2001.

[130] S. Kakuma, K. Ohmura, and R. Ohba. Improved uncertainty of optical frequency domain reflectometry based length measurement by linearizing the frequency chirping of a laser diode. *Optical Review*, 10(4):182–183, 2003.

[131] F. Kherbouche and B. Poumellec. UV-induced stress fields during Bragg grating inscription in optical fibers. *Journal of Optics A: Pure and Applied Optics*, 3:429–439, 2001.

List of Publications

Journal publications

1) O. H. Waagaard, G.B.Havsgård, G.Wang. An investigation of the pressure-to-acceleration responsivity ratio of fiber-optic mandrel hydrophones. *IEEE J. Lightwave Technol.* 19 (7): 994–1003, 2001.

2) J. Skaar and O. H. Waagaard. Design and characterization of finite length fiber gratings. *IEEE J. Quantum Electron.*, 39:1238–1245, 2003.†

3) O.H. Waagaard and J. Skaar. Synthesis of birefringent reflective gratings. *J. Opt. Soc. Am. A*, 21(7):1207–1220, 2004.†

4) O.H. Waagaard. Spatial characterization of strong fiber Bragg gratings using thermal chirp and optical-frequency-domain reflectometry. *IEEE J. Lightwave Technol.*, 23(2):909–914, 2005.†

5) O.H. Waagaard and J. Skaar. Synthesis of birefringent reflective gratings: Errata. Submitted to *J. Opt. Soc. Am. A*.†

6) O.H. Waagaard and J. Skaar. Inverse scattering in multi-mode structures Submitted to *SIAM J. Appl. Math.*†

7) O.H. Waagaard. Polarization-resolved spatial characterization of birefringent fiber Bragg gratings. To be submitted to *Optics Express*.†

Conference publications

1) O.H. Waagaard, G.B. Havsgård, and G. Wang. The acceleration responsivity of fiber-optic mandrel hydrophones. In *Proceeding of the 14th Conference on*

†This article is included in the thesis.

Optical Fiber Sensors, paper P3-07, Venice, Italy, October 2002.

2) O.H. Waagaard, Erlend Rønnekleiv, and J.T. Kringlebotn. Spatial characterization of FBGs using layer-peeling. In *Proceeding of the 28th European Conference on Optical Communication*, paper P1.32, Copenhagen, Denmark, September 2002.‡

3) O.H. Waagaard, E. Rønnekleiv, and J.T.Kringlebotn. Spatial characterization of strong fiber Bragg gatings. In V. Pruneri, R.P. Dahlgren, and G.M. Sanger, editors, *Proceedings of SPIE, Fiber-Based Components Fabrication, Testing, and Connectorization*, volume 4943, pages 16–24, Brügge, Belgium, October, 2002.†

4) O.H. Waagaard, J.T. Kringlebotn and E.M. Bruvik. Spatial charaterization of strong FBGs using thermal linear chirp and optical frequency domain reflectometry. In *Proceedings of Bragg grating, photosensitivity and poling in glass fibers and waveguides: Fundamentals and Applications*, Monterey, California, USA, September 2003.‡

5) O.H. Waagaard. Fiber laser with high sweep linearity. Submitted to *Nothern Light*, Bergen, Norway, June 2006.‡

Presentations

1) O.H. Waagaard, G.B. Havsgård, S. Knudsen and G. Wang. The acceleration responsivity of fiber-optic hydrophones. In *Norwegian Conference on Electro-optics*. Balestrand, Norway, May 1999.

2) O.H. Waagaard and Erlend Rønnekleiv, Complex spectral and spatial characterization of fiber Bragg gratings. In *Norwegian Conference on Electro-optics*. Flåm, Norway, May 2002.‡

3) O.H. Waagaard, J.T. Kringlebotn and E.M. Bruvik. Spatial charaterization of strong FBGs using thermal linear chirp and optical frequency domain reflectometry. In *Norwegian Conference on Electro-optics*. Tønsberg, Norway, May 2004.‡

‡This article is a part of the doctoral work but not included in the thesis.